University of Oxford

Department of Engineering Science

Physical Phenomena in Metal-Organic Frameworks: Mechanical, Vibrational, and Dielectric Response

Matthew Richard Ryder

Balliol College

Trinity 2017

A dissertation submitted for the degree of Doctor of Philosophy

I dedicate this thesis to my beloved Grandmother in celebration of her 80th birthday.

"*Nothing in life is to be feared, it is only to be understood. Now is the time to understand more, so that we may fear less.*" - Marie Skłodowska Curie

Preface

This thesis is a collection of selected research performed by the author in the Department of Engineering Science at the University of Oxford. The work is original, and no part of it has been submitted for any other degree.

The work contained in this thesis has been published in the following journal papers:

1. **M.R. Ryder** and J.C. Tan, "*Nanoporous Metal-Organic Framework Materials for Smart Applications*", *Mater. Sci. Tech.,* 30(13b), 1598 (2014).

2. **M.R. Ryder**, B. Civalleri, T.D. Bennett, S. Henke, S. Rudić, G. Cinque, F. Fernandez-Alonso and J.C. Tan, "Identifying *the Role of Terahertz Vibrations in Metal-Organic Frameworks: From Gate-Opening Phenomenon to Shear-Driven Structural Destabilization*", *Phys. Rev. Lett.*, 113, 215502 (2014).

3. **M.R. Ryder** and J.C. Tan, "*Explaining the Mechanical Mechanisms of Zeolitic Metal-Organic Frameworks: Revealing Auxeticity and Anomalous Elasticity*", *Dalton Trans.,* 45, 4154 (2016).

4. **M.R. Ryder**, B. Civalleri, G. Cinque and J.C. Tan, *"Discovering Connections Between Terahertz Vibrations and Elasticity Underpinning the Collective Dynamics of the HKUST-1 Metal-Organic Framework*", *CrystEngComm*, 18, 4303 (2016).

5. **M.R. Ryder**, B. Civalleri and J.C. Tan, "*Isoreticular Zirconium-Based Metal-Organic Frameworks: Discovering Mechanical Trends and Elastic Anomalies Controlling Chemical Structure Stability*", *Phys. Chem. Chem. Phys.*, 18, 9079 (2016).

6. **M.R. Ryder**, B. Van de Voorde, B. Civalleri, T.D. Bennett, S. Mukhopadhyay, G. Cinque, F. Fernandez-Alonso, D. De Vos, S. Rudić and J.C. Tan, "*Detecting Molecular Rotational Dynamics Complementing the Low-Frequency Terahertz Vibrations in a Zirconium-Based Metal-Organic Framework*", *Phys. Rev. Lett.*, 118, 255502 (2017).

7. **M.R. Ryder**, T.D. Bennett, C.S. Kelley, M.D. Frogley, G. Cinque and J.C. Tan, "*Tracking Thermal-Induced Amorphization of a Zeolitic Imidazolate Framework via Synchrotron In Situ Far-Infrared Spectroscopy*", *Chem. Commun*., 53, 7041 (2017).

8. **M.R. Ryder**, Z. Zeng, Y. Sun, T.D. Bennett, I. Flyagina, K. Titov, E.M. Mahdi, B. Civalleri, C.S. Kelley, M.D. Frogley, G. Cinque and J.C. Tan, "*Dielectric Properties of Metal-Organic Frameworks Probed via Synchrotron Infrared Reflectivity*", Submitted.

Some of the additional work performed by the author during the DPhil and out with the context of the thesis was published in the following journal papers:

9. I. Buchan, **M.R. Ryder**, and J.C. Tan, “*Micromechanical Behavior of Polycrystalline Metal-Organic Framework Thin Films Synthesized by Electrochemical Reaction*”, *Cryst. Growth Des.*, 15(4), 1991 (2015).
10. A.K. Chaudhari, **M.R. Ryder**, and J.C. Tan, "*Photonic Hybrid Crystals Constructed from In Situ Host-Guest Nanoconfinement of a Light-Emitting Complex in Metal-Organic Framework Pores*", *Nanoscale*, 8, 6851 (2016).
11. C.S. Coates, **M.R. Ryder**, J.A. Hill, J.C. Tan and A.L. Goodwin, “*Large Elastic Recovery of Zinc Dicyanoaurate*”, *APL Mater.*, 5, 066107 (2017).

Abstract

The desire to further our understanding of how things work at a fundamental level has existed since humanity first appreciated the study of science. However, with the dawn of next-generation materials, and the smart applications they are capable of, the time to develop new methodologies to analyse and explain their intrinsic properties at the atomic scale is upon us.

This thesis entails the utilisation of *ab initio* density functional theory (DFT) in conjunction with neutron and synchrotron spectroscopy to study the mechanical, vibrational, and dielectric response of metal-organic framework (MOF) materials at the molecular level. MOFs are crystalline materials with nanoscale porosity, which have garnered immense scientific and technological interest for a wide variety of innovative engineering applications.

One part of the thesis involves using low-frequency lattice vibrations to characterise the various physical motions that are possible for framework materials. These collective modes detected at terahertz (THz) frequencies have been used to reveal a broad range of exciting possibilities. New evidence has been established to demonstrate that THz modes are intrinsically linked to anomalous elasticity underpinning gate-opening and pore-breathing mechanisms, and to shear-induced phase transitions and the onset of structural instability. The phenomenon of molecular rotor mechanisms and trampoline-like motions are also observed, along with the first experimental confirmation of coordinated shear dynamics. Additionally, a new method to characterise the effects of temperature, and hence thermally-induced structural amorphisation is reported.

Finally, for the first time, the frequency-dependent (dynamic) dielectric response of MOF materials, across the extended infrared (IR) spectral region was reported. The results were obtained from experimental synchrotron radiation IR reflectivity and DFT to reveal the low-κ dielectric response of MOFs and established structure-property trends that highlight them as promising systems for microelectronic device applications.

Acknowledgments

Firstly, I thank my DPhil supervisor Prof. Jin-Chong Tan for giving me the opportunity to study at the University of Oxford and for introducing me to many great collaborators. I am especially grateful to Jin for encouraging me to be the best that I can and for his constant motivation with my research. I additionally thank the other co-supervisors I have had during my DPhil, namely: Dr Svemir Rudić, Prof. Bartolomeo (Mimmo) Civalleri, Dr Gianfelice Cinque, Prof. Felix Fernandez-Alonso, and Dr Sanghamitra Mukhopadhyay. I want to express my particular appreciation to Svemir for going beyond his role as a supervisor on multiple occasions, and for introducing me to the world of neutron scattering. Also, I am grateful to Mimmo for his valuable help and insights regarding the CRYSTAL code.

I would like to thank the Engineering and Physical Sciences Research Council (EPSRC) for a full scholarship and the Science and Technology Facilities Council (STFC) for an additional scholarship. Furthermore, I thank the EPSRC for awarding me with a Doctoral Prize Fellowship upon completion of my DPhil. I am also grateful for the numerous awards and prizes I have received throughout my DPhil, primarily from the following organisations: Royal Society of Chemistry (RSC), Institute of Physics (IOP), and British Zeolite Association (BZA).

I thank all my friends and collaborators at the ISIS Pulsed Neutron Source Facility and Diamond Light Source Synchrotron for helping and encouraging me, namely: Dr Mark Frogley, Dr Chris Kelley, Dr Jeff Armstrong, Dr James Taylor, Dr Gavin Stenning, and Dr Marek Jura. I would also like to thank my synthetic collaborators: Dr Tom Bennett, Dr Sebastian Henke, and Dr Ben Van De Voorde.

Furthermore, I would like to recognise all the past and present members of the Multifunctional Materials & Composites (MMC) Laboratory, especially Mahdi, Abhijeet, Jason, and Yueting. Likewise, I am glad to have made so many friends in the Solid Mechanics and Materials Engineering Group. I have especially enjoyed all the fun times in the office with Rodolfo and Rango, and the late night and weekend conversations with Elsiddig, Kurien, and Rima. I also want to thank Charles, Hisham, and Amanda for the countless great discussions, debates, and advice they have given me.

Outside my scientific life (despite most of them being scientists), I want to thank all my friends especially those at Balliol College who have made the past few years some of the best in my life.

Last but certainly not least, I want to acknowledge some of the people who have enabled me to become the scientist I am today. This includes Mr Mervyn Linklater, the amazing teacher who inspired me to study Chemistry, Physics, and Mathematics, and Prof. Maciej Gutowski, who made me fall in love with scientific research. Finally, I want to sincerely thank my incredible family. I am eternally grateful to my parents for continuously supporting me in every way possible, my brother Damian for always being there for me and giving me the best advice, my Granny for making me feel like I can do anything, and my girlfriend Jess for making my life an adventure and putting up with me on a daily basis.

I also want to thank anyone who reads this thesis; I sincerely hope you enjoy it!

Nomenclature

Below is a summary of some of the most commonly used terms throughout the thesis.

Term	Description
β	Linear Compressibility
β_{max}	Maximum Linear Compressibility
β_{min}	Minimum Linear Compressibility
ε	Strain
ϕ	Rotation Angle
γ	Shear Strain
κ	Dielectric Constant
ν	Poisson’s Ratio
ν_{max}	Maximum Poisson’s Ratio
ν_{min}	Minimum Poisson’s Ratio
σ	Stress
τ	Shear Stress
Γ-point	Gamma Point (Referring to Phonons)
4MR	4-Membered Ring
6MR	6-Membered Ring
8MR	8-Membered Ring
Å	Angstrom (equal to 10^{-10} metres)
A^*	Ledbetter Anisotropy
A_E	Anisotropy of Young’s Moduli
A_G	Anisotropy of Shear Moduli
ATR	Attenuated Total Reflection
B3LYP	Becke, Three-Parameter, Lee-Yang-Parr: DFT Functional
BET	Brunauer-Emmett-Teller
bIm	Benzimidazolate
BTC	Benzene-1,3,5-tricarboxylate
CIF	Crystallographic Information File
C_{ij}	Single-Crystal Elastic Constant
cm^{-1}	Wavenumber
DFT	Density Functional Theory
E	Young’s Modulus
E_{max}	Maximum Young’s Modulus
E_{min}	Minimum Young’s Modulus
FIR	Far-Infrared
FTIR	Fourier Transform Infrared

FWHM	Full-Width-Half-Maximum
G	Shear Modulus
G_{max}	Maximum Shear Modulus
G_{min}	Minimum Shear Modulus
GPa	Gigapascal
HKUST	Hong Kong University of Science and Technology
HT	High Temperature
Im	Imidazolate
INS	Inelastic Neutron Scattering
IR	Infrared
K	Bulk Modulus
K	Degrees Kelvin
KKT	Kramers-Kronig Transformation
kPa	Kilopascal
LT	Low Temperature
meV	Millielectronvolt
MIL	Materials Institute Lavoisier
mIm	2-Methylimidazolate
MIR	Mid-Infrared
MOF	Metal-Organic Framework
NIR	Near-Infrared
NLC	Negative Linear Compressibility
NPR	Negative Poisson’s Ratio
NTE	Negative Thermal Expansion
PBE	Perdew, Burke, Ernzerhof: DFT Functional
QENS	Quasi-Elastic Neutron Scattering
S	Compliance Matrix
$S(Q, \omega)$	Scattering Function
SAV	Solvent Accessible Volume
SBU	Secondary Building Unit
THz	Terahertz
TPa	Terapascal
UiO	Universitetet i Oslo
VRH	Voigt-Reuss-Hill
X_{R}	Thermal Shift Coefficient
ZIF	Zeolitic Imidazolate Framework
ZPR	Zero Poisson’s Ratio (Auxeticity)
ZrO	Zirconium Oxide

Table of Contents

Chapter 1

Introduction

This chapter provides a brief introduction to the motivation and structure of the thesis. It summarises the background literature in the field in Chapter 2, before explaining the intricacies of the experimental and theoretical methodologies throughout in Chapter 3. The results consist of four chapters focusing on the mechanical, vibrational, and dielectric response of metal-organic framework (MOF) materials. The thesis closes with a short conclusions section, to reflect on the results and make suggestions for how the work could progress in the future (Chapter 8).

1.1 Motivation

1.1.1 Metal-Organic Frameworks

Hybrid three-dimensional (3D) framework materials, known as metal-organic frameworks (MOFs) are crystalline materials constructed from inorganic and organic building blocks. They encompass a diverse range of nanoporous 3D structures (Figure 1.1) and are self-assembled at the molecular level. MOFs currently represent one of the most promising families of next-generation material due to their vast chemical and structural diversity and the ability to tune various structural properties.[1] This is supported through the potential they represent for areas such as energy (renewable hydrogen production and next-generation rechargeable batteries), environmental remediation and sustainability (CO_2 sequestration and water purification) and medicine (drug delivery and biosensing).[2]

The rapidly expanding field of MOF materials is evidenced by the exponential growth in the number of scientific publications reported and the accompanying new materials discovered over the past decade.[3] While the pioneering studies in the 1990s concerned with MOFs were largely confined to the chemistry discipline, nowadays, research activities on MOF-type materials are extraordinarily vibrant and highly cross-disciplinary. Unquestionably the remarkably large (internal) surface areas that exist in MOFs (Figure 1.2) have caught the attention and imagination of many scientists and

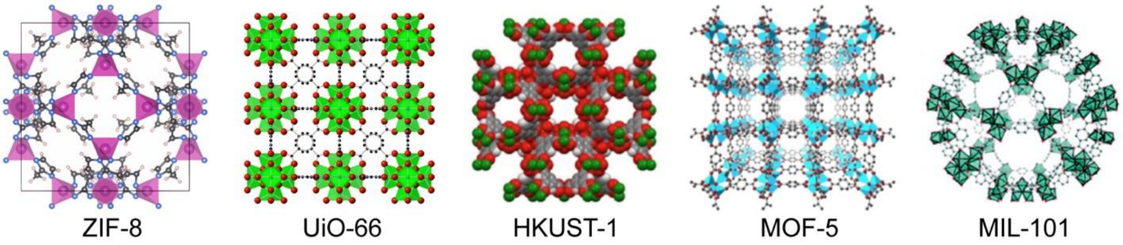

Figure 1.1. Different prototypical porous MOFs with various framework topologies.

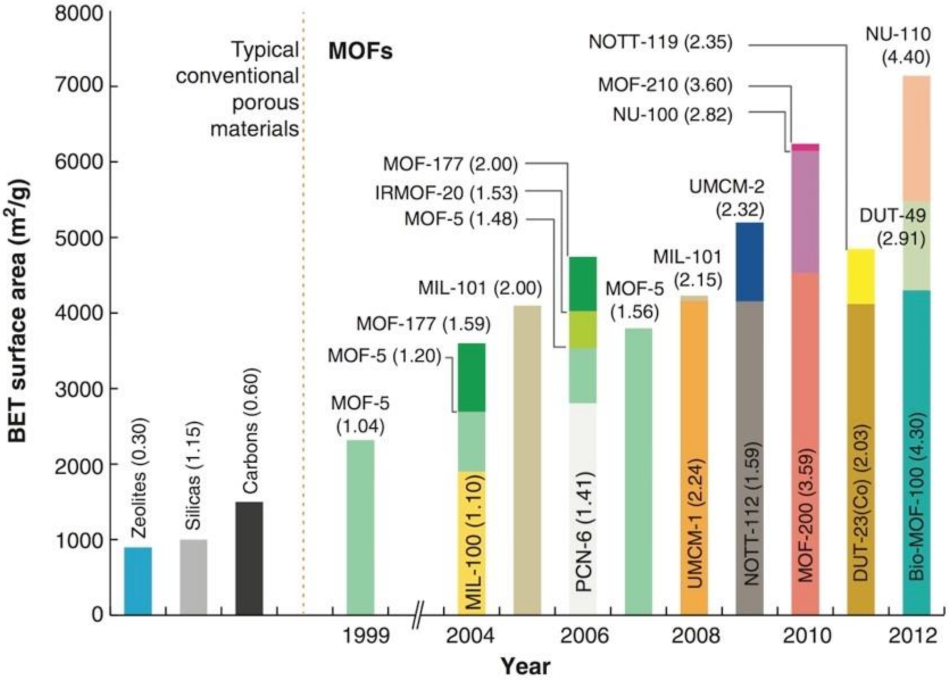

Figure 1.2. Progress in the synthesis of ultrahigh-porosity MOFs. Shown here are the surface areas of MOFs in comparison with conventional porous materials (inorganic zeolites, silicas and carbons), determined from gas adsorption experiments. The values in parentheses are the pore volume in cm^3 g^{-1}. Reprinted with permission from Ref. [3].

engineers alike. The capacity to precisely control and functionalise the nano-sized pore volume has allowed for unique multifunctional properties. The unique physicochemical and thermo-mechanical characteristics of MOFs have opened up new opportunities for exploitation in multiple branches of chemistry, materials science, nanotechnology, physics, biology, medicine, and engineering. For example, there are multiple specific review articles which cover in detail the inorganic-organic crystal structures[4, 5] and network topologies of MOFs.[1] There are also many excellent reviews covering gas adsorption,[6, 7] selective separations, and storage capacities. [6-8] Other specific applications are covered such as luminescence[9] and chemical sensing response.[10] Critical reviews are also associated with thermomechanical behaviour,[11] ferroelectricity,[12] magnetic response,[13] and catalytic applications of MOFs.[14]

These selected next-generation applications are highlighted to emphasise the importance and need for gaining a better understanding of the complex mechanisms possible for MOFs at the molecular level. As MOFs show such promise in a wide range of applications, it is crucial to understand the underlying fundamental mechanisms and properties that allow such desirable features and better comprehend the structural stabilities of the materials. However, research characterising fundamental mechanisms and physical properties are still in their infancy.

1.1.2 Mechanical and Electrical Properties

Two of the critical features that can have a direct effect on the suitability of a material for a specific application are the mechanical and electrical properties. However, the number of studies concerned with characterising these properties in framework materials is still quite low. Although still in the early stages, research has already started to show that the combined use of experimental methods such as Brillouin scattering, synchrotron infrared (IR) and neutron spectroscopy, along with theoretical methods such as density functional theory (DFT) and in some cases molecular dynamics (MD), can be vital in the investigation and explanation of mechanical and electrical properties. It is through this combined approach that important discoveries can be generated pertaining to the fundamental suitability of individual frameworks and families of frameworks for specific applications by exposing their unique physicochemical interdependencies.

1.2 Structure of the Thesis

The thesis includes eight chapters and focuses on the mechanical, vibrational, and dielectric response of MOF materials. After this Introduction, there is a chapter dedicated to the relevant literature (Chapter 2) that is helpful in setting the work in the context of the state-of-the-art in the field. The Background Literature is then followed by a chapter dedicated to the theoretical and experimental methods used throughout the thesis.

The following four chapters report the results, starting with the mechanical response of MOFs in Chapter 4. The mechanical properties of a range of MOF materials are discussed and explain the fundamental structural mechanisms responsible for several exciting discoveries, such as exceptionally low shear moduli, the presence of negative Poisson's ratios (auxeticity), and isoreticular structure-property trends.

With Chapter 4 setting a thorough introduction to the rich diversity of mechanical properties and structural flexibility present in MOF materials, Chapter 5 and Chapter 6 demonstrates the application of vibrational spectroscopy to investigate the structural motions. Chapter 5 focuses on identifying and elucidating the nature of the low-energy vibrational motions present in the terahertz (THz) spectral region. In addition to identifying characteristic frequencies of the metal-linker polyhedra deformation and linker deformation modes, the main novelty is in the discovery of vibrational motions reminiscent of the mechanisms responsible for the various structural phenomenon. This includes framework breathing in ZIF-7, gate-opening in ZIF-8 and trampoline-like motions in HKUST-1 and MIL-140A which could potentially be the source of anomalous mechanical phenomena such as negative thermal expansion (NTE). The Chapter also makes connections between THz vibrations and the mechanical properties discussed in Chapter 4. It reports coordinated shear dynamics that explain the minimum shear moduli and reveals the mechanism behind the negative Poisson's ratio of HKUST-1.

Chapter 6 extends the use of vibrational motions to study the thermally induced amorphisation of ZIF-4. The spectral changes observed upon thermal stimulus were tracked *in situ*, allowing for the nature of vibrational motion changes during the amorphisation process to be explained and reveals new insights into the effect that temperature has on the Zn–N tetrahedra.

The last results chapter (Chapter 7) is concerned with the low-κ dielectric response of MOFs, specifically ZIF materials. The results present for the first time the use of synchrotron spectroscopy to obtain the experimental frequency-dependent (dynamic) dielectric response in the extended IR spectral region for a group of topical polycrystalline ZIFs. The work also reveals the structure-property trends that link the THz region dielectric response to the framework porosity and structural density.

The concluding chapter provides an overview of the various results and discoveries and offers a brief description of the future of the field. The appendix section primarily contains supplementary data including the lattice parameters of the materials studied and additional descriptions of the vibrational modes.

Chapter 2

Background Literature

This chapter presents a brief introduction to the background literature concerning the physical properties of metal-organic framework (MOF) materials. It highlights the need for a better understanding of the mechanical stability and underlying mechanisms responsible for the highly anisotropic response of MOFs. Specifically, it gives a summary of the background literature regarding the mechanical, vibrational and dielectric properties of MOFs and the relevance of the results reported in later chapters.

2.1 Introduction

The purpose of this chapter is to provide a brief overview of the background literature concerning specifically the mechanical, vibrational, and dielectric properties of metal-organic framework (MOF) materials. In the past decade, it is evidenced that porous MOF materials are rapidly emerging as promising candidates for a wide range of applications. The industrial importance of these next-generation hybrid materials is evidenced by the fact many MOFs can now be obtained commercially, as summarised in Table 2.1.

One of the primary bottlenecks hindering the progress with many of the proposed next-generation applications of MOF materials is the current lack of understanding of the fundamental framework mechanisms resulting in the flexibility (lattice dynamics) and mechanical stability. It is this motivation that drives the work presented in this thesis, and the following sections in this chapter highlight the initial work building up to the results reported later in the thesis.

Table 2.1. List of commercially available MOF materials.

Structure	Trade Name	Company
ZIF-8	Basolite® Z1200	BASF Sigma-Aldrich MOF Technologies
HKUST-1	Basolite® C 300	
MIL-53(Al)	Basolite® A100	BASF Sigma-Aldrich
Fe-BTC	Basolite® F300	
MOF-177	Basolite® Z377	
ZIF-67	-	MOF Technologies
MOF-74(Mg)		
MOF-74(Ni)		
MOF-74(Co)		
CAU-10		
PCN-250		
TIFSIX(Ni)		

Note: BDC = 1,3,5-benzenetricarboxylate

2.2 Physical Properties

2.2.1 Mechanical Behaviour

Understanding the mechanical properties and long-term durability of MOF materials is considered as one of the key challenges to be addressed to warranty the future success of this vibrant field.[15] While the structure and adsorption properties of MOFs have been systematically studied and extensively characterised,[3, 16] considerably less attention has been focused on the important physical properties that are critical to many of the real-world applications.[2, 17, 18] In principle, to be able to predict whether a MOF will remain structurally stable when subject to external stress or pressure (not deforming excessively or collapsing under load), specific fundamental information relating to its mechanical behaviour is required.[11] However, such detailed data regarding the mechanical stability associated with MOFs remains scarce.[19]

More specifically, the core mechanical properties[11, 19, 20] and physical toughness,[21-23] in conjunction with long-term structural and chemical stability of MOFs are central for manufacturing,[15] shaping[24] and scaling up, and are currently limiting the successful deployment of applications in many diverse technological settings. The emerging field of MOF-mechanics,[20, 25, 26] particularly concerning the effects of elevated pressure (hydrostatic compression) on the structural transformation and chemical response of MOFs is an area of intense study.[27-30] The tunability of MOF mechanical properties made possible through isoreticular design and construction,[31-33] host-guest interactions,[34] and chemical modification[35] is another topic of current interest. Given the flexible nature of open frameworks[36] attributed to compliant metal coordination environments bridged by organic linkers, they offer exciting new opportunities to yield unusual elastic response (Figure 2.1 and Figure 2.2)[11, 37] which are rare in conventional materials. Large elastic anisotropy of

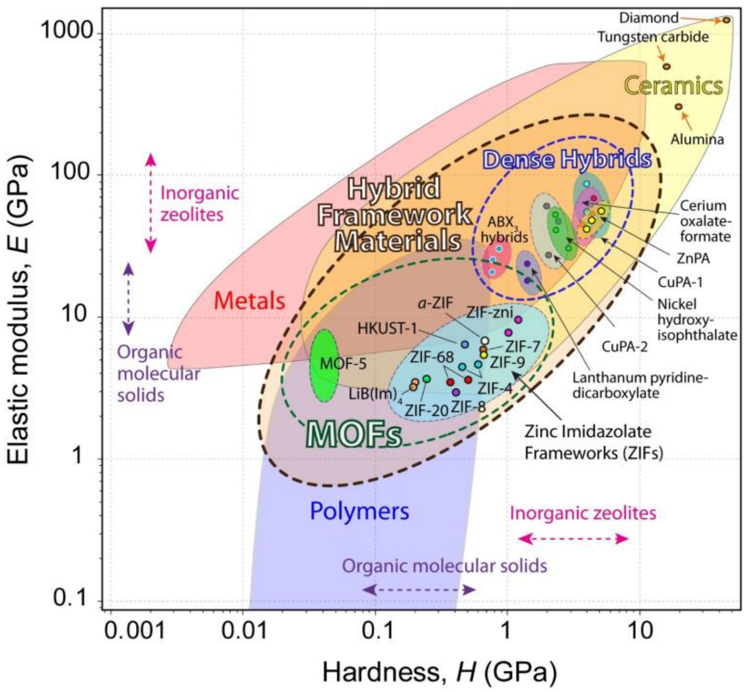

Figure 2.1. Elastic modulus versus hardness materials property map for hybrid framework materials, encompassing both dense and nanoporous MOFs presented with other major classes of materials: reprinted with permission from Ref. [11].

MOFs are notable,[38-40] and this property could have significant consequences on both mechanical and thermal stability determining the robustness of porous frameworks against structural destabilisation,[41-43] irreversible plastic deformation[11, 44, 45] and amorphisation.[42, 46]

From a more fundamental point of view, basic research on MOF mechanics can open the door to the discovery of exotic mechanical characteristics, for example zero Poisson's ratio (ZPR),[47] negative Poisson's ratio (auxeticity or NPR),[47-49] negative linear compressibility (NLC)[30, 50-53] and negative thermal expansion (NTE),[26, 54-57] all of which are controlled by the detailed chemical bonding and coordination framework architecture underpinning modular MOF structures. These so-called mechanical metamaterials[49] are extremely attractive for example to engineer crack-resistant thin-film devices and multifunctional coatings; provided that the associated manufacturing challenges can be alleviated. Above all, the core science of

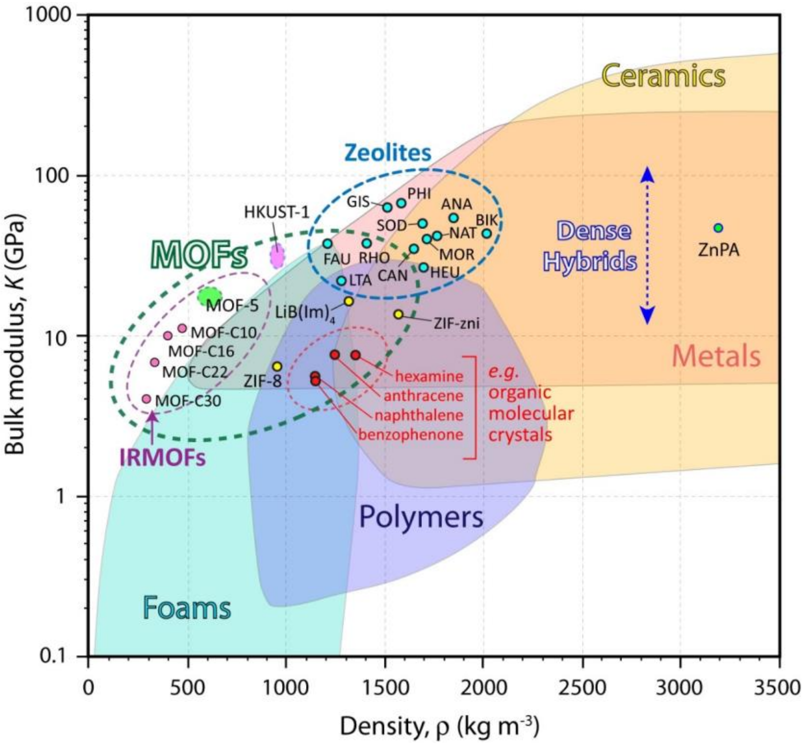

Figure 2.2. Bulk modulus versus density materials property map for hybrid framework materials, encompassing both dense and nanoporous MOFs presented with other major classes of materials: reprinted with permission from Ref. [11].

MOF-mechanics focusing on detailed elasticity analysis provides the crucial starting point to comprehending many associated MOF mechanical behaviours beyond the elastic limit, including structural yielding and irreversible plastic deformation,[58] cracking and intermolecular rupture,[59] and MOF structural distortions triggered by elastic destabilisation, amorphisation[60] and mechanochemistry.[61]

Despite the apparent need to better understand the mechanical behaviour of MOF materials, the number of studies concerned with understanding their molecular-scale elasticity and mechanical properties is still rather limited. Initially, research concentrated on the Young’s modulus (E) and the bulk modulus (K), as they are more straightforward to determine experimentally. However, especially for anisotropic materials such as MOFs, a complete understanding of the framework stability can only be obtained through additional properties, such as the shear modulus (G) and Poisson’s ratio (v).

The initial theoretical work concerning the mechanical stability of MOF materials focused on the simple cubic structure, MOF-5. Fuentes-Cabrera *et al.*[62] reported the bulk modulus of MOF-5 and some hypothetical analogues. Despite being limited to the bulk modulus, the work provided an excellent introduction to the level of mechanical stability of MOF materials. The method applied involved calculating the optimised energies of various volumetric displacements and subsequently fitting the resultant curves with the Birch-Murnaghan equation of state.[63]

The initial work encouraged additional elastic properties to be investigated by Zhou *et al.*,[64] who as part of their study of the lattice dynamics of MOF-5, calculated the single crystal elastic constants (C_{ij}). However, it was Bahr *et al.*[65] not long after who by a combined experimental and theoretical approach reported the Young's modulus. They reported the average value obtained from nanoindentation to be 2.7 GPa, although this value did not account for the anisotropy of the material. Hence after correcting for anisotropy, they estimated the Young's modulus for the <100> face to be 7.9 GPa. However, their theoretical DFT results gave a very different value, almost a factor of three greater (E_{100} = 21.6 GPa). Their theoretical results also gave E_{111} = 7.5 GPa, leading to an anisotropy factor of 2.9. In addition to the elastic constants: C_{11}, C_{12}, and C_{44} being in agreement with the results of Zhou *et al.*,[64] they also agreed well with other DFT studies that were simultaneously being performed by other groups investigating MOF-5 as a possible hydrogen storage material.[66] This discrepancy could indicate that the comparison was off due to the degradation of the crystal used for the experiments, supported by nanoindentation on partially decomposed samples being expected to produce much lower stiffness values.[11] It also demonstrated the limitations of isotropic methods such as nanoindentation for measuring the elastic response of anisotropic materials and highlighted the need for caution during the analysis of experimental results.

Another family of MOFs that have been of interest for elasticity studies are zeolitic imidazolate frameworks (ZIFs), where Tan *et al.*[31] demonstrated their structure-property relations, linking mechanical properties with chemical structure, network topology and porosity. They showed that the Young's moduli of the different ZIF materials scaled non-linearly with respect to the framework density, as illustrated in Figure 2.3. One of the ZIFs reported to have a significantly large porosity was ZIF-8 (one of the least dense in Figure 2.3), and a more detailed investigation of the elastic properties was performed. Using Brillouin scattering in conjunction with DFT, Tan *et al.*[41] studied the single-crystal elastic constants of ZIF-8, reporting the constants: C_{11}, C_{12} and C_{44}, under ambient conditions, to be 9.52, 6.87 and 0.97 GPa respectively. Tensorial analysis of the elastic constants showed the anisotropic elasticity and highlighted a

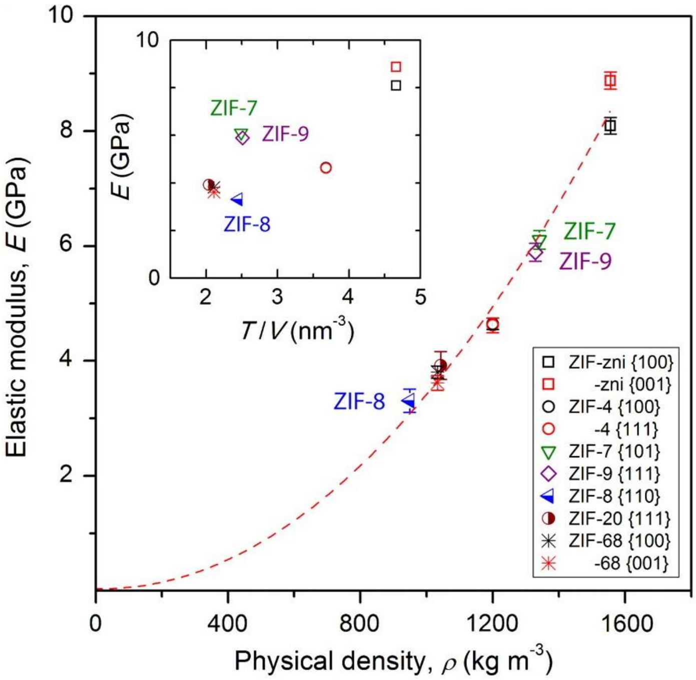

Figure 2.3. Elastic modulus (*E*) of ZIF single crystals as a function of the framework physical density and number of tetrahedral (metal) sites per unit volume (*T* / *V* in inset). The modulus-density correlation can be approximated by a quadratic relationship represented by the red dotted curve: reprinted with permission from Ref. [11].

remarkably low shear modulus ~1 GPa (at the time the lowest reported for a single-crystalline extended solid, although this has been predicted to have been succeeded by ZIF-3 in Chapter 4). The low shear modulus indicates that there could be a heightened chance of shear-induced amorphisation, which is supported by a recent study on the ball milling induced amorphisation of MOFs.[67] The work on ZIF-8 demonstrated that a greater understanding of the elastic properties is crucial for emerging applications and also highlighted the feasibility of DFT in obtaining these properties.

Five highly flexible MOFs: MIL-53(Al), MIL-53(Ga), MIL-47, and the square and lozenge structures of DMOF-1, were also studied using DFT by Ortiz *et al*.[38] Tensorial analysis of the elastic constants showed the materials to have much higher levels of anisotropy than MOF-5 or ZIF-8. The anisotropy was reported to reach a ratio of 400:1 between the most rigid and weakest directions. This would appear to be a feature of increased flexibility, as MOF-5 and ZIF-8 did not display such behaviour. The work also showed that flexible MOFs can display significant negative linear compressibility (NLC: elongation under pressure instead of compression) in specific directions, which has been confirmed experimentally by Serra-Crespo *et al*.[30] This phenomenon is reported and discussed further in Chapter 4 and has been identified as an important property for artificial muscles and new types of sensors.[53]

Many interesting properties have been shown for MOF materials, and contrary to the exceptionally low shear modulus witnessed for ZIF-8 discussed above, Wu *et al*.[68] reported unusually high shear stability present in UiO-66, a Zr-based MOF. Using DFT, they reported that the minimal shear modulus was 13.7 GPa, an order of magnitude higher than all other MOFs studied, even approaching that of zeolites. It was suggested that this high stability was due to the increased degree of coordination of the Zr metal centres. Not long after, Ortiz *et al*.[69] presented the tensorial analysis of the elastic constants for two additional flexible MOFs: MIL-122(In) and MIL-140A. They reported various mechanical properties including the directional Young's modulus, shear modulus, Poisson ratio, and linear compressibility. The shear modulus for MIL-122(In) was shown to be 12.5 GPa, close to that of UiO-66. They linked the mechanical properties to the geometry and compliance of the materials. The same group have studied CAU-13 and NOTT-300 (since renamed MFM-300), two aluminium (Al) based MOFs[70] with a similar topology to MIL-53(Al), thereby demonstrating that DFT can be used to obtain a thorough understanding of a wide selection of MOF materials, with varying metals, linkers and topologies.

It is encouraging to see that there has been an increasing range of research activities evolving in the past few years devoted to the emerging area of MOF-mechanics, encompassing both theoretical and experimental studies. To date, the state-of-the-art has involved the application of DFT to derive the theoretical values of single-crystal elastic constants, from which the elastic anisotropy and network flexibility can be characterised.[20, 38, 41, 68, 71] There has also been an increase in experimental studies to ascertain the bulk modulus and linear compressibility of MOFs using diamond anvil cells (DACs);[30, 50] hardness and Young's modulus measurements by means of nanoindentation;[31, 34, 72-74] shear modulus measurement using Brillouin scattering;[41] and nanoscratch experiments to characterise the cohesion and interfacial adhesion strengths of polycrystalline MOF films.[21, 22, 75]

However, there is a need for more in-depth analysis and explanation of the underlying mechanisms at the origin of these unusual mechanical properties. This can only be obtained *via* the use of DFT calculations and tensorial analysis but with additional care taken in the analysis of the structure-property relationships (Chapter 4). In addition, the work in this thesis demonstrates that a combined experimental and theoretical approach to establishing the dynamics and collective lattice vibrations of MOFs can offer rich insights into the basis of framework flexibility and to pinpointing potential sources of structural destabilisation (Chapter 5).

2.2.2 Vibrational Spectroscopy and Lattice Dynamics

Vibrational spectroscopy has been a popular method of analysing gas adsorption and substrate binding in MOF materials, and there is an extensive review on the topic available in Ref. [76]. However, the vibrational work reported in this thesis is concerned with using vibrational spectroscopy to investigate unique spectral regions, primarily the far-IR (FIR < 600 cm^{-1}) and THz (< 330 cm^{-1} $\approx$ 10 THz) domains. For this reason, the following section focuses on highlighting some of the more fundamental studies that have motivated the research in this thesis.

Civalleri *et al.*[77] were one of the first groups to calculate vibrational frequencies of a MOF material using DFT. They investigated the electronic structure properties and vibrational motions of MOF-5 using the B3LYP hybrid functional,[78-80] concluding that DFT could be used to obtain accurate data relating to the vibrational nature of MOFs. Shortly after Zhou *et al.*[64] investigated the lattice dynamics of MOF-5 using a combined approach of inelastic neutron scattering (INS) along with DFT. As mentioned in the previous section, they also predicted that MOF-5 was close to structural instability as the shear modulus was very low (~1.2 GPa) and could yield other phases under high pressure and strain. They noted that their simulated spectra agreed well with the experimental data and also highlighted several interesting vibrational modes including the softest twisting modes of the organic linker, which they were unable to thermally access, as the activation barrier was estimated to be ~537 meV. Zhou *et al.*[81] also reported the quantum methyl rotation present in ZIF-8. They showed the ground-state tunnelling transitions in both the hydrogenated and deuterated framework and indicated the barrier to internal rotation was low compared to most methylated compounds in the solid state. They estimated the methyl rotation barrier to be ~7 meV with a very low energy rotational oscillation, terming the motion as quasi-free methyl rotation.

Since then there have been several spectroscopic studies concerning ZIF-8, mainly due to its significant porosity and promise for storage applications. Hu *et al*.[82] were the first to investigate ZIF-8 at high pressure (up to ~39 GPa) *in situ* by Fourier transform IR (FTIR) spectroscopy, showing that the structural modifications observed were reversible only for pressure regions below 1.6 GPa and irreversible beyond this region, resulting in a disordered or amorphous phase. Despite the structural instabilities, ZIF-8 was shown to exhibit unusual chemical stability with Fairen-Jimenez *et al*. reporting unexpected adsorption of molecules that were larger than the standard pore aperture.[83] This indicated the existence of significant structural flexibility and was investigated *via* a combined experimental and theoretical approach. The results showed that the ZIF-8 framework underwent a gate-opening mechanism at 1.47 GPa. They reported that this was due to a swing effect of the organic linkers, providing increased access to the internal porosity. This exact mechanism is reproduced *via* vibrational spectroscopy for the first time in Chapter 5.

ZIF-8 has become a favorite MOF material for initial proof of concept studies due to its straightforward synthesis with good yield, the potential for applications, and the level of current characterisation already performed. The apparent chemical stability of ZIF-8 encouraged further studies, with Hu *et al*.[84] continuing their FTIR spectroscopy work, this time into the investigation of carbon CO_2 storage. The research involved the insertion of CO_2 into the ZIF-8 framework at pressures of 0.8 GPa. Two unique IR signals (from the internal and external CO_2 interactions) could then be identified by FTIR spectroscopy, providing insight into the interaction sites. The results showed enhanced storage of CO_2 inside the framework and the storage behaviour was shown to depend on pressure significantly. Soon after Kumari *et al.*[85] investigated ZIF-8 using Raman spectroscopy, showing temperature-induced structural transformations that allowed the framework to adsorb other gases such as N_2 and CH_4.

A similar study by Aguado *et al.* reported that ZIF-7 could also undergo a kind of gate-opening mechanism but this time more akin to breathing.[86] The motion was likened to that of a blowfish and showed that the reversible effect arises from a phase-transformation upon guest adsorption-desorption. The motion was again reproduced in Chapter 5, further highlighting the importance and impact of the lattice dynamics on understanding the structural flexibility and elasticity of framework materials. In addition, Noei *et al.*[87] studied the CO adsorption potential of a Ru-based MOF. The adsorption of hydrogen has been demonstrated for other MOFs, including a Ni-based MOF by Brown *et al.*[88] and the Cu-based MOF, HKUST-1 by Callear *et al.*[89]

Research regarding the vibrational nature of MOFs has traditionally concentrated on gas adsorption, as evidenced above. This is in part due to the mid-IR (MIR) region of the vibrational spectra being more accessible for studies. However, as will be revealed in Chapter 5, there are other spectral regions (FIR and THz) that can reveal interesting properties, and as both experimental resolution (at synchrotron and neutron facilities) and computing power increase these areas will become more accessible, allowing for a better understanding of the lattice dynamics. It is worth noting that these THz frequency vibrational modes had previously been highlighted in relation to the structural destabilisation of crystalline zeolites.[90] Greaves *et al.* suggested that the Boson peak in the glassy state of a zeolite could be linked to framework features at the nanoscale, namely, connected ring moieties.[90] It was this suggestion that instigated the motivation for Chapter 5.

2.2.3 Dielectric Response

The high potential to customise the building blocks has opened many new avenues of research, such as the use of MOFs in optical and microelectronics.[2, 15, 91] This area of interest is stimulated by the emergence of next-generation photonics, such as optical sensors and switches and requires the introduction of new low-κ dielectric materials ($\kappa < 2.0$) to be used as an interlayer for semiconducting devices.[91-93] Some years ago the International Technology Roadmap for Semiconductors[94] stated that desirable materials should possess a periodic structure, low density (e.g. high porosity), low moisture absorption, high chemical and thermal stability (as also discussed by Hatton *et al.*).[93] Notably, MOFs have been recently advocated as future emerging low-κ materials in the "More Moore - White Paper" by the International Roadmap for Devices and Systems.[95]

MOFs have the potential to show significantly small dielectric constants ε (referred to as κ in technological applications), due to their high porosity (low density) and low polarisability. Also, the integration of porous thin films such as MOFs for use as functional devices is currently an emerging field with promising application in gas sensing and flexible displays.[96] The current literature has already highlighted the potential of MOFs as low-κ dielectric materials.[97] Theoretical work in the field has initially involved the semi-empirical Clausius-Mossotti model, applied to study the dielectric response of cubic Zn-based MOFs.[97] There have also more recently been some *ab initio* studies on cubic frameworks and the complex dynamic dielectric constant in the near-ultraviolet (UV) region.[98, 99] These theoretical studies have encouraged experimental work on thin films, involving the use of spectroscopic ellipsometry (SE) to report the dielectric and optical properties of HKUST-1[100, 101] and ZIF-8 in the near-UV region.[102] This has confirmed that MOFs are indeed promising candidates as low-κ dielectrics.[103]

Other recent studies have investigated the dielectric properties of MOFs in the presence of solvent molecules and have reported higher thermal stability and increased dielectric constants.[104, 105] Mendiratta *et al.*[106] reported that the dielectric response was affected by host-guest interactions in the framework. They demonstrated that the dielectric constant of two Ni-based MOFs varied from ~4.8–12.6, depending on the polarisability of the guest molecule. The decrease in the dielectric constant witnessed when a less polarisable guest was present was attributed to the host-guest interactions resulting in the absence of electrical order. Sanchez-Andujar *et al.*[107] reported anomalies in the dielectric response as a result of order-disorder processes (Figure 2.4), where they showed a high-κ dielectric response at room temperature that decreased by a factor of 50 upon cooling. The unusual behaviour was attributed to the order-disorder process of the dipolar guest molecules in the framework.

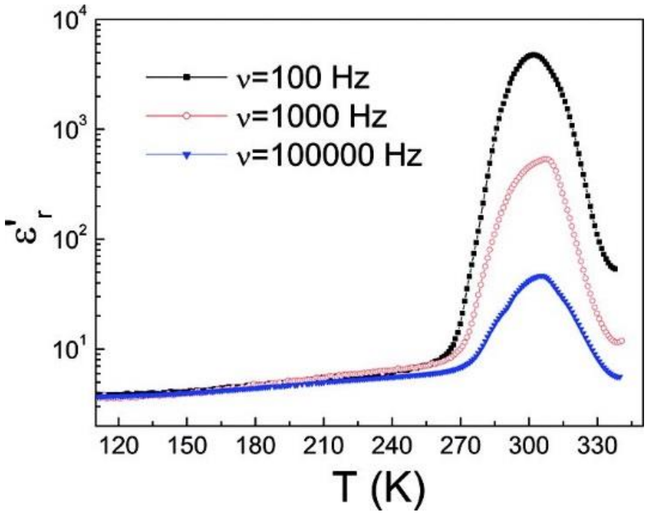

Figure 2.4. Temperature dependence of the dielectric constant of a Co-based MOF measured at three different frequencies in the temperature interval 100 < T(K) < 350: reprinted with permission from Ref. [107].

The motivation of the work is now moving towards calculating the dielectric constants of MOF materials using DFT, with Warmbier *et al.*[98] recently studying the static dielectric properties of eight unique IRMOFs. They reported the static dielectric constants to all be in the range of 1.3–1.5. Additional experimental dielectric constants have been reported and are summarised in Table 2.2. However, all of the values were obtained at frequencies below 100 kHz.[92]

One major limitation delaying these promising materials for low-κ dielectric applications is that experimental methods to study these properties across the IR spectral frequency range have been insufficient. The THz spectral region could be important for emerging communication technologies and applications such as optical sensors.[108] In

Table 2.2. Experimental low-κ dielectric values (κ < 6) for MOFs reported in the literature. All the values were obtained < 100 kHz.[92]

Structure	Dielectric Constant	Ref.
ZIF-8	2.33	[44]
$Sr_2(BDC)_2(H_2O)_2$	2.4	[169]
$[Pb(TAB)_2(BIPY)](PF_6)_2$	2.53	[165]
$Zn_2(L\text{-}TRP)_2(BPE)_2(H_2O)_2$	2.53	[165]
$Mn_2(D\text{-}CAM)_2(HPAO)_4$	2.8	[165]
$Co_2(D\text{-}CAM)_2\text{-}(ABPT)_2(H_2O)_3$	3.0	[165]
$Pb(TAB)_2]_2(PF_6)_4$	3.04	[165]
$Ni_2(BBIM)(H_2BBIM)_4$	4.8	[170]
Sr(BDC)	4.9	[165]
$Zn(TMPT)_2$	6.0	[165]
$Cu_2(EBTC)$	4.9–6.2	[165]

Note: BDC = 1,3-benzenetricarboxylate. TAB = 4-trimethylammoniobenzenethiolate. BIPY = 4,4’-bipyridine. L-TRP = l-tryptophan. BPE = 1,2-bis-4-pyridylethylene. D-CAM = D-camphoric acid. HPAO = 2-pyridinealdoxime. ABPT = 4-amino-3,5-bis-3-pyridyl-1,2,4-triazole. BBIM = bisbenzimidazole. TMPT = 1,2,4-triazol-1-yl-methyl-phenyl-tetrazole. EBTC = 1,1-ethyne-benzene-3,3,5,5-tetracarboxylate.

addition, theoretical methods are only starting to provide an accurate procedure to allow for calculation of the static dielectric constant. With recent advancements in the approach to calculating dynamic dielectric constants, it is also now possible to obtain the frequency-dependent values, which is of importance for high-frequency semiconductor and optical applications of MOFs.[109, 110] The current literature highlights the bright future of MOFs as low-κ dielectric materials, though little work has been done to tackle any of the above restrictions especially in the THz and extended IR frequency range.

2.3 Chapter Summary

This chapter has provided a summary of the background literature regarding the mechanical, vibrational and dielectric properties of MOFs and indicates the relevance of the work performed in the later chapters. In conclusion, it gives an overview of the work that has motivated the research performed in this thesis. The need for a better understanding of the mechanical stability and underlying mechanisms responsible for the highly anisotropic response of the framework materials is emphasised.

Chapter 3

Theoretical and Experimental Methodologies

This chapter provides a brief overview of each of the theoretical and experimental methods used throughout the thesis. It starts by introducing density functional theory (DFT) and the density functionals used for the specific types of calculations. The routine behind the geometry optimisation procedure is discussed followed by the method to calculate the theoretical elastic constants, vibrational frequencies, and dielectric response (static and dynamic). The various experimental vibrational spectroscopy techniques are explained, starting with inelastic neutron scattering (INS), where a list of the relevant neutron scattering cross sectional values is provided. Finally, brief descriptions of the synchrotron infrared (IR) and Raman spectroscopy setups are provided.

3.1 Introduction

The purpose of this chapter is to provide an overview of the theoretical and experimental methods and techniques used to obtain the results discussed in later chapters. The density functionals used for the density functional theory (DFT) calculations are highlighted. The routine behind the geometry optimisation procedure and the method of calculating the theoretical elastic constants, vibrational frequencies, and dielectric response (static and dynamic) is covered. The experimental vibrational spectroscopy techniques are explained, including inelastic neutron scattering (INS), synchrotron infrared (IR) and Raman spectroscopy.

3.2 Density Functional Theory (DFT)

The primary advantage of DFT over many-body wave function methods is that it can simplify everything down to one single variable, the electron density, $\rho(\mathbf{r})$, whereas other electronic structure methods must consider the 3N many-body coordinates (Appendix A3). The electron density for an anti-symmetrised wave function is represented as:

$$\rho(\mathbf{r}) = N\int \cdots \int \left|\Psi\left\{x_i\right\}\right|^2 d\sigma dx_2 \cdots dx_N \tag{3.1}$$

$$\int \rho(\mathbf{r}) d\mathbf{r} = N \tag{3.2}$$

$$\rho(\mathbf{r}) \geq 0 \tag{3.3}$$

It was suggested by Hohenberg and Kohn[111] that a universal functional of the energy of a chemical system regarding the density could be obtained precisely if the external potential (V^{ext}) was known.

$$E_{HK}\left[\rho(\mathbf{r})\right]=T^{e}\left[\rho(\mathbf{r})\right]+V^{ee}\left[\rho(\mathbf{r})\right]+\int V^{ext}(\mathbf{r})\rho(\mathbf{r})d\mathbf{r} \tag{3.4}$$

where the ground state energy (E) is the minimisation of Equation 3.4, while Equations 3.2 and 3.3 are simultaneously satisfied.

$$E=\min_{\rho}\left\{T^{e}\left[\rho(\mathbf{r})\right]+V^{ee}\left[\rho(\mathbf{r})\right]+\int V^{ext}(\mathbf{r})\rho(\mathbf{r})d\mathbf{r}\right\} \tag{3.5}$$

However, the issue with Equation 3.5 is that V^{ext} is system specific due to its dependence on the nuclear coordinates. Kohn and Sham[112] later realised that this could be simplified by separating the exchange-correlation contribution (E_{xc}) and the Coulomb term (E_H), as shown in Equation 3.6.

$$E_{KS}\left[\rho(\mathbf{r})\right]=T_{s}^{e}\left[\rho(\mathbf{r})\right]-\int V^{ext}(\mathbf{r})\rho(\mathbf{r})d\mathbf{r}+E_{H}\left[\rho(\mathbf{r})\right]+E_{xc}\left[\rho(\mathbf{r})\right] \tag{3.6}$$

Hence the exchange-correlation energy can be more accurately understood by combining the two definitions of the total energy (E_{HK} and E_{KS}):

$$E_{xc}\left[\rho(\mathbf{r})\right]=T^{e}\left[\rho(\mathbf{r})\right]-T_{s}^{e}\left[\rho(\mathbf{r})\right]+V^{ee}\left[\rho(\mathbf{r})\right]-E_{H}\left[\rho(\mathbf{r})\right] \tag{3.7}$$

where the first two terms on the right-hand side of Equation 3.7 equate to the difference between the kinetic energy of the interacting and non-interacting electrons, and the latter two terms are the difference between the full electron-electron interaction energy (Appendix A3) and the classical Coulomb energy.

3.2.1 Density Functionals

An exact solution for the exchange-correlation term (E_{xc}) in DFT currently does not exist. There are many approximations for calculating the term, and an entire field exists concerning the development of new and improved versions of DFT functional. The intricacies of the specific functionals used for the different types of calculations throughout the thesis and their respective references are given in Table 3.1.

The elasticity calculations were performed using the B3LYP hybrid exchange-correlation functional,[78-80] due to it being reported to produce accurate elastic coefficients without the need for extensive computationally expensive basis sets.[41] The term hybrid refers to the fact that the functional includes a contribution of exact exchange from Hartree–Fock theory with additional exchange and correlation contributions from *ab initio* methods.

The standard vibrational frequency calculations were performed using the PBE exchange-correlation functional with a semi-empirical dispersion correction to more accurately account for the van der Waals interactions and explicitly developed for solid crystalline systems (PBE-D*).[113-115] The PBE functional was used as it was shown to give consistent results to B3LYP without dispersion corrections and was in better agreement with experiment when the semi-empirical dispersion correction was included (Appendix A5.12). The optimised crystal structure obtained using the PBE-D* functional

Table 3.1. Summary of the specific DFT functionals used throughout the thesis.

Type of Calculation	Level of Theory	Chapters	References
Elastic Constants	B3LYP	4, 6	[78-80]
Vibrational Frequencies	PBE-D*	5, 6	[113-115]
Static Dielectric	B3LYP-D*	7	[78-80, 114, 115]
†Dynamic Dielectric	B3LYP-D*	7	[78-80, 114, 115]

†The prerequisite vibrational frequencies for the dynamic dielectric calculations were performed at the B3LYP-D* level of theory.

also showed better agreement with experimental neutron diffraction data than the PBE functional without the correction (Appendix A5.10).

Contrary to many of the initial studies in the literature on the electronic properties of MOF materials, Local Density Approximation (LDA) and Generalised Gradient Approximation (GGA) have been shown to be inadequate to properly describe the electronic band gap and dielectric response of solids.[116-120] It has been highlighted that hybrid functionals are required to compute the electronic properties of solids more accurately, and this has recently been confirmed for MOFs.[121] Therefore, the static and dynamic dielectric constants reported in Chapter 7 were calculated using the B3LYP hybrid exchange-correlation functional with the semi-empirical dispersion correction mentioned above (B3LYP-D*).[78-80, 114, 115]

3.2.2 Basis Sets

All of the DFT calculations discussed in this thesis were performed with the periodic *ab initio* code CRYSTAL14.[109] The code considers crystalline orbitals as linear combinations of Bloch functions (BF) and evaluates them using a regular three-dimensional (3D) mesh in the reciprocal space. Each BF is constructed from local atomic orbitals (AOs), which are linear combinations of Gaussian-type functions (GTFs). Each GTF is the result of a Gaussian multiplied by a solid spherical harmonic. The basis set is defined for each atom with fixed coefficients and exponents. The AOs belonging to a given atom are grouped into shells: s, sp, p, d, and f shells. The choice of the basis set is important, and the development of new optimised basis sets was not the aim of this thesis. Therefore, the established all-electron atom-centred Gaussian-type basis sets reported in Ref. [41] were used, as they have been confirmed to give accurate results for MOF materials. The elasticity calculations were performed using the double-zeta quality basis sets, and the rest of the calculations used the more extensive triple-zeta quality.

3.2.3 Geometry Optimisation

The lattice parameters and atomic coordinates of the unit cell are both optimised at constant symmetry (maintaining the symmetry space group) *via* a normalised combined set of symmetrised directions and deformations. The optimisation procedure is achieved by obtaining a gradient of the total energies of each optimisation step. A Hessian matrix (matrix of second derivatives) is constructed from the energy gradients, and a quasi-Newtonian optimisation algorithm is implemented in which a quadratic step (Broyden-Fletcher-Goldfarb-Shanno (BFGS) Hessian updating scheme) is combined with a linear parabolic fit.[122-126]

An optimised structure is defined by locating a minimum on the potential energy surface, and this is assumed when the forces acting on the atoms in the unit cell are numerically zero. The optimisation procedure defines this as the point where the root mean square (RMS) and the absolute value of the largest component of the gradients and the estimated displacements are below a defined threshold. The thresholds for the maximum and RMS gradient, and the maximum and RMS atomic displacement of all atoms were set to 1.5×10^{-4}, 1.0×10^{-4}, 3.0×10^{-4} and 2.0×10^{-4} a.u., respectively for all optimisations performed in the thesis. The optimisation was considered to have completed when all four conditions were simultaneously satisfied.

3.2.4 Elasticity Analysis

The single-crystal elastic constants (C_{ij}) are used to calculate the various mechanical properties discussed in Chapter 4 and briefly in Chapter 6. The link between the elastic constants and the mechanical response is from Hooke's law being related to stress (σ) and strain (ε) (both second-rank tensors) in the following equation:

$$\sigma_{\mathrm{ij}} = \sum_{kl} C_{ijkl}\varepsilon_{\mathrm{kl}} \tag{3.8}$$

C_{ijkl} represents the symmetric fourth-rank elasticity tensor connecting stress to strain and has up to 21 unique (independent) elastic constants, depending on the symmetry of the system (according to Laue classes).[127] The lowest symmetry materials discussed in the thesis are monoclinic and therefore have thirteen elastic constants.[127] However, the number of required elastic constants depends on the symmetry of the material, as shown in Table 3.2. The elasticity tensor is calculated from numerical second derivatives of the analytical first derivatives of the energy gradients, which corresponds to the individual elastic stiffness coefficients.[128]

The individual coefficients are calculated from derivatives of the total energy from deforming the optimised structure (from Section 3.2.3) using a three-point formula in the symmetrically required directions of both positive and negative amplitudes. The deformations correspond to tensile and compressive strains respectively. The magnitude

Table 3.2. Crystallographic information relating to the complexity of the anisotropic elastic response of the materials studied in the thesis.

Structure	Laue Class	Space Group	Number of Elastic Constants
HKUST-1	Cubic	$Fm\bar{3}m$	3
ZIF-1	Monoclinic	$P2_1/n$	13
ZIF-2	Orthorhombic	Pbca	9
ZIF-3	Tetragonal	$P4_2/mnm$	6
ZIF-4	Orthorhombic	Pbca	9
ZIF-zni	Tetragonal	$I4_1cd$	6
MIL-140A	Monoclinic	C2/c	13
MIL-140B	Monoclinic	Cc	13
MIL-140C	Monoclinic	C2/c	13
MIL-140D	Monoclinic	Cc	13

of the strain along each given deformation was defined as 1% for all calculations in the thesis, to remain in the purely elastic response region.

Voigt notation (u, v = 1, 2,…6) is used in the representation of the elastic coefficients, to avoid dealing with a complex 3D fourth-order elasticity tensor.[127] The simplified notation reduces the order and results in a two-dimensional (2D) tensor as shown later in Equation 3.12. The order of the elastic tensor is reduced by representing the stress and strain contributions as vectors instead of second-rank tensors, as shown below for the strain:

$$\varepsilon = \begin{pmatrix} \varepsilon_{aa} & \varepsilon_{ab} & \varepsilon_{ac} \\ \varepsilon_{ba} & \varepsilon_{bb} & \varepsilon_{bc} \\ \varepsilon_{ca} & \varepsilon_{cb} & \varepsilon_{cc} \end{pmatrix} \tag{3.9}$$

$$\varepsilon = (\varepsilon_{aa}, \varepsilon_{bb}, \varepsilon_{cc}, \gamma_{bc}, \gamma_{ac}, \gamma_{ab}) = (\varepsilon_1, \varepsilon_2, \varepsilon_3, \varepsilon_4, \varepsilon_5, \varepsilon_6) \tag{3.10}$$

where γ is the shear strain and equates to the sum of both equal off-diagonal strains. Therefore, due to the reduction in the order of the tensors (1 = *aa*, 2 = *bb*, 3 = *cc*, 4 = *bc*, 5 = *ac*, 6 = *ab*), the elastic coefficients can be calculated as shown below:

$$C_{ij} = \frac{1}{V}\frac{\partial^2 E}{\partial\varepsilon_i \partial\varepsilon_j} \tag{3.11}$$

where C_{ij} are the elastic coefficients (elements of the tensor), V is the volume of the crystallographic unit cell, E is the total energy, and ε_i and ε_j are the second-rank symmetric tensors of pure strain. Hence (for a monoclinic example) the 2D elastic tensor becomes:

$$C_{\text{monoclinic}} = \begin{pmatrix} C_{11} & C_{12} & C_{13} & 0 & C_{15} & 0 \\ & C_{22} & C_{23} & 0 & C_{25} & 0 \\ \vdots & & C_{33} & 0 & C_{35} & 0 \\ & & & C_{44} & 0 & C_{46} \\ & \iddots & & & C_{55} & 0 \\ \text{symm.} & & \cdots & & & C_{66} \end{pmatrix} \tag{3.12}$$

The diagonal coefficients C_{11}, C_{22} and C_{33}, represent the stiffness along each of the three principal crystallographic axes, *a*, *b*, and *c* under a uniaxial strain. The remaining diagonal coefficients C_{44}, C_{55} and C_{66}, signify the stiffness against angular distortions when subjected to shear strains. The off-diagonal coefficients correspond to coupling effects, such as tensile-tensile coupling (C_{12}, C_{13} and C_{23}) between any two orthonormal axes. The C_{i5} coefficients ($i = 1, 2, 3$) represent tensile-shear coupling, and the C_{46} coefficient represents shear-shear coupling. The mechanical properties are calculated from the inversion of the elasticity tensor, known as the compliance tensor in accordance to:

$$S_{ijkl} = C_{ijkl}{}^{-1} \tag{3.13}$$

The directional Young's modulus (E) is defined as the ratio of uniaxial stress (σ) to longitudinal strain (ε) along a unit vector **u**, where the surface corresponds to a spherical plot of $E(\mathbf{u})$ obtained from Equation 3.14. As such by definition, E is analogous to the stiffness property (ratio of load to displacement) of a classical Hookean spring.

$$E(\mathbf{u}) = \frac{1}{u_i u_j u_k u_l S_{ijkl}} \tag{3.14}$$

The anisotropic linear compressibility (β) represents the compression along a unit vector **u** upon hydrostatic compression, where the surface corresponds to a spherical plot of $\beta(\mathbf{u})$ obtained from Equation 3.15.

$$\beta(\mathbf{u}) = u_i u_j S_{ijkl} \tag{3.15}$$

The shear modulus (or rigidity modulus, G) is defined as the ratio of shear stress (τ) to shear strain (γ) under the influence of a pair of antiparallel shearing forces. G gives a measure of the rigidity of the framework structure against an angular deformation and can also be shown as a 3D representation but depends on an additional unit vector **v**, which is perpendicular to vector **u**. The surfaces of the spherical plots reported in Chapter 4 are the maxima and minima of $G(\mathbf{u}, \mathbf{v})$ obtained from the following equation:

$$G(\mathbf{u}, \mathbf{v}) = \frac{1}{u_i v_j u_k v_l S_{ijkl}} \tag{3.16}$$

The Poisson's ratio (ν) is analogous to the shear modulus in that it is also a function of two unit vectors (**u** and **v**). For this reason, the 3D surfaces reported in Chapter 4 are again the maxima and minima. However, this time the minima are represented as green and red, for positive and negative values respectively. The Poisson's ratio represents the ratio of the transverse strain to the axial strain under uniaxial deformation and can be obtained from the following equation:

$$\nu(\mathbf{u},\mathbf{v}) = -\frac{u_i u_j v_k v_l S_{ijkl}}{u_i u_j u_k u_l S_{ijkl}} \tag{3.17}$$

The mechanical properties discussed above are computed *via* tensorial analysis using the Mathematica code,[129] and the numerical values are confirmed for reproducibility using the ElAM code.[130]

3.2.5 Vibrational Analysis

The harmonic vibrational frequencies are calculated from a mass-weighted Hessian matrix, obtained by numerical differentiation of the analytical first derivatives (gradients). The total energies for the gradients are computed from geometries obtained by slightly displacing, in turn, each of the 3N nuclear coordinates with respect to the equilibrium geometry obtained *via* the method described in Section 3.2.3. The symmetry is maintained at each new deformed geometry to reduce the computational expense of the energy calculations required, and the second derivatives are performed only on the asymmetric unit cell (the irreducible atoms). The Hessian matrix is then constructed using the point group symmetry and diagonalised to obtain the eigenvalues and eigenvectors, resulting in the vibrational frequencies (cm^{-1}) and normal modes respectively.

Eckart conditions are imposed to the Hessian matrix to reduce statistical noise. This is achieved *via* an automated process to isolate the purely translational and rotational degree of freedom in the system. The vibrational frequencies reported throughout the thesis are the modes located at the Γ-point. Phonon modes beyond the Γ-point would require the calculations to be performed on supercells of the original unit cell following a direct-space approach. This would be significantly more computationally expensive and out with the resources available. The volume of each system studied is sufficiently large and hence the contribution from phonon dispersion should be negligible, confirmed by the good agreement between experiment and theory reported in Chapter 5.

The IR intensities have been computed through the Berry Phase approach,[131] by evaluating the Born atomic tensors as polarisation differences between the original and the distorted geometries. The Born atomic tensors are the derivative of the dipole moments with respect to the displacement of the atoms. This method then assumes that the polarisation difference is equal to the time-integrated transient macroscopic current that flows through the sample during the vibrations.[109]

The Raman intensities reported in Chapter 5 were calculated analytically *via* a Coupled-Perturbed Hartree-Fock/Kohn-Sham (CPHF/CPKS) approach.[132, 133] The theoretical spectra were then corrected for the experimental conditions by multiplying the intensities with the following prefactor:

$$C \approx (\omega_L - \omega_i)^4 \frac{1 + n(\omega_i)}{30\omega_i} \tag{3.18}$$

$$n(\omega_i) = \left[1 - \mathrm{e}^{-\frac{\hbar\omega_i}{k_B T}}\right]^{-1} - 1 \tag{3.19}$$

where ω_L is the laser frequency (532 nm), $n(\omega_i)$ is the Bose occupancy factor, k_B is the Boltzmann constant and T is the temperature (293 K).[109]

The experimental inelastic neutron scattering (INS) spectra are more complex than the theoretical spectra obtained from DFT, as higher orders of vibrational excitation take place and even though the probability is much lower, the collective contribution to the spectral results can be significant. Therefore, it is necessary to include in the theoretical results the overtones that would be expected from these excitations, which was achieved using the vibrational eigenvectors, generated from the DFT calculations, with the aClimax code.[134] The theoretical INS spectra reported in Chapter 5 include up to 10th order overtones with fully anisotropic external Debye-Waller effects. This approximation of the probability of higher order excitations allowed for the theoretical results to match exceptionally well with experiment, as shown in Figure 3.1 for ZIF-4 (other examples in Appendix A5.6).

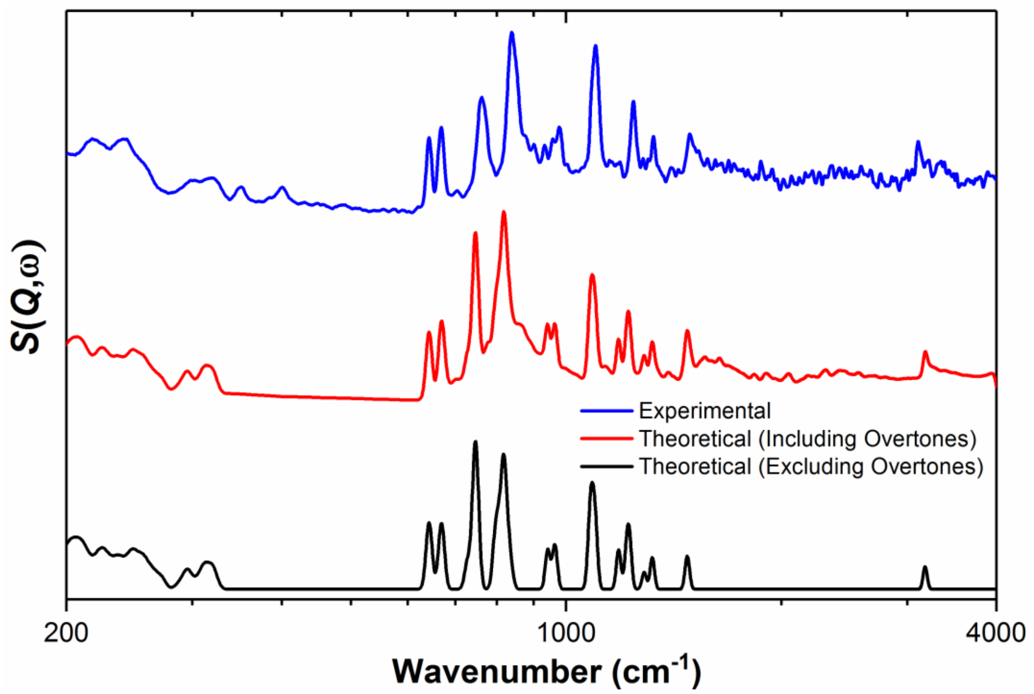

Figure 3.1. Comparison of DFT spectra, for ZIF-4, with and without the inclusion of higher order vibrational excitations.

3.2.6 Dielectric Response

The static dielectric constants discussed in Chapter 7 were calculated analytically *via* a CPHF/CPKS approach.[132, 133] The CPHF/CPKS method involves computing the polarisability (and dielectric) tensor and optionally the first and second order hyperpolarisability. However, for the work in Chapter 7, the total energy of the material in a constant static field is calculated from the following equation, truncated at the second order, therefore not including the contributions from the hyperpolarisabilities:

$$E(\varepsilon) = E(0) - \sum_t \mu_t \varepsilon_t - \frac{1}{2}\sum_{tu} \alpha_{tu}\varepsilon_t\varepsilon_u - \cdots \tag{3.20}$$

where $E(0)$ is the field-free energy, ε is the electric field, μ is the dipole moment and α is the polarisability. The dipole moment and the polarisability are related to the energy derivatives according to Equations 3.21 and 3.22, although a much more in-depth explanation can be found in Ref. [118].

$$\mu_t = -\frac{\partial E}{\partial \varepsilon_t} \tag{3.21}$$

$$\alpha_{tu} = -\frac{\partial^2 E}{\partial \varepsilon_t \partial \varepsilon_u} \tag{3.22}$$

The computed polarizability can then be transformed into the macroscopic first-order susceptibility (χ) from the following equation:

$$\chi_{tu} = \frac{4\pi}{V}\alpha_{tu} \tag{3.23}$$

where the susceptibility is strongly affected by the volume of the unit cell (V). The dielectric constant (ε or commonly κ when discussing applications) can then be computed from:

$$\varepsilon_{tu} = \chi_{tu} + \delta_{tu} \tag{3.24}$$

where $\delta_{tu} = 0$ except when t = u, where $\delta_{tu} = 1$. Hence, in the case of a vacuum when ε = 1, the susceptibility reduces to zero.

The frequency-dependent (dynamic) reflectance spectra, dielectric function and refractive index, discussed in Chapter 7, were calculated *via* combining the frequency-independent optical dielectric tensor with the vibrational frequencies obtained *via* the methodology mentioned in Section 3.2.5, with the difference that the IR intensities are obtained from the CPHF/CPKS approach.[132, 133] The complex dielectric tensor is calculated for each unique direction of polarisation *via* a classical Drude-Lorentz model:

$$\varepsilon_{a,b,c}(\nu) = \varepsilon_{\infty,a,b,c} + \sum_p \frac{f_{p,a,b,c}\nu_p^2}{\nu_p^2 - \nu^2 - i\nu\gamma_p} \tag{3.25}$$

where *a*, *b*, *c* indicates the polarisation direction in the crystal, ε_∞ is the static dielectric tensor, ν_p is the frequency, f_p is the oscillator strength and γ_p is a damping factor for the p^{th} vibrational mode (set to 5.0 cm^{-1} in the calculations). The reflectance curve is then calculated for each unique direction from Equation 3.26.

$$R_{ii}(\nu) = \left| \frac{\sqrt{\varepsilon_{a,b,c}(\nu) - \sin^2(\theta)} - \cos(\theta)}{\sqrt{\varepsilon_{a,b,c}(\nu) - \sin^2(\theta)} + \cos(\theta)} \right|^2 \tag{3.26}$$

where θ is the angle of incidence and was set to 30 degrees in the calculation to match with the reflectivity experiments performed in Chapter 7.

The optical properties are calculated for each of the crystallographic axes. Therefore, to compare with the polycrystalline experimental values, an average of the resultant spectra should be used. However, the dynamic dielectric spectrum reported for ZIF-8 in Chapter 7 is independent of the crystallographic direction, as the structure is cubic ($a = b = c$).

3.2.7 Robustness Screening

The robustness of the elasticity calculations was checked through multiple methods, first by redoing the calculations for MIL-140A using the new version of the code, CRYSTAL14 (utilised for all calculations other than the elastic constants of the MIL-140 series in Chapter 4).[109] The calculations for MIL-140A were also checked using the more extensive triple-zeta basis set (additional basis functions – 25% larger) to reduce any basis set superposition error (BSSE) and finally increased the number of deformation points from three to five. Table 3.3 shows the comparison of using CRYSTAL09 and CRYSTAL14 and indicates that the new CRYSTAL14 code is consistent. Also, it is evident that using additional points on the deformation does not affect the results beyond statistical noise and the use of a much larger basis set has only a negligible effect.

The results in Chapter 4 for MIL-140A differ from values already published in Ref. [69] and this is due to the previous results likely having been performed with a bugged version of CRYSTAL09 (version 2.0). This problem was removed in a patch fix for CRYSTAL09 (version 2.01) and is no longer present in the latest edition of the code (CRYSTAL14).[109] The main change in the patch fix (2.01) was the way the minimal set of deformations needed to compute the elastic tensor was defined. Also, a bug in the

Table 3.3. Robustness checks of CRYSTAL14 code on MIL-140A.

Elastic Property		CRYSTAL09 Results reported in Chapter 4	CRYSTAL14 Otherwise as Reported in Chapter 4	CRYSTAL14 Larger Basis Set Used	CRYSTAL14 Larger Basis Set and Additional Deformation Points
Young's Modulus (GPa)	E_{max}	142.0	142.7	137.7	137.9
	E_{min}	11.3	11.1	12.0	12.1
	$A_E = E_{\mathrm{max}}/E_{\mathrm{min}}$	12.6	12.8	11.5	11.4
Shear Modulus (GPa)	G_{max}	36.9	36.8	35.6	35.8
	G_{min}	3.2	3.1	3.4	3.4
	$A_G = G_{\mathrm{max}}/G_{\mathrm{min}}$	11.5	11.8	10.5	10.5
Linear Compressibility (TPa^{-1})	β_{max}	27.8	27.9	25.8	25.4
	β_{max}	-3.0	-3.0	-2.3	-2.1
Poisson's Ratio	ν_{max}	1.11	1.11	1.06	1.06
	ν_{min}	-0.13	-0.13	-0.08	-0.08
Ledbetter Anisotropy	A^*	12.5	12.6	11.5	11.2

transformation of the strain derivatives from primitive to conventional unit cells was also fixed. This was due to the transformation being done incorrectly in version 2.0. The result was that it worked for some lattice structures but not for non-orthogonal non-primitive lattices, including most monoclinic and hexagonal space groups.

Another obvious sign that the results previously published in Ref. [69] were incorrect is that they reported a lower maximum Young's modulus for the reinforced MIL-140A structure than for the flexible non-reinforced wine-rack frameworks.[69] This is not the case with the values reported in Chapter 4. The values shown in Equation 3.27 are obtained for MIL-140A using Crystal09 (2.01) and the values obtained using the bugged version of the code are shown in Equation 3.28.

$$C_{\mathrm{Voigt}} = \begin{pmatrix} 93.956 & 42.703 & 29.575 & 0 & -4.008 & 0 \\ & 163.020 & 17.443 & 0 & 0.270 & 0 \\ \vdots & & 52.706 & 0 & -10.384 & 0 \\ & & & 3.194 & 0 & 0.099 \\ & \iddots & & & 9.050 & 0 \\ \text{symm.} & & \cdots & & & 27.424 \end{pmatrix} \tag{3.27}$$

$$C_{\mathrm{Voigt}} = \begin{pmatrix} 46.553 & 21.429 & 29.372 & 0 & 1.296 & 0 \\ & 81.483 & 17.352 & 0 & 2.050 & 0 \\ \vdots & & 52.881 & 0 & 0.726 & 0 \\ & & & 1.637 & 0 & 0.140 \\ & \iddots & & & 3.355 & 0 \\ \text{symm.} & & \cdots & & & 13.429 \end{pmatrix} \tag{3.28}$$

The values obtained using the bugged 2.0 version of CRYSTAL09 give results more consistent with the values reported in Ref. [69] for MIL-140A. It is worth highlighting that the previously reported values are incorrect due to a bug in the CRYSTAL09 (2.0) code that has now been fixed in CRYSTAL09 (2.01) and the new release CRYSTAL14, and not due to any mistake by the authors of Ref. [69].

3.2.8 Ferromagnetic and Antiferromagnetic HKUST-1

Due to the open-shell nature of the Cu atoms in HKUST-1, the elastic constants of the antiferromagnetic phase[135] were also calculated (Equation 3.29) to ensure they were consistent with the values reported for the ferromagnetic phase (Equation 3.30). The elastic constants were compared using the B3LYP DFT functional with reduced basis sets (double-zeta basis sets were used for the ferromagnetic results reported in Chapter 4). The values differed by less than 1% and were the result of numerical noise arising from the lower symmetry of the antiferromagnetic phase.

$$C_{\text{Voigt}} = \begin{pmatrix} 27.163 & 26.442 & 26.442 & 0 & 0 & 0 \\ & 27.163 & 26.442 & 0 & 0 & 0 \\ \vdots & & 27.163 & 0 & 0 & 0 \\ & & & 5.129 & 0 & 0 \\ & \iddots & & & 5.129 & 0 \\ \text{symm.} & & \cdots & & & 5.129 \end{pmatrix} \tag{3.29}$$

$$C_{\text{Voigt}} = \begin{pmatrix} 27.153 & 26.456 & 26.456 & -0.007 & -0.014 & -0.014 \\ & 27.153 & 26.456 & -0.014 & -0.007 & -0.014 \\ \vdots & & 27.153 & -0.014 & -0.014 & -0.007 \\ & & & 5.124 & 0.001 & 0.001 \\ & \iddots & & & 5.124 & 0.001 \\ \text{symm.} & & \cdots & & & 5.124 \end{pmatrix} \tag{3.30}$$

3.3 Experimental Vibrational Spectroscopy

3.3.1 Inelastic Neutron Scattering (INS)

The inelastic neutron scattering (INS) spectra reported in Chapter 5 were recorded using the TOSCA spectrometer at the ISIS Pulsed Neutron and Muon Source Facility at the Rutherford Appleton Laboratory. TOSCA is a high resolution (ΔE/E ~1.25%) broadband (0–4000 cm^{-1}) indirect geometry time-of-flight (TOF) spectrometer. It operates with a pulsed, polychromatic (multi-energy) beam of neutrons that collide with the sample at a distance of ~17 m from a water moderator source (Figure 3.2). The inelastically scattered neutrons are then Bragg-reflected, according to the following equation by a pyrolytic graphite analyser (PG002):

$$\lambda = 2d\sin\theta \tag{3.31}$$

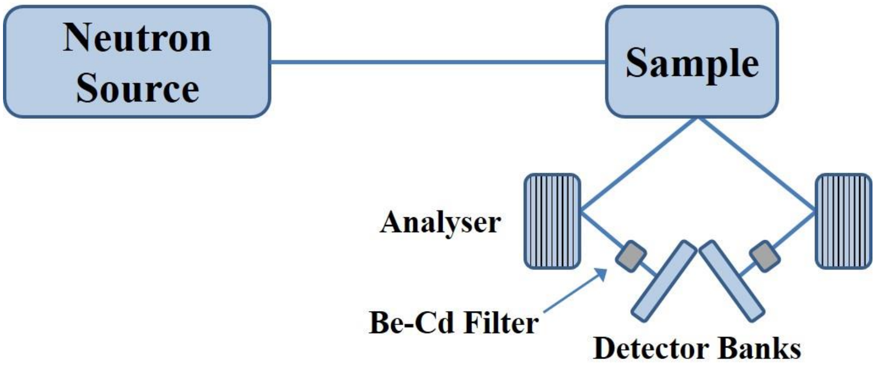

Figure 3.2. Schematic diagram of the TOSCA indirect geometry time-of-flight (TOF) spectrometer.

where λ (Å) is the wavelength of the scattered neutron, d (Å) is the interplanar distance in the crystalline analyser, and θ is the angle of incidence on the analyser. Therefore, since the interplanar distances and the angle of incidence do not change, all the scattered neutrons will have the same wavelength (and higher order reflections of the wavelength: $\lambda/2$, $\lambda/3$, $\lambda/4$ …). Higher-order reflections are suppressed by a cooled ($T < 50$ K) beryllium (Be) high-pass filter with cadmium (Cd) inserts, to selectively analyse neutrons of consistent final energy (neutron wavelength). The 120 mm thick Be-Cd filter works by allowing only the first-order harmonic ($\lambda/1$) from the analyser to pass through to the detectors. Therefore, on TOSCA, neutrons with final energy of approximately 3.5 meV are passed towards the ^{3}He detector banks. The detector array is comprised of a total of ten banks each having thirteen ^{3}He tubes with an effective length of 250 mm. Five detector banks collect neutrons scattered in the forward direction (scattering angle ~45º) and five in the backwards direction (~135º). Also, to improve the instrument background by suppressing the gamma-flash and fast neutrons a double disk chopper is positioned at a distance of ~8 m from the moderator. The disk chopper also has a sheet of boron carbide on the leading edge to restrict low-energy neutrons and reduce frame overlap.

The energy transferred to the sample (E_{trans}) that occurs when the neutrons collide with the sample can be expressed as follows:

$$E_{\mathrm{trans}} = E_{\mathrm{i}} - E_{\mathrm{f}} \tag{3.32}$$

where E_{i} is the incident energy, and E_{f} is the final energy. Therefore, the TOF can be obtained by dividing the distance of the flight of the neutron (L) by its velocity (v) during the flight. However, there are two different TOF velocities to consider. Firstly, there is the neutron flight from the source to the sample, and secondly the scattered distance from the sample to the detectors *via* the analyser. This is a result of the velocity of the neutron being affected by the collision with the sample. The total time can be obtained from the following equation:

$$T = \frac{L_1}{v_i} + \frac{L_2}{v_f} \tag{3.33}$$

Therefore, the de Broglie equation can be used to associate the energy of a neutron with its velocity:

$$E = \hbar\omega = \frac{mv^2}{2} \tag{3.34}$$

$$v = \sqrt{\frac{2E}{m}} \tag{3.35}$$

where E is the kinetic energy of the neutron, $\hbar$ is the reduced Planck constant ($h/2\pi$), ω is the angular frequency of the neutron, m is the mass of the neutron and v is the velocity of the neutron. Therefore, when Equation 3.35 is substituted into Equation 3.33, the total TOF can be obtained from:

$$T = \frac{L_1}{\sqrt{\frac{2E_i}{m}}} + \frac{L_2}{\sqrt{\frac{2E_f}{m}}} \tag{3.36}$$

Now since the flight paths (L_1 and L_2), the mass of a neutron (m) and the final energy (E_f) are all fixed and known, then the measurement of the TOF will provide the incident energy (E_i) and hence from Equation 3.32 will give the associated energy transfer (E_trans).

The use of a fixed small final energy translates into a direct relationship between energy transfer (E_trans, cm^{-1}) and momentum transfer (Q, Å^{-1}) such that $E_\mathrm{trans} \approx 16Q^2$. This relation originates from the fact that the mass of a neutron is comparable to that of a hydrogen atom and as a result, an inelastic collision will result in a significant momentum transfer. The energy relationship of $E_\mathrm{trans} \approx 16Q^2$ and the singular value of Q for each energy are both due to the specific experimental setup on the TOSCA spectrometer.

Energy transfer and spectral intensity can then be calculated to convert to the conventional $S(Q, \omega)$.[136] This comes about from the following equation for the intensity (I) of the i^th molecular vibrational transition:

$$S(Q, \omega_i) \approx I_i = Q^2 U_i^2 \exp(-Q^2 U_\mathrm{total}^2)\sigma \tag{3.37}$$

where U_i is the amplitude of vibration of the atoms involved in the vibrational mode, and U_total is the mean square displacement of the molecular structure, and hence its magnitude is related to the thermal motion. Therefore, the exponential part of Equation 3.37 is what is referred to as the Debye-Waller factor.[137, 138] Equation 3.37, therefore, highlights the need to perform INS experiments at low temperatures, to minimise the values of U_{total} and as a result, increase the intensity of the signal of the vibrational mode. The INS spectra reported in Chapter 5 were obtained at ~5 K *via* the use of a closed cycle refrigerator (CCR).

The final part of Equation 3.37 is the inelastic neutron scattering cross section (σ), which is different depending on the atoms involved (Table 3.4). The scattering cross-sections are characteristic of each element and do not rely on the chemical environment. It is important to note that the total cross-section (σ_{total}) for hydrogen (H) is significantly high while that for most other elements is much lower. This means that vibrational modes involving the displacement of hydrogen will dictate the resultant INS spectrum. The dependence of the spectra on hydrogen content is one of the primary benefits of the INS results presented in Chapter 5. Another advantage of using scattering instead of absorption (IR or Raman) is the absence of optical selection rules since all transitions are, in principle, active.[136] The INS technique differs from infrared (IR) and

Table 3.4. Neutron scattering cross sections of the elements discussed in the thesis.

Element	σ_{coherent} (barn)	$\sigma_{\text{incoherent}}$ (barn)	σ_{total} (barn)
H	1.7883	80.27	82.03
C	5.551	0.001	5.551
N	11.01	0.5	11.51
O	4.232	0.0008	4.232
Cl	11.5257	5.3	16.8
Cu	7.485	0.55	8.03
Zn	4.054	0.077	4.131
Zr	6.44	0.02	6.46

The values in this table are from Ref. [136]. 1 barn = 10^{-28} m^2.

Raman spectroscopy, as the spectral intensities of the latter depend on changes in the electronic properties of the material (the dipole moment and the polarisability for IR and Raman respectively). The Mantid software was used to process and analyse the experimental INS data.[139]

3.3.2 Synchrotron Infrared (IR) Spectroscopy

All of the infrared (IR) spectroscopy results reported in Chapters 5–7 were performed at the Multimode InfraRed Imaging and Microspectroscopy (MIRIAM) Beamline (B22) at the Diamond Light Source synchrotron facility.[140] The main advantage of the synchrotron radiation (SR) source was the brightness of the beam (photon flux density several orders of magnitude higher than conventional sources) and broadband spectral range (covering simultaneously from the visible to the sub-THz region). The storage ring was operating in the standard user mode, therefore 900 bunches filling pattern for a total circulating current of 300 mA, topped up every 10 minutes (resulting in a lifetime of ~18 hours and the photon flux fluctuation limited to 0.3%).

The IR spectroscopy experiments were performed under vacuum (except for the temperature-controlled ones, which were performed under N_2) *via* a Bruker Vertex 80 V Fourier Transform IR (FTIR) interferometer equipped with a DLaDTGS detector. The measurements were obtained at a resolution of 2 cm^{-1} with a 6 μm thick Mylar broadband multi-layer coated beam-splitter to allow for measurements to be obtained in the spectral range below 700 cm^{-1}. For the mid-IR (MIR) spectra reported in Chapter 7, a KBr beam-splitter was used to measure the spectral range from 600–9000 cm^{-1}. An external IR Labs liquid helium-cooled Si bolometer was used to enhance the signal-to-noise ratio and hence the detection of THz signals.

3.3.2.1 Attenuated Total Reflection (ATR) Setup

The IR spectra reported in Chapter 5 were obtained at room temperature (RT) using the single-bounce Attenuated Total Reflection (ATR) method (Figure 3.3) for the advantage of measuring powdered samples. Precisely, each sample was placed on top of a diamond ATR crystal and held in position by pressure applied onto a high-density polyethylene (HDPE) disk *via* a clamp mechanism. Schematically, the synchrotron IR beam enters the ATR crystal from the bottom at an angle of approximately 45° and is reflected by the sample, then redirected *via* a 45° mirror to the detector pupil. Provided the refractive index of the sample is lower than the ATR material (diamond $n = 2.4$), which it is for all the MOF materials discussed in this thesis, only a fraction of the radiation reaches into the sample (evanescent wave). At the wavelength where the sample absorbs energy the evanescent wave is attenuated, and consequently, the beam exiting is modulated similarly to a transmission measurement.

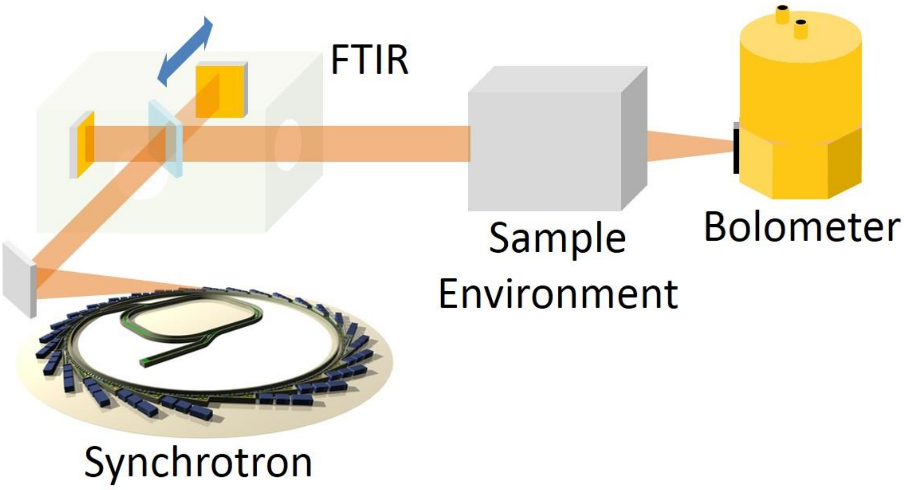

Figure 3.3. Schematic of the standard experimental setup used for the FIR spectroscopy study conducted at the B22 Beamline (MIRIAM) at Diamond Light Source.

3.3.2.2 Linkam Cell Setup

The *in situ* temperature controlled spectra discussed in Chapter 6 were obtained *via* the use of a N_2 purged (not under vacuum) Linkam cell and a Hyperion 3000 microscope.[140] The specific setup (Figure 3.4) was similar to that used by Greenaway *et al*. for the *in situ* mid-IR (MIR) microspectroscopy of CO_2 adsorption on single crystals of functionalized Sc-MOFs.[141] A small quantity of ZIF-4 powder was loaded on the heat stage of the Linkam cell, and the cell was sealed with an IR grade double polished Si window and mounted on the microscope. There was a constant flow of nitrogen, and the sample was allowed to equilibrate for approximately 5 minutes at each temperature point. The peak located in the 250–350 cm^{-1} spectral region was fitted using a Gaussian in the OriginPro 9.1 software. The result can be seen in Figure 3.5 for the room temperature spectrum. The error values were within a range comparable to the size of the symbols used in Figure 6.3 in Chapter 6, and hence error bars were unnecessary.

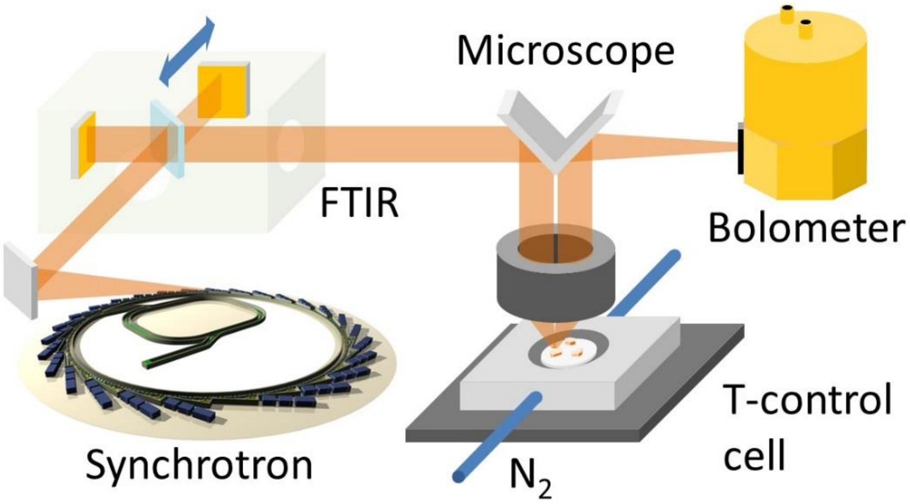

Figure 3.4. Schematic of the novel experimental setup used for the *in situ* FIR spectroscopy study conducted at the B22 Beamline (MIRIAM) at Diamond Light Source.

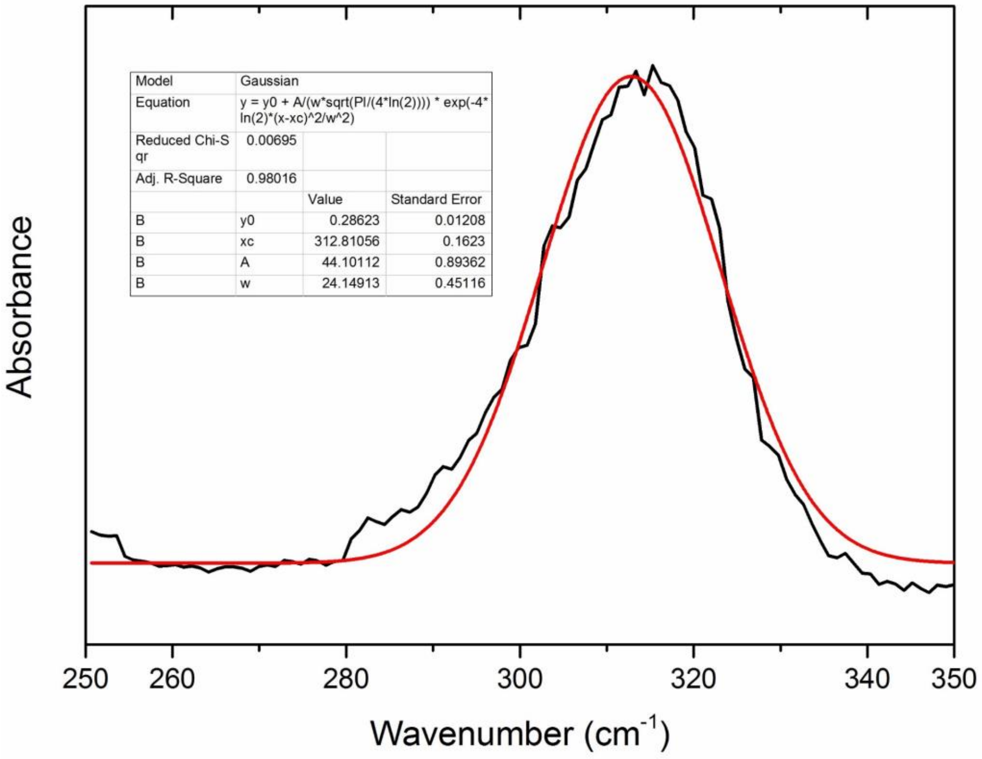

Model	Gaussian		
Equation	y = y0 + A/(w*sqrt(PI/(4*ln(2)))) * exp(-4*ln(2)*(x-xc)^2/w^2)		
Reduced Chi-Sqr	0.00695		
Adj. R-Square	0.98016		
		Value	Standard Error
B	y0	0.28623	0.01208
B	xc	312.81056	0.1623
B	A	44.10112	0.89362
B	w	24.14913	0.45116

Figure 3.5. Spectrum showing the fitting method for the 298 K peak of ZIF-4.

3.3.2.3 Specular Reflectance Setup

The reflectance and dynamic dielectric spectra reported in Chapter 7 were recorded *via* the use of a Pike Technologies VeeMAX II variable angle specular reflectance accessory (Figure 3.6). The reflectivity spectra were obtained at an angle of incidence of 30 degrees. Kramers-Kronig Transformations (KKT) were then performed to calculate the complex dielectric function from the reflectivity spectra as implemented in the Bruker OPUS software.

As a direct result of the causality principle, the complex refractive index and dielectric constant are related to the reflectivity. The values discussed in Chapter 7 were all calculated using KKTs implemented by the Bruker OPUS software. The reflectivity (Γ) of the air/sample interface is calculated using the Fresnel equation:

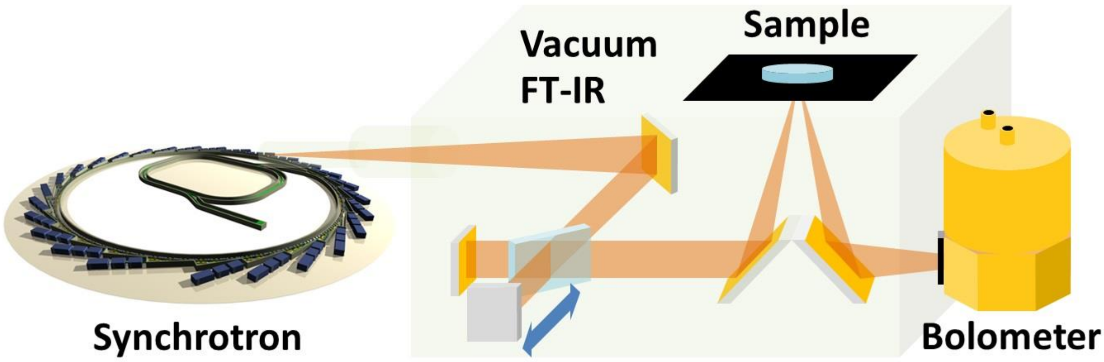

Figure 3.6. Schematic of the experimental setup used for the synchrotron reflectivity measurements conducted at the B22 Beamline (MIRIAM) at Diamond Light Source.

$$\Gamma(\nu)e^{i\phi(\nu)} = \frac{n(\nu)-1}{n(\nu)+1} \tag{3.38}$$

where $\phi(\nu)$ is the phase rotation angle calculated from the frequency (wavenumber). The real (*n*) and imaginary (κ) parts of the frequency-dependent (dynamic) refractive index are then obtained from:

$$n(\nu) = \frac{1-R(\nu)}{1+R(\nu)-R^{1/2}(\nu)\cos(\phi(\nu))} \tag{3.39}$$

$$\kappa(\nu) = \frac{2R^{1/2}(\nu)\sin(\phi(\nu))}{1+R(\nu)-2R^{1/2}(\nu)\cos(\phi(\nu))} \tag{3.40}$$

The real (ε') and imaginary (ε'') parts of the dynamic dielectric function are simply:

$$\varepsilon' = n^2 - \kappa^2 \tag{3.41}$$

$$\varepsilon'' = 2n\kappa \tag{3.42}$$

3.3.3 Raman Spectroscopy

The Raman spectra reported in Chapter 5 were obtained *via* a Bruker Senterra confocal Raman microscope setup with a 50× objective and a high numerical aperture of 0.8. The setup was operated with an excitation wavelength of 532 nm at 50 mW with a 50 μm aperture setting. The spectral range was 40–4,000 $\mathrm{cm^{-1}}$ with a resolution of 6–9 $\mathrm{cm^{-1}}$. The spectra were detected by a depleted silicon (Si) CCD Peltier cooled to −80 °C.

3.4 Chapter Summary

The chapter has provided a summary of the theoretical and experimental methods used throughout the thesis. The reason for using the specific DFT functionals is provided, and the geometry optimisation procedure is discussed along with the methods to calculate the theoretical elastic constants, vibrational frequencies, and dielectric response (static and dynamic). The experimental techniques are also explained, including inelastic neutron scattering (INS), synchrotron infrared (IR) and Raman spectroscopy.

Chapter 4

The Mechanical Response of Metal-Organic Frameworks

This chapter discusses the mechanical response of metal-organic framework (MOF) materials. The single-crystal elastic constants were computed using density functional theory (DFT) and used to generate a complete three-dimensional (3D) representation of the significant mechanical properties, encompassing Young's modulus, shear modulus, linear compressibility and Poisson's ratio. The work begins by showing the level of anisotropy present in the cubic Cu-based structure, HKUST-1, before moving onto four zeolitic imidazolate frameworks (ZIFs). The four ZIF structures were studied to understand the effect that crystal structure and network topology can have on the mechanical response of the material; despite having the same chemical composition, each structure features a distinct network topology, crystal symmetry and pore architecture. Also, the isoreticular Zr-based MIL-140 series was studied to understand the effect of systematic organic linker exchange. Of particular interest, the results in this chapter include negative Poisson's ratios (NPR) and negative linear compressibilities (NLC), as well as the lowest shear modulus reported for any ZIF material. The mechanisms responsible for the various elastic anomalies are explained. The bulk moduli were analysed to understand the framework structural resistance against hydrostatic pressure and the averaged mechanical behaviour of bulk (polycrystalline) MOF materials were also determined.

4.1 Introduction

This chapter involves the calculation and explanation of the elasticity and mechanical properties of a variety of topical metal-organic framework (MOF) materials using density functional theory (DFT). The full elasticity solutions accompanying detailed deformation mechanisms that control the anisotropic mechanical properties have been established, ranging from Young's and shear moduli to linear compressibility and Poisson's ratio. The single-crystal elastic coefficients (C_{ij}) were computed using the B3LYP DFT functional,[78-80] as described in Chapter 3.

The first structure discussed is the Cu-based paddle-wheel MOF, HKUST-1.[142] Despite the relatively simple structure and high symmetry of HKUST-1, the mechanical response is significantly anisotropic. Of particular interest is the directional dependent negative Poisson's ratio ($\nu_{\mathrm{min}} = -0.3$) and this is discussed in Section 4.3.2.

Four zeolitic imidazolate frameworks (ZIF-1, ZIF-2, ZIF-3, and ZIF-4) were examined to understand the effect of crystal structure and network topology on the mechanical response. While the chemical compositions of ZIF-1 to ZIF-4 are the same, each structure features a distinct network topology, crystal symmetry and pore architecture, which translates into different structure-property mechanical correlations. The theoretical results suggest that ZIF-3 has an extremely low shear resistance ($G_{\mathrm{min}} = 0.1$ GPa), which underpins the flexible mechanism responsible for its negative Poisson's ratio ($\nu_{\mathrm{min}} = -0.4$). Interestingly, it has been identified that ZIF-1, ZIF-2, and ZIF-4 can all exhibit a nearly zero Poisson's ratio for specific crystal orientations (Section 4.4.3), which is reminiscent of a rare cork-like phenomenon where there is practically no lateral deformation corresponding to an applied axial strain.

Some fascinating families of MOFs are porous compounds whose physical structure and chemical affinity can be manipulated while keeping the core topology of the framework consistent. These families are termed isoreticular MOFs,[143-146] and the MIL-140 series,[147-149] investigated in this chapter represents a promising example of such a system. The unique ability to rationally design, construct and tune isoreticular MOFs has further expanded their possible applications. Therefore, the effect of systematic organic linker exchange on the mechanical stability was analysed in this chapter by studying the isoreticular Zr-based MIL-140 series. The MIL-140 (A–D) series consists of four unique materials achieved by varying the complexity of the dicarboxylic acid derived linkers, starting with terephthalic acid, one of the simplest dicarboxylic acids after oxalic acid,[150-152] and the least complicated containing an aromatic ring.

4.2 Single-Crystal Elastic Stiffness Coefficients

The mechanical properties discussed in this chapter were calculated by tensorial analysis of the single-crystal elastic constants, C_{ij}, as described in Chapter 3. HKUST-1 has only three unique elastic constants due to its cubic symmetry. Monoclinic ZIF-1 and the four MIL-140 structures have thirteen elastic constants, whereas orthorhombic ZIF-2 and ZIF-4 have nine and tetragonal ZIF-3 has six. The computed single-crystal elastic constants are summarised for each material in Table 4.1.

The diagonal coefficients C_{11}, C_{22} and C_{33}, represent the stiffness along each of the three principal crystal axes, *a*, *b*, and *c* under a uniaxial strain. The other diagonal coefficients C_{44}, C_{55} and C_{66}, are the stiffness against angular distortions when subjected to shear strains. The off-diagonal coefficients correspond to coupling effects, such as tensile-tensile coupling (C_{12}, C_{13} and C_{23}) between any two orthonormal axes, and are present for all four structures. The C_{i5} coefficients ($i = 1, 2, 3$) are only present for ZIF-1 and the MIL-140 series due to the monoclinic symmetry and represent tensile-shear coupling. Finally, the C_{46} coefficient represents shear-shear coupling. These are only

Table 4.1. Single-crystal elastic stiffness coefficients (C_{ij}) in GPa.

Structure	C_{11}	C_{22}	C_{33}	C_{44}	C_{55}	C_{66}	C_{12}	C_{13}	C_{15}	C_{23}	C_{25}	C_{35}	C_{46}
HKUST-1	27.7	= C_{11}	= C_{11}	5.40	= C_{44}	= C_{44}	25.7	= C_{12}	-	= C_{12}	-	-	-
ZIF-1	8.34	4.12	4.59	1.70	1.57	1.20	1.89	2.30	−0.85	1.25	−0.50	−0.87	0.04
ZIF-2	7.69	8.22	4.89	1.27	1.54	1.11	5.41	3.42	-	4.46	-	-	-
ZIF-3	3.80	= C_{11}	6.20	0.86	= C_{44}	1.53	3.58	3.52	-	= C_{13}	-	-	-
ZIF-4	3.07	3.36	2.95	0.77	0.90	1.53	0.57	0.60	-	0.77	-	-	-
MIL-140A	94.0	163.0	52.7	3.19	9.05	27.4	42.7	29.6	−4.01	17.4	0.27	−10.4	0.10
MIL-140B	80.5	143.1	47.2	5.00	6.56	20.9	36.4	29.3	11.7	12.3	4.65	2.11	6.41
MIL-140C	64.0	129.2	32.6	2.41	4.27	18.4	30.3	17.8	−10.5	12.6	−4.17	−2.76	−4.27
MIL-140D	62.2	109.4	29.3	1.59	2.97	17.0	25.2	17.6	7.16	8.44	2.77	0.14	3.61

present for the monoclinic systems due to $\beta \neq 90°$. Directionally dependent mechanical properties were derived from these elastic coefficients using tensorial analysis *via* the Mathematica[129] and the ElAM codes.[130]

4.3 Anisotropic Response of a Cubic Structure

This section explores the anisotropic mechanical response of the cubic paddle-wheel MOF, HKUST-1. The chemical formula of HKUST-1 is $Cu_3(BTC)_2$ where BTC stands for benzene-1,3,5-tricarboxylate and the framework structure is shown in Figure 4.1. The maximum and minimum values of all the mechanical properties of HKUST-1, together with the extent of elastic anisotropy, are summarised in Table 4.2. The values for HKUST-1 are reported for B3LYP and B3LYP-D. The differences are minor (Table 4.2 and Appendix A4.4), but the values were calculated using the dispersion corrected functional to be consistent with the vibrational studies of HKUST-1 discussed in

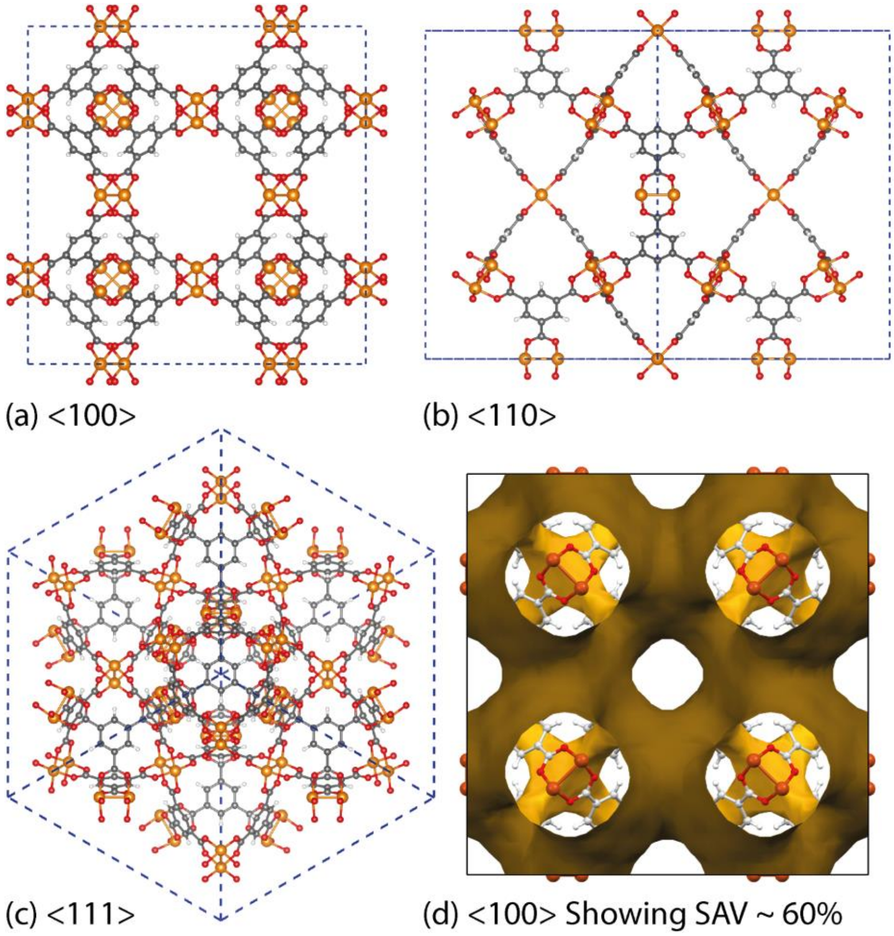

(a) <100>

(b) <110>

(c) <111>

(d) <100> Showing SAV ~ 60%

Figure 4.1. Crystal structure of HKUST-1 looking down the (a) <100>, (b) <110> and (c) <111> directions and (d) <100> direction displaying the Solvent Accessible Volume (SAV = yellow surfaces). Colour code used: copper orange; carbon grey; oxygen red; hydrogen white.

Chapter 5. The properties are namely: Young's modulus, shear modulus, linear compressibility and Poisson's ratio, and are discussed in the following sections.

4.3.1 Framework Elastic Anisotropy

The elastic anisotropy of HKUST-1 can be witnessed when examining the 3D directional Young's and shear moduli (Figure 4.2 and Table 4.2). Both the minimum and maximum Young's moduli of HKUST-1 can be explained by simple structure-property relationships. The origin of $E_{\max}$ (~15 GPa) is related to compression in the direction of the planarity of the aromatic rings. The link between deforming aromatic rings of the

Table 4.2. Elastic properties of HKUST-1. Young's and shear moduli anisotropy are $A_E = E_{\max}/E_{\min}$ and $A_G = G_{\max}/G_{\min}$, respectively.

Elastic Property		B3LYP	B3LYP-D
Young's modulus (GPa)	$E_{\max}$	15.2	14.8
	$E_{\min}$	3.0	3.1
	A_E	5.1	4.9
Shear modulus (GPa)	$G_{\max}$	5.4	5.3
	$G_{\min}$	1.0	1.0
	A_G	5.4	5.1
Linear compressibility (TPa^{-1})	β	12.6	12.8
Poisson's ratio	$\nu_{\max}$	1.21	1.19
	$\nu_{\min}$	−0.31	−0.28
Zener Anisotropy		5.4	5.1
Acoustic Velocities (km s^{-1})	max	6.2	6.1
	min	5.6	5.6

organic linker and the direction of $E_{\max}$ is quite intuitive and has also been detected in the ZIFs and MIL-140 framework structures discussed later.[25, 39] In the case of HKUST-1 these maxima are located along the <111> axes. Another interesting uniaxial property is the minimum Young's moduli, $E_{\min}$ (Figure 4.2). The minimum is located along the <001> axes and can be related to only a partial reinforcement of the linker-paddle-wheel-linker (L–PW–L) moiety oriented along each axis. The L–PW–L unit does not provide as much mechanical rigidity as would be expected from a single-linker reinforcement and hence results in an $E_{\min}$ of ~3 GPa.[39] The mechanical stability of single linker reinforcement is discussed later in Section 4.5 for the Zr-based MIL-140 series.

Moving on to the angular rigidity of HKUST-1, the shear modulus was analysed and can again be explained *via* structure-property relationships. Unlike the uniaxial directions of the 3D Young's modulus surface, the shear modulus depends on an

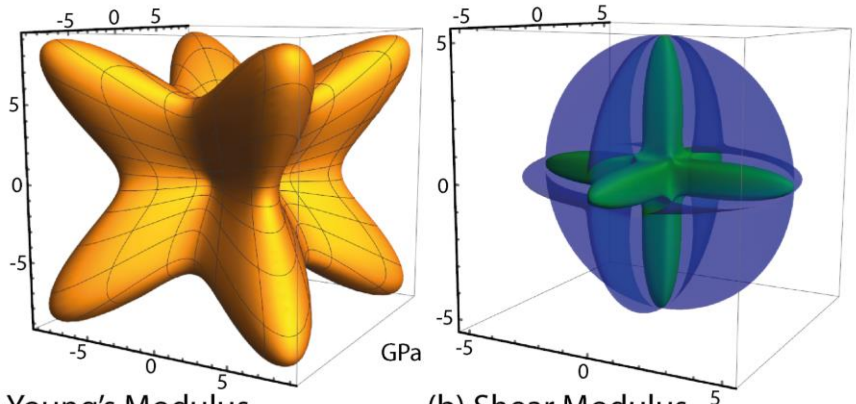

(a) Young's Modulus

(b) Shear Modulus

E_{min} in the <100> Direction
E_{max} in the <111> Direction

G_{min} in the <110> Direction
G_{max} in the <100> Direction

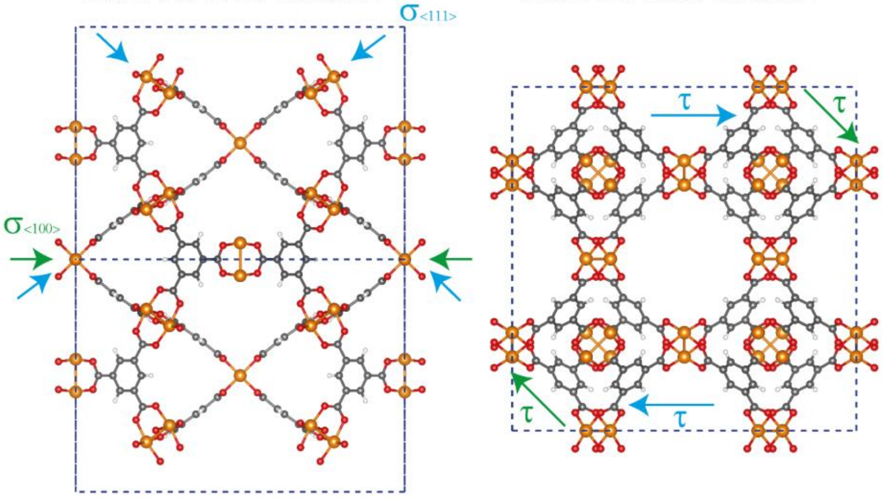

(c) <110> View

(d) <100> View

Figure 4.2. Young's modulus representation surface $E(\mathbf{u})$ in 3D spherical coordinates, along with (b) shear modulus representation surface $G(\mathbf{u}, \mathbf{v})$. The accompanying structure-property relationships are for (c) E_{min} along the <100> axes and E_{max} along the <111> axes. (d) G_{min} is along the <110> axes and G_{max} is along the <100> axis.

additional unit vector **v**, and hence the representation shown in Figure 4.2 depicts the maximum (blue) and minimum response (green) resulting from angular deformations in the respective directions.

Due to the cubic symmetry, the maximum and minimum values (G_{max} and G_{min}) are in multiple symmetric directions, with G_{max} lying along each principal crystallographic axis <100> and G_{min} in the <110> directions. This is due to the directions inclusive of flexible organic linkers deforming more efficiently than the ones with inorganic-based paddle-wheel moieties on their own. This effect is illustrated very clearly in Figure 4.2, where the different nodes are highlighted.

Before moving on to more complex elastic behaviour, it is worth noting that due to the cubic space group of HKUST-1, the linear compressibility (β) response of the framework upon hydrostatic compression is isotropic, unlike all the other mechanical properties discussed in this section. The magnitude of β in all directions is calculated to be ~12.6 $\mathrm{TPa^{-1}}$.

4.3.2 Auxetic Behaviour and Poisson's Ratio

An interesting elastic property of HKUST-1 is the Poisson's ratio, wherein specific directions a negative value is predicted, indicating an auxetic response. As per the shear modulus discussed before, the Poisson's ratio depends on two unit vectors (**u**, **v**) and hence the 3D representation (Figure 4.3) is again limited to the maximum and minimum in each direction. In this instance, due to the auxetic directions, the maximum is depicted as blue and the minimum as green and red for positive and negative values, respectively.

The minimum values of ν_{min} and the auxetic response of −0.3 are in the <110> direction, with the corresponding transverse response in the $<1\bar{1}0>$ direction. The mechanism behind this response is non-trivial to explain but could be linked to the dynamics of the inorganic-organic clusters, highlighted later in Chapter 5, rotating upon being stretched to allow for elongation in the transverse direction instead of the intuitive and more common response of contraction. The suggested mechanism shows the complex nature of the origins of anomalous elastic behaviour in MOFs. This is also an excellent example of why this level studies are vital in obtaining an accurate structure-property relationship between the framework and the directionally dependent anisotropic elastic properties.

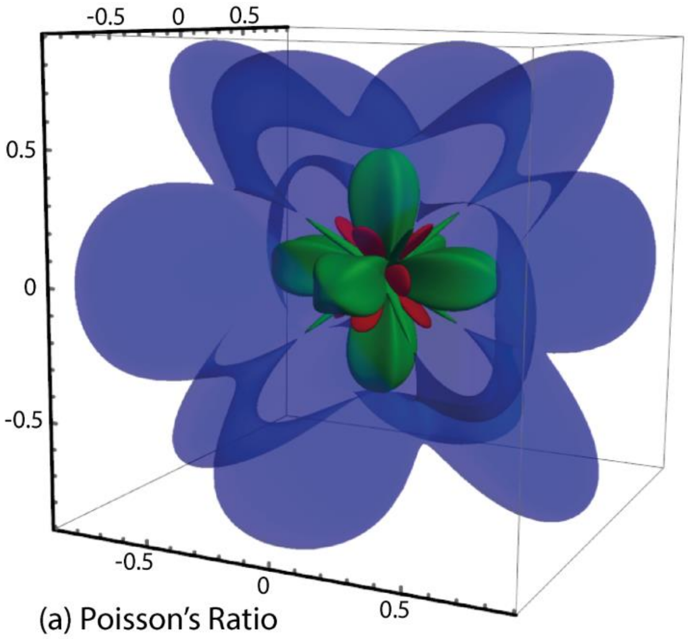

(a) Poisson’s Ratio

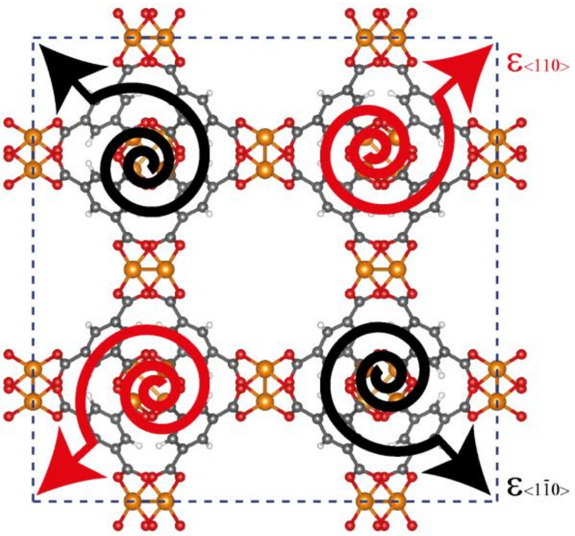

(b) ν_{min} in the <110> Direction

Figure 4.3. Poisson’s ratio representation surface ν(**u**, **v**), where blue signifies the maximum Poisson’s ratio and green and red denote the positive and negative minimum Poisson’s ratios respectively. (b) Demonstration of the plausible mechanism associated with cluster rotational dynamics responsible for the auxetic response.

4.4 The Effect of Crystal Structure and Network Topologies

This section explores the mechanical bounds of zeolitic imidazolate frameworks (ZIFs),[153] which represent a subfamily of MOFs with potential for technological applications. The results focus on the elastic properties of four ZIF structures (ZIF-1, ZIF-2, ZIF-3, and ZIF-4, all of which feature an identical chemical composition of $Zn(Im)_2$ where the divalent Zn^{2+} cations are coordinated to unsubstituted imidazolate linkers (Im = $C_3H_3N_2^-$). However, their crystal symmetries, network topologies, geometrical parameters and physical properties are all remarkably different. Using DFT calculations, it has been demonstrated that the elastic characteristics and structure-property relationships of ZIF-1 to ZIF-4 are distinctive to each framework. Some previously unreported elastic anomalies present in ZIF materials have been uncovered, for which the molecular origins and their physical significance have been identified.

All four of the ZIF structures feature the Zn–Im–Zn connectivity. Although each of the materials has the same chemical basis, they are all unique structures as shown in Figure 4.4. Their structural and physical parameters are summarised in Table 4.3. ZIF-1 and ZIF-2 share the same network topology, that of **crb**, whereas ZIF-3 and ZIF-4 have the **dft** and **cag** network topologies, respectively. However, the network topologies are only an indication of the connectivity of the various atoms and do not necessarily mean that the response of the frameworks will be correlated. This is confirmed by the fact that ZIF-2 and ZIF-4 have the same crystal symmetry (orthorhombic) despite having different topologies. Of greater importance is the unique packing of each framework, as this has a direct effect on the porosity of the framework. Multiple values can describe the porosity,

Table 4.3. Structural properties of ZIF-1 to ZIF-4.

Structure	Symmetry	Density	SAV	Topology	*T* / *V*
ZIF-1	Monoclinic	1.10	33.9	**crb**	3.6
ZIF-2	Orthorhombic	0.93	56.1	**crb**	2.8
ZIF-3	Tetragonal	0.80	57.7	**dft**	2.7
ZIF-4	Orthorhombic	1.03	34.3	**cag**	3.9

Density = g cm^{-3}; *T* / *V* = density of metal atoms per nm^3;[153] SAV = solvent accessible volume (%).

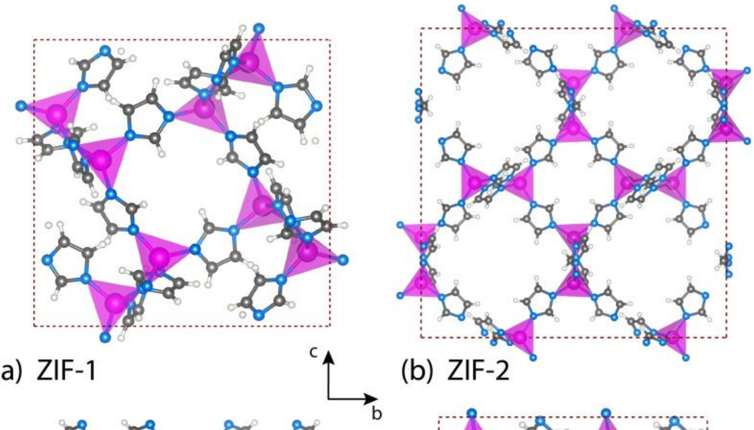

(a) ZIF-1 (b) ZIF-2

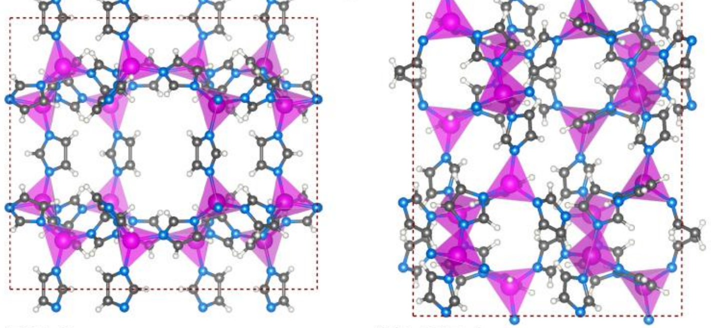

(c) ZIF-3 (d) ZIF-4

(e) Zn-Im-Zn

Figure 4.4. Crystal structures of (a) ZIF-1, (b) ZIF-2, (c) ZIF-3, and (d) ZIF-4. (e) The Zn–Im–Zn linkages subtending an angle of ~145° at the centre of the imidazolate ring. Purple tetrahedra are ZnN_4. Colour code used: zinc purple; carbon grey; nitrogen blue; hydrogen white.

and one of the most helpful is that of the solvent accessible volume (SAV),[154] as this can be a useful metric for applications such as gas storage or guest encapsulation. All the structures considered in this section show large SAVs; the most substantial being ZIF-3, closely followed by ZIF-2, with almost 60% of the internal volume being accessible to solvent (probe size 1.2 Å). This is linked to the packing of the frameworks; a good measure of this is the number of metal centres (ZnN_4 tetrahedral sites)[31] present in each unit cell (designated as T / V). It is therefore not surprising that ZIF-2 and ZIF-3 have the fewest number of Zn atoms per unit cell compared to the other two structures, and this is represented by the physical densities of each material.

4.4.1 Anisotropic Framework Stiffness

The maximum values for Young's moduli ($E_{\max}$ in Table 4.4) are due to the direction of the compression (likewise tension) coinciding with the planarity of an aromatic ring of the imidazolate groups, similar to that mentioned for HKUST-1. This explains why the shapes of the 3D surfaces are similar for ZIF-2 and ZIF-4 (Figure 4.5), as the directions of the orientations of the aromatic rings are quite varied. However, in the case of ZIF-4, the rings are less inclined in the <001> axes thereby giving a more anisotropic appearance. An interesting feature is the maximum Young's modulus of ZIF-1 which is simply due to two aromatic rings being compressed per unit cell in the <100> direction. This explains why the Young's modulus for ZIF-1 ($E_{\max}$ = 6.9 GPa) is almost a factor of two times greater than that of the other three structures (3.2–3.6 GPa) which contain only one aromatic ring in the plane.

Table 4.4. Elastic properties of ZIF-1 to ZIF-4. Young’s and shear moduli anisotropy are $A_E = E_{\max} / E_{\min}$ and $A_G = G_{\max} / G_{\min}$, respectively.

Elastic property		ZIF-1	ZIF-2	ZIF-3	ZIF-4
Young’s modulus (GPa)	$E_{\max}$	6.9	3.6	3.2	3.3
	$E_{\min}$	2.8	2.4	0.4	2.2
	A_E	2.5	1.5	7.6	1.5
Shear modulus (GPa)	$G_{\max}$	2.0	1.5	1.5	1.5
	$G_{\min}$	1.2	0.9	0.1	0.8
	A_G	1.7	1.7	13.9	2.0
Linear compressibility (TPa^{-1})	$\beta_{\max}$	225.1	172.9	127.6	241.2
	$\beta_{\min}$	−0.6	-13.3	16.4	202.1
Poisson’s ratio	$\nu_{\max}$	0.63	0.56	1.34	0.41
	$\nu_{\min}$	0.03	0.07	−0.43	0.06

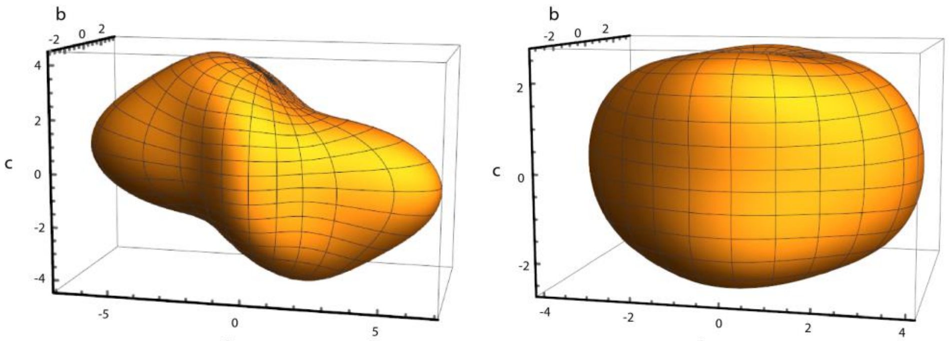

(a) ZIF-1 (b) ZIF-2

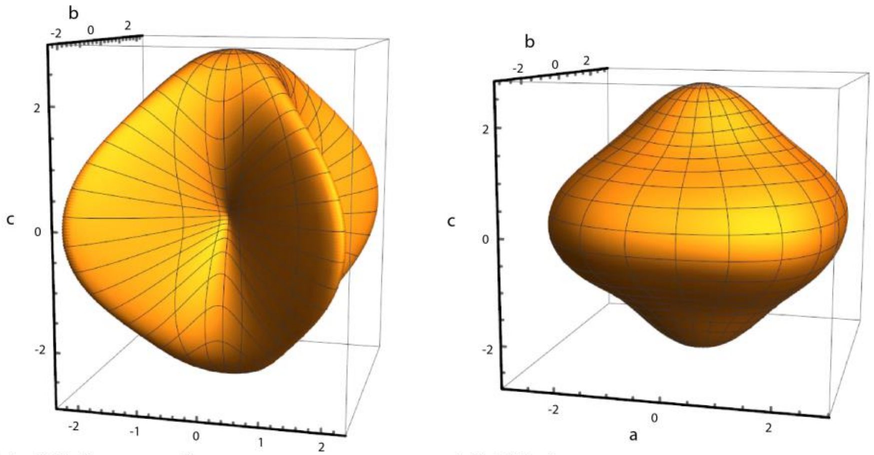

(c) ZIF-3 (d) ZIF-4

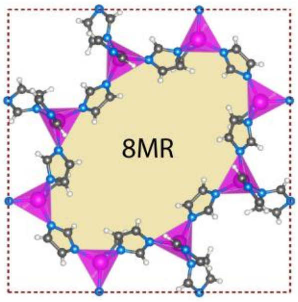

(e) ZIF-3

Figure 4.5. Young’s modulus representation surfaces *E*(**u**) of (a) ZIF-1, (b) ZIF-2, (c) ZIF-3, and (d) ZIF-4 (in GPa). (e) Projection down the *c*-axis highlighting the location of an 8MR resembling a boat-like conformation in ZIF-3.

Lastly, the other interesting property is the minimum Young's modulus of ZIF-3, which is significantly lower than the other three structures. This is due to the deformation of the structural rings constructed of the ZnN_4 tetrahedra. More specifically the flexible 6-membered rings (6MR) present in ZIF-1, ZIF-2 and ZIF-4 (discussed in this section) and ZIF-8 (discussed in Ref. [41]) give minimum Young's moduli of 2.2–2.8 GPa.

However, in ZIF-3 there is an even more flexible 8MR not present in the other ZIFs studied, and this results in an exceptionally low Young's modulus (E_{min}) of 0.4 GPa.

4.4.2 Exceedingly Low Framework Rigidity

The maximum values for the shear moduli are similar for each of the four structures (G_{max} in Table 4.4), with ZIF-1 being slightly higher due to the denser packing of the framework. The most exciting feature, however, is the significantly low minimum shear modulus of ZIF-3 (G_{min} = 0.1 GPa). It is predicted to be almost a factor of ten times lower than that of ZIF-8 ($G_{\text{min}} \approx 1$ GPa), which was previously reported to be “exceptionally low”.[41] Therefore, ZIF-3 has the lowest shear modulus ever predicted for a ZIF material. ZIF-3 is considerably more anisotropic than the other ZIFs discussed, as demonstrated by the shape of the 3D surface shown in Figure 4.6. It can be postulated that this is likely the reason that ZIF-3 is limited to the powder form[67] because its structural shear instability (facile plane slippage)[155] may hinder the growth of sizeable crystals. Unfortunately, this effect has restricted any experiments investigating the elastic response of ZIF-3, such as Brillouin scattering or single-crystal nanoindentation work.

The reason that ZIF-3 is significantly less stable to shear strain is linked to the discussion about the uniaxial compression presented in Section 4.4.1. The 8MR highlighted in Figure 4.5e simply does not provide the same support as the 6MRs found in the other frameworks. In fact, this is not surprising as it is analogous to the structural differences between cyclohexane (or benzene; in ZIF-8 due to the planarity of the 6MR)[156] and cyclooctatetraene. Therefore, there is less structural hindrance in ZIF-3, which results in a decreased energy requirement for deformation and the mechanism responsible for the remarkably low shear modulus of 0.1 GPa (Figure 4.6). It is evident

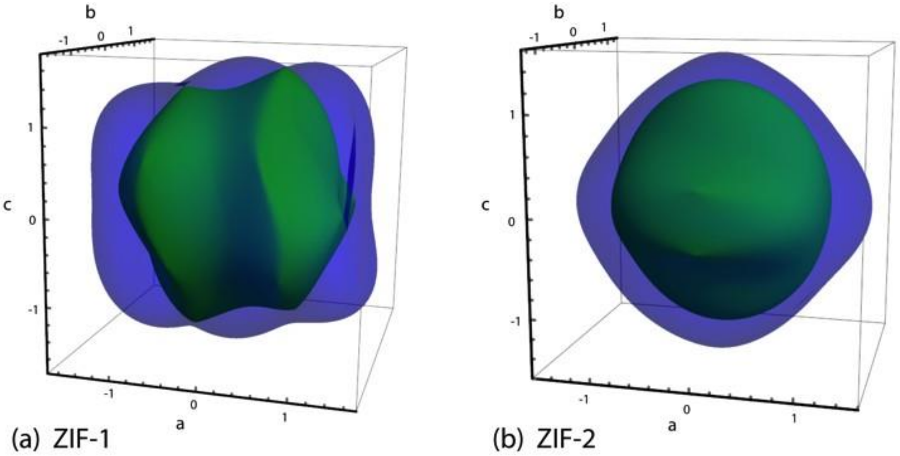

(a) ZIF-1 (b) ZIF-2

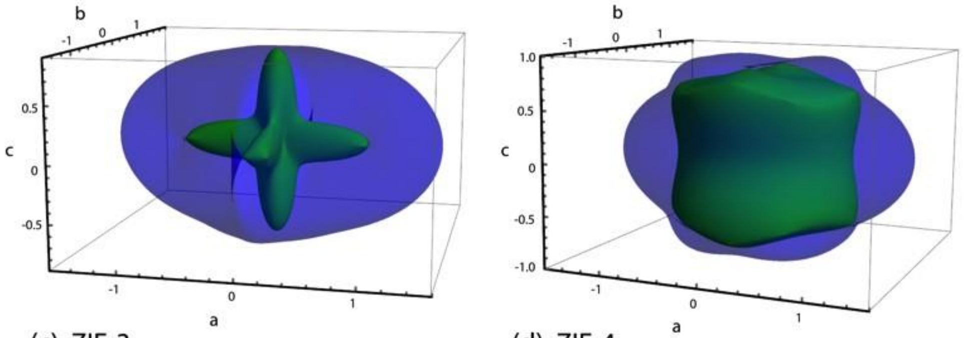

(c) ZIF-3 (d) ZIF-4

(e) ZIF-3

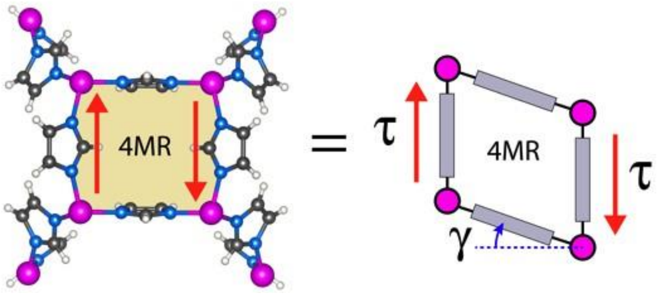

Figure 4.6. Shear modulus representation surfaces $G(\mathbf{u}, \mathbf{v})$ of (a) ZIF-1, (b) ZIF-2, (c) ZIF-3, and (d) ZIF-4 (in GPa). The maximum and minimum values are represented as blue and green surfaces, respectively. (e) Projection down the [110] axis of ZIF-3, highlighting the location of the 4MR. The accompanying pivot-and-strut model further emphasises its pliant 4-node configuration, which is highly susceptible to a shear strain γ (angular distortion) generated by a pair of antiparallel shear stresses τ.

in Figure 4.6e that there is negligible structural support restricting the shearing of the flexible 4MR facilitated by the 'boat' conformation of the adjoining 8MRs (Figure 4.5e).

A previous study showed that ZIF-1, ZIF-3 and ZIF-4 could all mechanically and thermally amorphise, albeit amorphisation by ball milling is considerably faster compared with heating (~300 °C) or under hydrostatic pressure.[67] The new findings reported here reinforce the suggestion that the relatively low shear moduli of ZIFs (Table 4.4: $G_{\max} < 2$ GPa) is the cause of the ball-milling amorphisation and more generally shear-induced structural instability and collapse.[156]

4.4.3 Anomalous Poisson's Ratio and Auxeticity

Firstly, it is worth mentioning that ZIF-8 was previously reported[41] to have a minimum Poisson's ratio of 0.33 due to the contrasting planarity of the 6MR compared to ZIF-1, ZIF-2 and ZIF-4. As mentioned in Section 4.4.2, relating to the rigidity under angular deformation, the 6MR in ZIF-8 is planar (analogous to benzene) whereas the 6MRs in ZIF-1, ZIF-2 and ZIF-4 (which have a minimum Poisson's ratio of approximately zero) are not (they are analogous to cyclohexane). This is the reason for the new 'cork-like' behaviour ($\nu \approx 0$), as the deformation of the 6MR is akin to a cyclohexane ring inversion, and as a result has negligible lateral dimension change upon axial strain in specific directions. This is observed clearly in the minimum 3D surfaces, where a similar response is witnessed at rotated orientations, consistent with the coordination of the 6MRs.

However, of considerable interest is the significant negative Poisson's ratio predicted for ZIF-3 ($\nu_{\min} = -0.43$). This is again due to the unique presence of the 8MRs, which are distinct from the 'chair' conformations of the 6MRs in ZIF-1, ZIF-2 and ZIF-4, and the planar 6MRs in ZIF-8. The 8MRs in ZIF-3 display a 'boat-like' conformation analogous to that of cyclooctatetraene and can be seen in Figure 4.7. This 'boat' conformation is the reason for the extraordinary response to deformation. It occurs due to the elongation in the loading axis propagating an elongation in the transverse direction, instead of a contraction, due to the ring expansion upon planarity. ZIF-3 is so far, the only ZIF structure possessing an 8MR to have its mechanical properties investigated and highlights the interesting phenomena that are still undiscovered for ZIFs.

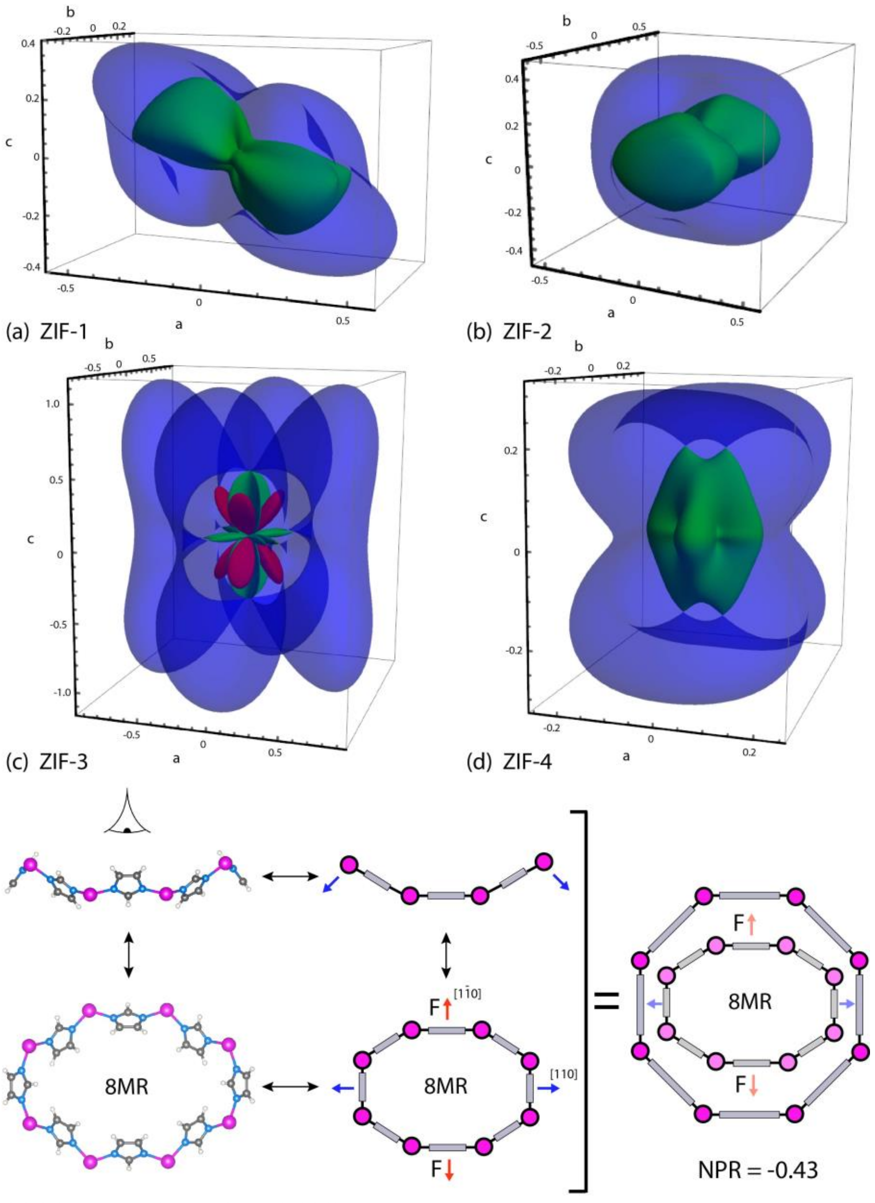

(a) ZIF-1 (b) ZIF-2 (c) ZIF-3 (d) ZIF-4

(e) ZIF-3 Negative Poisson's Ratio

Figure 4.7. Poisson's ratio representation surfaces $\nu(\mathbf{u}, \mathbf{v})$ of (a) ZIF-1, (b) ZIF-2, (c) ZIF-3, and (d) ZIF-4. The maximum values are designated in blue, while green and red surfaces corresponding to positive and negative minima, respectively. (e) View down the [1$\bar{1}$0] and [001] axes of ZIF-3, showing the boat-like conformation of the 8MR. The diagram to the right demonstrates the mechanism involved when force is applied in the [1$\bar{1}$0] direction, depicting both (an amplified) lateral and transverse extension of the 8MR explaining the anomalous auxetic response.

4.4.4 Negative Linear Compressibility

The 3D anisotropic linear compressibility is shown in Figure 4.8, with the positive and negative values shown as green and red respectively. It is worth noting that the magnitude of the negative linear compressibility (NLC) present in ZIF-1 and ZIF-2 are considerably lower than their respective maxima. The NLC values for ZIF-1 and ZIF-2 are small and are likely due to the linkers rotating slightly upon compression. The increased maximum values for ZIF-1 and ZIF-4 compared to ZIF-2 and ZIF-3 are due to the presence of pore channels in the latter. ZIF-3 has its minima in the direction of the pore channel and shows a transverse isotropic response due to its tetragonal symmetry. ZIF-4 shows an almost isotropic response due to the uniformity of the pores in each direction, unlike the other three frameworks.

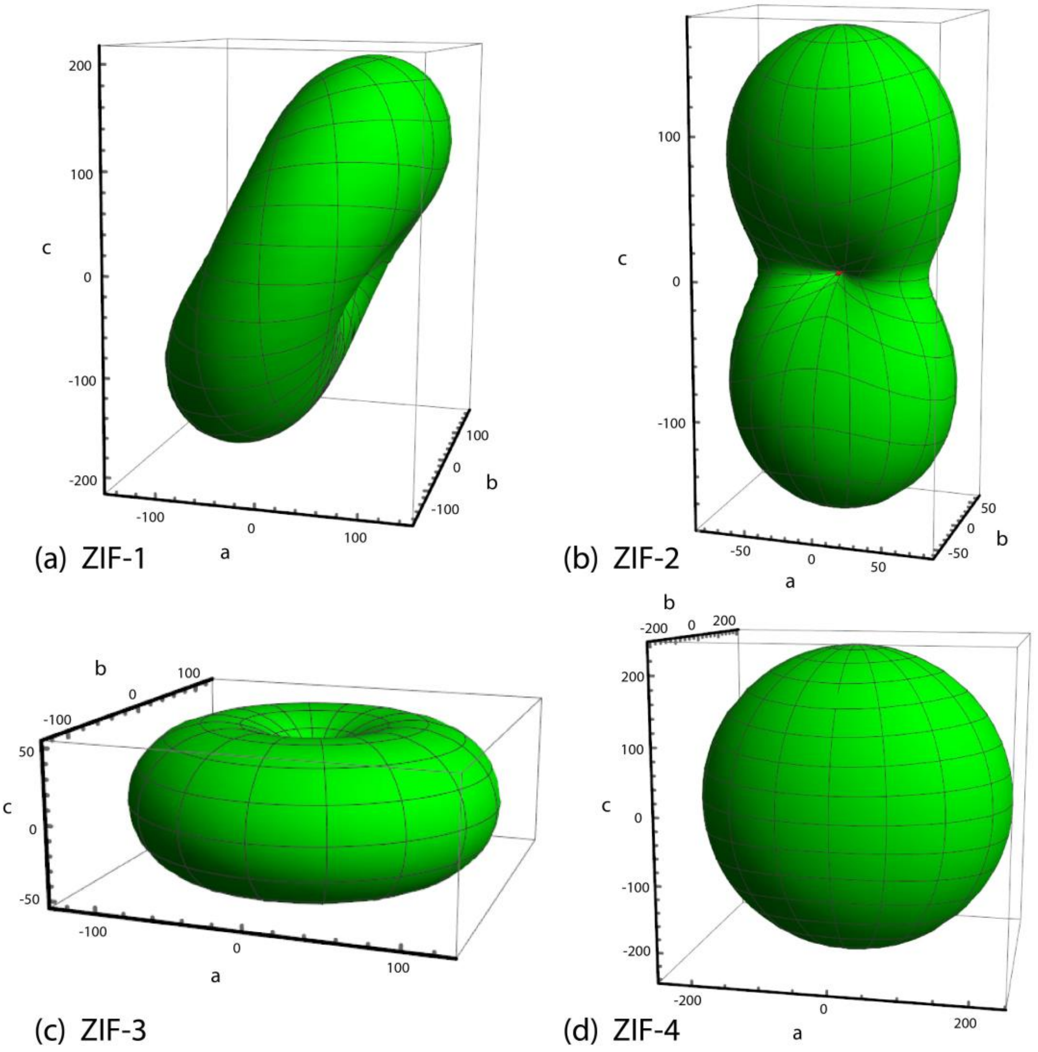

(a) ZIF-1 (b) ZIF-2 (c) ZIF-3 (d) ZIF-4

Figure 4.8. Linear compressibility representation surfaces $\beta(\mathbf{u})$ of (a) ZIF-1, (b) ZIF-2, (c) ZIF-3, and (d) ZIF-4 (in TPa^{-1}). The green and red surfaces designate positive and negative compressibility, respectively.

4.5 The Effect of Isoreticular Expansion

The isoreticular MIL-140 series,[147-149] whose chemical structures are shown in Figure 4.9, is ideal for understanding precisely how the mechanical response can be affected by the systematic expansion of a porous isoreticular framework. The MIL-140 structures are polymorphs of the topical UiO-66(Zr) material.[157] However, instead of isolated Zr_6O metal-oxo clusters, in the MIL-140 frameworks infinite one-dimensional (1D) zirconium oxide (ZrO) chains act as secondary building units (SBU) and are located

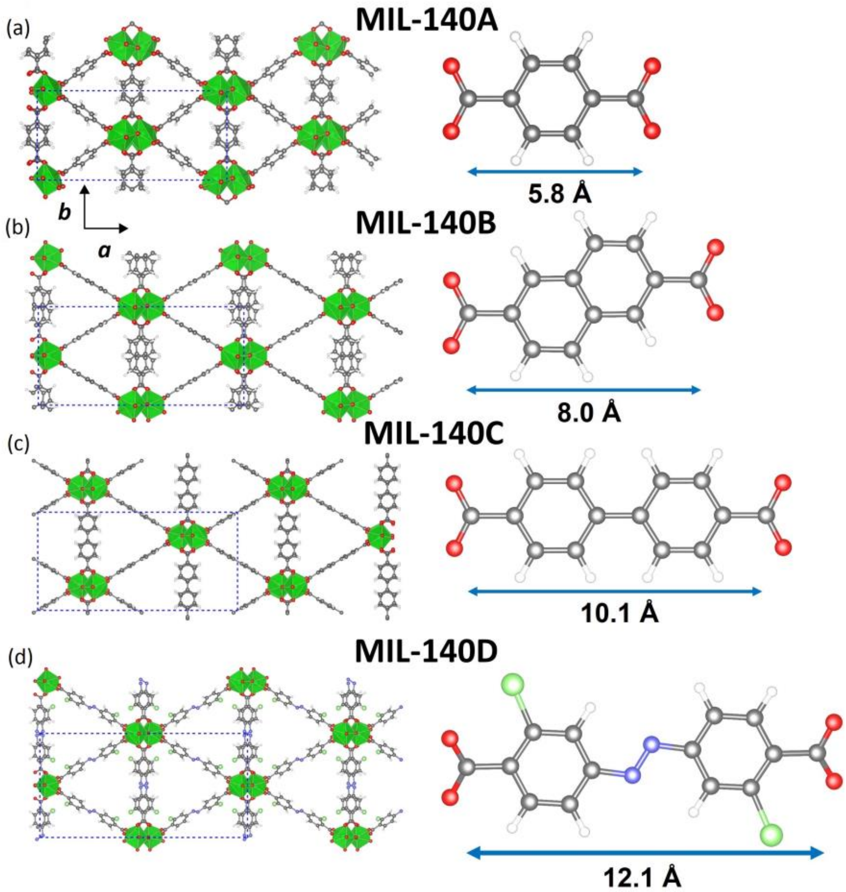

Figure 4.9. (Left) Framework structures of the MIL-140 series featuring a general chemical formula $[ZrO(O_2C\text{-}R\text{-}CO_2)]$: (a) MIL-140A where R = C_6H_4, (b) MIL-140B (R = $C_{10}H_6$), (c) MIL-140C (R = $C_{12}H_8$) and (d) MIL-140D (R = $C_{12}N_2H_6Cl_2$). The inorganic building units are ZrO_6 coordination polyhedra (green) forming 1D chains along the crystallographic *c*-axis. The dashed blue lines represent a unit cell. (Right) The organic linker of each respective framework. Colour code used: zirconium green; carbon grey; oxygen red; nitrogen blue; chlorine light green. The length of each linker is defined as the distance from the carboxylate carbon atoms.

along the crystallographic *c*-axis (Figure 4.9). Experiments have demonstrated that UiO-66(Zr) has excellent thermal and chemical stabilities,[157] albeit its mechanical stability against structural collapse (amorphisation) has recently been measured to be inferior to those of the MIL-140 series.[23] Furthermore, it has been suggested that the enhanced hydrothermal stability of MIL-140 is a result of both the reduced flexibility of its ZrO chains (compared to Zr_6O clusters in UiO-66) together with the $\pi\cdots\pi$ interactions of the aromatic rings of the MIL-140 linkers.[147] Although Zr-based MOFs are gaining significant popularity in the latest mainstream scientific literature,[148, 149, 158-162] relatively little, in fact, is reported about their underpinning mechanical trends.

Table 4.5. Elastic properties of MIL-140(A–D). Young's and shear moduli anisotropy are $A_E = E_{\mathrm{max}}/E_{\mathrm{min}}$ and $A_G = G_{\mathrm{max}}/G_{\mathrm{min}}$, respectively.

Elastic property		MIL-140 series			
		A	B	C	D
Young's modulus (GPa)	E_{max}	142.0	126.5	114.0	99.2
	E_{min}	11.3	9.6	4.8	3.0
	A_E	12.6	13.2	23.8	33.1
Shear modulus (GPa)	G_{max}	36.9	32.7	29.2	26.8
	G_{min}	3.2	2.7	1.3	0.8
	A_G	11.5	12.1	22.4	33.5
Linear compressibility (TPa^{-1})	β_{max}	27.8	23.8	52.5	35.4
	β_{min}	-3.0	0.2	-10.0	1.1
Poisson's ratio	ν_{max}	1.11	0.98	1.16	1.37
	ν_{min}	−0.13	−0.15	−0.29	−0.61
Ledbetter anisotropy	A^*	12.5	13.6	23.1	36.9

4.5.1 Young’s Modulus Describing Framework Stiffness Response

It can be seen in Figure 4.10 that the framework stiffness response of the single crystals of MIL-140(A–D) are remarkably anisotropic, significantly more than that of HKUST-1 or the ZIFs discussed in Section 4.4. The 3D representation of Young’s moduli of MIL-140A is shown in Figure 4.10a. Figure 4.10b shows the systematic trends

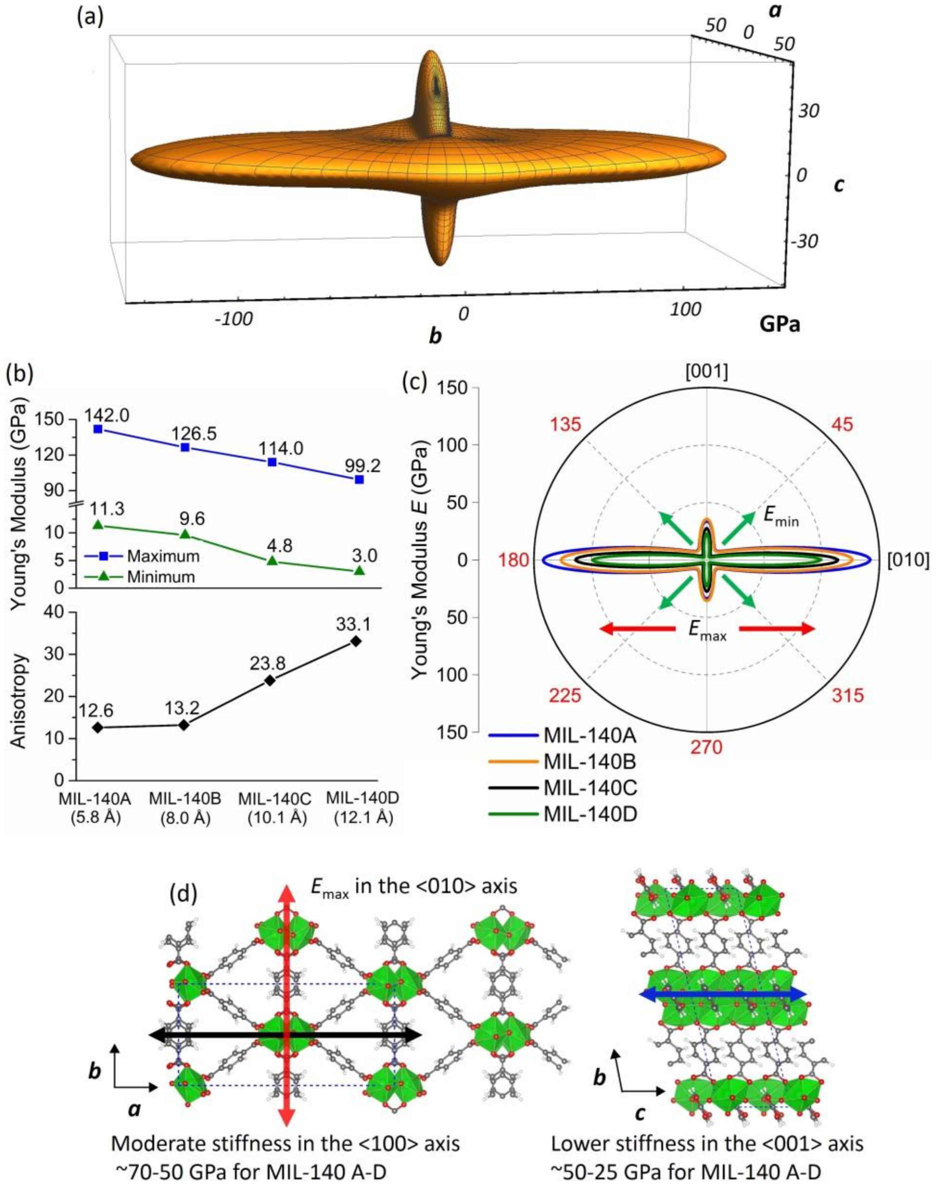

Figure 4.10. (a) Young’s modulus representation surface $E(\mathbf{u})$ of MIL-140A where $E_{\max}$ is along the <010> axis. (b) Trends in $E_{\max}$ and $E_{\min}$ and their anisotropy values (A_E). (c) 2D representation of the projections down the c-axis, showing $E_{\min}$ in the vicinity of <011>. (d) Framework diagrams elucidating the origin of the directional Young’s modulus along the three principal axes.

determined in the maximum and minimum Young's moduli for MIL-140(A–D), along with the corresponding degree of anisotropies ($A_E = E_{\max}/E_{\min}$). Interestingly, it was found that the general morphology and shape of the anisotropic surfaces are similar for each structure (Appendix A4.5). The extent of anisotropy (A_E) increases when going through the isoreticular series, with the precise values being 12.6, 13.2, 23.8 and 33.1 for MIL-140A to MIL-140D, respectively. These magnitudes are also consistent with the Ledbetter anisotropy values (A^*), also shown in Table 4.5, which are established from the ratio of transverse sound velocities ($V_{\min}^2/V_{\max}^2$).[163] The elastic response along each axis can be explained by the underlying framework design, shown in Figure 4.10d. The maximum for each framework, observed along the <010> crystal axis (values are given in Figure 4.10b), is the result of the rigid organic linkers (aligned in the *b*-axis) and the strain energy required to deform the aromatic rings. As would be expected, when additional structural flexibility (higher degrees of freedom) is introduced in the linker, the Young's modulus decreases. It is also worth noting that there will be an additional decrease expected in the Young's modulus going through the series, due to the presence of increased porosity. Therefore, an almost linear decline of uniaxial stiffness is observed when stepping through the MIL-140 series, reflecting the nearly steady rise in linker length from structure A to D (Figure 4.9). The second direction of interest is the <100> axis along which moderate stiffness has been determined, and this can be explained by the compression of the 3-node ring architecture with each node constituting a Zr-polyhedra. The third direction along the <001> axis is due to the 1D chains of Zr-polyhedra, conferring a relatively lower stiffness. The variation in Young's moduli of the <100> and <001> axes going from MIL-140A to MIL-140D are less drastic (~70–50 and ~50–25 GPa respectively) than the variation of the maximum moduli ($E_{\max}$) along the <010> axis. As these crystallographic orientations are less strongly affected by the flexibility of the rigid linkers; this supports the claim that the ligand flexibility plays a significant role in addition to the increase in porosity.

4.5.2 Shear Modulus Defining Framework Rigidity

A 3D representation surface of the shear modulus (*G*) of MIL-140A is shown in Figure 4.11a, whose 2D projections normal to the (100) and (001) planes are given in

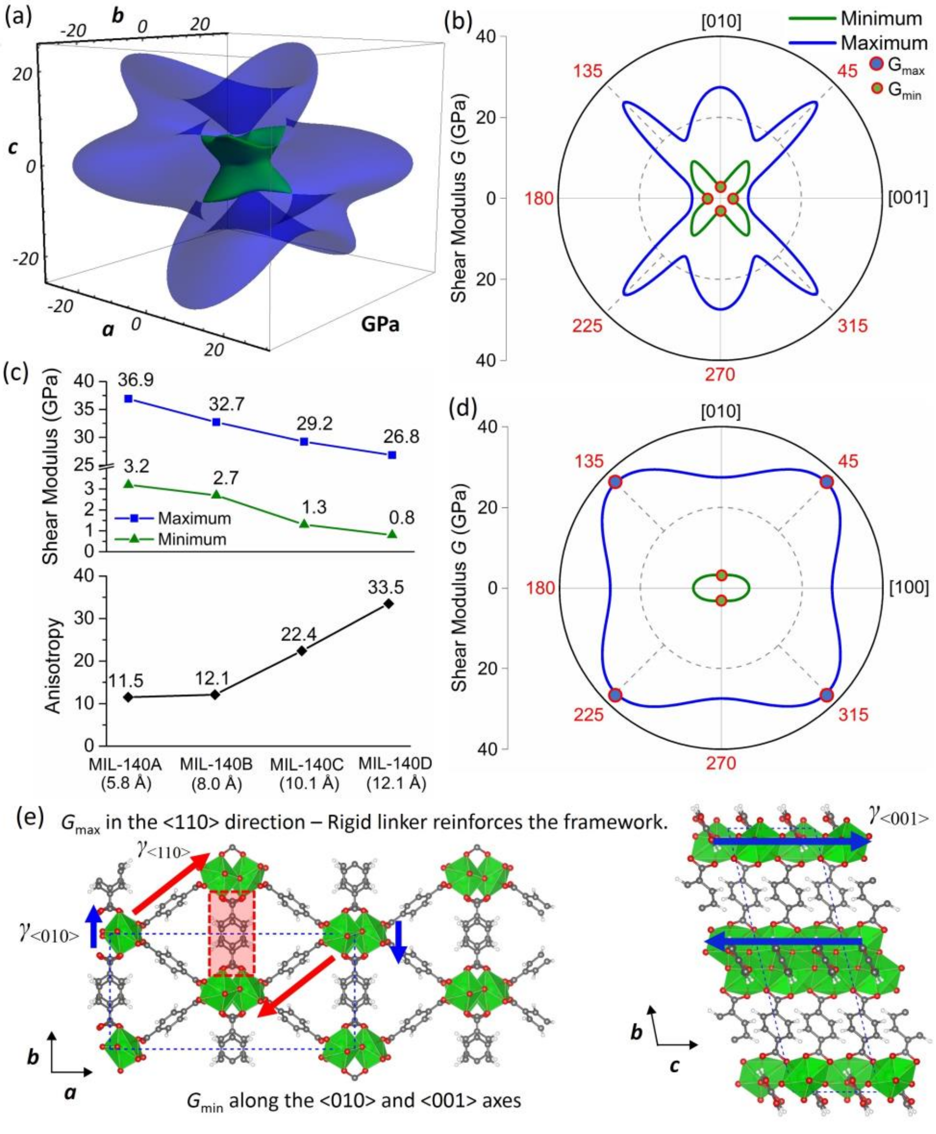

Figure. 4.11. (a) Shear modulus representation surface $G(\mathbf{u}, \mathbf{v})$ of MIL-140A, where the colour coding: blue and green denotes the maximum and minimum moduli respectively. (b) Trends in G_{max}, G_{min} and the anisotropy values (c) 2D representation of the (100) plane; (d) 2D representation of the (001) plane; (e) Diagram showing the origin of the maximum and minimum shear modulus for MIL-140A. The red dotted box highlights the position of the reinforcing linker.

Figure 4.11b, d. The monotonic trend in the maximum and minimum shear moduli for MIL-140(A–D), along with the corresponding anisotropies are mimicking that observed for the Young's modulus. Notably, one should recognise that these trends are consistent with recent mechanical stability experiments conducted on the same series of materials *via* ball milling.[23] The grinding time required to cause mechanical collapse (framework amorphisation) decreased in the same sequence in line with declining extremal shear moduli (Figure 4.11c): MIL-140A > MIL-140B > MIL-140C > MIL-140D.

The general shape of the anisotropic shear moduli surface is again similar for each structure and can be seen in Appendix A4.6, supporting the observed trends. The maximum shear modulus (G_{max}) for all MIL-140 structures is approximately in the <110> directions (there are small deviations due to the angle of the linkers). This can be explained by the rigid linker reinforcing the (otherwise pliant) 4-noded framework structure; this mechanism is illustrated in Figure 4.11e. The reduction in the maximum shear modulus, going through the MIL-140 series, is associated with the decrease in the rigidity of the more extended linker, hence enhancing the flexibility. The minimum shear modulus (G_{min}) is less evident; it has been discovered that two separate mechanisms may result in approximately the same low values (Figure 4.11e). These minimum rigidity values are in the vicinity of the <010> and <001> axes (again with small deviations due to the angle of the linkers). The connection between the two similar values is the 1D chains of Zr polyhedra, where the shear strain exerted along the *b*-axis (denoted as $\gamma_{<010>}$) generates an angular deformation of the 4-noded ring configuration. However, this time in the absence of any structural resistance by the reinforcing linker because it is positioned parallel to $\gamma_{<010>}$. The other pliant angular distortion mechanism is along the *c*-axis ($\gamma_{<001>}$), involves shearing the 'tunnel-shaped' pore of the framework, for which the reinforcing linkers essentially fold in the <001> directions thus maintaining their planarity.

4.5.3 Negative Linear Compressibility

The variation in the maximum and minimum linear compressibility for MIL-140(A–D) does not obey the same trend as the properties discussed above. While the general shape of the anisotropic surface is similar for each structure, the direction of the maximum and minimum is the same for MIL-140A and MIL-140C but in the opposite direction for MIL-140B and MIL-140D. Another striking feature that these pairs have in common is that MIL-140A and MIL-140C both exhibit negative linear compressibility (NLC), whereas MIL-140B and MIL-140D do not. Indeed NLC is a rare and a much sought after elastic anomaly,[164] whereby the framework experiences a linear expansion (instead of contraction) under hydrostatic pressure. It is noted that the NLC of both MIL-140A ($\beta_{\min} = -3$ TPa^{-1}) and MIL-140C ($\beta_{\min} = -10$ TPa^{-1}) are relatively high. The magnitudes are on par with other contemporary NLC materials, such as hybrid zinc formate (-1.8 TPa^{-1}),[50] $Ag_3[Co(CN)_6]$ (-5 TPa^{-1}),[164] and a Ag-based MOF (-28 TPa^{-1}).[52]

The maximum values for each framework can be explained by the π-stacking of the aromatic rings (Figure 4.11e), with the stacking occurring approximately in the <001> axis and the rings tilting in the corresponding direction of the maximum for each structure. This explains why a reversal of the direction is revealed for MIL-140B and MIL-140D compared to that of MIL-140A and MIL-140C. The direction of maximum linear compressibility ($\beta_{\max}$) is in line with the direction of the centroid of the phenyl rings since the attraction of the $\pi\cdots\pi$ stacking allows for contraction upon hydrostatic compression. It follows that the minimum values ($\beta_{\min}$) will exist in the orthogonal

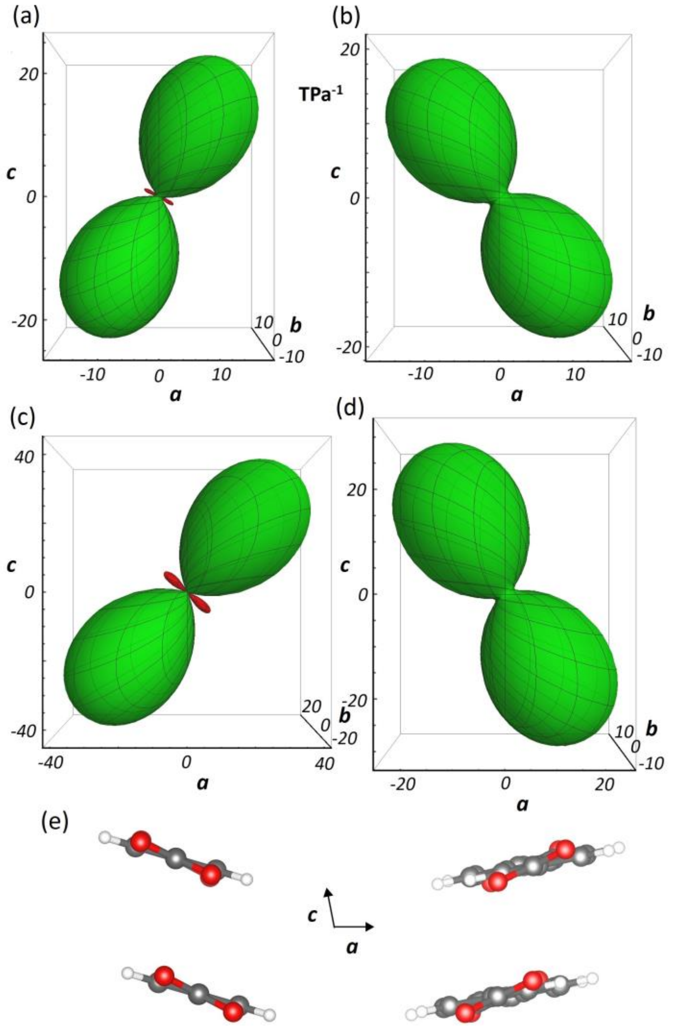

Figure 4.12. Linear compressibility representation surface $\beta(\mathbf{u})$ in 3D spherical coordinates. (a) MIL-140A, (b) MIL-140B, (c) MIL-140C and (d) MIL-140D, where green and red designates positive and negative values of linear compressibility, respectively. Rings are tilting in opposite directions for (e) MIL-140A versus MIL-140B.

direction to the maximum axis (due to phenyl ring rigidity), which matches the direction that is compressing the phenyl rings in the plane. Furthermore, the NLC effect observed for MIL-140A and MIL-140C is likely the result of the phenyl rings rotating (yielding expansion) due to the higher level of rotational flexibility when compared with the more rigid linker present in MIL-140B and the bulkier linker of MIL-140D. The presence of the bulky chlorine atoms of MIL-140D (Figure 4.9d) can lead to mechanical responses due to a balance between $\pi\cdots\pi$ stacking and repulsive force interactions. The negative values witnessed for MIL-140A, and MIL-140C would encourage further experimental studies to investigate and further validate the postulated mechanisms suggested in this theoretical work.

4.5.4 Poisson’s Ratio and Mechanism of Anomalous Auxeticity

Conventional isotropic materials typically feature a positive value of ν not exceeding 0.5,[48] since an axial expansion will be accompanied by a lateral contraction in the transverse direction (and vice versa) such that volume is conserved. However, being elastically anisotropic, the Poisson’s ratios of the MIL-140 series are complicated which can be seen by 3D representations for MIL-140A and MIL-140D in Figure 4.13a, b (Appendix A4.7).

The representation surface is highly anisotropic with one of the most interesting values being the ‘auxetic’ directions giving negative Poisson’s ratios (NPR). The most

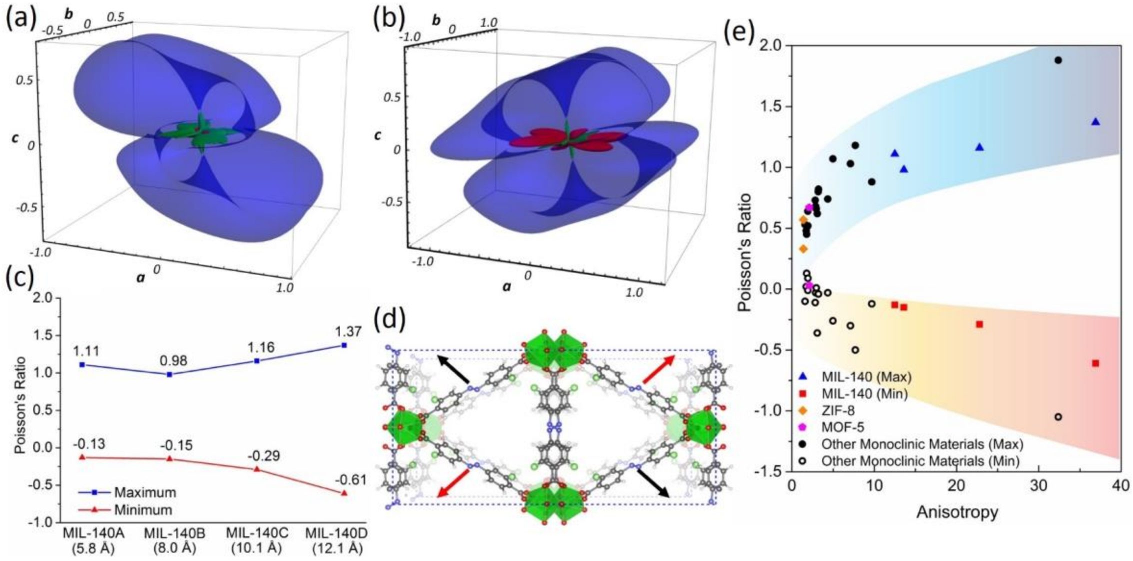

Figure. 4.13. Poisson’s ratio representation surface $\nu(\mathbf{u}, \mathbf{v})$ of (a) MIL-140A and (b) MIL-140D, where blue signifies the maximum Poisson’s ratio and green and red denote the positive and negative minimum Poisson’s ratios, respectively. (c) Trends in ν_{max} and ν_{min}. (d) Illustration of the auxetic mechanism responsible for the NPR response with the slightly transparent inset representing the original structure. (e) Correlation between the Ledbetter anisotropy A^* and extremal Poisson’s ratios, incorporating data of other monoclinic materials,[47] MOF-5,[43] and ZIF-8,[41] where the blue and red bands designate the positive and negative values.

auxetic direction, exhibiting $\nu_{min} \approx -0.1$ to -0.6 (Table 4.5), is the result of a complex mechanism and not trivial to fully describe, but can be explained by the expansion of the 4-noded ring architecture (Figure 4.13d) connected by ZrO_6 clusters behaving like hinges. This effect would be larger if the structures were not reinforced (by the bridging linker) and this has been demonstrated for example by Ortiz *et al*. for MIL-53.[38] Herein the NPR trend observed when going through the MIL-140 series (Figure 4.13c) is a systematic response to the reduction in the rigidity of the linker present. Also, it was established that the direction of the maximum Poisson's ratio is a result of the $\pi\cdots\pi$ interactions of the aromatic rings. This also explains the change in the direction of the maximum Poisson's ratio witnessed for MIL-140A compared to MIL-140D due to the difference in the tilting of the aromatic rings (elaborated in Section 4.5.3) illustrated in Figure 4.12e. In Figure 4.13e, it is promising to see that the values matched very well when comparing the relationship between both the maximum and minimum Poisson's ratio with the level of elastic anisotropy, and when comparing to that of other monoclinic structures and reported values for other MOF materials.[47]

4.6 Polycrystalline Powder Averaged Mechanical Properties

Lastly moving away from the single-crystal properties, the isotropic bulk modulus (*K*) and the averaged polycrystalline properties of all the materials studied in this chapter are presented in Table 4.6. The bulk modulus represents the resistance to (uniform) hydrostatic compression. The isotropic averaged properties of *K*, *E*, *G* and ν, physically correspond to a homogeneous compacted powder, fabricated by a pelletisation process. The Voigt-Reuss-Hill (VRH) average values are reported, which equate to the numerical average of the Voigt and Reuss methods that assume a uniform strain, and uniform stress respectively.[127] It is also worth noting that the calculated values are based on perfect polycrystalline materials assuming no residual solvent molecules or defects. Therefore, it is logical to expect experimental values to differ slightly. However, these values can be used to approximate the elastic properties of MOFs in other forms than a single crystal, such as thin-film coatings and bulk extrudates,[21, 22, 24, 165-169] provided that their polycrystalline grain arrangements are randomly oriented (no preferred textures).

The bulk modulus value obtained for HKUST-1 was ~26 GPa, which is in agreement with the experimental values in the literature (~25–30 GPa).[71, 170] All of the four ZIF materials give bulk modulus values in the range of 1.5–4.9 GPa, confirming that the structures are in general more compressible than other MOFs reported. Such as HKUST-1 (~25–30 GPa),[71, 170] MOF-5 (~17 GPa),[11] ZIF-8 (~8 GPa),[41] MIL-53(Al) (~7 GPa),[38] and the UiO series frameworks (14–42 GPa).[68] However, there is no apparent correlation with the densities or packing of the frameworks as all four structures have significantly large solvent-accessible volumes (Table 4.3). The shear moduli of the polycrystalline ZIF structures are relatively small with the upper and lower bounds being 1.6 GPa and 0.6 GPa respectively. These results substantiate the hypothesis that mechanical amorphisation of polycrystalline ZIF powders[67] could be straightforwardly triggered by shear-induced angular distortions causing an eventual framework collapse.[41] Finally, the MIL-140 structures are predicted to have higher resistance to uniform hydrostatic compression (bulk moduli), as would be expected from the reinforced structures, ranging from ~29–45 GPa.

It is important to note that the polycrystalline average Poisson’s ratios of all the structures are positive, despite many of them (HKUST-1, ZIF-3 and the entire MIL-140 series) exhibiting a significant degree of auxeticity in single crystal form. It is also worth noting that all the polycrystalline values for the Poisson’s ratio are almost identical for each isoreticular expanded structure in the MIL-140 series ($\nu_{VRH} \approx 0.35$–0.37) despite the

Table 4.6. Isotropic aggregate elastic properties based on the Voigt-Reuss-Hill (VRH) averages, corresponding to a texture-free polycrystalline material. The bulk (K), Young's (E) and shear (G) moduli are in GPa. Poisson's ratio (ν) is dimensionless.

Structure	K_{VRH}	E_{VRH}	G_{VRH}	ν_{VRH}
HKUST-1	26.4	8.1	2.8	0.45
ZIF-1	2.8	4.0	1.6	0.26
ZIF-2	4.9	3.4	1.3	0.38
ZIF-3	3.8	1.8	0.6	0.42
ZIF-4	1.5	2.7	1.1	0.21
MIL-140A	45.3	42.0	15.6	0.35
MIL-140B	41.4	35.6	13.1	0.36
MIL-140C	30.2	26.8	9.9	0.35
MIL-140D	28.7	23.0	8.4	0.37

single crystal values varying significantly. This result emphasises that the materials would have to be grown in a controlled epitaxial manner to yield the desired crystal orientations to utilise the auxetic response for polycrystalline thin films.

4.7 Chapter Summary

This Chapter has demonstrated the mechanical response of a wide variety of MOF materials. A full analysis of the mechanical properties of HKUST-1 was demonstrated highlighting the level of anisotropy and explaining the structure-property relationships underlying the mechanics of the Cu-based MOF. A mechanism for the auxeticity present in specific directions for HKUST-1 was suggested and will be further discussed in Chapter 5 with a reported link to the THz vibrations. Due to the trivial synthesis of HKUST-1, the hope is that further experimental studies will be performed to confirm the level of mechanical anisotropy, with regards to the DFT predicted directional dependent Young's modulus, shear modulus and Poisson's ratio.

The elastic properties of four structurally polymorphic ZIFs have been calculated and explained. The structures are all constructed from divalent Zn^{2+} cations coordinated by unsubstituted imidazolate linkers and have very distinctive network topologies, porosity, and physical properties. Notably, the calculations indicated that ZIF-1, ZIF-2, ZIF-3 and ZIF-4 exhibit unusual mechanical behaviours. Ranging from an almost zero Poisson's ratio to auxeticity (NPR) in ZIF-3, and from negative linear compressibility to an extremely low shear modulus in ZIF-3; the lowest reported for any MOF structure.

Isoreticular MIL-140(A–D) were also studied where each structure adopts the same network topology but features different organic linker sizes and degrees of flexibility. This provided an opportunity to establish structure-property trends to understand further the fundamental connections that underpin elastic anisotropy and physical anomalies of MOFs. Significantly, the shear moduli trend matched recent experiments revealing the rates at which MIL-140 will undergo mechanically-induced amorphisation,[23] confirming the value of applying rigorous elasticity theory to explaining and predicting structural stability trends of isoreticular MOF systems.

The theoretical approach provides new insights into the molecular mechanisms surrounding the elastic anisotropy of MOFs, thereby enabling the elucidation of the anomalous elastic phenomena highlighted above. Overall, the findings reiterate the many undiscovered possibilities offered by the field of MOF mechanics and the exciting opportunities that it might bring to basic science (mechanical metamaterials) and practical engineering. The detailed mechanical data and new property predictions discussed herein will be advantageous to guide the future experimentation, design, manufacturing and theoretical work of both rigid and flexible framework materials.

Chapter 5

Terahertz Vibrations of Metal-Organic Frameworks

This chapter reports the origin of low-frequency terahertz (THz) vibrations in a variety of metal-organic framework (MOF) materials. The techniques involve a combination of inelastic neutron scattering (INS), synchrotron radiation far-infrared (FIR) spectroscopy and Raman spectroscopy, all in conjunction with *ab initio* density functional theory (DFT). The DFT calculations reveal the complex nature of the collective THz modes, which enables detailed correlations with experiments to be established. The low-energy conformational dynamics offer multiple pathways to elucidate novel physical phenomena observed in MOFs. The results demonstrate that THz modes are intrinsically linked to anomalous elasticity underpinning gate opening and pore breathing mechanisms in ZIFs and 'trampoline-like' deformations in HKUST-1 and MIL-140A. Shear-induced phase transitions and the onset of structural instability are also revealed with links to the mechanical properties discussed in Chapter 4.

The work supports the notion that the coexistence of soft modes and intrinsic shear distortions connected to the THz lattice dynamics dictate a range of anomalous elastic phenomena, for example, negative Poisson's ratios (auxeticity), negative thermal expansion (NTE), and exceedingly low shear moduli.

5.1 Introduction

The origin of the mid-infrared (MIR) vibrational spectra can often be explained by standard characteristic vibrations (e.g. bond stretching and bending), for which spectroscopic interpretation is well established. Even in materials as complex as MOFs, the variations are minor.[82, 171] Therefore, the real thrust of this chapter is to interrogate the lower energy vibrational bands observed in the far-infrared (FIR) region of the spectrum (< 600 cm^{-1}), with emphasis on the low-frequency vibrations under ~3 THz (< 100 cm^{-1}). Unlike in MIR spectroscopy, since no known characteristic frequencies are resulting from stereotypical functional groups, the identification of the nature of the vibrational modes is challenging and can only be accomplished here through *ab initio* quantum mechanical calculations.

5.2 First Example of THz Vibrations of ZIFs

This section concerns the use of inelastic neutron scattering (INS) and synchrotron infrared (IR) vibrational spectroscopy, in conjunction with DFT calculations to study the vibrational properties and low-frequency conformational dynamics of three prototypical ZIF materials: ZIF-4, ZIF-7 and ZIF-8. Their unique open-framework structures are depicted in Figure 5.1, and their corresponding chemical composition and topological information are summarised in Table 5.1.

It is evident from Figure 5.2b that the predicted spectra from DFT match remarkably well with the INS data for vibrational modes located in the mid-IR (MIR) spectral region. With regards to low-frequency modes in Figure 5.2a, the shape of the predicted spectra of ZIF-4 and ZIF-7 matches well with experiment, though such agreement for ZIF-8 was challenging to attain. By comparing theory and experiment, it was established that the spectra of ZIFs could be subdivided into four distinct regions

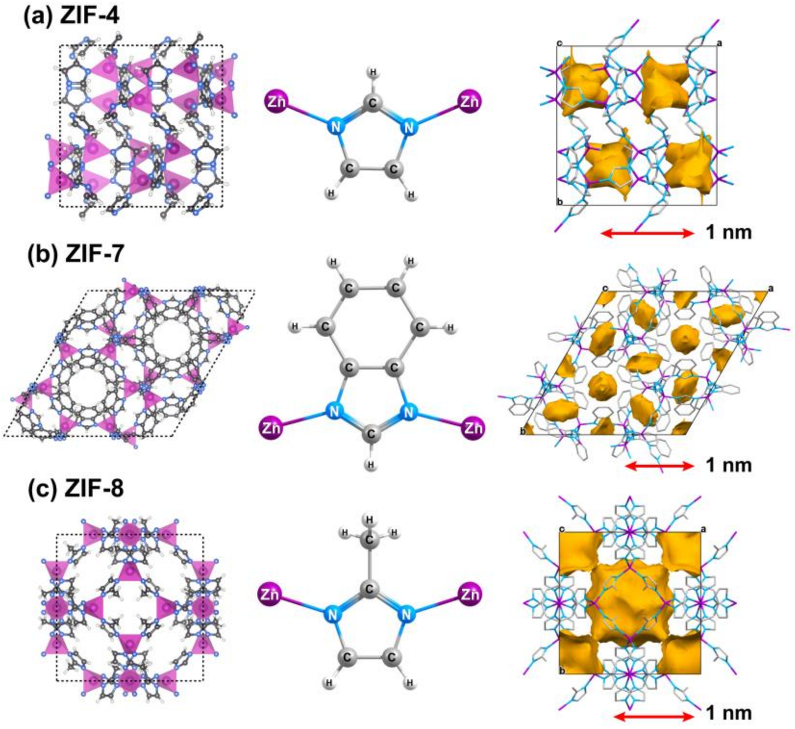

Figure 5.1. Framework structures of (a) ZIF-4, (b) ZIF-7, and (c) ZIF-8, in which the inorganic building units are represented by the ZnN_4 tetrahedra (purple). Middle panel shows the imidazole-based organic building units bridging the adjacent ZnN_4 inorganic tetrahedra. Right panel depicts the complex pore morphologies and SAV (yellow surfaces). Hydrogen is omitted in the frameworks for clarity. Colour scheme: zinc: purple; carbon: grey; nitrogen: blue; hydrogen: white.

(Figure 5.2): (I) 3,100–3,200 cm^{-1}, where aromatic C–H stretching modes are observed; (II) 960–1,600 cm^{-1}, where C–C and C–N stretching modes of aromatic rings and C–H bending vibrations are observed; (III) 420–945 cm^{-1} for modes involving in-plane and out-of-plane deformations of aromatic rings; (IV) the THz region, 0–325 cm^{-1} (< 10 THz), which is the most interesting in relation to ZIFs and MOFs as it reveals the dynamics of the open framework, along with collective vibrations and associated low-energy lattice modes.

The INS results indicate that the vibrational spectra for each framework beyond 700 cm^{-1} (~21 THz) are linked to higher-frequency vibrational signatures of the imidazolate-based organic building blocks. Considering this, to explain the basic lattice dynamics of ZIFs, the focus is on the FIR region under 21 THz. FIR absorption

Table 5.1. Chemical compositions and physical data of the structures. ZIF-4 represents a pure imidazolate (Im) ZIF, adopting the **cag** topology (after variscite $CaGa_2O_4$). ZIF-7 and ZIF-8 represent substituted ZIFs adopting the **sod** (sodalite) topology, comprising benzimidazolate (bIm) and 2-methylimidazolate (mIm) ligands, respectively.

Structure	Composition	Crystal Space Group	Network topology	SAV %†
ZIF-4	$Zn(Im)_2$	$Pbca$	**cag**	34.3
ZIF-7	$Zn(bIm)_2$	$R\bar{3}$	**sod**	26.6
ZIF-8	$Zn(mIm)_2$	$I\bar{4}3m$	**sod**	50.4

†Solvent Accessible Volume (SAV) values from Ref. [31].

spectroscopy is intrinsically a high sensitivity probe of the vibrational modes associated with C, N and H which are prevalent in ZIFs. Using synchrotron radiation FIR spectroscopy allowed for THz data with a high signal-to-noise ratio to be obtained down to 20 cm^{-1} (0.6 THz), i.e. the typically hard to gain low-frequency region. As discussed in Chapter 2, before this work others had only managed to achieve limited results for the MIR region of ZIF-8, describing the peaks below ~800 cm^{-1} simply as "out-of-plane bending" and "beyond the limitations of the equipment used".[82] These challenges are overcome herein *via* synchrotron radiation FIR techniques.

The experimental and calculated FIR spectra for each ZIF material is presented in Figure 5.3 with the major peaks and specific characteristics summarised in Appendix A5.3. For each spectrum, good agreement between experiment and theory was obtained; the terahertz (THz) signatures match well not only with regards to peak position but also their relative intensities. The difference in intensities between experiment and theory around 675-700 cm^{-1} is due to the cut-off of the beam-splitter used for the FIR experiments. From comparing the spectra of the three ZIF structures (Figure 5.3a), it was discovered that the peaks relating to the ring deformations of the imidazole-derived linkers are present at 600–700 cm^{-1} (18–21 THz). The comparison also identified another universal motion; specifically, Zn–N bond stretching originating from flexible ZnN_4 tetrahedra, positioned at 265–325 cm^{-1} (8–10 THz).

It was discovered that all framework-specific modes are in the THz region of the vibrational spectra, notably under 10 THz (< 333 cm^{-1}), with the primary signatures associated with the lattice dynamics located below 3 THz (< 100 cm^{-1}). The experimental and theoretical INS spectra for the 0–100 cm^{-1} region are presented in Figure 5.2a, with additional details in Appendix A5.5. It should be emphasised that for this low-wavenumber region it is challenging to establish a precise agreement between experiment and theory for complex framework materials [55, 57, 172].

The THz vibrational signatures can be described as collective, which means that they encompass contributions from the complete crystalline lattice of the porous

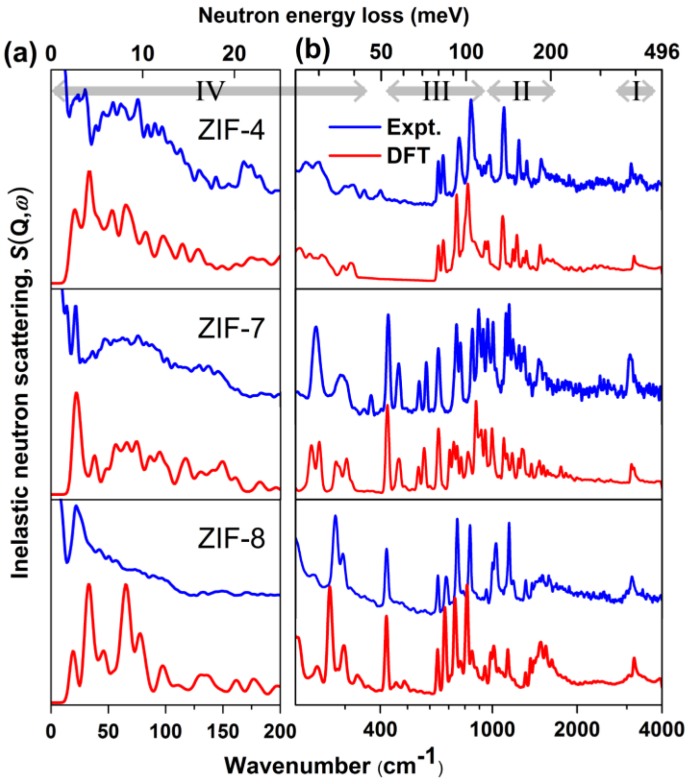

Figure 5.2. INS spectra in the (a) 0–200 cm^{-1} (linear scale), and (b) 200–4,000 cm^{-1} (log scale) regions. Comparison of experimental (blue) and DFT theoretical spectra (red) for ZIF-4, ZIF-7 and ZIF-8. The theoretical spectra simulate the purely inelastic response including overtones (Chapter 3 and Appendix A5.6). The four spectral regions are designated as I to IV. N.B. 1 THz ≈ 33.3 cm^{-1}.

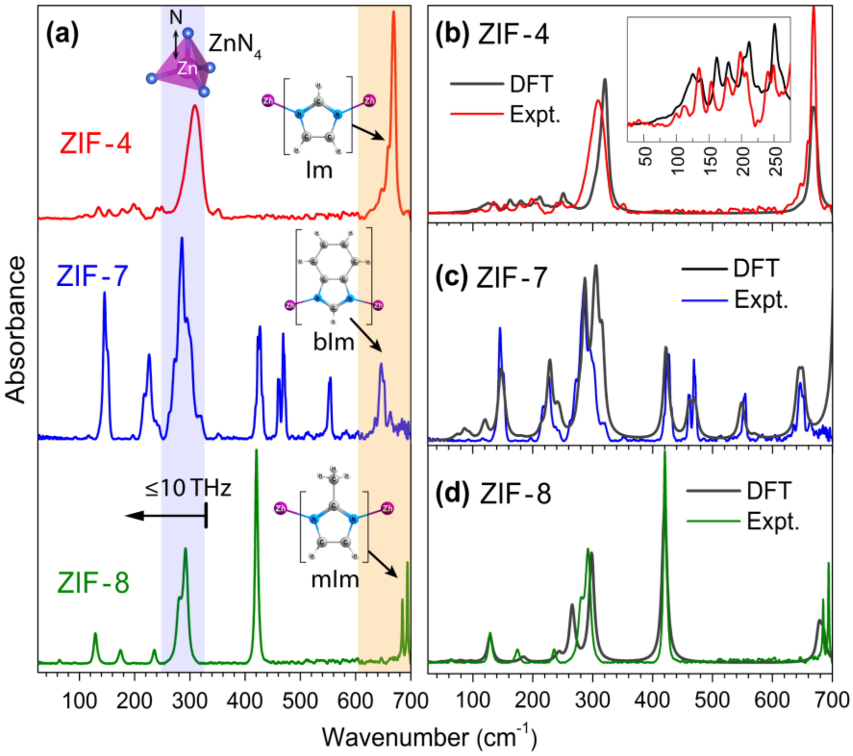

Figure 5.3. FIR spectra in the 25–700 cm^{-1} region. (a) Synchrotron radiation FIR spectra. Comparison of experimental and theoretical DFT spectra for: (b) ZIF-4, (c) ZIF-7 and (d) ZIF-8. An empirical 10 cm^{-1} FWHM Lorentzian line shape was applied to the DFT spectra to aid in comparison to FIR data.

framework. The THz modes of most considerable interest are the ones associated with framework shearing (zeolite-like cage distortion), pore breathing and gate-opening effects, and soft modes [173]. Detailed information on the lattice dynamics was determined from DFT to elucidate the core physical phenomena responsible for some exceptionally promising applications of ZIFs, as exemplified below.

5.2.1 Low-Energy THz Vibrations of ZIF-4

In the case of ZIF-4, two particularly interesting, low-frequency lattice vibrational motions were pinpointed (Figure 5.4). The first at ~0.2 THz (7 cm^{-1}) is a soft mode, which suggests the possibility of a phase transition instigated through shearing of the 4-membered ring (4MR). The distorted framework appears to be uniaxially stretched in the direction normal to the 4MR aperture, resulting in a higher accessible pore volume.

(a) Soft mode at ~0.2 THz

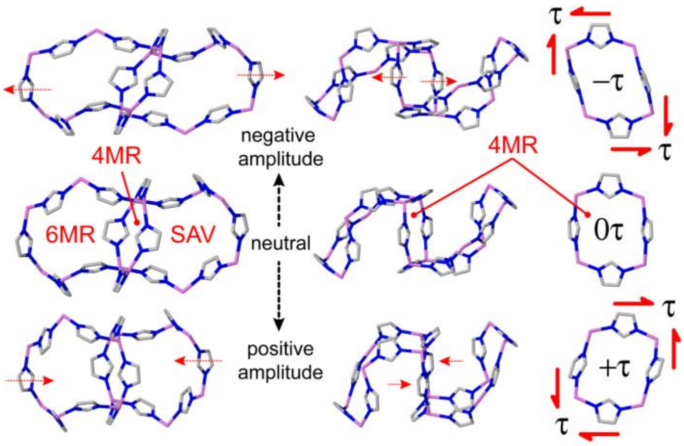

(b) Gate-opening mechanism at ~1 THz

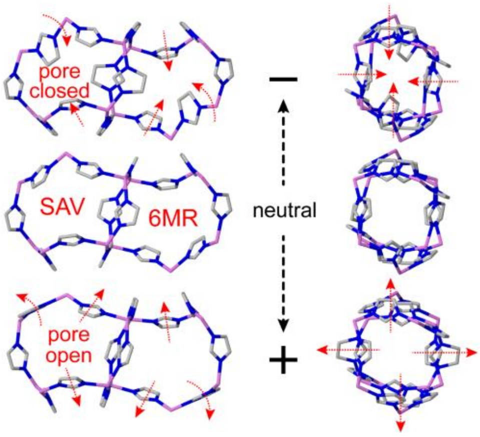

Figure 5.4. Low-energy THz vibrations of ZIF-4 viewed normal to the 4MR and 6MR orientations. (a) Soft mode facilitated by lattice distortion from shearing of the 4MR, where negative shear stresses (-τ) generate an elongated 6MR. (b) Gate-opening mechanism, red arrows designate collective dynamics affecting pore cavity.

This mechanism, in conjunction with the gate-opening mode at ~1 THz could explain the anomalous gas adsorption isotherms reported in the literature,[67] which hinted a significant phase alteration under pressure (~35 kPa) that substantially raised the N_2 uptake capacity.

5.2.2 Framework Breathing and Structural Phase-Change of ZIF-7

For ZIF-7, notably, a low-frequency mode at 0.65 THz (21.8 cm^{-1}) was identified (Figure 5.5a), which is identical to the distorted structure observed in the phase transition of ZIF-7 to ZIF-7-II [174] due to solvent removal from pore cavities. These cavities

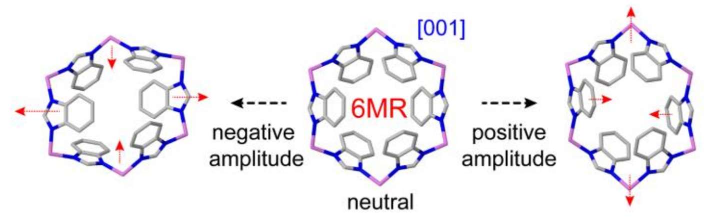

(a) Soft mode at 0.652 THz

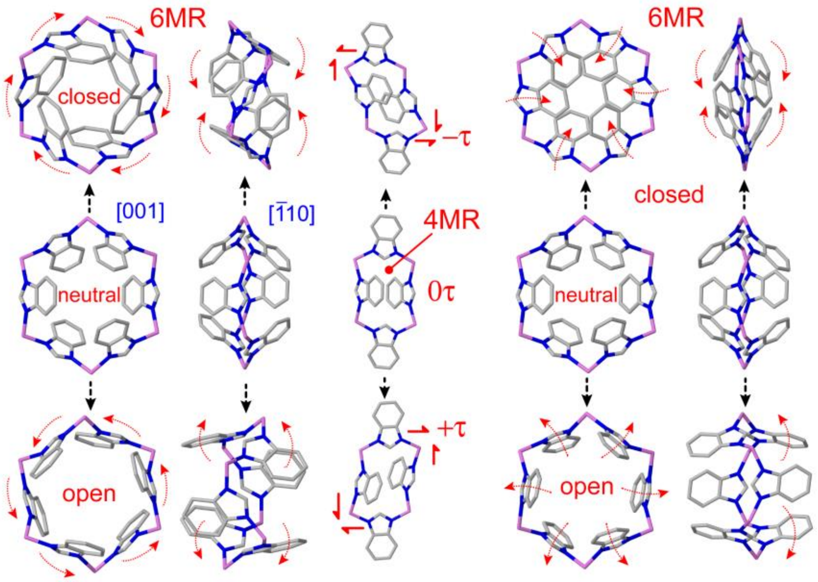

(b) Breathing & shearing at 0.654 THz (c) Breathing at 1.47 THz

Figure 5.5. Low-energy lattice dynamics in ZIF-7. (a) Soft mode matching the experimentally determined phase transition.[174] (b) Breathing mode accommodated by collective 6MR spiral screw motion and 4MR shearing. (c) Breathing mode *via* synchronous flapping of organic linkages. Shear induced framework deformations are denoted by τ.

comprise of benzimidazolate (bIm) ligands coordinated by six Zn atoms, forming 6-membered rings (6MR). Such a deformation mechanism elucidates phase transitions triggered by tilting of the ZnN$_4$ tetrahedral units. This result is significant since benzimidazolate linkers strongly influence the structural flexibility of ZIF-7,[86] thus controlling the CO$_2$ adsorption affinity. To this end, an improved understanding of the lattice dynamics could have a positive impact on enhancing gas sequestration potentials in MOFs. Moreover, at least four distinctive modes associated with gate-opening and breathing motions were discovered, located at 0.654, 1.47, 2.01 and 4.61 THz. Two interesting examples are illustrated in Figure 5.5b, c. The first is propagated by the shear deformation of the 4MR resulting in a twisting spiral motion of bIm functional groups; the second is a conventional gate-opening mechanism *via* synchronous flapping (wagging) of bIm linkers.

5.2.3 Gate-Opening Mechanism and Phase-Change of ZIF-8

Turning finally to ZIF-8, a soft mode at 0.57 THz (18.9 cm^{-1}) was discovered (Figure 5.6a), this low-frequency vibration could explain the phase transition observed when ZIF-8 is subjected to high pressure.[175] The deformed framework shows shear distortion to the geometry of the sodalite cage resembling that of the ZIF-7-II phase [174] discussed above; both of which exhibit the elongated 6MR configuration. This result

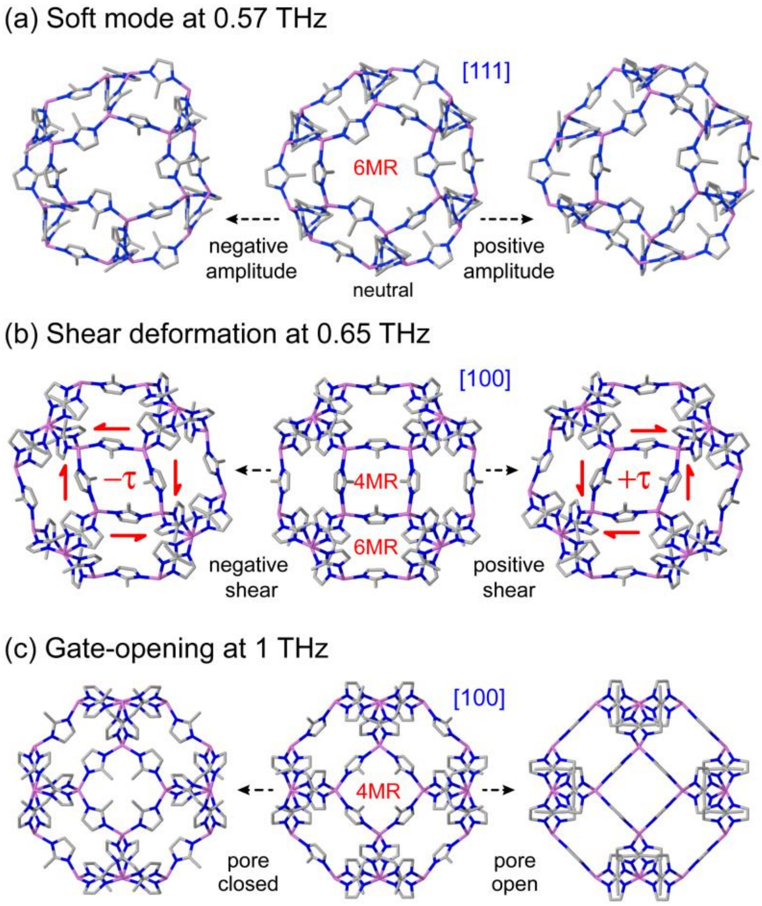

Figure 5.6. Low-energy lattice dynamics in a sodalite cage of ZIF-8. (a) Soft mode mechanism causing geometrical distortion of the 6MR. (b) Shear deformation of the 4MR. (c) Gate opening mechanism of pore apertures.

suggests that such a guest-induced structural instability may be a standard feature of ZIFs with sodalite topology. Crucially at 0.65 THz, another intense topological shear-induced deformation of the 4MR was identified (Figure 5.6b).

There are similar shear dynamics in ZIF-4 (Figure 5.4a) and ZIF-7 (Figure 5.5b), all of which amorphise *via* ball-milling [176]. Therefore, it is postulated that the stress-induced amorphisation of ZIFs can be triggered by shearing of 4MRs, which are intrinsically unstable under shear forces due to the 4-noded rectangular configuration being susceptible to collapse. This builds on the claims made in Chapter 4 regarding the minimum shear moduli of ZIFs. A gate-opening mode at 1 THz (33.4 cm^{-1}) was further identified (Figure 5.6c), explaining why such a lattice motion can facilitate the process of gas adsorption. This mechanism is, in part, due to the conformational changes involving all the 2-methylimidazole (mIm) ligands twisting coherently, raising the pore volume and opening the pore apertures. Remarkably, the ‘open’ sodalite cage at 1 THz is indeed identical to the X-ray proven crystallographic structure.[175]

5.3 Linking the THz Vibration with Elasticity in HKUST-1

In this section, Raman and synchrotron far-infrared (FIR) spectroscopy were used in combination with DFT to pinpoint and elucidate low-energy vibrational modes and associated deformation mechanisms detected in HKUST-1 (Figure 5.7), the Cu-based MOF discussed in Chapter 4. Advancing on the previous work relating to ZIFs, this section makes a connection between the behaviour of the THz vibrational dynamics and the elastic anisotropy discussed in Chapter 4. Therefore, providing additional understanding of basic core mechanisms of MOFs.

5.3.1 Vibrational Motions Present in HKUST-1

The vibrational modes located in the mid-infrared (MIR) region are again due to the typical vibrational motions of any system containing organic moieties. These motions are well characterised and understood and are primarily the result of bond stretching and bending. However, as mentioned in the previous section, the low-energy vibrations located in the FIR region are not as trivial to explain as they involve the collective motion of the framework (lattice vibrations).[156] In HKUST-1, particularly interesting lattice vibrations were detected in the spectral region under 600 cm^{-1} (< 18 THz). These vibrational modes involve contributions varying from Cu-paddle-wheel deformations, indicative of possible molecular rotor potentials,[177] to organic linker movements which could explain the phenomenon of negative thermal expansion (NTE) experimentally confirmed in HKUST-1.[178]

The experimental and theoretical IR-active and Raman-active vibrational motions have been identified in the region under 18 THz. As can be seen from Figure 5.8, the agreement is good for both IR and Raman spectra. To be consistent with the elasticity

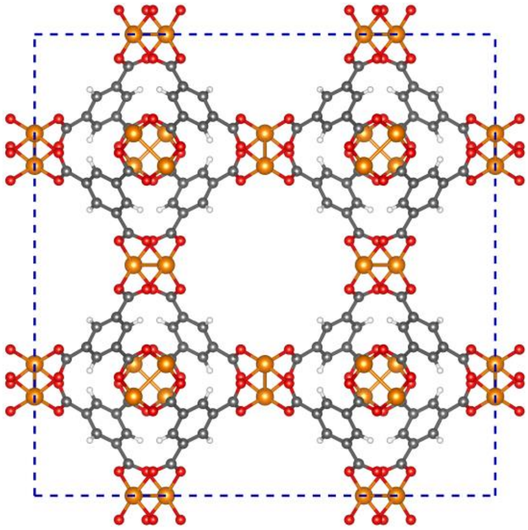

Figure 5.7. Crystal structure of cubic HKUST-1 looking down the symmetric <100> crystallographic axis. Colour code used: copper orange; carbon grey; oxygen red; hydrogen white.

results for HKUST-1 reported in Chapter 4, the theoretical vibrational spectra were calculated using DFT, with the B3LYP-D* functional. Due to the high cubic symmetry present in HKUST-1, there are not that many unique vibrational modes in this critical region, specifically 12 and 25 unique IR and Raman active motions respectively are located under 600 cm^{-1}. It is worth mentioning, however, that many of the modes are triply degenerate, due to the symmetry of the framework. There are also 44 unique non-optically active vibrational motions in the same spectral region. In the next section, all the IR and Raman active modes are summarised, and some of the non-optically active modes that are of significant interest to the framework elastic properties and its anisotropy are highlighted.

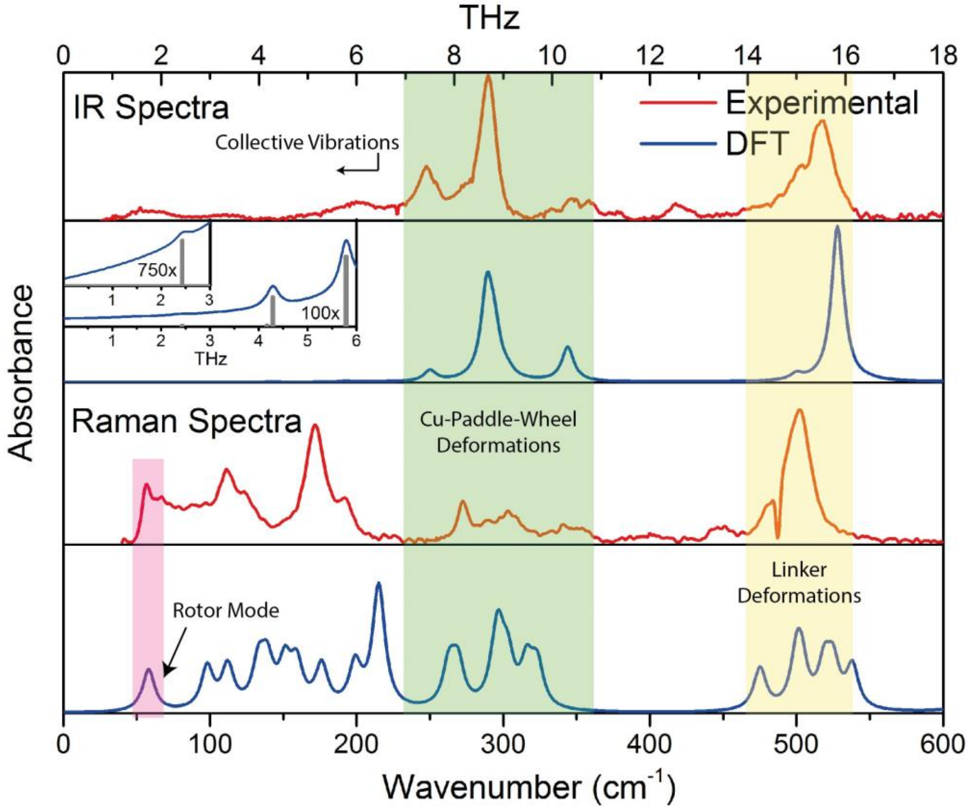

Figure 5.8. Comparison of the experimental and theoretical FIR and Raman spectra in the 0–600 cm^{-1} (0–18 THz) region. An empirical 10 cm^{-1} FWHM Lorentzian line shape was applied to the DFT spectra to aid in comparison with the experimental data and a bar representation is present for the low intensity IR region below 6 THz.

5.3.2 Distinct Regions of THz Vibrational Modes of HKUST-1

Altogether HKUST-1 has 81 unique vibrational motions located below 600 cm^{-1}; summarised in Appendix A5.8. The majority are due to the deformational movements of either the organic linker moieties or the inorganic Cu-centric paddle wheel units and can be grouped into distinctive spectral regions with many interesting motions located in the low-energy region under 100 cm^{-1}. Precisely, the vibrational modes can be characterised into the following regions, working from the higher energy modes downwards:

- Above 530 cm^{-1} (> 16 THz) are Cu–O stretching motions;
- Modes lying within 400–530 cm^{-1} (12–16 THz) are in-plane and out-of-plane aromatic ring deformations;
- Modes located at 100–400 cm^{-1} (3–12 THz) involve various combinations of ‘paddle-wheel’ deformations and linker rotational motions. These oscillatory deformations consist of Cu–O stretching, O–Cu–O bending, and an interesting Cu–Cu buckling motion similar to vibrational buckling motions in small organic molecules.[150] Another interesting observation in this region are modes where the symmetry of the displacements results in a swelling or ‘breathing’ appearance of the Cu-based paddle-wheel unit. These motions are all Raman-active and located around 3.4 and 6.4 THz, (112, 214 and 215 cm^{-1}), with the lowest energy example exhibiting the strongest structural deformation effect;
- Modes under 100 cm^{-1} (< 3 THz) are associated with collective framework vibrations, including ‘trampoline-like’ motions, paddle-wheel rotors, and symmetric collective motions that could explain the source of anomalous mechanical behaviour.

5.3.3 Noteworthy Collective Vibrations

Eight unique collective vibrations of significant interest have been discovered, each originating from three specific classes of motion (Table 5.2). The first interesting motion can be described as a 'trampoline-like' deformation and is depicted in Figure 5.9. Four vibrational modes demonstrate this motion, located at 58, 81, 94 and 98 cm^{-1} (from 1.7 to 3 THz) corresponding to the Raman, IR, non-optically active, and Raman-active modes, respectively. The IR and non-active motions involve simply the movement of the organic linker in a trampoline-like fashion. However, the Raman-active modes are more distinct due to the symmetry of the mode located at 98 cm^{-1}, resulting in a breathing effect of the organic-inorganic cluster. In addition, the lower-energy Raman active mode at 58 cm^{-1} also shows the second class of motion, involving a rotation of the paddle-wheel unit simultaneously. This particular combination of motions is analogous to modes that

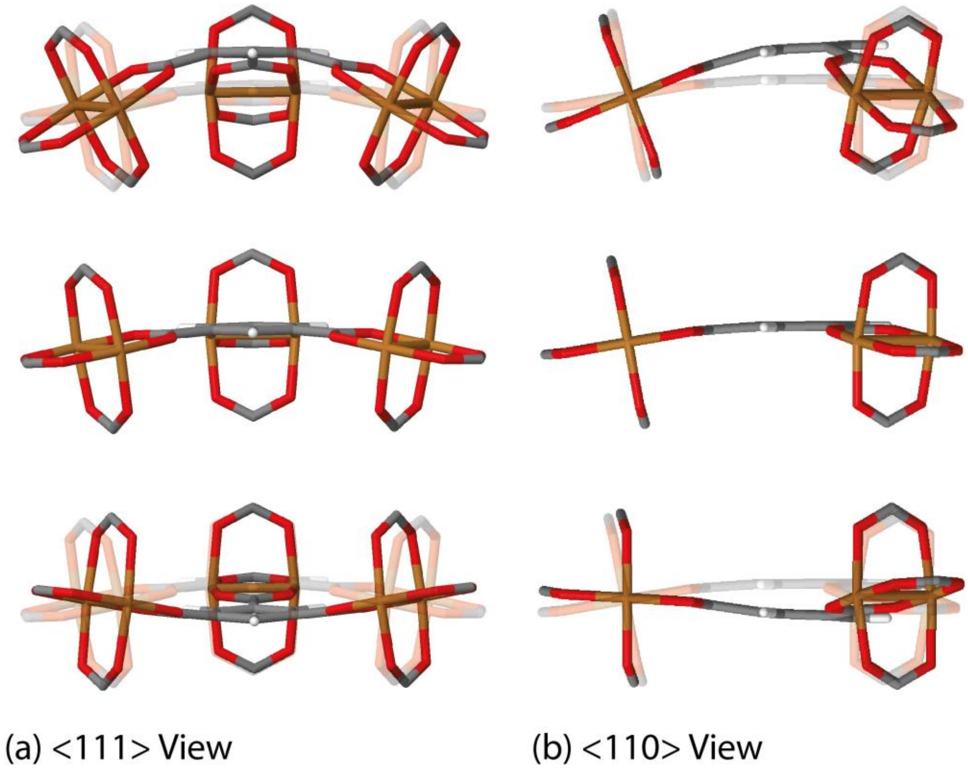

Figure 5.9. Low-energy collective vibration, located at 81 cm^{-1} (2.4 THz), viewed down the (a) <111> and (b) <110> directions, showing a trampoline-like motion linked to negative thermal expansion (NTE).

have been suggested experimentally to drive negative thermal expansion (NTE).[178] The previous work showed thermal ellipsoids suggesting the trampoline-like motion at a temperature range of 100–404 K and also proposed that the liberation of the aromatic rings and twisting of the paddle-wheel unit contribute to the expansion upon thermal stimulus.[178] All of these low-energy deformations have been demonstrated in full, with the indication that NTE can be driven by a combination of THz vibrational motions. Such NTE phenomenon is possibly also linked to the other non-active modes (located at 16, 20, 63 and 78 cm^{-1}), showing translational and rotating motions of the organic linker and Cu-based paddle-wheel, which are all located in the low-energy (THz) region (Table 5.2). It is also worth noting that similar motions have been suggested to be the source of NTE in other less complex MOF materials, such as the cubic framework material, MOF-5.[54]

Table 5.2. Notable collective vibrational modes of HKUST-1.

Mode		Activity	IRREP*	Description
(cm^{-1})	(THz)			
16.32	0.49	Non	F_{2u}	Strong Paddle Wheel Deformation and Translational Motion (Symmetric Cluster Rotation)
20.43	0.61	Non	E_u	Strong Paddle Wheel Deformation and Translational Motion
58.07	1.74	Raman	F_{2g}	Strong Paddle Wheel Rotation with Organic Linker Trampoline-like Motion
63.17	1.89	Non	F_{2u}	Paddle Wheel Deformation and Translational Motion with Organic Linker Rotating
78.28	2.35	Non	B_g	Paddle Wheel Deformation with Organic Linker Rotating (Symmetric Cluster Rocking)
81.47	2.44	IR	F_{1u}	Organic Linker Trampoline-like Motion
94.15	2.82	Non	B_u	Organic Linker Trampoline-like Motion
98.41	2.95	Raman	A_g	Organic Linker Trampoline-like Motion (Symmetric Cluster Breathing)

*IRREP = Irreducible representation; Non = non-optically active mode

The second intriguing class of collective dynamics already mentioned above is the strong paddle-wheel rotor (Figure 5.10) shown to be linked to the Raman-active mode at 58 cm^{-1} (1.7 THz). This particular motion is of high interest as it could suggest the possibility of utilising the mechanism for potential 'molecular' rotor applications.[179] This is a topical area of research with some examples in MOFs starting to appear.[177, 180-182] However, most work done on MOFs has concentrated on the use of the organic linkers, which is dissimilar from the rotation attributed to the metal-containing units, such as the rotor dynamics identified here regarding the paddle-wheel of HKUST-1.

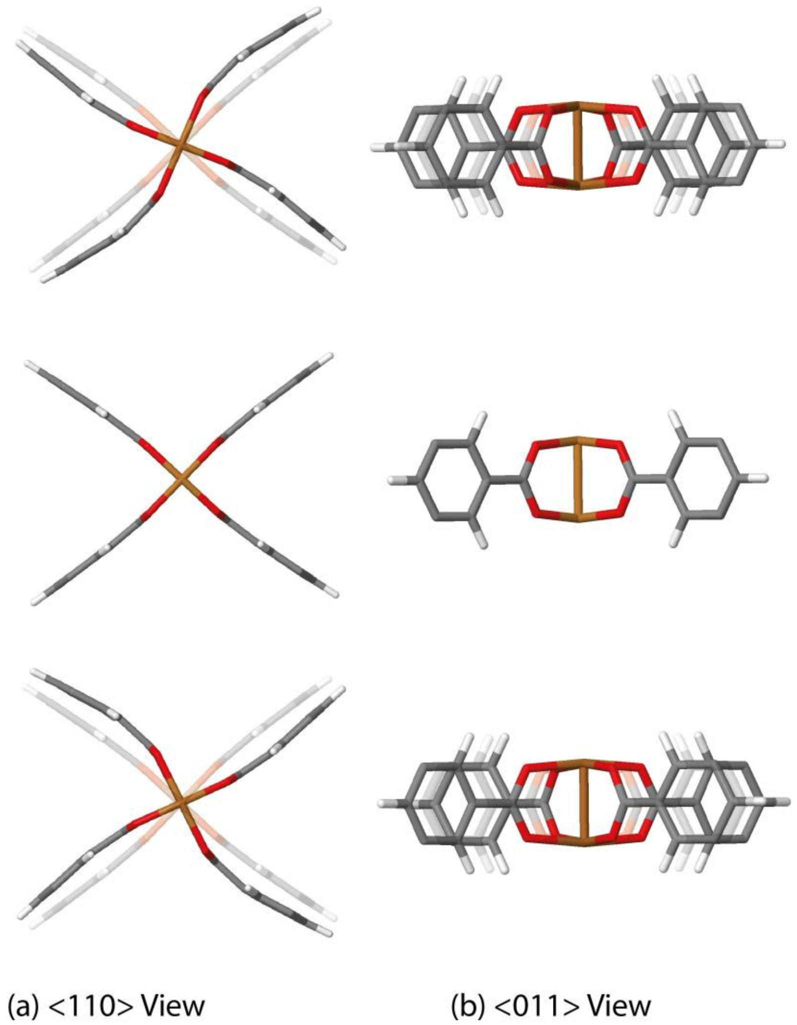

Figure 5.10. Low-energy collective vibration, located at 58 cm^{-1} (1.7 THz), viewed down the (a) <110> and (b) <011> directions, showing a rotor motion of the Cu-based paddle-wheel moiety.

The last significant vibrational mode revealed in this section is a motion that fully involves the collective framework and the organic-inorganic clusters (Figure 5.11), briefly mentioned when discussing the Raman-active mode at 98 cm^{-1} (~3 THz). There are other modes in HKUST-1 whose dynamics are reminiscent of this motion, although they are due to the symmetry of the mode resulting in the effect of synchronous cluster dynamics. Examples, other than the Raman-active mode discussed, include a non-active cluster rocking motion located at 78 cm^{-1} (2.3 THz), accompanied by another non-active

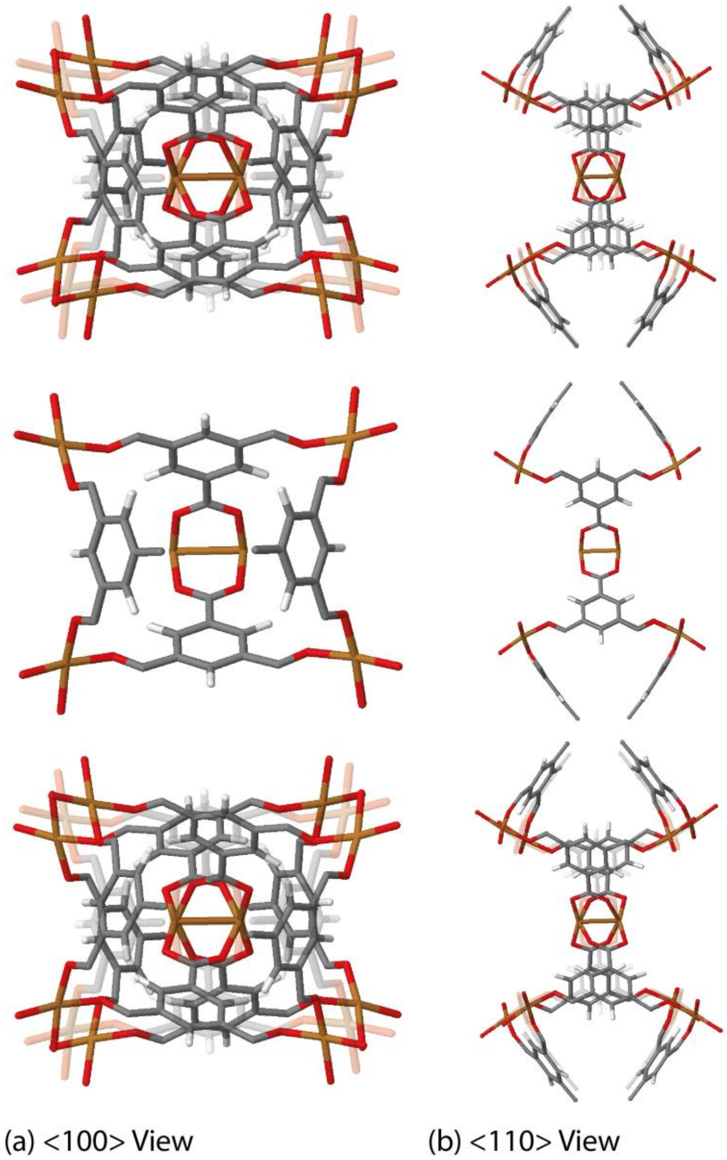

Figure 5.11. Low-energy collective vibration, located at 16 cm^{-1} (0.5 THz), viewed down the (a) <100> and (b) <110> directions, showing a cluster rotation mechanism, linked to auxeticity.

higher energy cluster rocking motion at 138 cm^{-1} (~4 THz). However, the most interesting cluster-linked motion is the non-active mode at 16 cm^{-1}, which is the lowest energy vibrational mode of HKUST-1 found at ~0.5 THz. This motion involves a combination of rocking and translational dynamics resulting in the rotation of the linker-paddle-wheel 4-noded cluster. The rotational movement of the cluster could reveal the nature of the mechanism behind anomalous elastic behaviour present in the material. Specifically, the directional auxetic response (negative Poisson's ratio), discussed in Chapter 4.

5.4 THz Vibrations of the Monoclinic Structure MIL-140A

This section reports the low-energy THz dynamics present in one of the Zr-based MOFs discussed in Chapter 4, namely MIL-140A,[147] whose chemical structure is shown in Figure 5.12. Inelastic neutron scattering (INS) (Figure 5.13) and synchrotron FIR and Raman spectroscopy (Figure 5.14) were used, in conjunction with DFT calculations to gain a complete insight into the complicated cooperative framework dynamics. The results provide the unique opportunity to confirm three interesting physical phenomena predicted by DFT calculations, specifically at under 3 THz (< 100 cm^{-1}): (i) hindered rotational dynamics, (ii) cooperative trampoline-like motions, and (iii) coordinated shearing dynamics.

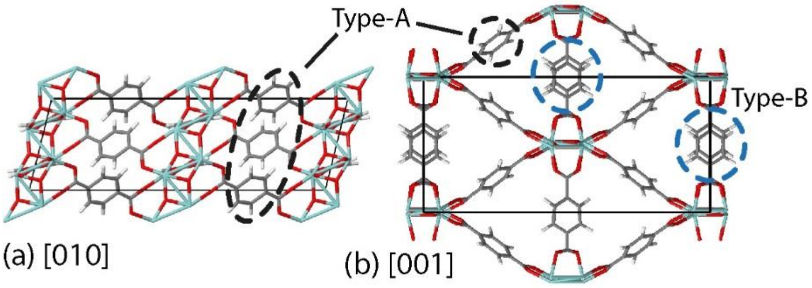

Figure 5.12. Framework structure of MIL-140A [ZrO(BDC); BDC = O_2C-C_6H_4-CO_2] looking down the crystallographic (a) *b*-axis and (b) *c*-axis. The inorganic building units are ZrO_6 coordination polyhedra, forming 1D chains along the *c*-axis. The black line represents one unit cell. Colour code used: zirconium light blue; carbon grey; oxygen red; hydrogen white. Circles denote Type-A and Type-B organic linkers.

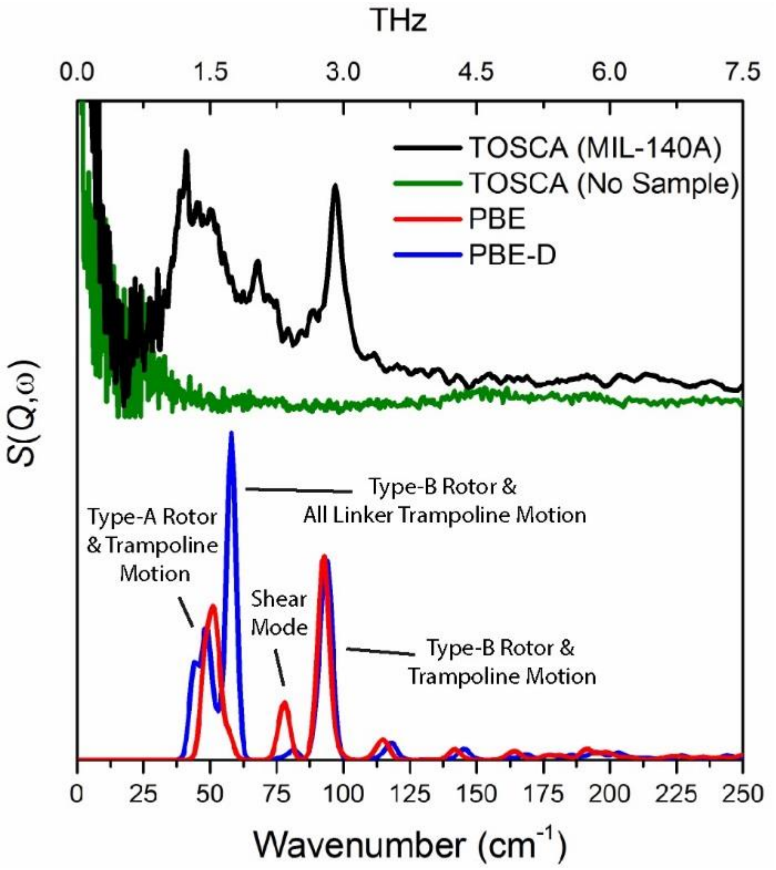

Figure 5.13. Comparison of the experimental (black and green) and theoretical INS spectra (red: PBE; blue: PBE-D) in the region of 0–250 cm^{-1}, measured at 5 K. Note that 1 THz ≈ 33.3 cm^{-1}. The experimental spectra excluding the MIL-140A sample (green trace) is included to confirm that the detected peaks are resulting from the framework vibrations of MIL-140A.

5.4.1 Aromatic Ring Rotations – Type-A and Type-B

Figure 5.15 presents THz vibrations associated with the hindered rotor motions involving the BDC organic linkers (1,4-benzenedicarboxylate), specifically the C_6H_4 aromatic rings demonstrating out-of-plane torsional dynamics. Interestingly, no specific mode involves the simultaneous motion of all phenyl rings. Therefore, each rotational motion can be classified as Type-A or Type-B: depending on whether the linkers involved are the ones supporting the 4-node architecture of the framework (Type-A), or the linker in the middle reinforcing the 4-node unit (Type-B), as highlighted in Figure 5.12.

Four modes encompassing rotor-like dynamics were discovered for MIL-140A. These modes are mainly Raman-active, except the IR-active asymmetric Type-B rotor-like vibrational motion located at 1.74 THz (58.1 cm^{-1}), which shows a simultaneous trampoline-like motion (discussed in section 5.4.2). The other vibrations exhibiting the rotational motion are two modes: pinpointed at 1.34 and 1.48 THz (44.7 and 49.2 cm^{-1}), involving the asymmetric and symmetric Type-A rotor-like motions, respectively. Moreover, a higher energy mode at 2.82 THz (94.2 cm^{-1}) was also identified, exhibiting the symmetric Type-B rotations.

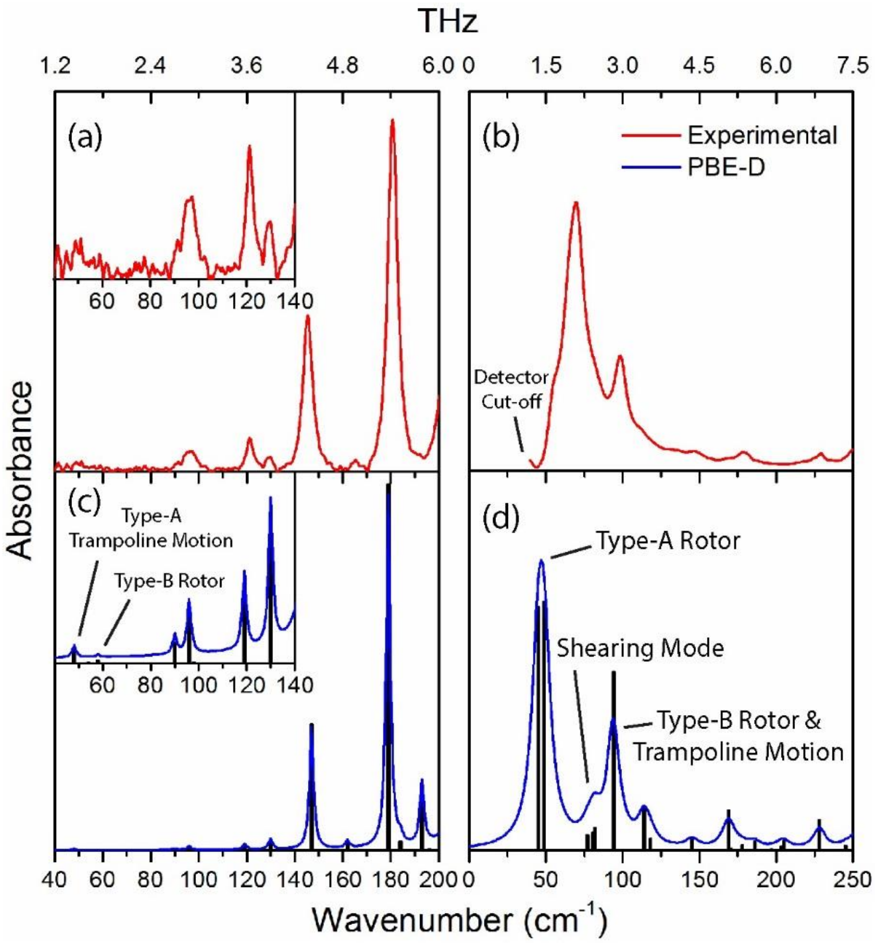

Figure 5.14. (a and c) Synchrotron radiation FIR and (b and d) offline Raman spectra in the region of 40–200 and 0–250 cm^{-1} respectively. Comparison of experimental (red) and theoretical spectra (blue and black) for MIL-140A. The blue theoretical spectra have a full-width-half-maximum (FWHM) Lorentzian line fit applied to aid in comparison with the experimental data (2 cm^{-1} for FIR and 5 cm^{-1} for Raman). For the Raman spectra, it is noted that a discrepancy near the detector cut-off of ~20 cm^{-1} is within the limit of such offline measurements.

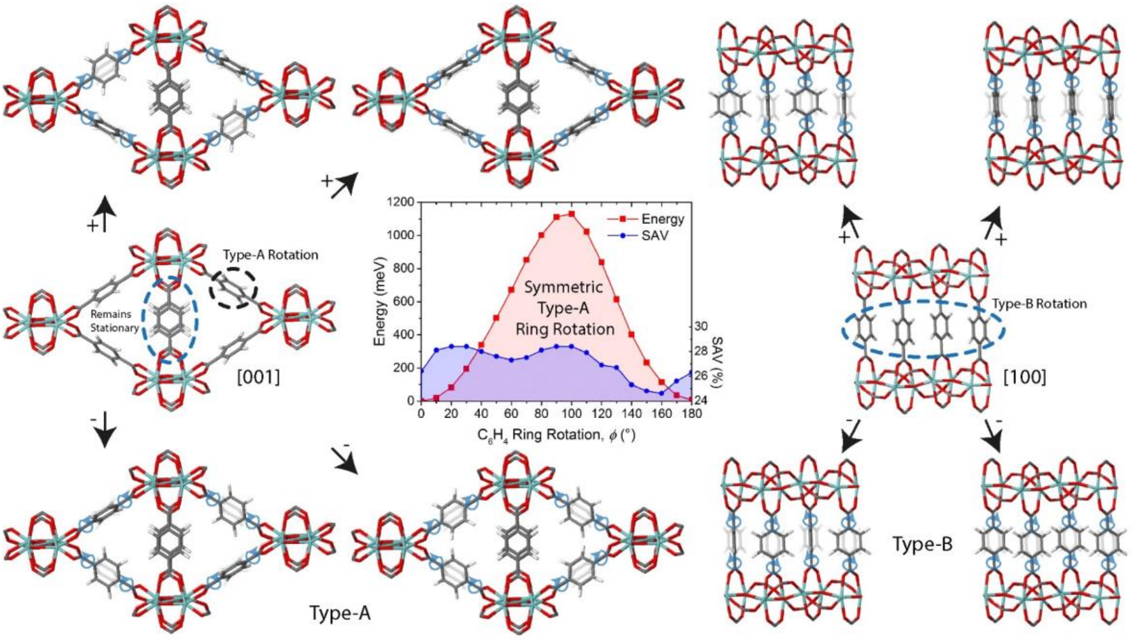

(a) Asymmetric - 1.34 THz (b) Symmetric - 1.48 THz (c) Asymmetric - 1.74 THz (d) Symmetric - 2.82 THz

Figure 5.15. Rotational dynamics of MIL-140A determined from DFT calculations, in accordance with experimental observations (Figure 5.13 and 5.14). (a) Asymmetric and (b) symmetric Type-A rotor-like motions along with (inset) the energy barrier and change in SAV for the 180° ring rotations during the symmetric Type-A motion. (c) Asymmetric and (d) symmetric Type-B rotor-like motions. Blue circular arrowheads are used to mark the rotational directions.

Of additional interest are the energy barriers to full phenyl rotation and the modification of the solvent accessible volume (SAV: quantifies accessible voids in the framework, calculated *via* PLATON)[154] at each degree of rotation. Single-point energies were calculated using DFT with the PBE-D* functional, for the full 180° twist (ϕ) for both the symmetric Type-A and Type-B rotors. The energy barriers reported in Figure 5.15 (inset) represent the simultaneous rotation of all Type-A phenyl rings of the unit cell, containing four rings. The barrier for the Type-A rotation is approximately 1,130 meV, hence ~283 meV per aromatic ring. This is significantly lower than the ~537 meV value reported for MOF-5 [64] (Ref. [64] rotated just one of the six phenyl rings present in the primitive cell).

The modification of the SAV on the full Type-A rotation was studied, demonstrating a 2% increase from 26.4% at equilibrium (ϕ = 0° and 180°) to 28.4% at

20–30° and 90–100° (Figure 5.15 inset). There is also a decrease to a minimum SAV of 24.6% at 160°. The varying level of SAV for the Type-A rotation can be directly linked to the changing morphology of the pore geometry (Figure 5.16); although this is not as straightforward as ‘gate-open’ or ‘gate-closed’ configurations (as discussed in section 5.2 for ZIFs).[156] Remarkably, the position of the rings resulting in the fully ‘gate-open’ geometry translates to the minimum SAV ($\phi_{\min}$ = 160°), as the pores are transformed into pure 1D channels oriented along the *c*-axis (Figure 5.16c).

Unlike the simultaneous Type-A rotations, the energy barrier and SAV for the Type-B rotation cannot be identified reliably, due to steric hindrance (caused by linkers overlapping). The full 180° rotation cannot be calculated, as the rings come into very close contact, as depicted in the negative amplitude of Figure 5.15d. The associated energies for the Type-B rotation can be seen in Appendix A5.12 for comparison.

5.4.2 Trampoline-like Vibrational Motions

The next type of motion of interest involves the organic linker moieties moving in a trampoline-like fashion (Figure 5.17). Such deformation mechanisms have been suggested to yield negative thermal expansion (NTE) detected in the simpler cubic MOF structures: HKUST-1 and MOF-5.[56, 178] Trampoline-like motions minimise the

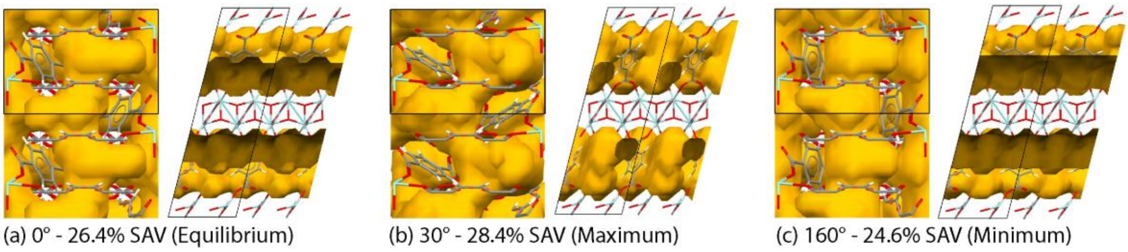

Figure 5.16. Modification of the SAV of the (a) equilibrium geometry, with the structures obtained when the Type-A aromatic rings are rotated symmetrically by (b) ϕ = 30°, resulting in an increased SAV, and (c) ϕ = 160°, resulting in a decreased SAV and formation of purely 1D pore channels along the *c*-axis.

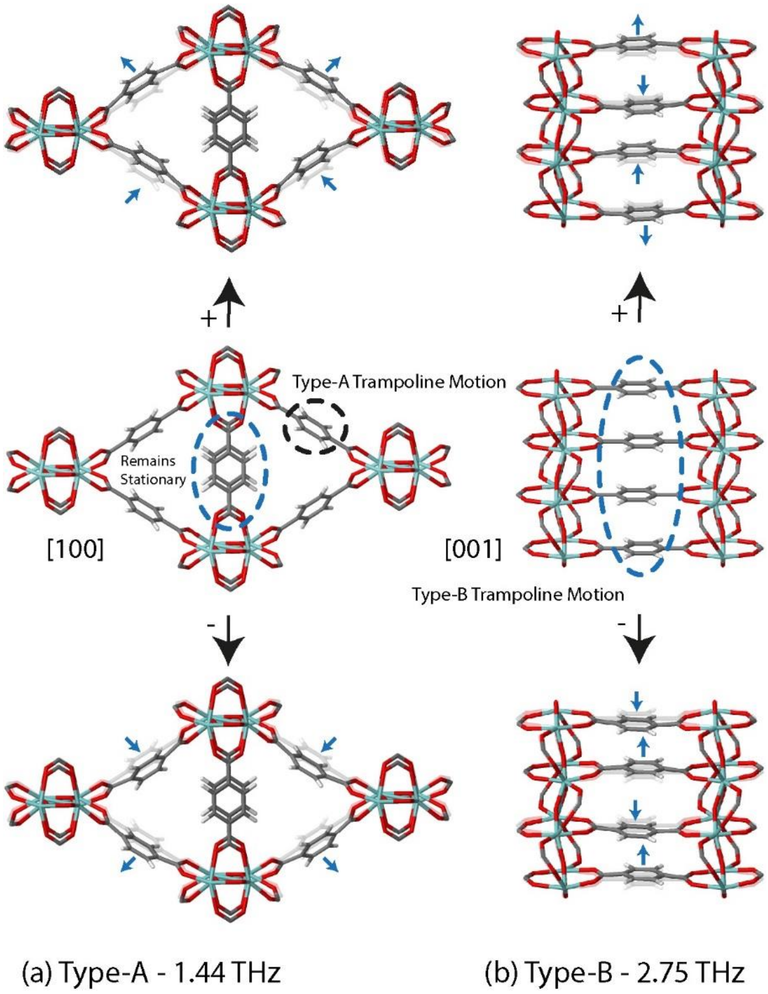

Figure 5.17. (a) Asymmetric Type-A and (b) asymmetric Type-B trampoline-like vibrational motions of MIL-140A.

deformation of the carboxylate and aromatic groups, involving translation of the phenyl rings in and out of the plane of the equilibrium position of the linker. Figures 5.13 and 5.14 show four such vibrational modes, discernible by the Type-A or Type-B linkers involved. As with the rotor-like motions, not all the vibrations encompass every linker group. However, unlike the rotor-like motions, there are in fact two unique modes exhibiting the trampoline movement of every linker, simultaneously. They are both IR-active and located at 1.44 THz (48.2 cm^{-1}) and 1.61 THz (53.6 cm^{-1}); differing only in the direction of the Type-B trampoline motion which is simultaneous to the Type-A motion (the positive and negative amplitudes of the Type-B linkers for the 1.44 THz motion (Appendix A5.14) are reversed in the mode located at 1.61 THz). The latter of the two modes, involving all the linker moieties, is of significantly reduced IR intensity (26 times lower than the other IR-active trampoline motions). The other trampoline-like motions consist of another IR-active mode at 1.44 THz (48.2 cm^{-1}), however only involving the Type-A linkers, and a Raman-active mode demonstrating the trampoline motion located at 2.75 THz (91.8 cm^{-1}), which involves exclusively Type-B linkers.

5.4.3 Coordinated Shear Dynamics

Finally, a Raman-active mode was observed at 2.47 THz (82.5 cm^{-1}), visible in the INS spectra (Figure 5.13), albeit shifted by ~10 cm^{-1}, which could point to the mechanism responsible for structural destabilisation *via* a coordinated shearing-type angular distortion in the <010> directions. Notably, this vibrational signature has been predicted *via* DFT to have a lower intensity than the other collective motions discussed, also evidenced in the experimental INS spectra (Figure 5.13). Of significant importance, it was established that this shear motion arises in the exact direction that was previously predicted in Chapter 4 to give the minimum value of shear modulus ($G_{\min}$= 3.2 GPa) for MIL-140A [39], substantiating the current observation. The origin of the minimum shear modulus is discussed in more detail in Chapter 4. Crucially, this is the first report demonstrating a direct experimental link to shear dynamics in a MOF structure. This is an important result because shear-type deformations have previously been speculated to be the mechanism behind the framework destabilisation of MOF systems, causing the loss of crystallinity *via* amorphisation.[23, 24, 183]

5.5 Chapter Summary

This chapter demonstrates that high-resolution inelastic neutron scattering (INS) and synchrotron infrared (IR) and Raman spectroscopy in combination with *ab initio* DFT calculations can open new opportunities to understanding the fundamental lattice dynamics of porous framework materials such as MOFs. The work shows, that collective vibrations and low-energy THz modes offer new insights into many possible unique physical mechanisms in ZIFs, including gate-opening and breathing phenomena, soft modes that suggest possible phase transitions, and the onset of shear-induced structural destabilisation. The results are promising as a selection of these physical phenomena have recently been observed experimentally, thus confirming the validity of the computational approach. The work on the vibrational modes of ZIFs presented the much-needed starting point to instigate further research into the detailed physics surrounding the low-frequency vibrations and soft modes of more complex hybrid framework materials and to link them to structural response properties such as the elasticity discussed in Chapter 4.

The section relating to the study of HKUST-1 made the explicit connection between the THz vibrational modes of the framework and some of the mechanical properties discussed in Chapter 4. Importantly, the vibrational calculations provided insights into significant vibrational modes including trampoline-like motions, paddle-wheel rotors, and soft modes linked to symmetric collective mechanisms, which could explain the origin of the auxeticity and negative thermal expansion (NTE) of HKUST-1 evidenced in specific crystallographic directions.[156, 173, 178] The findings highlight that many of the mechanical mechanisms responsible for the anomalous elasticity of MOF materials are yet to be fully understood.

The THz vibrations of MIL-140A revealed a multitude of rotor-like dynamics of linkers and associated ‘trampoline-like’ vibrational motions. The first validation of the existence of low-energy shear dynamics that may trigger the destabilisation of MOF crystals was achieved as the vibrational mode relating to the shearing motion was visible in the experimental spectra. The trampoline-like vibrational modes could be the source of NTE previously unreported for MIL-140A. Therefore, these new findings encourage more intense efforts to search for and unravel the nature and level of anisotropy originating from the structural response to thermal stimulus.

Chapter 6

Tracking the Thermal-Induced Amorphisation of ZIF-4

This chapter presents the first use of *in situ* far-infrared (FIR) spectroscopy to analyse the thermal amorphisation of a zeolitic imidazolate framework material (ZIF-4). The accurate temperature-controlled spectra were obtained *in situ* using a novel setup *via* a N_2 purged Linkam cell and a Hyperion 3000 microscope. The technique allowed for the nature of the individual vibrational motion changes during the amorphisation process to be explained and reveals new insights into the effect that temperature has on the Zn–N tetrahedra. The chapter also introduces a possible new thermal-shift coefficient that links the likelihood of amorphisation to the magnitude of a specific spectral shift.

6.1 Introduction

This chapter advances on the far-infrared (FIR) vibrational spectroscopy discussed in Chapter 5 by following the *in situ* thermal transformations of ZIF-4, which has the chemical composition $Zn(Im)_2$ (Im = imidazolate, $C_3H_3N_2^-$). The framework was selected as it has been shown to demonstrate significant flexibility regarding its phase transition ability.[60] It is known to amorphise to a structure called a-ZIF at approximately 573 K, which is separate from the solvent-induced collapse of ZIFs. The amorphous structure is reported to be a continuous random network analogous to that of amorphous silica (a-SiO_2).[60, 184] Upon further heating (above 673 K) a-ZIF recrystallises into the higher symmetry dense structure, ZIF-zni.[60] Dense ZIF-zni is the lower energy of the two crystalline structures[185] but only becomes thermally accessible above 673 K. ZIF-zni has an identical chemical composition to ZIF-4. However, their crystal symmetries, network topologies and geometrical parameters are remarkably different.[60, 186] ZIF-4 has also been reported to undergo a discontinuous porous to dense phase transition upon cooling to under 140 K, due to cooperative rotations of the organic linkers.[187] The temperature ranges of these phases are indicated in Figure 6.3 by ZIF-4 (LT/HT). For comparison, the thermal effects on the vibrational spectra of ZIF-8 (whose linker is mIm = 2-methylimidazolate), which does not amorphise thermally, were also investigated.[42] It is worth noting that these materials can also amorphise through other sources of external stimuli, such as pressure[188] and mechanical impact.[23] However, it has been suggested that the mechanisms for the various routes to amorphisation are different, with a shear instability being the likely cause of the mechanically induced amorphisation (Chapter 4).[25, 189] The thermal-induced amorphisation route of ZIFs is currently a phenomenon only witnessed for structures possessing the unsubstituted Im linker. The results in this chapter were used to postulate

Table 6.1. Nature of the IR-active modes in the 150–700 cm^{-1} region.

Structure	Spectral Region (cm^{-1})	Description of Vibrational Motion
ZIF-4	160–275	4-Membered and 6-Membered Ring Deformation; Ligand Rotation (Rocking); N–Zn–N Bending and Zn–N Stretching (Tetrahedral Deformation)
ZIF-zni	155–280	
ZIF-4	295–325	Zn–N Stretching (Belonging to ZnN_4 Tetrahedra)
ZIF-zni	290–330	
ZIF-4 and ZIF-zni	640–700	Aromatic Ring Deformation and Torsion Modes (In-Plane and Out-of-Plane)

a reason for this observation and propose a practical measure to quantify the structural flexibility determining the likelihood of temperature enabled amorphisation.

6.2 Specific Spectral Regions

As reported in Chapter 5, the low-energy vibrations of ZIF materials originate from three sources of vibrational motion located in the spectral region below 700 cm^{-1}:

i. Aromatic ring deformations
ii. ZnN_4 tetrahedra deformations
iii. Framework-specific collective motions

The results from Chapter 5 have been confirmed, demonstrating that the peaks relating to the ring deformations of the Im organic linkers in ZIF-4, a-ZIF and ZIF-zni are all present at approximately 640–700 $cm^{-1.}$ Also, the universally shared Zn–N bond stretching motion, specifically originating from the compliance of $Zn(Im)_4$ tetrahedra, is again positioned at 265–325-cm^{-1} as expected (Figure 6.2).[156]

6.3 Temperature Dependent Spectral Shift

Unsurprisingly there is no significant effect on the peaks relating to the organic linkers, as the structurally rigid Im linkers do not strain significantly upon heating, structural amorphisation, or recrystallisation into ZIF-zni. Changes to the peaks at approximately 323 cm^{-1} (assuming zero thermal effects, calculated *via* DFT) are however pronounced and include a temperature induced spectral shift due to the Zn–N stretching modes of the ZnN_4 tetrahedra deformation in $Zn(Im)_4$. These vibrational modes are expected to be sufficiently anharmonic to show a red shift because of the thermal stimulus (upon

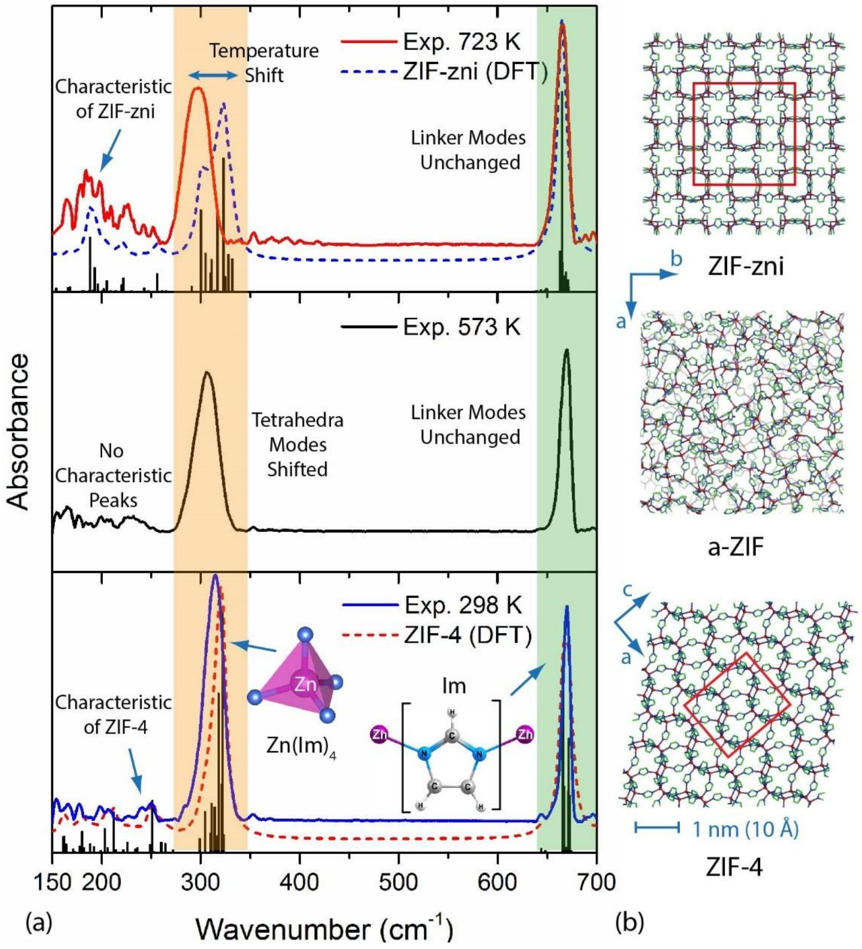

Figure 6.2. (a) FIR spectra in the region of 150–700 cm^{-1}, showing the spectral changes observed at 298, 573 and 723 K. The red and blue dotted lines are the theoretical ZIF-4 and ZIF-zni spectra obtained from DFT (comparable to 0 K). The modes relating to the Zn–N deformations of the $Zn(Im)_4$ tetrahedra and the deformations of the aromatic Im linkers are highlighted. (b) Framework structures adapted from Ref. [60] of ZIF-4, a-ZIF and ZIF-zni are shown for clarity, with the unit cells of the two crystalline phases highlighted in red.

heating) allowing for increased flexibility in the deformation of the $Zn(Im)_4$ tetrahedra. Due to these modes being independent of the specific framework, yet still the result of a cluster-like moiety, they could be considered as quasi-delocalised and obey a Bose-Einstein distribution.[190, 191] The exact nature of the phenomenon would require further investigation. However, the frequency shift (Figure 6.3) does appear to correlate with the following equation, based on Bose-Einstein statistics:

$$v(T) = v_0 - \frac{X_R T_C}{e^{\frac{T_C}{T}} - 1} \tag{6.1}$$

$$T_C = \frac{h v_0}{k_B} \tag{6.2}$$

where v_0 is the frequency of the mode at zero temperature (calculated *via* DFT); T is the absolute temperature that the experimental spectra were obtained at; T_C is the vibrational temperature, related to the energy of the particular mode, obtained from statistical thermodynamics *via* the use of the Planck constant (h) and the Boltzmann constant (k_B); and a curve fitting variable, X_R , which could be described as a thermally-induced spectral shift coefficient, as it is speculated that the value is linked to the specific M–X polyhedral deformation, present in the distinct polyhedral environment. It is possible that the value of X_R could be dependent on both the type of metal and importantly the linker involved. The current work gives the value of X_R to be 0.045 cm^{-1} K^{-1} ($R^2 = 0.970$) for the $Zn(Im)_4$ tetrahedral deformations in ZIF-4. An increase in the gradient of the data points beyond the curve fitted for ZIF-4 is also observed. This is due to the presence of the amorphous a-ZIF structure and is confirmed by the decrease in gradient at higher temperature due to the energetically more stable ZIF-zni phase. If the value of X_R is essentially an indication

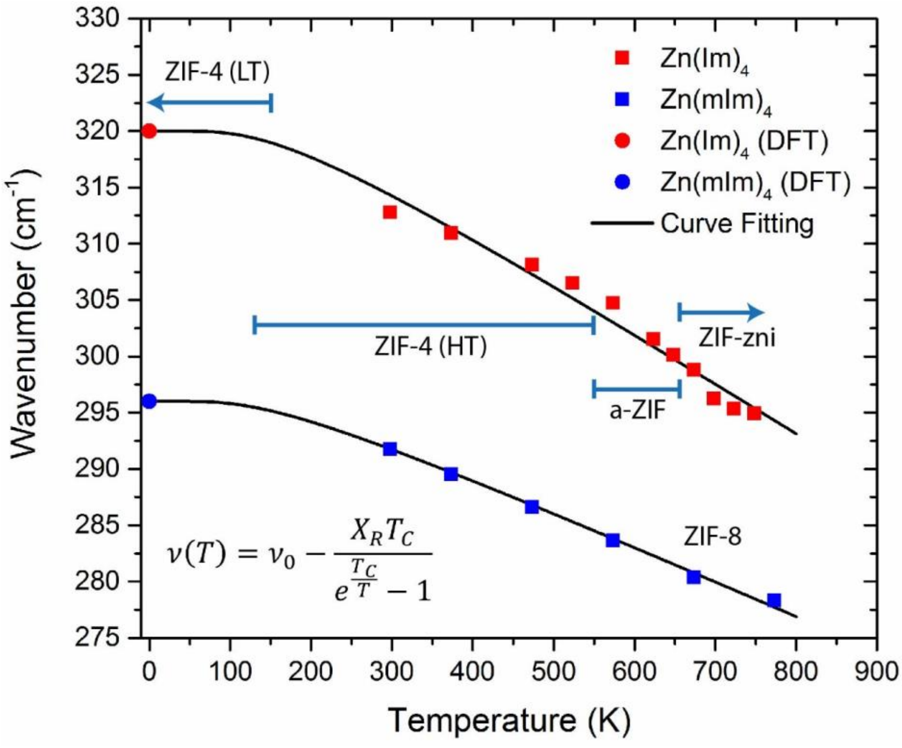

Figure 6.3. Temperature dependence of the $Zn(Im)_4$ and $Zn(mIm)_4$ tetrahedra deformation modes, hence explaining the disparity between the theoretical ZIF-zni spectra and the experimental spectra obtained at 723 K. The thermal range of each structure has been highlighted for clarity.

of how flexible the M–X polyhedral environment is under thermal stimuli, prior to amorphisation, then it could be postulated that MOF structures that demonstrate a higher value of X_R could be more susceptible to thermal-induced amorphisation, as a more flexible M–X polyhedral environment would increase the probability of framework amorphisation. In the case of ZIF materials, this would be the unsubstituted $Zn(Im)_4$ containing frameworks, which all show thermal-induced amorphisation. To support this hypothesis, the value of X_R for ZIF-8, which is well accepted not to amorphise thermally was also investigated.[42] Importantly, the linker is different, mIm, so another value of X_R could be provided, this time applied to $Zn(mIm)_4$ tetrahedral deformations. The resultant value for ZIF-8 is 0.032 cm^{-1} K^{-1} ($R^2 = 0.995$), hence supporting the hypothesis that a lower value of X_R could imply an increased thermal stability to amorphisation. This is possibly due to the increased steric contribution from the substituted linkers, translating into a more rigid M–X polyhedra. This is of course still a postulation, and the numerical evidence is limited. However, the increased flexibility of the polyhedral motion can be linked to the structural stability. Therefore, the work shows that the polyhedral deformation (flexibility) upon thermal stimulus can be precisely monitored using *in situ* FIR synchrotron spectroscopy.

6.4 Comparison of Crystalline Phases

Moving on to the distinction between the two crystalline structures, the final modes observed are the collective vibrational motions that are specific to the framework structure and symmetry. These modes are located in the region of 155–280 cm^{-1} (Figure 6.2) and are all due to specific motions involving the 4-membered and 6-membered ring deformations, simultaneously coupled with ligand rocking.[156] Due to the differences in crystal packing and symmetry between ZIF-4 and ZIF-zni the intensities of the peaks in this region are distinct to each framework. For example, in

Table 6.2. Mechanical properties of ZIF-4 and ZIF-zni, derived from the elastic constants calculated by DFT using the B3LYP functional. Young's and shear moduli anisotropy are $A_E = E_{\max}/E_{\min}$ and $A_G = G_{\max}/G_{\min}$, respectively.

Elastic property		ZIF-4†	ZIF-zni
Young's modulus (GPa)	$E_{\max}$	3.3	10.2
	$E_{\min}$	2.2	6.8
	A_E	1.5	1.5
Shear modulus (GPa)	$G_{\max}$	1.5	3.3
	$G_{\min}$	0.8	2.3
	A_G	2.0	1.4
Linear compressibility (TPa^{-1})	$\beta_{\max}$	241.2	29.5
	$\beta_{\min}$	202.1	5.2
Poisson's ratio	$\nu_{\max}$	0.41	0.49
	$\nu_{\min}$	0.06	0.32

†The values for ZIF-4 are from Chapter 4.

ZIF-4 a broader distribution of modes is observed due to the lower symmetry of the framework, with the highest in intensity located at approximately 250 cm^{-1}. In ZIF-zni, there are more degenerate modes, and therefore there is a significant intensity at approximately 195 cm^{-1}. This region shows less prominent features at 573 K, as the amorphous nature of the framework will negate any structural symmetry and result in such motions being so widely (randomly) distributed that no identifiable characteristic intensities are observed. It is worth noting that this region does not include the low-energy THz modes, reported in Chapter 5, involving phase-change and gate-opening motions.[156] This spectral region (0–100 cm^{-1}) was out with the scope of the current experimental setup.

6.5 Mechanical Properties of ZIF-zni

For completeness, the mechanical properties of ZIF-zni (Table 6.2) were also analysed, for comparison to the previous elasticity work on the other Im containing ZIFs (ZIF-1, ZIF-2, ZIF-3 and ZIF-4) in Section 4.4 of Chapter 4.[25] The theoretical calculations were performed using the same DFT functional (B3LYP)[78-80] as Chapter 4, to be able to comment on the quantitative differences in the mechanical properties. Because of the higher density and increased symmetry of the ZIF-zni structure compared with ZIF-4, an increase in the framework stiffness of the material (Young's moduli) is observed by a factor of approximately three. In addition, there is a two-fold increase in the resistance to shear strain through a doubling of the maximum shear modulus (G_{max}), which can contribute to the mechanical destabilisation of ZIF materials.[25, 156] The Poisson's ratio was also affected, in that it no longer possesses the cork-like response (zero Poisson's ratio) in any direction, as is the case with ZIF-4 whose ν_{min} was found to be approximately zero. The values for the Young's moduli agree with experimental nanoindentation values,[60] with the experimental $E_{\max}$ of ZIF-zni in the <001> direction ~9 GPa, and the experimental $E_{<100>} \approx 8$ GPa (DFT value from this work, $E_{<100>} = 8.6$ GPa). Plots of the various anisotropic mechanical properties of ZIF-zni are shown in Appendix A6.1.

6.6 Chapter Summary

In conclusion, the thermally induced amorphisation of ZIF-4 into a-ZIF and its subsequent recrystallisation upon additional heating to transform into ZIF-zni has been followed *in situ* using synchrotron FIR spectroscopy for the first time. Vibrational spectroscopy has been used to gain a better understanding of how thermal stimulus can affect the stability of framework materials. This chapter confirms the nature of each different vibrational motion and makes the connection between the flexibility (mechanical compliance) of the Zn–N tetrahedral moieties and the likelihood of thermal-induced amorphisation. The thermal stability to amorphisation has been measured *via* an observed spectral shift in relation to the vibrational motions resulting from the polyhedral deformations and encourages future work in this area to test its wider applicability. In relation, it is expected that other ZIF structures that possess the unsubstituted Im organic linker (e.g. ZIF-1, -2, -3, and -10) will demonstrate a similar thermal response to that reported for ZIF-4 in this work ($X_R = 0.045$ cm^{-1} K^{-1}). It is also of great interest to further the research into MOFs with different metal polyhedra coordination, such as the high stability UiO series[157] and the isoreticular MIL-140 series discussed in Chapter 4 (Section 4.5) and Chapter 5 (Section 5.4).[39, 147, 192]

Chapter 7

Dielectric Response of Zeolitic Imidazolate Frameworks

This chapter involves the first report of experimental frequency-dependent (dynamic) dielectric response for a group of polycrystalline zeolitic imidazolate framework (ZIF) materials in the extended infrared (IR) spectral region. Using synchrotron-based IR spectroscopy in specular reflectance, in conjunction with density functional theory (DFT) calculations, detailed structure-property trends linking the terahertz (THz) region dielectric response to the framework porosity and structural density have been revealed. The work demonstrates that MOFs are promising candidate materials not only for low-κ dielectric applications but could also be revolutionary for THz applications, such as next-generation communications technologies.

7.1 Introduction

This chapter reports the first study of the frequency-dependent (dynamic) infrared (IR) region dielectric constant and refractive index values for five topical polycrystalline ZIF materials (Figure 7.1).[193] The focus of the chapter is on the dielectric constants, as the static dielectric constant is simply the square of the static refractive index ($\kappa = n^2$). Synchrotron IR specular reflectance spectroscopy, as discussed in Chapter 3, was used to obtain high signal-to-noise data at room temperature, and *via* Kramers-Kronig Transformation (KKT), the complex dielectric constants were extracted (Figure 7.2 and Figure 7.3).

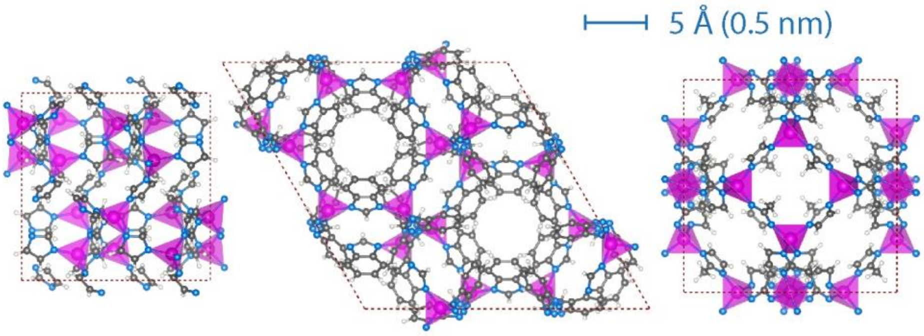

(a) ZIF-4 (b) ZIF-7 (c) ZIF-8

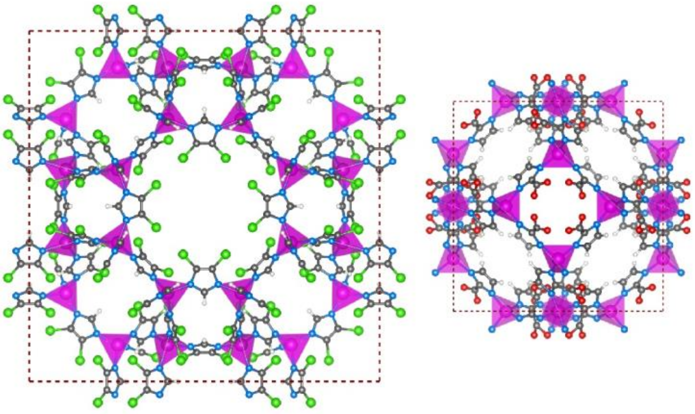

(d) ZIF-71 (e) ZIF-90

Figure 7.1. Framework structures of (a) ZIF-4, (b) ZIF-7, (c) ZIF-8, (d) ZIF-71 and (e) ZIF-90, looking down the crystallographic *c*-axis. The inorganic building units are ZnN_4 coordination tetrahedra, highlighted in purple, connected *via* a series of imidazolate-derived organic linkers. The dashed lines represent one unit cell. Colour code used: zinc purple; carbon grey; nitrogen blue; oxygen red; chlorine green; hydrogen white.

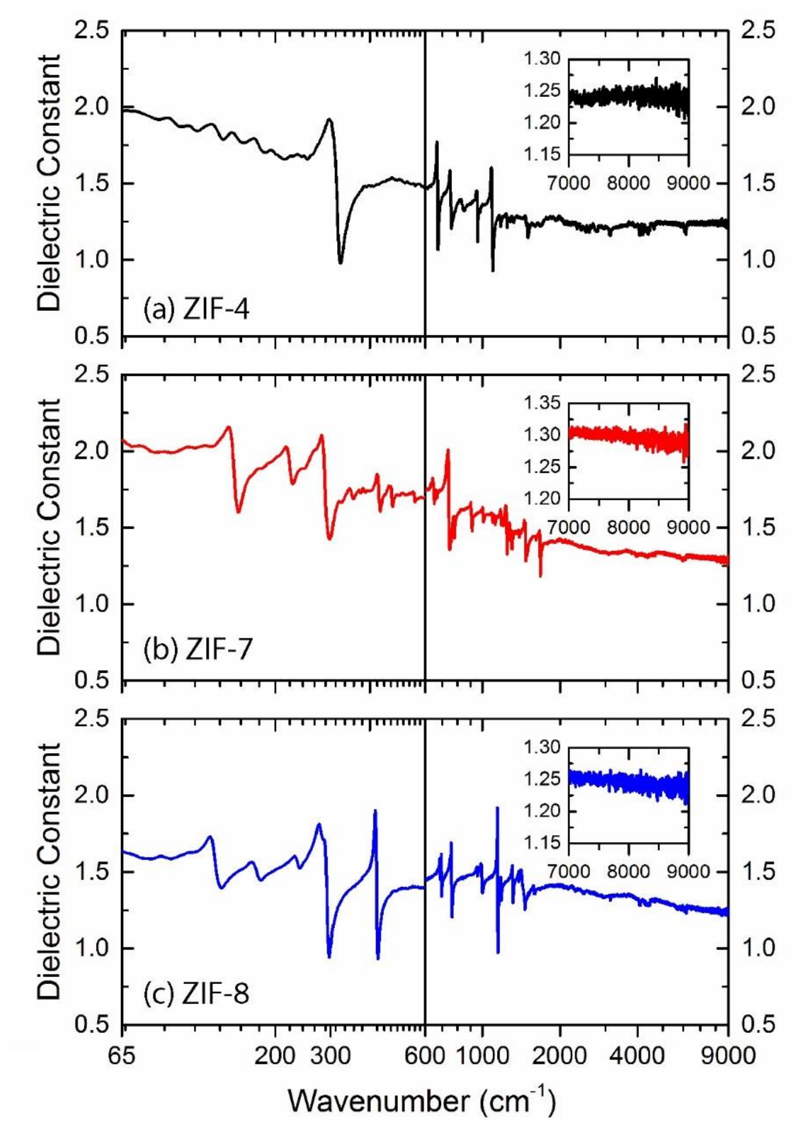

Figure 7.2. Spectra of the FIR and MIR spectral regions of (a) ZIF-4, (b) ZIF-7 and (c) ZIF-8. The spectra show the frequency dependent dielectric data, obtained *via* KKT. The FIR and MIR regions are both plotted on separate logarithmic axes for additional clarity. The spectral region at the boundary between the MIR and NIR (7000–9000 cm^{-1}) is shown as an inset to show the dielectric values more clearly.

As discussed in Chapter 2, materials, such as MOFs, featuring low-κ dielectric constants ($\kappa < 2.0$) and tuneable structural properties and porosity, are ideal candidate materials for the future microelectronics industry; for example in devices that can lead to integrated circuits MOFs have the potential to act as an interlayer dielectric insulating material.[92] There are, however, some requirements for the engineering of functional devices including new low-κ materials for real-world applications.[194] These include thermal stability at high temperature, predictable mechanical behaviour and long-term stability, electrical insulation, and excellent adhesion to other interlayers.

IR spectroscopy is becoming increasingly popular for analysing the structural dynamics of MOFs. Synchrotron-based far-IR (FIR) spectroscopy and inelastic neutron scattering (INS), in conjunction with *ab initio* density functional theory (DFT), was shown in Chapter 5 to explain the framework specific terahertz (THz) region collective vibrational motions of a variety of MOF structures.[156, 192, 195] These low-frequency THz vibrational motions were linked to various physical phenomena, including gate-opening and breathing mechanisms in ZIF-8 and ZIF-7, and shear-driven destabilisation motions for multiple ZIF structures (Chapter 4 and Chapter 5). The latter

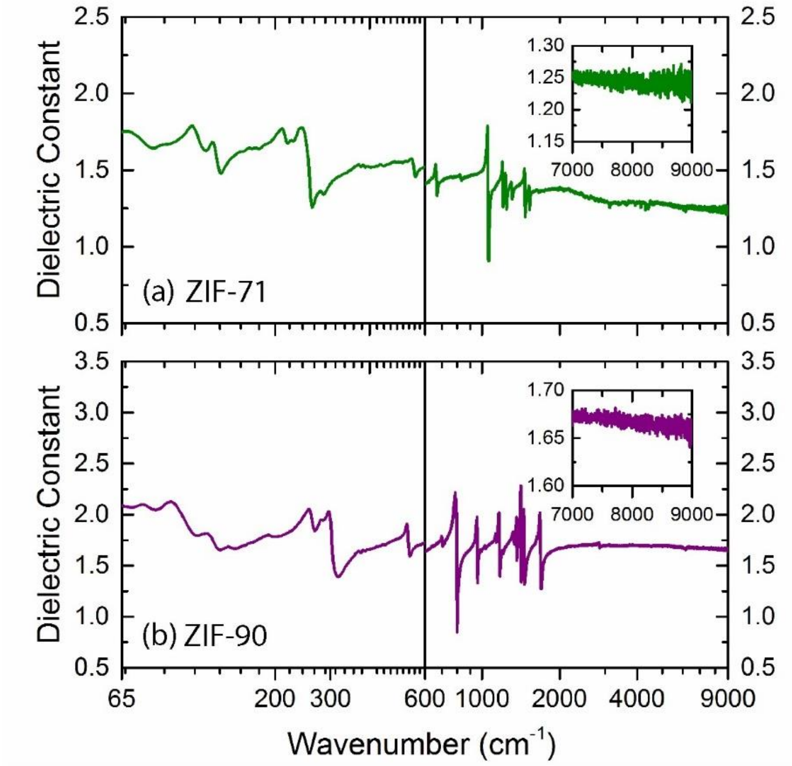

Figure 7.3. Spectra of the FIR and MIR spectral regions of (a) ZIF-71 and (b) ZIF-90. The spectra show the frequency dependent dielectric data, obtained *via* KKT. The FIR and MIR regions are both plotted on separate logarithmic axes for additional clarity. The spectral region at the boundary between the MIR and NIR (7000–9000 cm^{-1}) is shown as an inset to show the dielectric values more clearly.

has been associated with the mechanical induced amorphisation that is observed for ZIF pellets prepared under significant pressure.[25, 41, 156]

KKT is valid under certain conditions which must be satisfied to produce accurate dielectric and refractive index data. One of these conditions is the requirement for reflection to take place at the surface. Therefore, the samples should exhibit a low roughness (< 100 nm) and hence it was ensured that the ZIF pellets were as smooth as was practically possible. This was investigated using an Alicona InfiniteFocus 3D Profilometer which confirmed that the root-mean-square (RMS) roughness of the pellets was ~40 nm. Importantly, this was not affected by the magnitude of pressure used to press the specific pellet (Appendix A7.4). Also, if the material is absorbing of IR radiation (as is the case with most materials, including MOFs), then the reflectance spectra will be affected by the absorption bands, and it is, therefore, critical to ensure that the selected spectral cutoffs for the KKT do not coincide with any absorption features. This is not a major concern in the near-IR (NIR) region, as the absorptions are very weak. However, care must be taken when selecting the spectral cutoff in the mid-IR (MIR) and FIR regions where there are a significant amount of absorption peaks.[156, 196]

7.2 Dynamic Dielectric Spectra

This section reports the first example of experimental frequency dependent dielectric properties of MOF materials in the extended IR spectral region (65–9000 cm^{-1}). The dynamic dielectric data was obtained for five ZIF structures, namely: ZIF-4, ZIF-7, ZIF-8, ZIF-71, and ZIF-90 which are all Zn-based materials with different imidazolate derived linkers (Figure 7.1). It is observed that all dielectric constant values, excluding absorption effects, are within the range of 1.2–2.5. Of interest are the low-κ values witnessed when leaving the MIR region and going into the NIR spectral region (beyond

4000 cm^{-1}); these values are ~1.2 for all the structures excluding ZIF-90. This is likely due to the structural disorder present in ZIF-90, and for this reason it will be excluded from the discussions later in this chapter regarding systematic trends. Therefore, the NIR spectral region appears insensitive to framework structure.

One clear observation from the spectral data is that the dielectric constant (excluding absorption bands) reduces with increasing frequency, therefore consistent with the assumption that the static dielectric constant is also the maximum for each material. Also, the gradient in the decrease of the dielectric constant with respect to wavenumber is higher in the low-frequency FIR region, compared with the MIR and NIR (Figure 7.5e). The data reported in Figure 7.6 show that the FIR dynamic dielectric constants are significantly more structure dependent and show a direct link to the porosity and the solvent assessable volume (SAV) of the framework. The direct correlation to the level of porosity is to be expected from a fundamental point-of-view. As the dielectric constant is a measure of the ability of a substance to store electrical energy in an electric field and as the porosity increases the dielectric constant will tend towards the value of a vacuum ($\kappa = 1$) or air ($\kappa \sim 1$).

7.3 Effects of Pelletisation Pressure

To perform the specular reflectance experiments, the MOF materials were pressed into ~1 mm thick, 13 mm diameter circular pellets using a hydrostatic press. The effects of pelletisation were therefore investigated, to ensure that accurate dielectric constant values were being reported and ensure that no pressure-induced amorphisation or phase transitions, as often reported for the ZIF family, had occurred.[197]

An extensive investigation was performed into the effects of pressure on the ZIF-8 material. As can be seen from Figure 7.5, there is a linear trend in the increase of the dielectric constant at each spectral region with increased pelletisation pressure. Of interest was the discovery that increased pelletisation pressure had a more significant effect on the THz/FIR region with an increased gradient (slope) of 0.71 GPa^{-1}, more than double that of the near-IR region (gradient = 0.35 GPa^{-1}).

The increase in dielectric constant was confirmed to be primarily an effect of the structure reacting to the pelletisation pressure and an additional contribution resulting from the higher densification of the pellet (as mentioned below). This was confirmed *via* XRD, linking the increase in dielectric constant to the decrease in Bragg intensities (shown in Appendix A7.1). The onset of the pressure induced phase transition of ZIF-8 was observed at pressures above 0.3 GPa, indicated by the evolution of a new spectral feature at ~385 cm^{-1} (further highlighted in Appendix A7.3). The spectral feature observed at ~450 cm^{-1} is a numerical artefact resulting from the spectral range used for the KKT. The removal of the artefact is shown in Appendix A7.3. Pellets pressed with

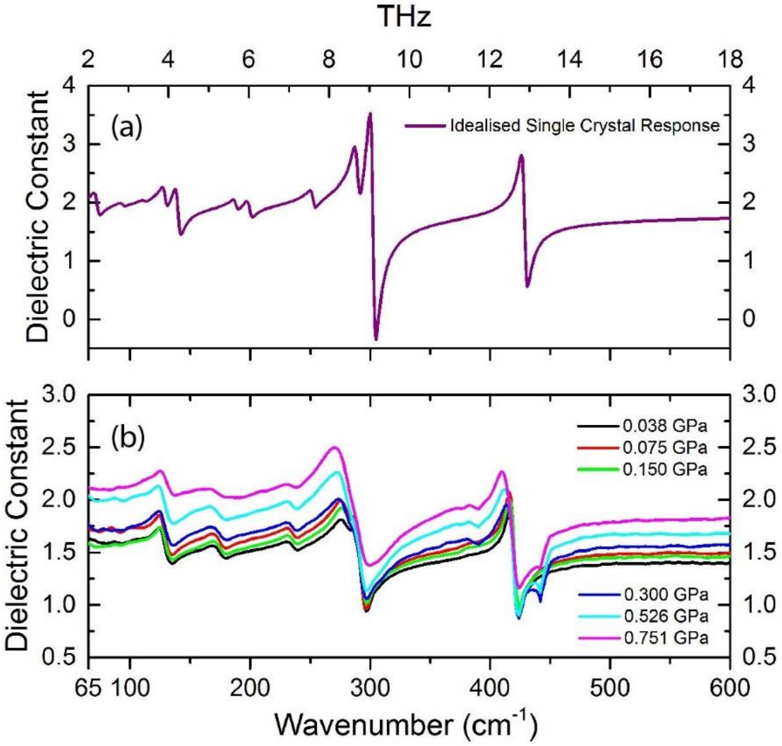

Figure 7.4. Spectra of the (a) theoretical and (b) experimental FIR dielectric data of ZIF-8 showing the step-wise effect of pelletisation pressure.

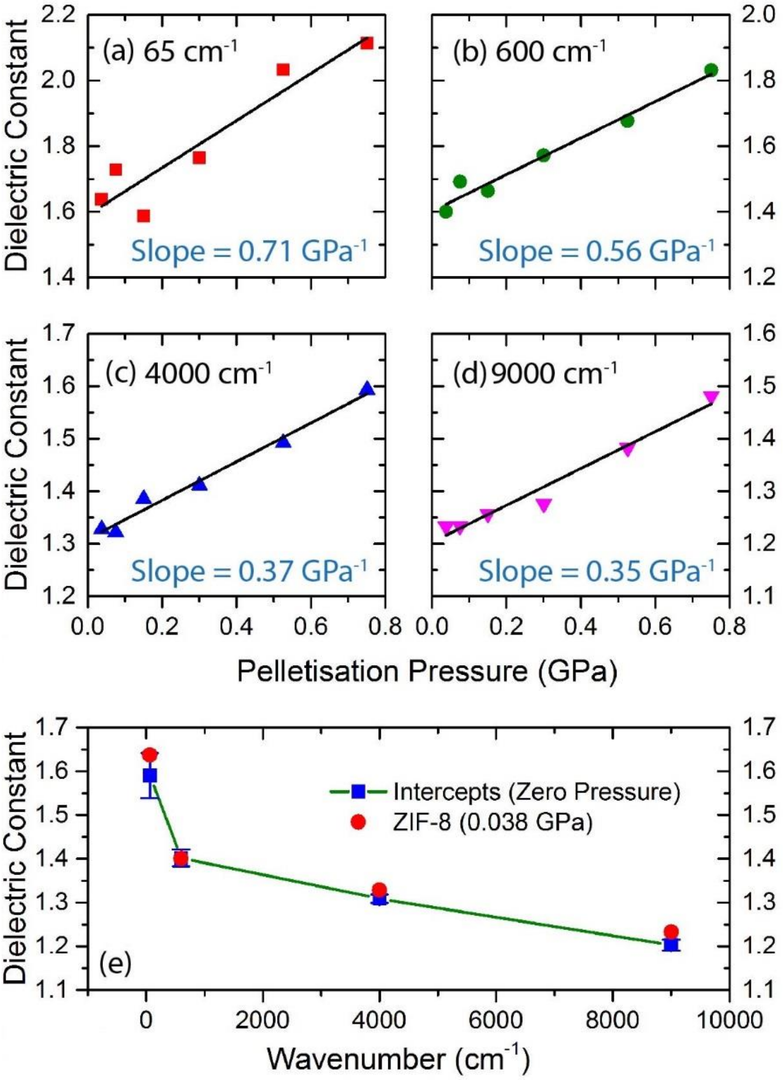

Figure 7.5. Plots showing the change in the dielectric constant of ZIF-8, upon increased pelletisation pressure, at a range of specific spectral points: (a) 65 cm^{-1}; (b) 600 cm^{-1}; (c) 4000 cm^{-1}; (d) 9000 cm^{-1}. The gradient of the trends highlights that the dielectric constant is more reactive to increased pelletisation in the THz-frequency region (1.95 THz ≈ 65 cm^{-1}). (e) The dielectric constant values for ZIF-8 at 65, 600, 4000 and 9000 cm^{-1}, extrapolated to assume zero pressure effects.

0.038–0.150 GPa of pressure (0.5–2.0 tonnes over a 13 mm diameter pellet) did not affect the resultant dielectric values significantly, as can be seen from Figure 7.5e, and values obtained using these pellets were therefore used to analyse structural trends in the ZIF series (Figure 7.6).

7.4 Structure-Property Trends

A direct linear dependency on the THz region dielectric constant with framework SAV and framework density was observed. However, the experimental values are slightly lower than the theoretical dynamic values of an idealised single crystal (Figure 7.5a), due to the polycrystalline nature of the pellets. This minor disparity can be solved by treating the experimental THz dielectric constants on a similar platform to the theoretically calculated static values (effectively zero frequency). Another major advantage of using the theoretical static values is that the dielectric response can be obtained for additional

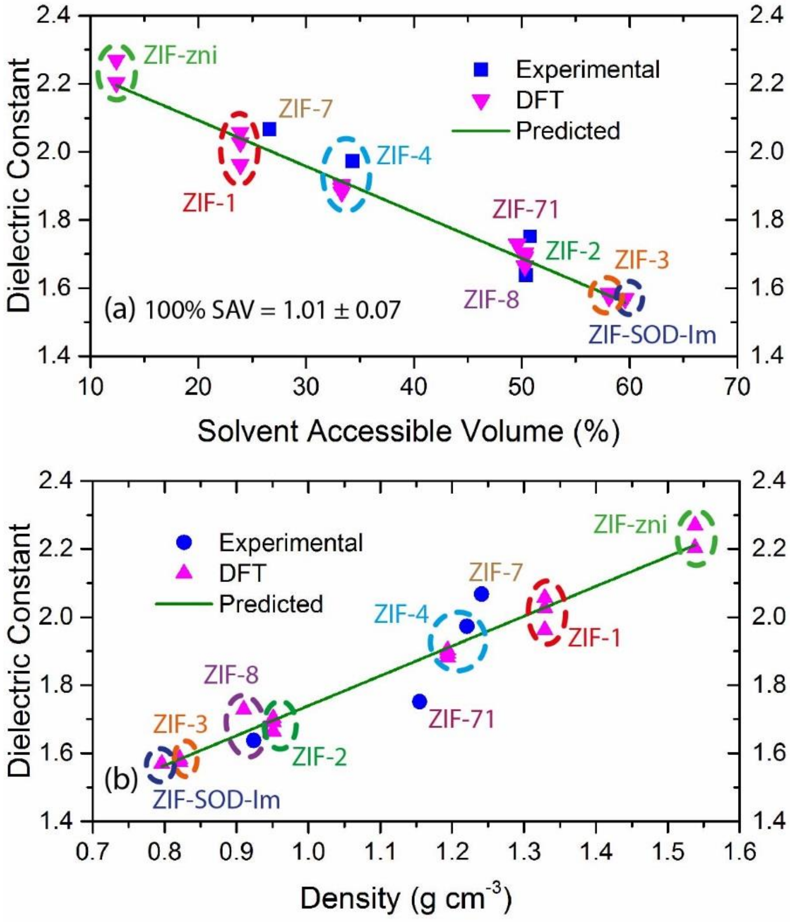

Figure 7.6. The trends observed in the THz-frequency (1.95 THz ≈ 65 cm^{-1}) dielectric constant compared with (a) SAV and (b) framework density. The experimental SAV and density values are calculated from the experimental crystallographic information file (CIF) using the PLATON code.[154] The theoretical values are obtained from optimised structures using DFT with the B3LYP-D* functional. The theoretical dielectric constants are static values (zero frequency or constant electric field).

ZIF structures providing for a more accurate trend in the structure-property relationship shown in Figure 7.6. The comparison between the DFT values (static) and the experimental values (THz) is remarkably good. This, allows the prediction that the THz-frequency dielectric constant (and refractive index) of any ZIF structure based on the structure-property trends highlighted in Figure 7.6. The porosity and SAV values were calculated using the VOID algorithm implemented *via* the PLATON code.[154]

While all the dielectric constant values considered in this chapter are for Zn-based materials, it is expected that the effect of the specific metal node will be less significant than the steric effects of the specific linkers. Hence, the primary contributing factors to the dielectric constant are the levels of porosity and degree of SAV which are related to the framework density (although not linearly). If the trend is extrapolated to a SAV value of 100%, it will result in a dielectric constant of ~1.0. This is to be expected as a SAV of 100% is essentially air. Therefore, when considering some of the most porous MOFs, the predicted dielectric constants will have approximately the same response as they would to air. For example, the Zn-based MOF with the lowest density obtained from the hypothetical MOF database,[198] would give a dielectric constant of ~1.0 (density = 0.118 g cm^{-3}). Also, if the choice of metal indeed does not make a major difference, then the recently synthesised and lowest-density MOF to be experimentally synthesised, uranium(U)-based NU-1301 (density = 0.124 g cm^{-3}), would also have a dielectric constant of ~1.0.[199]

7.5 Chapter Summary

This chapter demonstrates the first use of specular reflectance spectroscopy to obtain experimental frequency-dependent (dynamic) dielectric properties and refractive index values of MOFs in the critical IR spectral region (65–9000 cm^{-1}). Of interest are the THz region dielectric response and the remarkably good agreement with theoretical static values calculated *via* DFT. The dynamic dielectric data for the five ZIF structures, namely: ZIF-4, ZIF-7, ZIF-8, ZIF-71 and ZIF-90 were analysed, and the THz-frequency dielectric constants were found to be highly structure-dependent and have a linear trend linked to the framework density and its associated SAV. The structure-property trends highlighted in this chapter can now be exploited to target future research concerned with the dielectric properties of MOFs and other framework structures and sets the foundation for the promising field of low-κ dielectric porous framework materials.

Chapter 8

Concluding Remarks

This chapter provides a summary of the results and conclusions made throughout the thesis. The primary purpose is to reflect on the findings and novelty of the research and make recommendations for how the work could be advanced in the future. Unusual mechanical properties revealed at the molecular level in Chapter 4 are highlighted, including the first ZIF material predicted to show auxeticity (negative Poisson's ratios), negative linear compressibility (NLC) for multiple MOF structures, and the lowest shear modulus predicted for any MOF. Structure-property trends originating from the isoreticular expansion of the MIL-140 series are also reported. One of the most significant findings presented in this thesis is that the terahertz (THz) vibrational motions can reveal all the underlying physical and structural mechanisms possible for framework materials. This has encouraged further work using vibrational spectroscopy to uncover the molecular scale mechanisms responsible for some of the unusual anisotropic properties present in hybrid framework materials, such as MOFs. Some of the most relevant mechanisms exposed so far have included gate-opening motions, framework breathing modes and the shearing dynamics responsible for structural amorphisation. The use of reflectance spectroscopy to measure the dynamic (frequency-dependent) dielectric response across the infrared (IR) spectral region of MOFs for the first time is one of the most industrially relevant discoveries made in the thesis. Predominantly due to the promising low-κ dielectric trends that were revealed.

8.1 Unusual Mechanical Behaviour of MOFs

The elastic properties of cubic HKUST-1 were computed along with four structurally polymorphic ZIFs, and the isoreticular MIL-140 series of Zr-based MOFs. The mechanical response of the three types of structures studied, allowed for the underlying mechanisms to be identified and explained. The Zn-based ZIF structures were chemically analogous and constructed from divalent Zn^{2+} cations coordinated by unsubstituted imidazolate linkers. However, as a result of their distinctive network topologies, porosity, and physical properties they demonstrated a range of unusual mechanical responses. The mechanical properties included an almost zero Poisson's ratio (cork-like response) to auxeticity (negative Poisson's ratio, NPR), and from negative linear compressibility (NLC) to an extremely low shear modulus in ZIF-3. In fact, the minimum shear modulus of ZIF-3 is the lowest shear stability predicted for any MOF material, and ZIF-3 is also the only ZIF to be predicted to display an auxetic response.

The MIL-140 series was also investigated to understand the mechanical response to isoreticular framework expansion. The MIL-140 structures all adopt the same network topology, though each structure features a different organic linker size and degree of flexibility. These differences provided the unique opportunity to precisely establish the structure-property trends, and illuminate the underlying connections that underpin elastic anisotropy and physical anomalies of MOFs. Importantly, the shear moduli calculated for the MIL-140 structures correlated well with recent experiments reporting the rates at which the series undergoes mechanically-induced amorphisation.[23] The agreement with experiment strengthens the value of applying rigorous elasticity theory to explaining and predicting structural stability trends of isoreticular MOF systems.

The results in Chapter 4 dedicated to the analysis of the elasticity of MOFs laid the foundation to understanding the mechanical property landscape of framework materials and the intersection of MOFs with ceramics, metals, polymers and foams. Thereby bridging the structural characteristics of the intrinsically rigid inorganic solids and the relatively flexible polymers; this effect is indeed considerably stronger than was previously believed in the literature.[11]

The theoretical approach provides an insight into the molecular mechanisms surrounding the elastic anisotropy of MOFs, thereby providing a better understanding of the anomalous elastic phenomena highlighted above. Notably, the source of unusual mechanical phenomena such as NLC and auxeticity has been explained at the molecular level. Overall, the findings reiterate the many undiscovered possibilities offered by the field of MOF mechanics and the exciting opportunities that might be possible in engineering science and industrial applications.

8.2 THz Vibrations of Framework Materials

The results reported in Chapter 5, showed that terahertz (THz) vibrations can be used to uncover the underlying physical mechanisms and phenomena possible for framework materials (namely MOFs in the context of the thesis). The discovery that THz vibrations contain so much structural information has resulted in additional studies using a combination of experimental spectroscopy methods in conjunction with *ab initio* density functional theory (DFT) calculations to open new opportunities to understand the fundamental lattice dynamics. The results show, that collective vibrations and low-energy THz modes can offer new insights into many possible and competing pathways governing unique physical mechanisms in MOFs. The section relating to ZIF materials in Chapter 5 demonstrated the gate-opening and pore breathing phenomena in ZIF-8 and ZIF-7 respectively. Each of the ZIF structures investigated showed soft modes that suggest possible phase transitions, and the onset of shear-induced structural destabilisation. The results were encouraging as a selection of the physical phenomena had recently been observed experimentally, thus confirming the validity of the computational approach. The initial work on ZIFs provided the much-needed starting point to instigate further research into the detailed physics surrounding the low-frequency vibrations and soft modes of framework materials.

The THz vibrational modes of HKUST-1 provided valuable insights into trampoline-like mechanisms, paddle-wheel rotors, and soft modes linked to symmetric collective mechanisms. Of interest was the explicit link some of these motions had with the mechanical properties reported for HKUST-1 in Chapter 4. This included the origin of negative Poisson's ratios (auxeticity) and negative thermal expansion (NTE) both present in the Cu-based cubic framework material. The findings further highlighted that many of the mechanical mechanisms responsible for the anomalous elasticity of MOF materials are yet to be fully understood and that THz vibrational motions could help in furthering the understanding. The hope is that further experimental studies will be performed on MOFs to confirm the level of anisotropy, with regards to the DFT predicted directional mechanical properties.

The THz vibrations of MIL-140A allowed for new physical phenomena beyond that reported for ZIFs or HKUST-1, by revealing a multitude of new motions involving rotor-like dynamics of linkers and associated trampoline-like mechanisms. Also, the shearing motion reported was the first validation of the existence of low-energy shear dynamics by directly matching the crystallographic direction of the minimum shear modulus reported for MIL-140A in Chapter 4.

8.4 Tracking Thermal Amorphisation

It was reported in Chapter 6 that the thermally induced amorphisation of ZIF-4 into a-ZIF and its subsequent recrystallisation upon additional heating to transform into ZIF-zni can be tracked *in situ* using synchrotron far-IR (FIR) spectroscopy. The work confirmed the nature of each vibrational motion and connected the flexibility (mechanical compliance) of the Zn–N tetrahedral moieties to the likelihood of thermal-induced amorphisation.

One of the discoveries was a possible thermal-shift coefficient to relate the spectral shift of the Zn–N tetrahedra signal to the ease of thermal-induced amorphisation. Also, it is expected that other ZIF structures that possess the unsubstituted imidazolate linkers (such as those in Chapter 4) would demonstrate a similar thermal response to that reported for ZIF-4 (X_R = 0.045 cm^{-1} K^{-1}). Therefore, future work in this area to test its wider applicability is strongly encouraged.

8.5 Low-κ Dielectric MOFs

The final discovery made in this thesis relates to the structure-property trends linking framework porosity and low-κ dielectric response. Specular reflectance spectroscopy was used to obtain an experimental dynamic (frequency-dependent) dielectric response for a variety of Zn-based ZIF materials over the extended IR spectral region (65–9000 cm^{-1}). The dielectric response in the mid-IR (MIR) and near-IR (NIR) was relatively consistent with each framework. However, the THz-frequency dielectric constants were shown to be highly structure-dependent and demonstrated a linear trend with framework density and associated solvent assessable volume (SAV). The structure-property trends have already been used to focus the future search for promising dielectric materials on subgroups of MOFs and set the foundation for the promising field of low-κ dielectric porous framework materials.

8.6 Future Work

The results reported in this thesis have motivated many new areas of research. Most of the follow-on work is related to using THz vibrations to investigate the possible structural phenomena possible for MOFs and the discovery of trends identifying MOFs as significantly promising low-κ dielectric materials. The next step is to focus on the following areas of research.

8.6.1 Mechanical Properties of Framework Materials

The examples given below will build on the elasticity and mechanical response work of the thesis and will be highly advantageous to the field.

- Additional Brillouin scattering experiments to obtain accurate experimental values of the single crystal elastic constants. These values would allow for a direct comparison with the theoretical results reported in Chapter 4. Also, it would provide an insight into the level of structural defects and disorder in the framework materials, as the theoretical values assume an idealised single crystal.

- Advancing the work on the mechanical response to include host-guest interactions and systematic structural defects would provide additional insight into the real stability of MOF single crystals and better model the response of the frameworks for industrial applications.

- The introduction of thermal and pressure effects to the elasticity of framework materials would be a major step forward. The most promising method for such advancements would be *via* the combined use of quasi-harmonic and quasi-static approximation to obtain the thermal effect on the elastic constants and develop new experimental techniques to study these effects in conjunction.

- It is predicted that the techniques introduced in this thesis, regarding the THz lattice dynamics, will become more widely used to reveal the underlying mechanical and structural mechanisms of framework materials. The methodology of using THz vibrational motions will continue to improve, and as a result, it will become possible to understand the elastic and mechanical response better.

8.6.2 THz Vibrations of Framework Materials

The examples given below will build on the new field originating from the THz vibrational work introduced in the thesis.

- The vibrational frequencies reported throughout the thesis are the modes located at the Γ-point. This is assumed to be sufficient as the volume of each framework material studied is large enough to expect negligible phonon dispersion. However, it would be interesting to advance the results to include the contributions of full phonon dispersion and compare the subtle differences and the presence of any additional vibrational motions that may be discovered.

- With the constant advancement in experimental neutron scattering techniques, the possibility of investigating the pressure effects on the THz vibrational modes is becoming within reach. Some of the most promising technological improvements involve the introduction of more accurate neutron guides and filters to increase the intensity and reduce the background noise respectively. The resultant increase in signal-to-noise in the THz region will also allow for the effects of guest inclusion to be investigated. One of the outstanding limitations holding back obtaining data at high-pressures is the need for suitable sample environments, specifically diamond anvil cells (DACS) tailored for neutron experiments.

- The quantum effects of specific framework materials could be investigated using a combination of INS and quasi-elastic neutron scattering (QENS) techniques. This would allow for an in-depth investigation of various tunnelling effects that can exist in the isolated environment of the framework porosity. The most intriguing is the methyl tunnelling potential present in the linkers of ZIF-8. The effects of gas adsorption and guest inclusion could be monitored to provide additional knowledge of the host-guest interactions possible for MOF materials.

- The possibility of a thermal shift coefficient X_R was suggested in Chapter 6, and it would be of interest to further characterise the dependence of X_R on MOFs with varying metal polyhedra coordination, such as the high stability UiO series and the isoreticular MIL-140 series discussed in Chapter 4 and Chapter 5. Also, tracking the thermal shift in the opposite direction to validate the theory at low temperature would be advantageous in progressing and confirming the robustness of the use of the possible coefficient.

8.6.3 Dynamic Dielectric Response of MOFs

The dynamic dielectric work reported in Chapter 7 provided the first example of frequency-dependent (dynamic) dielectric constants for MOFs in the extended infrared (IR) region. Therefore, the technique will be used to investigate a variety of additional frameworks and families of materials. The examples below would be interesting materials to study in the future.

- Exploring the dielectric response of isoreticular series of framework materials, such as the MIL-140 series discussed in Chapter 4 and Chapter 5 would be a good way to establish further the linear trends connecting the low-κ response with porosity and SAV.

- Investigating and comparing the dielectric response of MOFs in single crystal form would be advantageous in understanding the polycrystalline effects and allow for the influence of the pelletisation pressure to be fully exposed. Also, it would be interesting to study the effects of pelletisation pressure further on materials that undergo predictable amorphisation or phase transitions, such as the pressure responsive MOFs, MFM-300 (previously NOTT-300) and the various metal analogues of MIL-53.[200]

Appendix

Supplementary Data

A3 Additional Methodology Data (Chapter 3)

A3.1 Electronic Structure Theory

The electronic structure of a molecule or material is the state of motion of electrons in an electrostatic field created by stationary nuclei. There are many excellent textbooks on the subject.[201-203] This section provides a brief introduction to the basic mathematical foundations leading to the use of density functional theory (DFT). For any chemical system of nuclei and electrons, the following Schrödinger equation can be satisfied:

$$H\Psi = E\Psi \tag{A3.1}$$

$$E = \min_{\Psi} \left\langle \Psi \middle| H \middle| \Psi \right\rangle \tag{A3.2}$$

where H is the Hamiltonian, E is the energy of the system and Ψ is the many-body wave function. The ground state energy can be obtained from Equation A3.2 where the minimisation is over all the antisymmetric particle wavefunctions. The following reduced equation describes the general Hamiltonian for any system:

$$H = T^{n} + V^{nn} + T^{e} + V^{ee} + V^{ne} \tag{A3.3}$$

where T^{n} and T^{e} are the kinetic energy terms and V^{nn}, V^{ee} and V^{ne} are the interaction terms (the superscripts ^{n} and ^{e} signify if the contribution is from the nuclei or electrons respectively). Intuitively the interaction terms V^{nn} and V^{ee} are repulsive, and the V^{ne} term is attractive. The dynamics of the system can then be described precisely by the time-dependent Schrödinger equation:

$$H\Psi(t) = i\frac{\partial}{\partial t}\Psi(t) \tag{A3.4}$$

However, only the simplest systems (a hydrogen atom or positronium) can be solved exactly. Therefore, several approximations are introduced, including the Born-Oppenheimer Approximation which is related to the differences in the mass of the electrons and the nuclei in the system. It states that since the nuclei are significantly heavier than the electrons in the same system that they can be treated as stationary in relation to the instantaneous motion of the electrons. Hence if the nuclei are stationary (clamped), then the nuclear and electron motions are decoupled, and Equation A3.3 simplifies to a purely electronic problem with V^{ne} contributing to an external potential, and the Hamiltonian can be rewritten as:

$$H^e = T^e + V^{ee} + V^{ne} \tag{A3.5}$$

This many-body equation is still complicated to calculate as it is not separable into single-body equations due to the electron-electron repulsion interactions (V^{ee}). The individual terms of Equation A3.5 consist of the following:

$$T^e = -\frac{1}{2}\sum_{j=1}^{N}\nabla_j^2 \tag{A3.6}$$

$$V^{ee} = \frac{1}{2}\sum_{i\neq j}\frac{1}{\left|\mathbf{r}_i - \mathbf{r}_j\right|} \tag{A3.7}$$

$$V^{ne} = \sum_{j=1}^{N} v(\mathbf{r}_j) \tag{A3.8}$$

where N is the number of electrons and $\mathbf{r}$ is the electronic coordinates. However, there are currently many sophisticated methods for solving the many-body Schrödinger equation based primarily on expanding the wave function *via* the use of Slater determinants.[204] One of the simplest methods is Hartree-Fock theory.[201] However, Hartree-Fock energies on their own can be highly inaccurate due to neglecting electron correlation effects and should therefore at best be the starting point for a more refined and numerically robust method. There are indeed multiple more sophisticated approaches to expanding the wave function and include electron correlation contributions. They are usually referred to as post-Hartree-Fock methods and include the higher accuracy Møller-Plesset Perturbation Theory (discussed briefly in Appendix A5.4)[205] and the even higher accuracy Coupled Cluster (CC) theory.[201] However, the limitation of these accuracy quantum chemical methods is the enormous computational cost, which makes it impossible to apply them effectively to large, complex systems such as MOFs.

A4 Additional Elasticity Data (Chapter 4)

A4.1 HKUST-1 Lattice Parameter Comparisons

Summarised below is the comparison of lattice parameters calculated from DFT (for ideal crystalline structures) versus experimental values reported in the literature.[57]

HKUST-1		
Method	*Lattice parameters* (Å)	*Volume* (Å^3)
	a	
Experimental CIF	26.30	18199.8
B3LYP	26.33	18247.5
B3LYP-D	26.30	18183.2

- Average difference in experimental and theoretical lattice parameters for B3LYP: 0.09%
- Average difference in experimental and theoretical lattice parameters for B3LYP-D: 0.03%

A4.2 ZIF Lattice Parameter Comparisons

Summarised below are the comparisons of lattice parameters calculated from DFT (for ideal crystalline structures) versus experimental values reported in the literature.[206]

ZIF-1					
Method	*Lattice parameters* (Å)				*Volume* (Å^3)
	a	*b*	*c*	*β*	
Experimental CIF	9.74	15.27	14.94	98.6	2196.0
B3LYP	10.07	15.50	15.42	97.1	2389.4
• Average error in lattice parameters (including angle): 1.46%					

ZIF-2				
Method	*Lattice parameters* (Å)			*Volume* (Å^3)
	a	*b*	*c*	
Experimental CIF	9.68	24.11	24.45	5706.6
B3LYP	9.71	24.89	23.36	5643.7
• Average error in lattice parameters (including angle): 2.65%				

ZIF-3			
Method	*Lattice parameters* (Å)		*Volume* (Å^3)
	a	*c*	
Experimental CIF	18.97	16.74	6024.1
B3LYP	19.48	17.25	6548.3
• Average error in lattice parameters (including angle): 2.87%			

ZIF-4				
Method	*Lattice parameters* (Å)			*Volume* (Å^3)
	a	*b*	*c*	
Experimental CIF	15.40	15.31	18.43	4342.1
B3LYP	16.17	16.78	18.80	5098.1
• Average error in lattice parameters (including angle): 5.54%				

A4.3 MIL-140 Lattice Parameter Comparisons

Summarised below are the comparisons of lattice parameters calculated from DFT (for ideal crystalline structures) versus experimental values reported in the literature.[147]

MIL-140A

Method	*Lattice parameters* (Å)				*Volume* (Å^3)
	a	*b*	*c*	*β*	
Experimental CIF	24.42	11.18	7.80	103.9	2068.4
B3LYP	24.76	11.28	7.98	102.5	2175.0

- Average error in lattice parameters (including angle): 1.49%

MIL-140B

Method	*Lattice parameters* (Å)				*Volume* (Å^3)
	a	*b*	*c*	*β*	
Experimental CIF	28.16	13.47	7.89	93.4	2986.3
B3LYP	28.19	13.49	8.02	94.6	3040.7

- Average error in lattice parameters (including angle): 0.78%

MIL-140C

Method	*Lattice parameters* (Å)				*Volume* (Å^3)
	a	*b*	*c*	*β*	
Experimental CIF	31.89	15.61	7.94	84.8	3934.3
B3LYP	31.80	15.63	8.02	86.0	3973.0

- Average error in lattice parameters (including angle): 0.54%

MIL-140D

Method	*Lattice parameters* (Å)				*Volume* (Å^3)
	a	*b*	*c*	*β*	
Experimental CIF	34.86	17.48	7.86	90.3	4798.4
B3LYP	35.49	17.59	7.98	95.3	4957.7

- Average error in lattice parameters (including angle): 2.37%
- The increased error for MIL-140D is due to the Literature CIF file not containing the disordered Cl atoms.

A4.4 HKUST-1 Dispersion Correction

Table A4.1. Single-crystal elastic stiffness coefficients (C_{ij}) of HKUST-1 computed from the DFT method.

Functional	C_{11}	C_{12}	C_{44}
B3LYP	27.72	25.72	5.40
B3LYP-D	27.54	25.48	5.27

Table A4.2. Isotropic Voigt-Reuss-Hill (VRH) averaged elastic properties, corresponding to the polycrystalline state. The bulk (K), Young's (E) and shear (G) moduli are in GPa and the Poisson's ratio (ν) is dimensionless.

Functional	K_{VRH}	E_{VRH}	G_{VRH}	ν_{VRH}
B3LYP	26.4	8.1	2.8	0.45
B3LYP-D	26.2	8.1	2.8	0.45

A4.5 Additional Young's Moduli Plots for the MIL-140 Series

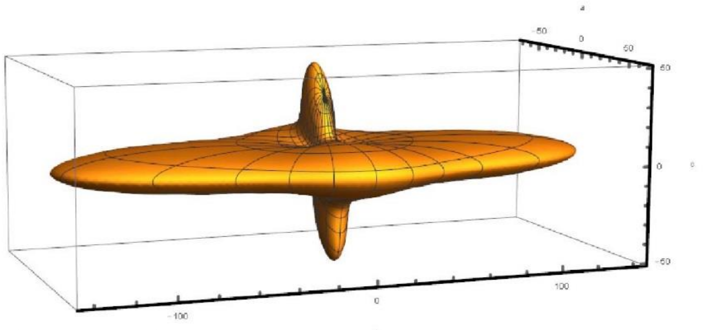

(a) MIL-140A

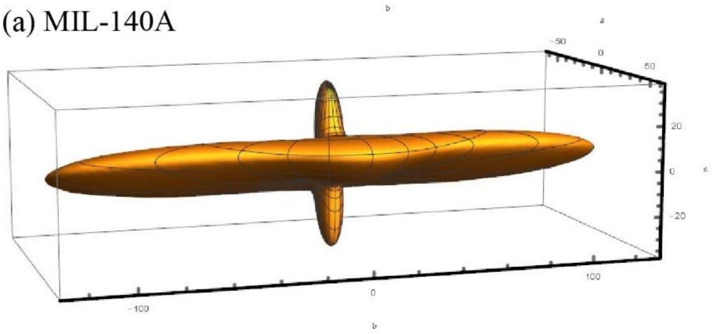

(b) MIL-140B

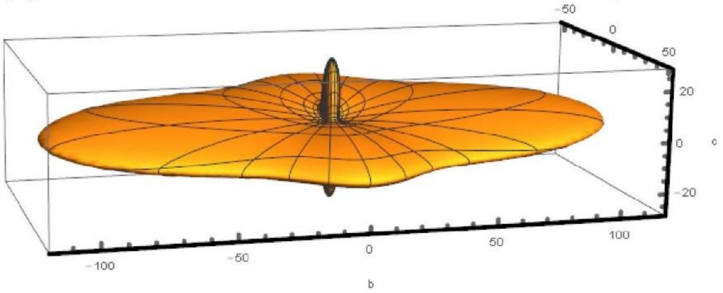

(c) MIL-140C

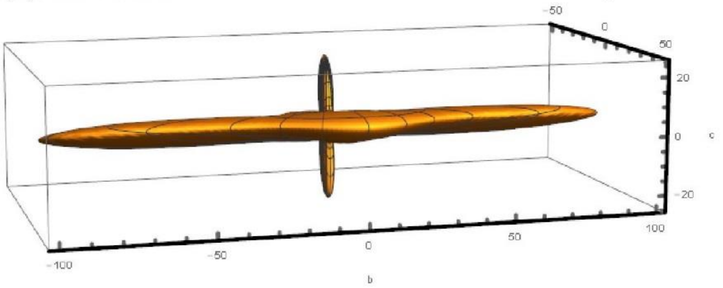

(d) MIL-140D

Figure A4.1. Anisotropic Young's moduli plot for (a) MIL-140A, (b) MIL-140B, (c) MIL-140C and (d) MIL-140D (in GPa).

A4.6 Additional Shear Moduli Plots for the MIL-140 Series

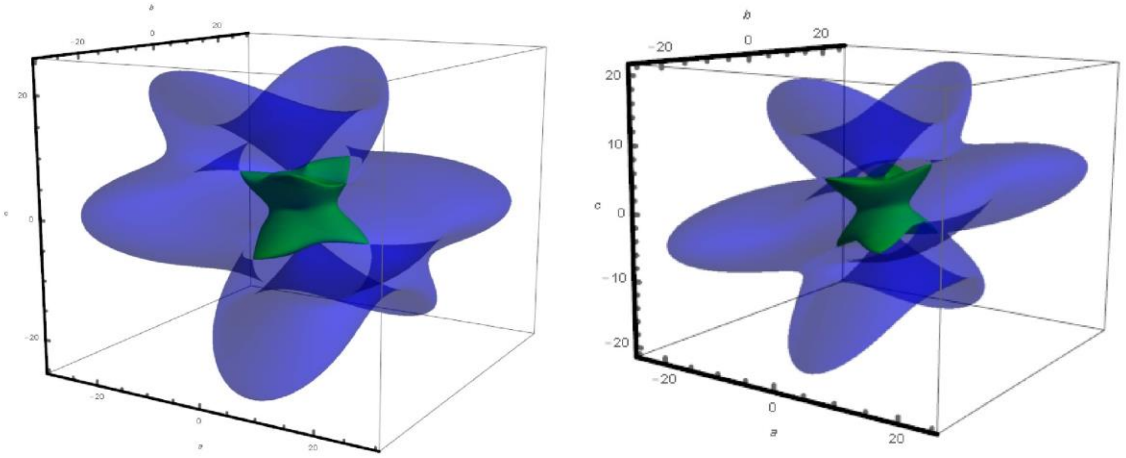

(a) MIL-140A (b) MIL-140B

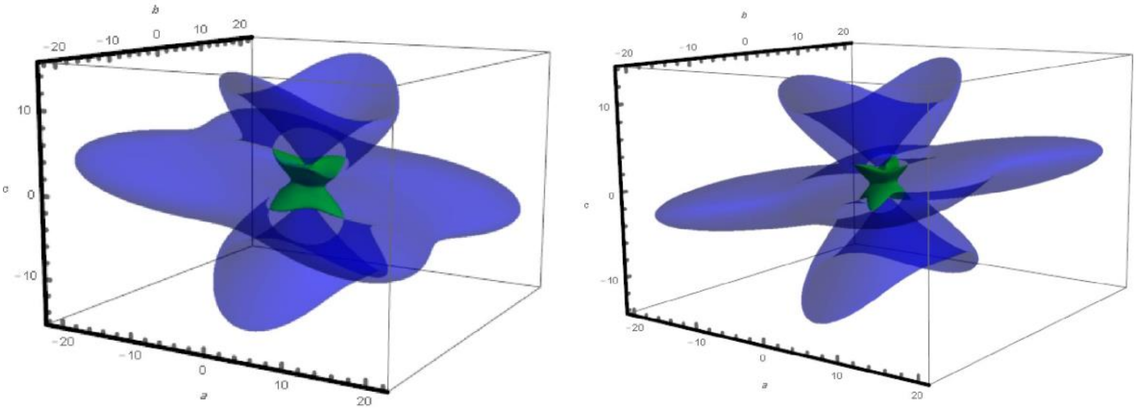

(c) MIL-140C (d) MIL-140D

Figure A4.2. Anisotropic shear moduli plot for (a) MIL-140A, (b) MIL-140B, (c) MIL-140C and (d) MIL-140D (in GPa).

A4.7 Additional Poisson's Ratio Plots for the MIL-140 Series

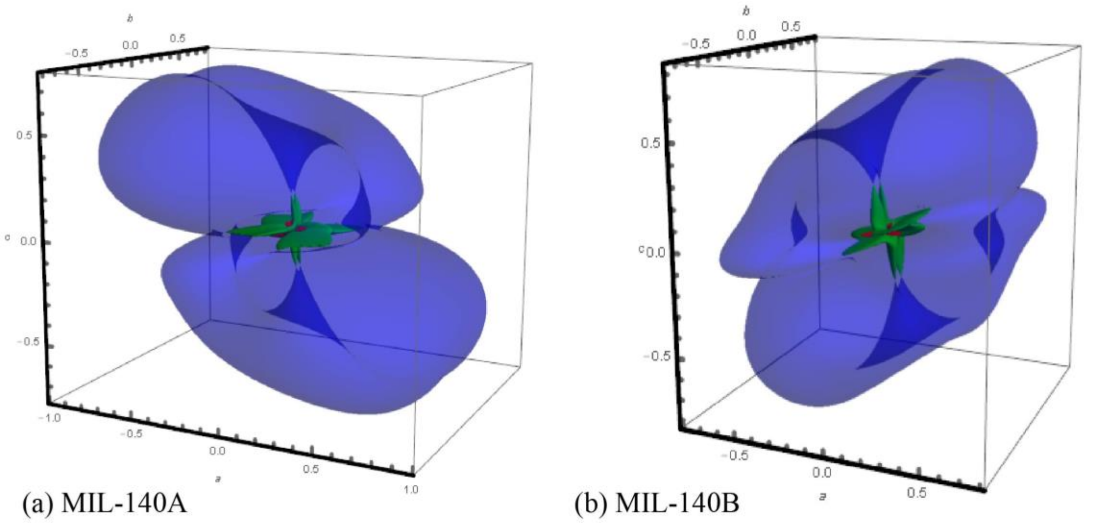

(a) MIL-140A (b) MIL-140B

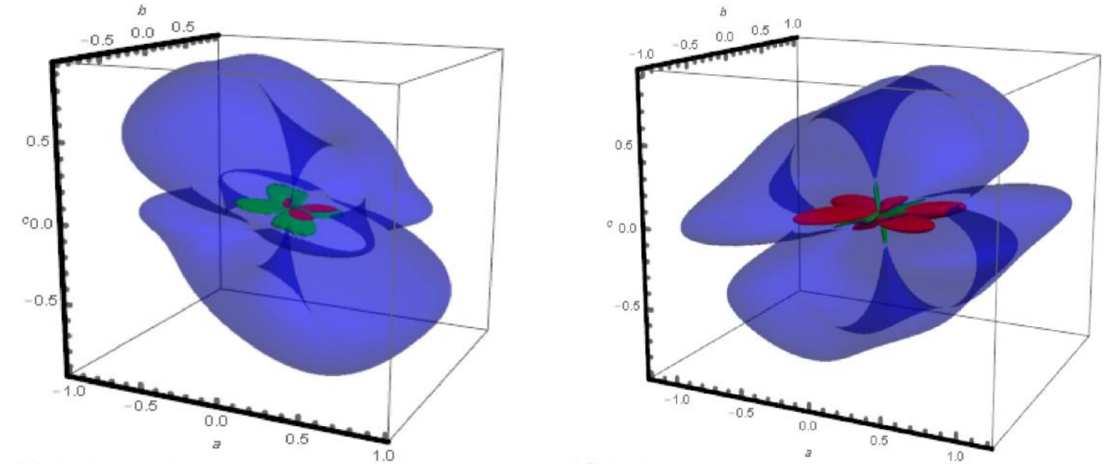

(c) MIL-140C (d) MIL-140D

Figure A4.3. Anisotropic Poisson's ratio plots for (a) MIL-140A, (b) MIL-140B, (c) MIL-140C and (d) MIL-140D.

A5 Additional Vibrational Data (Chapter 5)

A5.1 ZIF Lattice Parameter Comparisons

Summarised below are the comparisons of lattice parameters calculated from DFT (for ideal crystalline structures) versus experimental values reported in the literature.[206]

ZIF-4				
Method	*Lattice parameters* (Å)			*Volume* (Å^3)
	a	*b*	*c*	
Experimental CIF	15.40	15.31	18.43	4342.1
PBE-D	15.42	15.34	18.62	4406.0
• Average error in lattice parameters: 0.49%				

ZIF-7			
Method	*Lattice parameters* (Å)		*Volume* (Å^3)
	a	*b*	
Experimental CIF	22.99	15.76	7214.6
PBE	23.26	16.07	7528.5
PBE-D	21.38	16.42	6499.5
• Average error in lattice parameters using PBE is 1.56%. The error is relatively higher for PBE-D (5.57%) due to dispersion correction overestimating the interactions caused by extended aromaticity of the bulky benzimidazolate ligands. Figure A5.1 shows that the predicted vibrational spectra are consistent with experiments.			

ZIF-8				
Method	*Lattice parameters* (Å)			*Volume* (Å^3)
	a	*b*	*c*	
Experimental CIF	16.99	16.99	16.99	4906.1
PBE-D	16.87	16.95	17.16	4907.4
• Average error in lattice parameters: 0.66%				

The symmetry was lowered in the optimisation of ZIF-8, due to imaginary frequencies being present when using the experimentally assigned space group (293 K). To account for this effect, the symmetry of the system was relaxed to allow for a stable structure with minimum potential energy to be optimised.

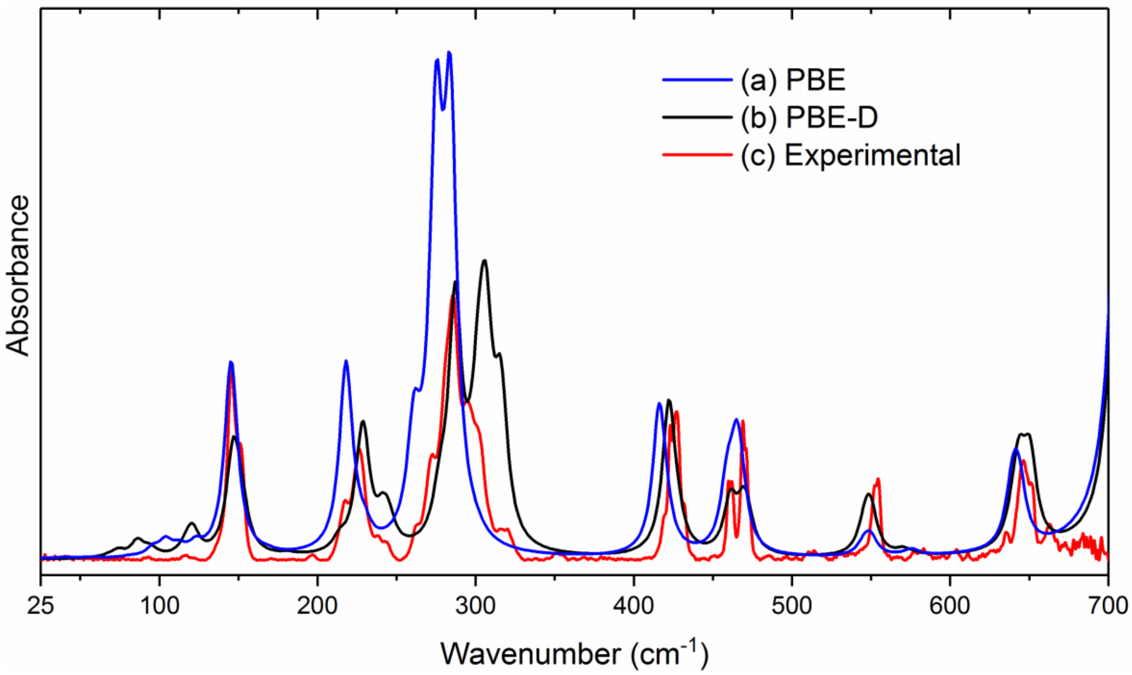

Figure A5.1. Comparison of the far-IR (FIR) spectra of ZIF-7 in the 25–700 cm^{-1} region between (a) PBE, (b) PBE-D and (c) synchrotron radiation FIR measurements.

A5.2 MIL-140 Lattice Parameter Comparisons

Summarised below is the comparison of lattice parameters calculated from DFT (for ideal crystalline structures) versus experimental values reported in the literature.[147]

MIL-140A					
Method	*Lattice parameters* (Å)				*Volume* (Å^3)
	a	*b*	*c*	*β*	
Experimental CIF	24.42	11.18	7.80	103.9	2068.4
PBE	24.89	11.28	7.98	102.7	2239.7
PBE-D	24.91	11.26	7.83	104.5	2195.0

- Average difference in experimental and theoretical lattice parameters for PBE: 1.55%
- Average difference in experimental and theoretical lattice parameters for PBE-D: 0.89%

A5.3 Vibrational Modes of ZIFs in the Spectral Region < 700 cm^{-1}

Table A5.1. Assignment of vibrational modes < 700 cm^{-1} of ZIF-4.

Structure	Wavenumber (cm^{-1})	Energy Loss (meV)	Description of vibrational motions
ZIF-4	< 100	< 12.4	See Table A5.5
	100–185	12.4–22.9	4-Membered and 6-Membered Ring Deformation; Ligand Rotation (Rocking)
	185–275	22.9–34.1	N–Zn–N Bending and Zn–N Stretching (Tetrahedral Deformation); Ligand Rotation (Rocking)
	285–325	35.3–40.3	Zn–N Stretching (Belonging to $\mathrm{ZnN_4}$ Tetrahedra)
	640–700	79.3–86.8	Aromatic Ring Deformation (In-Plane and Out-of-Plane)

Table A5.2. Assignment of vibrational modes < 700 cm^{-1} of ZIF-7.

Structure	Wavenumber (cm^{-1})	Energy Loss (meV)	Description of vibrational motions
ZIF-7	< 100	< 12.4	See Table A5.6
	100–150	12.4–18.6	4-Membered and 6-Membered Ring Deformation; Ligand Rocking
	150–225	18.6–27.9	N–Zn–N Bending and Zn–N Stretching (Tetrahedral Deformation) (Due to the symmetry of the mode at 153.8 cm^{-1} it results in 6-membered ring breathing/pore expansion)
	225–245	27.9–30.4	Bending at the Bridge of the Aromatic Rings (Due to the symmetry of the mode at 234.3 cm^{-1} it results in 6-membered ring gate opening)
	275–290	34.1–36.0	Zn–N Stretching
	295–315	36.6–39.1	Ligand Twisting (Torsion)
	420–430	52.1–53.3	Phenyl Ring Distortion (Ring Flapping/Wagging)
	460–470	57–58.3	Ligand Bending (Zn–N–C and N–C*–C) *Ring Bridging
	545–700	67.6–86.8	Aromatic Ring Deformation (In-Plane and Out-of-Plane)

Table A5.3. Assignment of vibrational modes < 700 cm^{-1} of ZIF-8.

Structure	Wavenumber (cm^{-1})	Energy Loss (meV)	Description of vibrational motions
ZIF-8	< 100	< 12.4	See Table A5.7
	100–195	12.4–24.2	4-Membered and 6-Membered Ring Deformation; Ligand Rotation (Rocking) (Due to the symmetry of the mode at 101.1 cm^{-1} it results in 4MR gate opening, 126.3 cm^{-1} results in 4MR and 6MR gate opening and 131.3 cm^{-1} results in 4MR gate opening)
	195–245	24.2–30.4	N–Zn–N Bending and Zn–N Stretching (Tetrahedral Deformation)
	260–270	32.2–33.5	Ligand Bending (Methyl Group Out-of-Plane Rocking)
	280–305	34.7–37.8	Zn–N Stretching
	415–425	51.5–52.7	Ligand Bending (Zn–N–C and N–C–Me)
	638–700	79.1–86.8	Aromatic Ring Deformation (In-Plane and Out-of-Plane)

A5.4 MP2 Harmonic Frequency Calculations of Imidazole Molecules

To further pinpoint the exact nature of the vibrational modes, the theoretical spectra of the isolated gas-phase molecules that constitute the organic bridging linkers in each ZIF material were calculated. The minimum energy structure and harmonic frequency calculations for the three individual organic linker molecules: imidazole (Im), benzimidazole (bIm), and 2-methylimidazole (mIm), were carried out with the Gaussian 09 code.[207] The calculations were performed at the MP2 level of theory[205] with the aug-cc-pVDZ basis set.[208]

The predictions obtained are tabulated in Table A5.4 below, which are found to be consistent with spectroscopic measurements available in the literature.[209-211] Vibrational signatures of the isolated molecular systems confirmed that the major vibrational modes of ZIFs are indeed those that involve a contribution from the inorganic building units (ZnN_4 tetrahedra). On this basis, certain modes corresponding to organic linker vibrations are being shifted to lower energy levels upon formation of 3D extended frameworks.

Table A5.4. Theoretical IR-active vibrational modes of the imidazole-based molecules.

Organic Linker (Ligand)	Energy band (cm^{-1})	Description of vibrational modes
Imidazolate (Im) 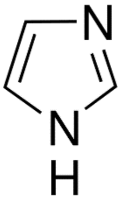 	550, 644, 680, 735, 819, 868	Out-of-Plane Ring Deformation
	903, 940	In-Plane Ring Deformation
	1070, 1090, 1138, 1164, 1275, 1365, 1435, 1495, 1553	C–C/C–N Stretch and C–H Bend
	3250, 3254	Asymmetric C–H Stretch
	3280	Symmetric C–H Stretch
	3650	N–H Stretch

Benzimidazole (bIm) 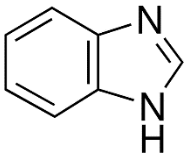	226	Bend at the Bridging of the Rings
	256	Asymmetric Ring Rotation
	416	N–C*–C Bend (* Ring Bridging)
	434	Phenyl Ring Deformation (Wing Flapping)
	475, 549, 594, 627, 651, 750, 788, 790, 857, 874, 884, 944, 945, 988	In-plane and Out-of-plane Ring Deformation
	1025, 1092, 1124, 1161, 1198, 1268, 1283, 1330, 1383, 1419, 1471, 1515, 1529, 1624, 1663	C–C/C–N Stretch and C–H Bend
	3174, 3182, 3194	Asymmetric C–H Stretch of Phenyl Ring
	3203	Symmetric C–H Stretch of Phenyl Ring
	3242	C–H Stretch of Im Ring
	3653	N–H Stretch
2-Methylimidazole (mIm) 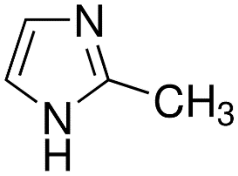	70	Methyl Rotation
	253	Out-of-Plane Me–Im Bend
	349	In-Plane Me–C–N Bend
	543, 641, 678, 690, 728, 859, 926, 963, 1001, 1050	In-plane and Out-of-plane Ring Deformation
	1093, 1131, 1179, 1270, 1378, 1403, 1427, 1459, 1482, 1513, 1593	C–C/C–N Stretch and C-H Bend
	3027	Symmetric C–H Stretch of Methyl Group
	3079, 3146	Asymmetric C–H Stretch of Methyl Group
	3248	Asymmetric C–H Stretch of Im Ring
	3278	Symmetric C–H Stretch of Im Ring
	3645	N–H Stretch

A5.5 Nature of THz Vibrational Modes < 100 cm^{-1} (~ 3 THz)

Table A5.5. Nature of the THz vibrational modes obtained from DFT for ZIF-4.

Wavenumber (cm^{-1})	Band (THz)	Activity	Distinct characteristics of the vibrational motions
6.98	**0.21**	**Raman**	**Strong 4-Membered Ring Shearing and Strong 6-Membered Ring Deformation (Phase Transition)**
14.40, 14.50, 17.96	0.43, 0.43, 0.54	Raman	4-Membered Ring Shearing and 6-Membered Ring Deformation
18.36, 20.47	0.55, 0.61	Raman	Strong 6-Membered and 4-Membered Ring Deformations
21.29, 21.89	0.64, 0.66	IR	
22.55	0.68	Raman	
23.34	0.70	IR	
26.65, 26.84, 27.04, 30.84	0.80, 0.80, 0.81, 0.92	Raman	
33.06	**0.99**	**Raman**	6-Membered and 4-Membered Ring Deformations; Ligand Rocking (Due to the symmetry of the mode at 33.06 cm^{-1} it results in gate opening)
33.08, 33.51	0.99, 1.00	IR	
33.95	1.02	Raman	
34.87	1.05	IR	
35.13, 37.70	1.05, 1.13	Raman	
40.57	1.22	IR	
41.12, 41.19, 43.20, 45.61, 47.28	1.23, 1.24, 1.30, 1.37, 1.42	Raman	
47.71	1.43	IR	
49.62, 49.77	1.49, 1.49	Raman	
52.25, 53.68	1.57, 1.61	IR	
53.93	1.62	Raman	
55.26, 55.56	1.66, 1.67	IR	
57.96, 58.01, 58.74	1.74, 1.74, 1.76	Raman	
62.01, 63.65	1.86, 1.91	IR	
63.74, 64.30	1.91, 1.93	Raman	
64.74	1.94	IR	

65.02, 65.92, 67.97, 68.57, 69.71	1.95, 1.98, 2.01, 2.06, 2.09	Raman	6-Membered and 4-Membered Ring Deformations; Ligand Rocking (Due to the symmetry of the mode at 33.06 cm^{-1} it results in gate opening)
69.91	2.10	IR	
70.67, 70.82	2.12, 2.12	Raman	
71.41, 71.74	2.14, 2.15	IR	
73.60, 74.07	2.21, 2.22	Raman	
76.83	2.30	IR	
79.50	2.38	Raman	
80.48	2.41	IR	
81.14, 83.13	2.43, 2.49	Raman	
83.14	2.49	IR	
83.82, 85.67	2.51, 2.57	Raman	
88.54, 88.97	2.65, 2.67	IR	
91.55, 93.93, 94.50, 95.51, 97.05	2.74, 2.82, 2.83, 2.86, 2.91	Raman	
97.21, 97.80	2.91, 2.93	IR	
98.86	2.96	Raman	
99.15	2.97	IR	
99.71, 99.77	2.99, 2.99	Raman	

Table A5.6. Nature of the THz vibrational modes obtained from DFT for ZIF-7.

Wavenumber (cm^{-1})	Band (THz)	Activity	Distinct characteristics of the vibrational motions
21.76, 21.76	**0.652**	**Raman**	**6-Membered Ring Deformation (Phase Transition); 4-Membered Ring Rotation**
21.81	**0.654**	**Raman**	**Strong 6-Membered Ring Rotational Expansion (Breathing); 4-Membered Ring Shearing Induced Breathing**
25.00, 25.00	0.75, 0.75	IR	Strong Asymmetric Ligand Flapping/Wagging
31.56	0.95	IR	Strong 6-Membered and 4-Membered Ring Deformation
38.73	1.16	Raman	Low-amplitude (weak) 6-Membered Ring Rotational Expansion (Breathing); 4-Membered Ring Shearing

38.77, 38.77	1.16, 1.16	Raman	Strong 6-Membered Ring Deformation; 4-Membered Ring Deformation; Asymmetric Ligand Flapping/Wagging
48.56	1.46	IR	6-Membered Ring Deformation; Light 4-Membered Ring Deformation; Asymmetric Ligand Flapping/Wagging
48.99	**1.47**	**Raman**	**Strong Symmetric Ligand Flapping/Wagging (Gate Opening)**
55.77, 55.77	1.67, 1.67	Raman	6-Membered and 4-Membered Ring Deformation
56.48, 56.48	1.69, 1.69	IR	6-Membered and 4-Membered Ring Deformation
60.22	1.81	Raman	Light 6-Membered Ring Translational Expansion (Breathing); 4-Membered Ring Rocking
61.74	1.85	IR	Light 6-Membered Deformation; Ligand Rocking
65.06, 65.06	1.95, 1.95	Raman	6-Membered and 4-Membered Ring Deformation
66.94	2.01	Raman	Strong 6-Membered and 4-Membered Ring Expansion (Breathing)
68.23, 68.23	2.05, 2.05	IR	Light 6-Membered Deformation; Ligand Rocking
74.16, 74.16	2.22, 2.22	Raman	Light 6-Membered and 4-Membered Ring Deformation; Ligand Rocking
74.16, 74.16, 78.34	2.22, 2.22, 2.35	IR	Light 6-Membered and 4-Membered Ring Rocking; Ligand Rocking
78.49	2.35	Raman	6-Membered and 4-Membered Ring Rocking; Ligand Rocking
85.20, 85.20	2.55, 2.55	Raman	6-Membered Ring Deformation; Ligand Rocking
85.93	2.58	IR	Strong 6-Membered Ring Deformation; 4-Membered Ring Rocking
87.44, 87.44	2.62, 2.62	IR	6-Membered and 4-Membered Ring Deformation; Ligand Rocking
92.95	2.79	IR	Light 6-Membered Ring Deformation; 4-Membered Ring Rocking; Strong Ligand Rocking
94.26, 94.26	2.83, 2.62	IR	6-Membered Ring Deformation; 4-Membered Ring Rocking; Ligand Rocking
96.57	2.90	IR	6-Membered Ring Deformation; 4-Membered Ring Rocking
97.19	2.91	Raman	Ligand Rocking with 6-Membered Ring Rotational Expansion (Breathing); 4-Membered Ring Deformation

Table A5.7. Nature of the THz vibrational modes obtained from DFT for ZIF-8.

Wavenumber (cm^{-1})	Band (THz)	Activity	Distinct characteristics of the vibrational motions
18.38, 18.94, 20.08	**0.55, 0.57, 0.60**	**IR**	**6-Membered Ring Deformation (Phase Transition); 4-Membered Ring Rotation; Methyl Group Rotation**
21.84	**0.65**	**Raman**	**6-Membered Ring Rotation; 4-Membered Ring Shearing; Methyl Group Rotation**
30.81	0.92	Raman	Symmetric 4-Membered Ring Gate Opening with Strong Methyl Rotation Blocking Open Gates
33.36	**1.00**	**Raman**	**Symmetric 4-Membered Ring Gate Opening**
33.39, 34.73, 37.38	1.00, 1.04, 1.12	IR	Ligand Rocking (Asymmetric Gate Opening) and Methyl Group Rotation
42.73	1.28	Raman	4-Membered Ring Deformation (Some Gate Opening/Breathing); Strong Methyl Group Rotation
46.73, 47.20, 47.93	1.40, 1.41, 1.44	IR	6-Membered and Strong 4-Membered Ring Deformation (Some Gate Opening/Breathing); Strong Methyl Group Rotation
53.05, 54.10, 55.35	1.59, 1.62, 1.66	IR	6-Membered and Strong 4-Membered Ring Deformation; Methyl Group Rotation
60.19, 60.77, 60.78	1.80, 1.82, 1.82	IR	6-Membered and 4-Membered Ring Deformation; Methyl Group Rotation
61.92, 64.25	1.86, 1.93	IR	6-Membered and 4-Membered Ring Deformation
64.44	1.93	IR	6-Membered and 4-Membered Ring Deformation; Strong Methyl Group Rotation
64.61	1.94	Raman	Light 4-Membered Ring Shearing; Strong Methyl Group Rotation
65.55	1.97	IR	6-Membered and 4-Membered Ring Deformation; Light Methyl Group Rotation
67.10, 69.75	2.01, 2.09	IR	Ligand Rocking and Strong Methyl Group Rotation
75.32	2.26	Raman	Ligand Rocking and Methyl Group Rotation; Light 4-Membered Ring Breathing
77.05, 77.31	2.31, 2.32	IR	Ligand Rocking and Methyl Group Rotation; Light 6-Membered Ring Deformation
78.55	2.35	Raman	Ligand Rocking and Methyl Group Rotation
79.57, 79.99, 80.27	2.39, 2.40, 2.41	IR	6-Membered and 4-Membered Ring Deformation; Strong Methyl Group Rotation

81.38, 82.44	2.44, 2.47	IR	6-Membered and 4-Membered Ring Deformation; Light Methyl Group Rotation
82.86, 83.71	2.48, 2.51	IR	Ligand Rocking and Methyl Group Rotation
94.22	2.82	Raman	6-Membered Ring Deformation; 4-Membered Ring Breathing (Cage Opening)
94.90, 95.45	2.84, 2.86	IR	6-Membered and 4-Membered Ring Deformation
96.20, 96.75, 96.77	2.88, 2.90, 2.90	IR	6-Membered Ring Expansion; 4-Membered Ring Deformation
97.84	2.93	Raman	Ligand rocking; 4-Membered Ring Breathing
98.56	2.95	IR	6-Membered and 4-Membered Ring Deformation

A5.6 Overtones Associated with Higher-Order Vibrational Excitations

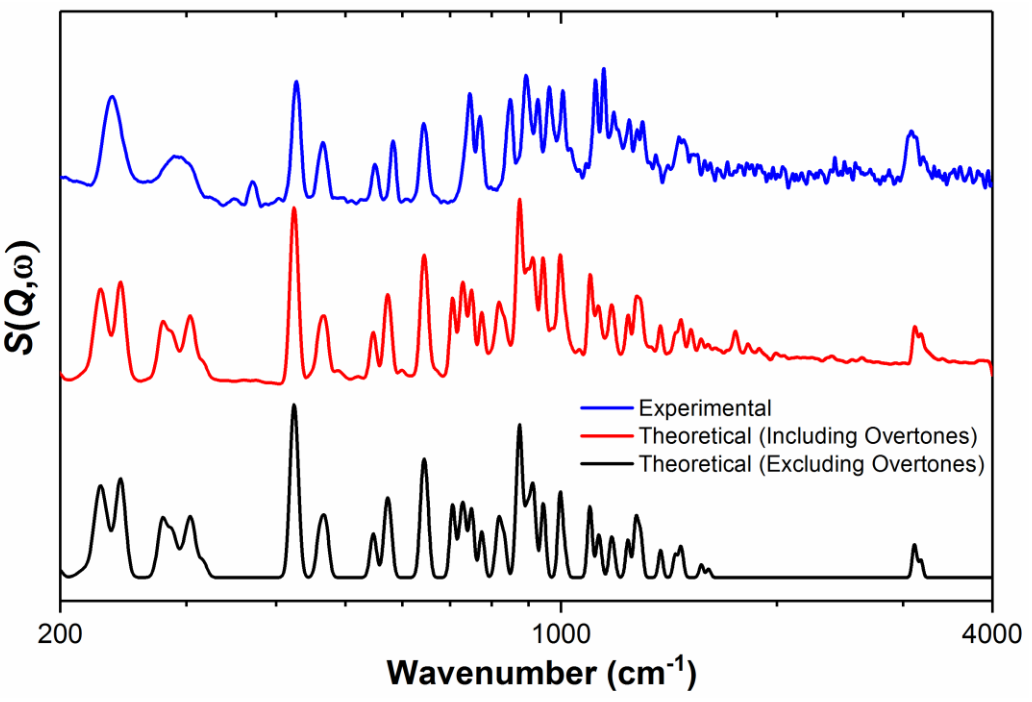

Figure A5.2. Comparison of DFT spectra, for ZIF-7, with and without the inclusion of higher order vibrational excitations.

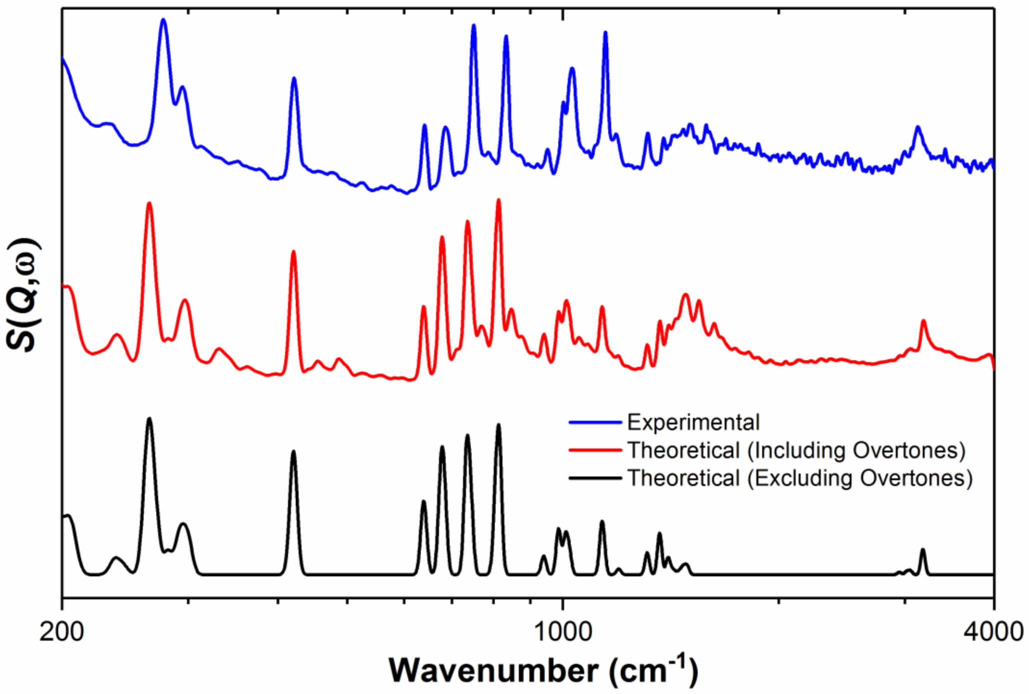

Figure A5.3. Comparison of DFT spectra, for ZIF-8, with and without the inclusion of higher order vibrational excitations.

A5.7 ZIF-4 Pore Modification Mechanisms Associated with THz Vibrations

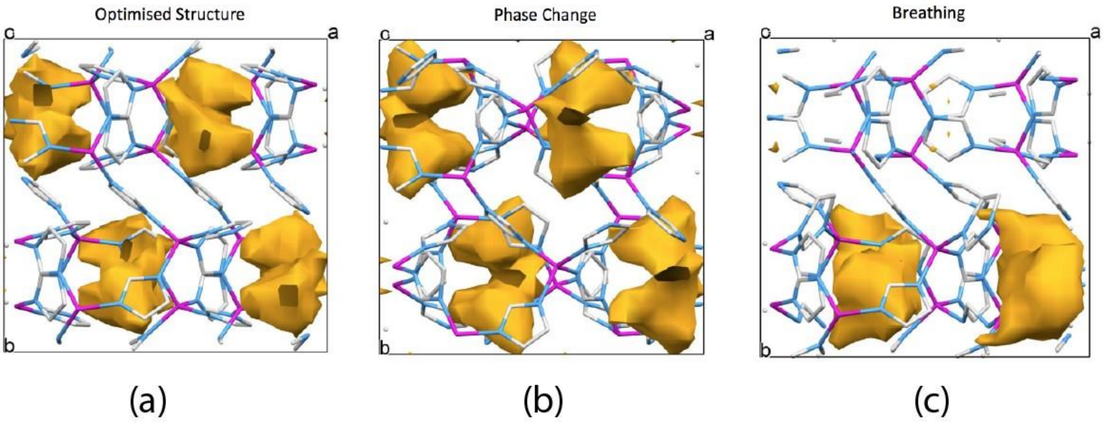

Figure A5.4. (a) DFT optimized structure where the solvent accessible volume (SAV) is represented by the yellow surfaces. (b) Increase of SAV by 2–3% due to the 0.2 THz soft mode. (c) Coalescence of adjacent SAV at 1 THz (gate-opening mode) to yield further raise in the SAV.

A5.8 Terahertz vibrational modes (< 600 cm^{-1}) of HKUST-1

IRREP = Irreducible representation; IP = in-plane; OP = out-of-plane

Table A5.8. Assignment of IR-active vibrational modes up to 600 cm^{-1}.

Mode (cm^{-1})	IRREP	Description
81.47	**F_{1u}**	**Organic Linker Trampoline-like Motion**
138.88	F_{1u}	Paddle Wheel Rocking with Organic Linker Rocking
142.91	F_{1u}	Paddle Wheel Deformation (Cu–Cu Buckling) and Translation with Linker Rocking
192.76	F_{1u}	Organic Linker Rocking
250.10	F_{1u}	Paddle Wheel Deformation (Strong Cu–Cu Buckling)
288.99	F_{1u}	Paddle Wheel Deformation (O–Cu–O Bending and Cu–Cu Buckling)
294.17 303.05	F_{1u} F_{1u}	Asymmetric Cu–O Stretching - Paddle Wheel Deformation (O–Cu–O Bending)
344.19	F_{1u}	Paddle Wheel Deformation with Linker Rocking
500.18	F_{1u}	OP Aromatic Ring Deformation
527.83	F_{1u}	IP Aromatic Ring Deformation with Partially Symmetric Cu–O Stretching
550.42	F_{1u}	Partially Symmetric Cu–O Stretching (Symmetric with respect to each carboxyl group)

Table A5.9. Assignment of Raman-active vibrational modes up to 600 cm^{-1}.

Mode (cm^{-1})	IRREP	Description
58.07	**F_{2g}**	**Strong Paddle Wheel Rotation with Organic Linker Trampoline-like Motion**
98.41	**A_g**	**Organic Linker Trampoline-like Motion (Symmetric Cluster Breathing)**
112.40	E_g	Strong Paddle Wheel Deformation and Swelling/Breathing
133.33	F_{2g}	Asymmetric Paddle Wheel Deformation with Organic Linker Rocking
138.93	F_{2g}	
150.91	E_g	Paddle Wheel Rocking
158.92	F_{2g}	
176.25	E_g	Organic Linker Rocking
198.81	F_{2g}	
214.35	E_g	Paddle Wheel Swelling/Breathing (Cu–Cu Stretching)
215.10	A_g	
263.44	E_g	Asymmetric Paddle Wheel Deformation (O–Cu–O Bending)
269.24	F_{2g}	Asymmetric Paddle Wheel Deformation (O–Cu–O Bending and Cu–Cu Rocking)
294.91	E_g	Symmetric Cu-O Stretching - Paddle Wheel Swelling/Breathing (O–Cu–O Bending) with Linker Rocking
297.00	F_{2g}	
303.36	A_g	Symmetric Cu-O Stretching - Paddle Wheel Swelling/Breathing (O–Cu–O Bending)
316.02	F_{2g}	Paddle Wheel Deformation with Linker Rocking
322.83	E_g	
475.16	F_{2g}	IP Aromatic Ring Deformation with Partially Symmetric Cu–O Stretching
499.81	F_{2g}	OP Aromatic Ring Deformation
503.05	E_g	
519.49	E_g	IP Aromatic Ring Deformation with Symmetric Cu–O Stretching
524.80	F_{2g}	
537.82	A_g	Symmetric Cu–O Stretching (Paddle Wheel Swelling/Breathing)

Table A5.10. Assignment of non-optically-active vibrational modes up to 600 cm^{-1}.

Mode (cm^{-1})	IRREP	Description
16.32	**F_{2u}**	**Strong Paddle Wheel Deformation and Translational Motion (Symmetric Cluster Rotation)**
20.43	**E_u**	**Strong Paddle Wheel Deformation and Translational Motion**
63.17	**F_{2u}**	**Paddle Wheel Deformation and Translational Motion with Organic Linker Rotating**
78.28	**B_g**	**Paddle Wheel Deformation with Organic Linker Rotating (Symmetric Cluster Rocking)**
79.66	A_u	Paddle Wheel Deformation with Organic Linker Rotating
81.72	F_{1g}	Paddle Wheel Deformation and Rotation with Organic Linker Rocking
84.54	F_{1g}	
94.15	**B_u**	**Organic Linker Trampoline-like Motion**
102.09	E_u	Strong Asymmetric Paddle Wheel Deformation and Rotation
103.01	F_{2u}	
107.99	A_u	
118.29	F_{1g}	
137.97	B_g	Paddle Wheel Rocking with Organic Linker Rocking (Symmetric Cluster Rocking)
139.94	F_{1g}	Paddle Wheel Rocking with Organic Linker Rocking
141.64	F_{2u}	
160.95	F_{1g}	Paddle Wheel Deformation
170.78	E_u	Organic Linker Rocking
174.88	B_u	Paddle Wheel Translational Motion
191.10	F_{2u}	Asymmetric Paddle Wheel Deformation (Cu–Cu Buckling) with Linker Rocking
194.69	E_u	Asymmetric Paddle Wheel Deformation (O–Cu–O Bending)

215.91	F_{1g}	Paddle Wheel Rotation with Strong Linker Rocking
239.39	F_{2u}	Paddle Wheel Deformation (Strong Cu–Cu Buckling) with Linker Rocking
262.09	F_{1g}	Asymmetric Paddle Wheel Deformation (O–Cu–O Bending)
268.62	B_g	
270.22	F_{1g}	Asymmetric Paddle Wheel Deformation (O–Cu–O Bending and Cu–Cu Rocking)
274.07	F_{2u}	Asymmetric Paddle Wheel Deformation (O–Cu–O Bending and Cu–Cu Buckling)
281.69	E_u	
298.14	B_u	
300.70	F_{2u}	
303.88	F_{1g}	Paddle Wheel Deformation with Linker Rocking
317.89	E_u	
330.41	F_{2u}	
412.51	A_u	IP Aromatic Ring Rotation with Asymmetric Cu–O Stretching
441.34	F_{2u}	
456.51	B_g	
456.68	F_{1g}	
476.25	F_{1g}	IP Aromatic Ring Deformation with Partially Symmetric Cu–O Stretching
492.60	F_{1g}	OP Aromatic Ring Deformation
498.36	F_{2u}	
499.94	E_u	
519.46	E_u	IP Aromatic Ring Deformation with Partially Symmetric Cu–O Stretching
523.70	F_{2u}	
552.23	B_u	Partially Symmetric Cu–O Stretching (Symmetric with respect to each carboxyl group)
590.28	E_u	Fully Asymmetric Cu–O Stretching (Asymmetric with respect to each carboxyl group)

A5.9 OSIRIS Low-Energy High-Resolution Inelastic Spectrum

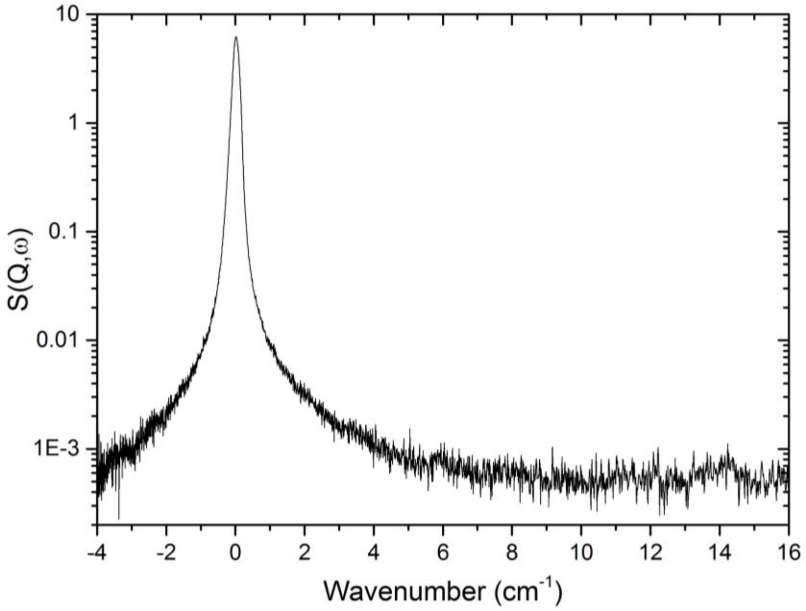

Figure A5.5. Low energy INS spectrum of MIL-140A near the elastic line recorded with the OSIRIS neutron spectrometer at 5 K. The intensity was calibrated with a vanadium sample and highlights the absence of vibrational modes in the low energy region.

A5.10 OSIRIS Diffraction Data of MIL-140A

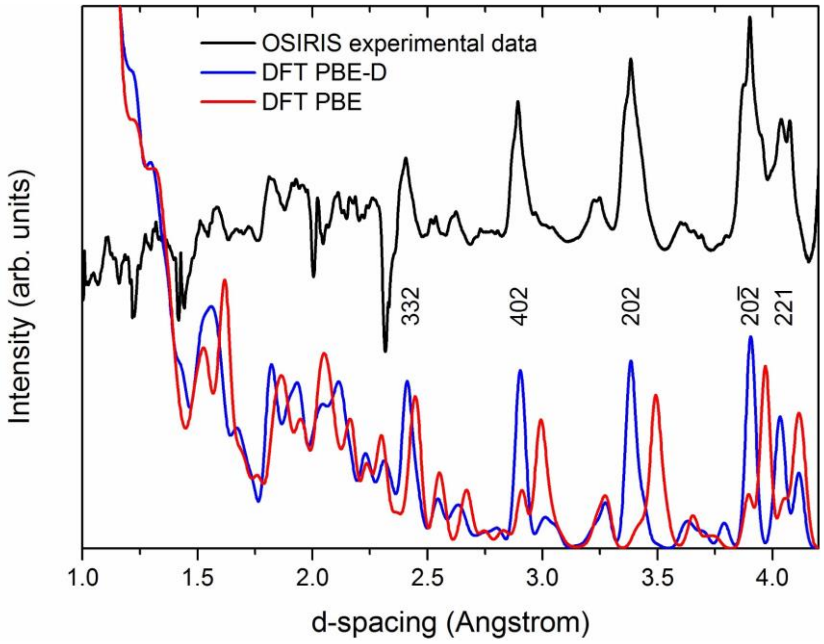

Figure A5.6. Neutron diffraction data measured using the OSIRIS spectrometer, compared to the predicted pattern for MIL-140A obtained by DFT using the PBE and PBE-D* functionals. The peaks obtained using PBE-D* are in better agreement with the experimental OSIRIS data.

A5.11 INS Spectra in the Range of 200–4000 cm^{-1}

New characteristic frequencies have been identified for semi-local motions such as organic linker and metal polyhedra deformations, as follows: 625–854 cm^{-1} for phenyl ring deformation; 486–595 cm^{-1} for Zr–O stretching of the polyhedra. Furthermore the experimental mid-IR (MIR) has been compared with theory, allowing for a full explanation of every region of the INS spectra, corresponding to local motions, as follows: 3123–3138 cm^{-1}, aromatic C–H stretching; 1281–1604 cm^{-1}, C–H bending; 1481–1543 cm^{-1}, C–O stretching; 1347–1429 cm^{-1}, C–C stretching; 859–1281 cm^{-1}, C–C stretching and C–O bending modes.

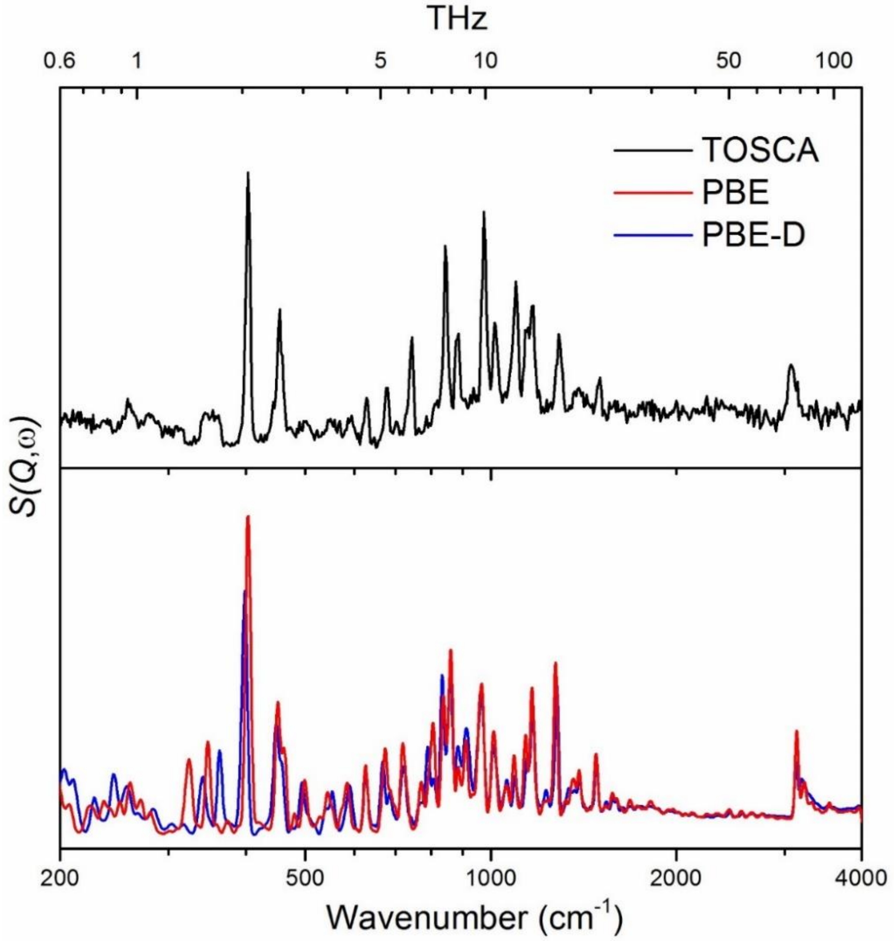

Figure A5.7. Comparison of the experimental and theoretical INS spectra in the 200–4,000 cm^{-1} range (log scale). The theoretical spectra include overtones to the 10th order, calculated using the aClimax software.[134]

A5.12 Comparison of PBE and B3LYP with Experimental INS Data

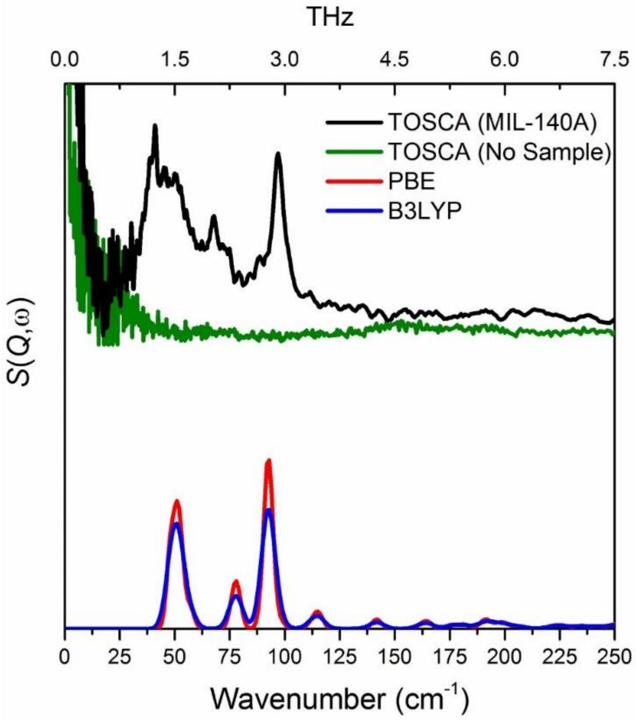

Figure A5.8. Comparison of the INS spectra obtained using the PBE and B3LYP DFT functionals with experiment in the 0–250 cm^{-1} region. The spectra show that there is a negligible difference observed between the two functionals.

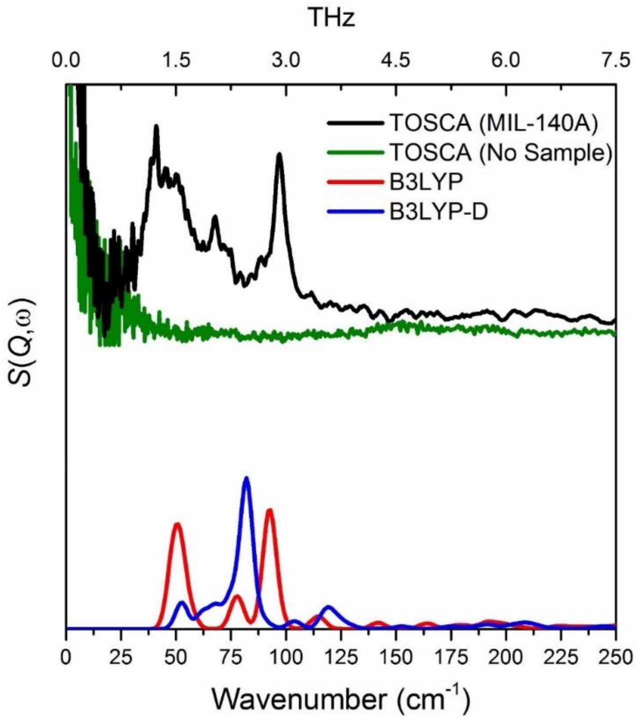

Figure A5.9. Comparison of the INS spectra obtained using the B3LYP and B3LYP-D DFT functionals with experiment in the 0–250 cm^{-1} region. The spectra show that the Grimme-D2 dispersion correction does not produce an accurate theoretical INS spectrum with the B3LYP functional, likely due to over-binding.

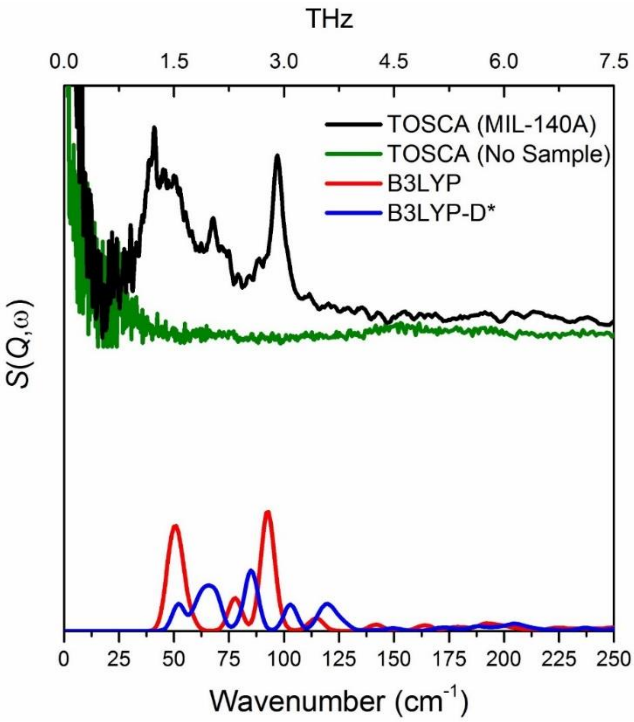

Figure A5.10. Comparison of the INS spectra obtained using the B3LYP and B3LYP-D* DFT functionals with experiment in the 0–250 cm^{-1} region. The spectra show that even using the dampened dispersion correction, designed to improve the agreement in crystal structures, still does not produce as accurate a theoretical INS spectrum as the one reported in Chapter 5 using the PBE-D* functional.

A5.13 Energetics and Solvent Accessible Volumes of the Type-A and -B Rotors

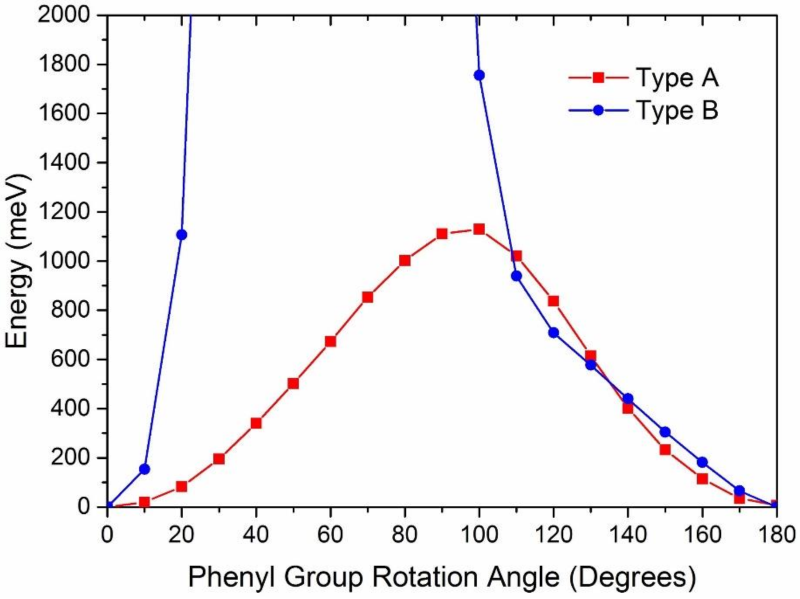

Figure A5.11. Comparison of the energy barriers of full Type-A and Type-B linker rotation. Highlighting a similar energy change between 110–180°, hence a similar response until the Type-B linkers overlapped.

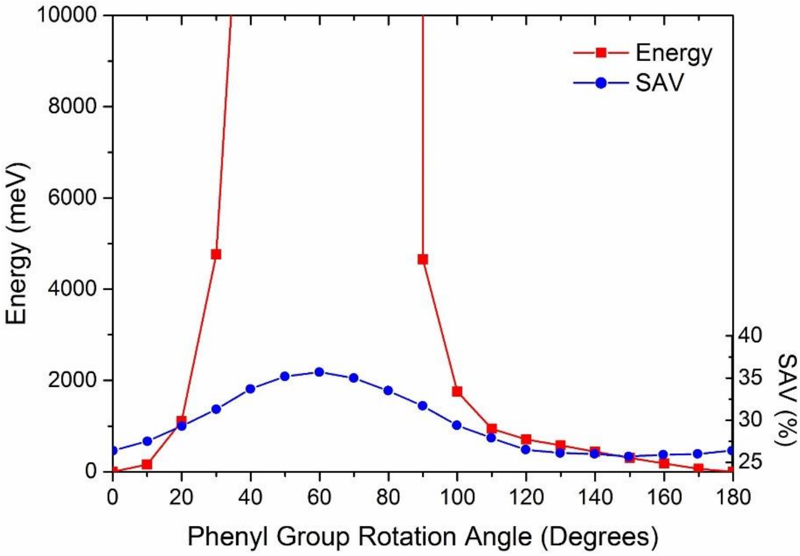

Figure A5.12. Comparison of the energy barrier and solvent assessable volume (SAV) changes for a full Type-B linker rotation. Highlighting that the significant increase in SAV is a direct result of the overlapping Type-B linkers.

A5.14 Type-A and Type-B Trampoline Motions

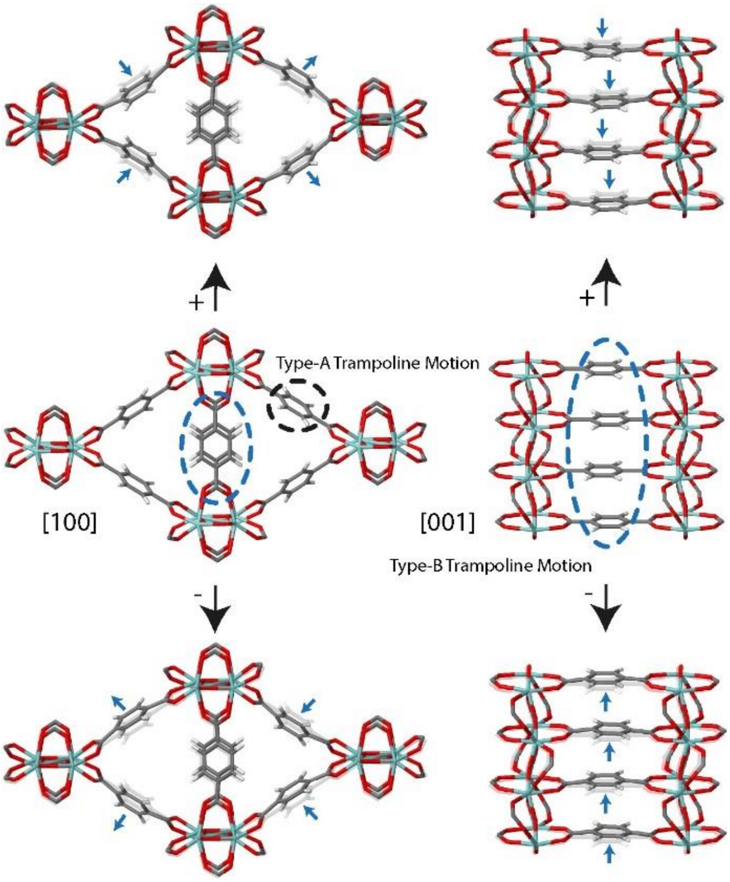

Figure A5.13. Simultaneous Type-A and Type-B trampoline motions of MIL-140A at 48.16 cm^{-1} (1.44 THz).

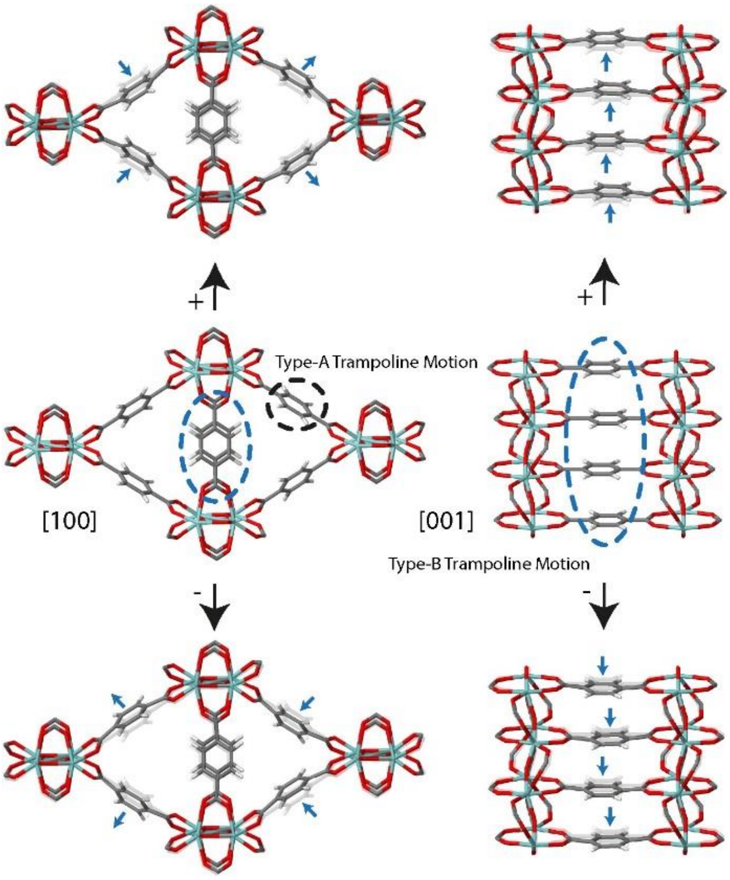

Figure A5.14. Simultaneous Type-A and Type-B trampoline motions of MIL-140A at 53.62 cm^{-1} (1.61 THz).

A6 Additional ZIF Amorphisation Data (Chapter 6)

A6.1 Mechanical Property Plots for ZIF-zni

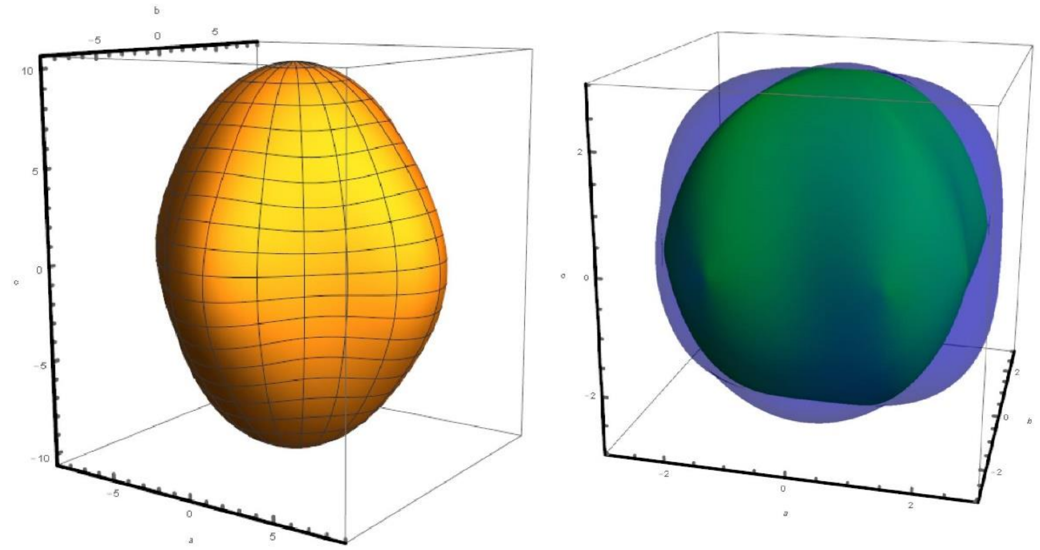

(a) Young’s Moduli

(b) Shear Moduli

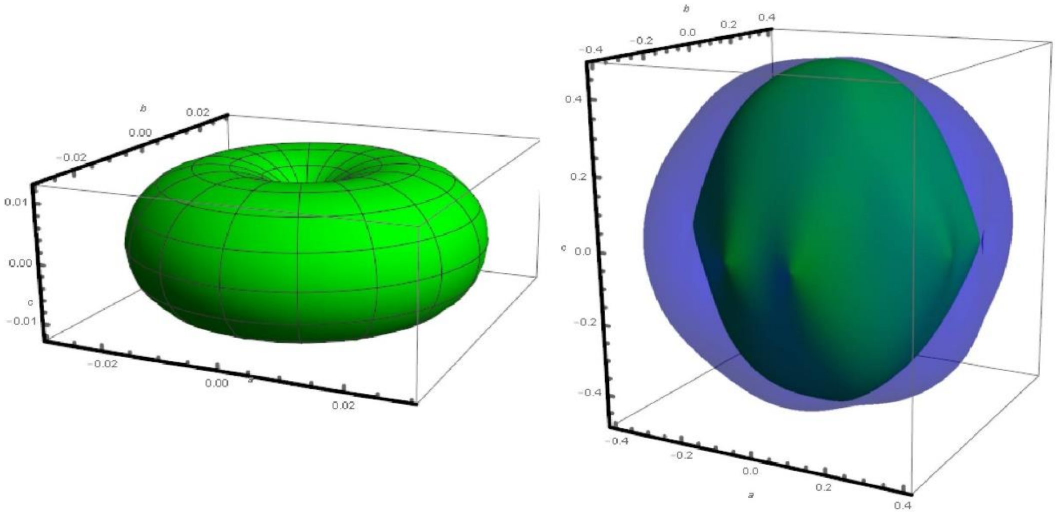

(c) Linear Compressibility

(d) Poisson’s Ratios

Figure A6.1. Plots of (a) Young’s moduli (in GPa), (b) shear moduli (in GPa), (c) linear compressibility (in TPa^{-1}) and (d) Poisson’s ratios of ZIF-zni.

A6.2 Curve Fitting Data

The curve fitting and resultant X_R values reported in Chapter 6 were obtained using the OriginPro 9.1 software. The X_R values with associated errors for each tetrahedral environment are shown below in Table A6.1.

Table A6.1. Curve Fitting Parameters for Chapter 6.

Tetrahedra	X_R	Standard Error	Adj. R-Squared	Reduced Chi-Square
$Zn(Im)_4$	0.045	8.198E-4	0.970	1.192
$Zn(mIm)_4$	0.032	3.913E-4	0.995	0.132

A7 Additional ZIF Dielectric Data (Chapter 7)

A7.1 PXRD Spectra of the ZIF Pellets

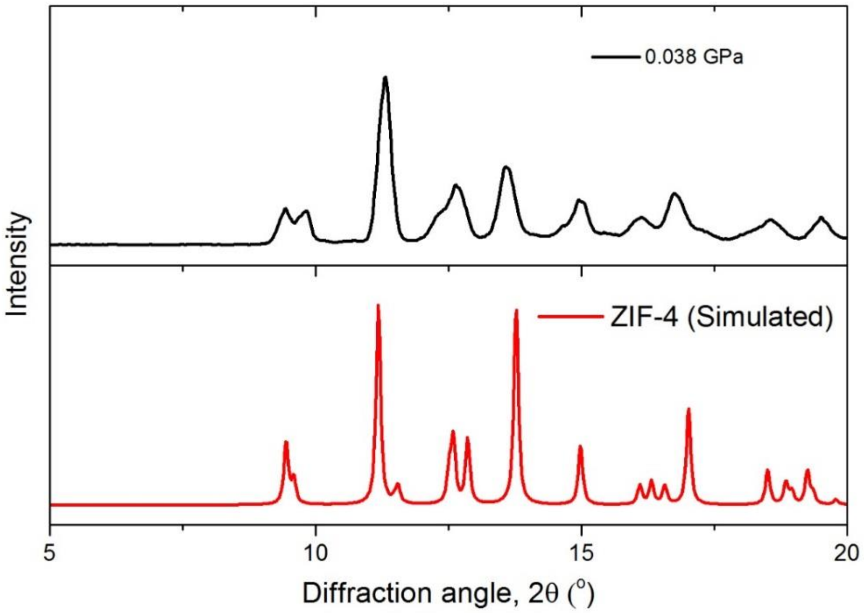

Figure A7.1. PXRD of the ZIF-4 pellet compared with the simulated spectrum from the CIF file in the literature.[60, 196]

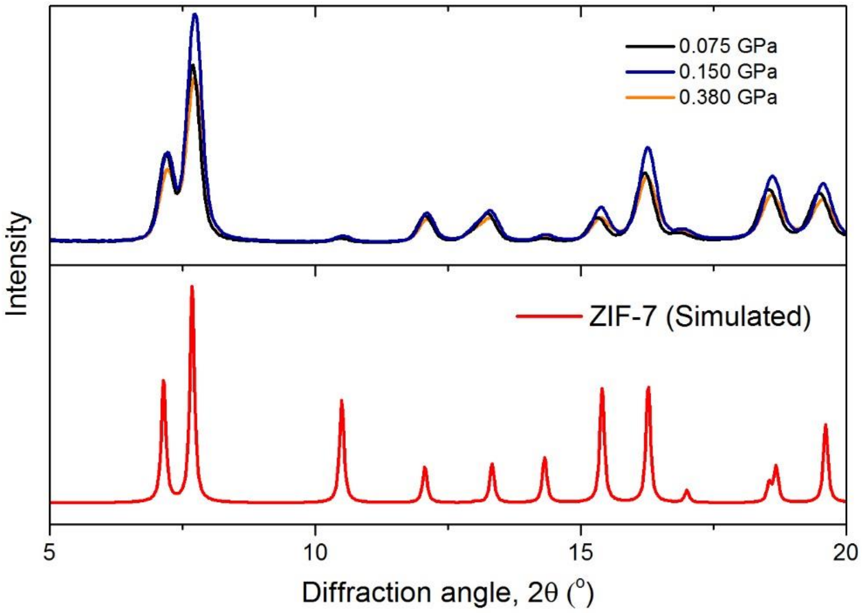

Figure A7.2. PXRD of the ZIF-7 pellets at the different pelletisation pressures compared with the simulated spectrum from the CIF file in the literature. The spectra show remarkable resilience to pelletisation pressure.

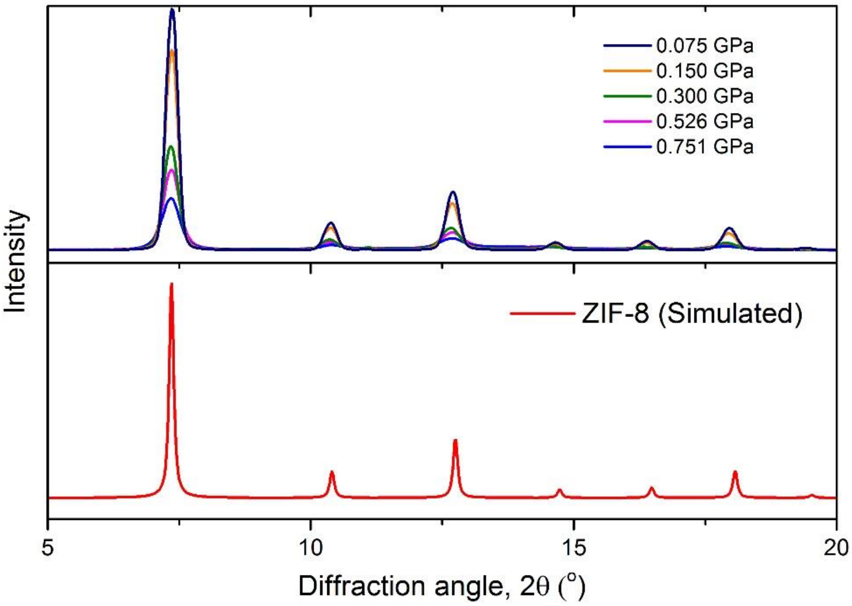

Figure A7.3. PXRD of the ZIF-8 pellets at the different pelletisation pressures compared with the simulated spectrum from the CIF file in the literature. The spectra show the loss of Bragg intensity linearly with pelletisation pressure.

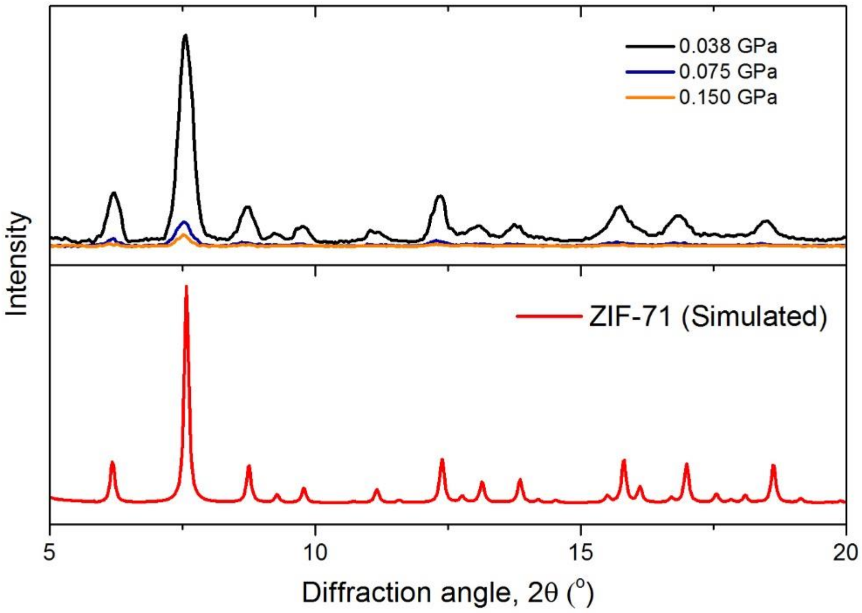

Figure A7.4. PXRD of the ZIF-71 pellets at the different pelletisation pressures compared with the simulated spectrum from the CIF file in the literature. The spectra show the loss of Bragg intensity linearly with pelletisation pressure.

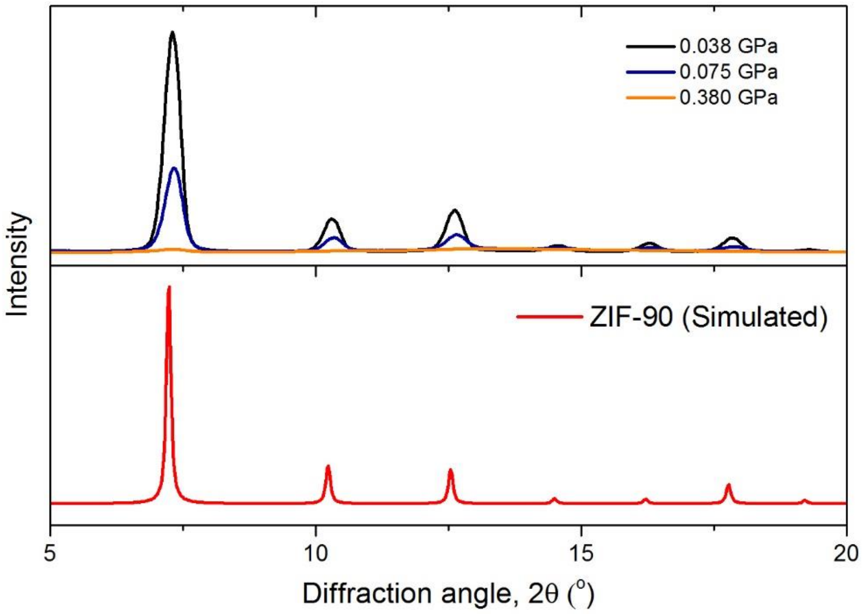

Figure A7.5. PXRD of the ZIF-90 pellets at the different pelletisation pressures compared with the simulated spectrum from the CIF file in the literature. The spectra show the loss of Bragg intensity linearly with pelletisation pressure.

A7.2 Reflectivity Spectra of the ZIF Structures

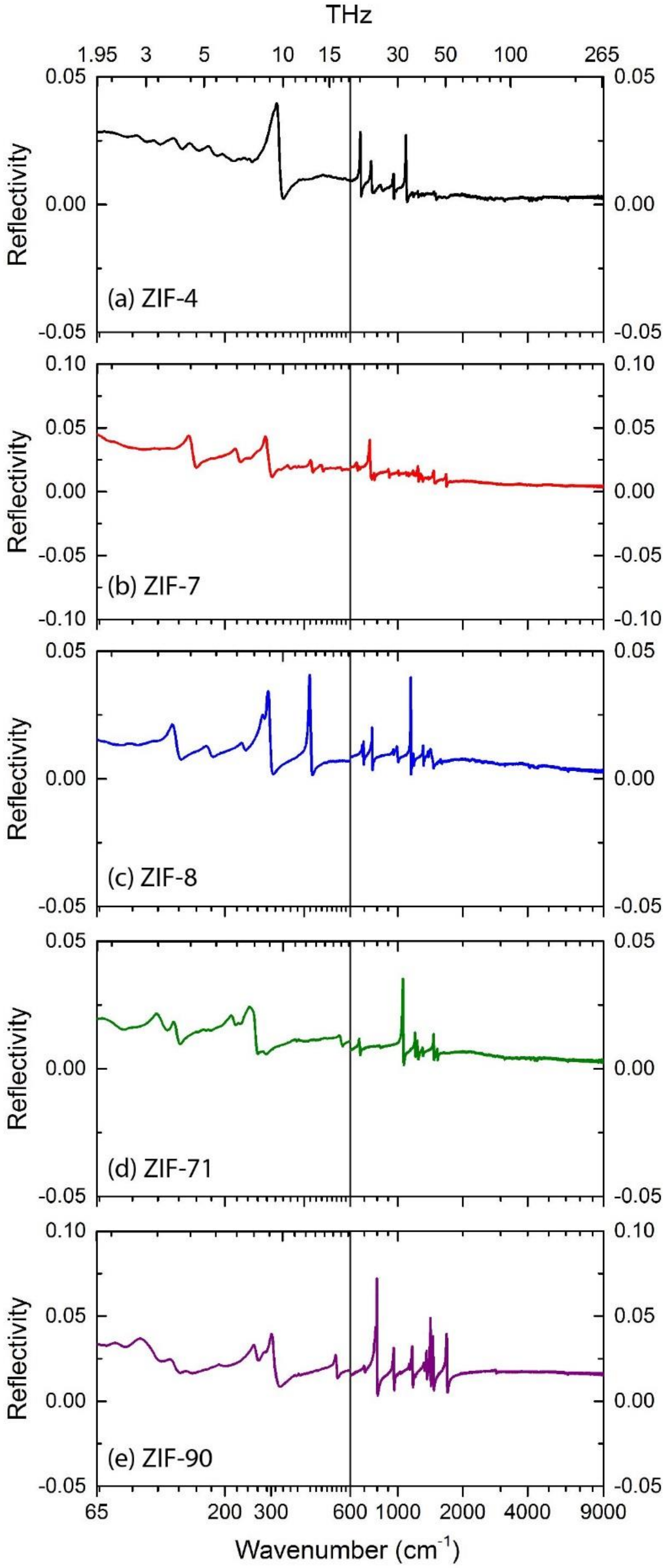

Figure A7.6. Spectra of the FIR and MIR spectral regions of (a) ZIF-4, (b) ZIF-7, (c) ZIF-8, (d) ZIF-71 and (e) ZIF-90. The spectra show the raw reflectivity data. The FIR and MIR regions are both plotted on separate logarithmic axes for additional clarity.

A7.3 Pressure-Induced Spectral Features and Correction of ZIF-8

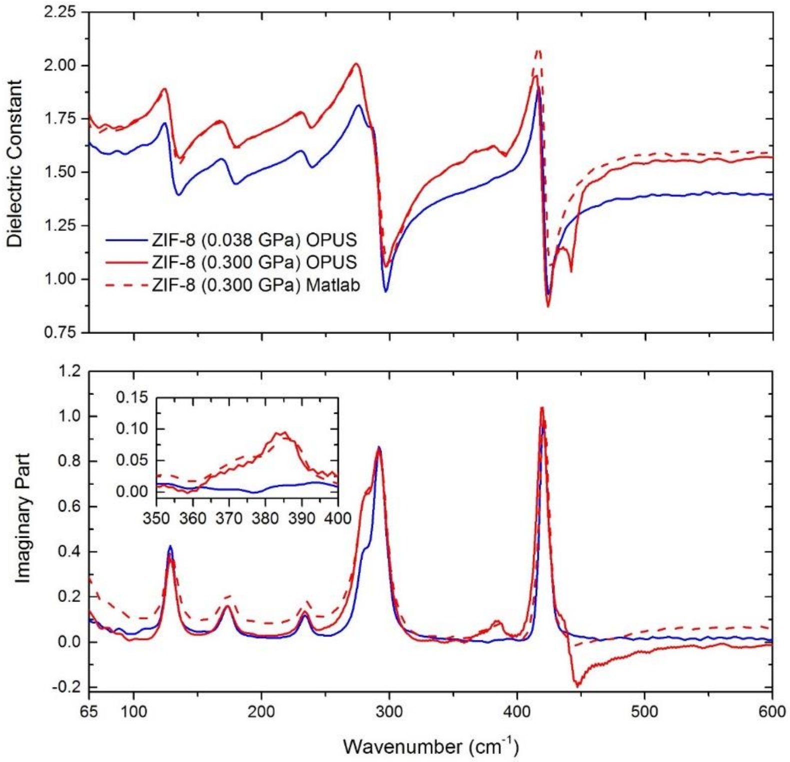

Figure A7.7. Plots of the real (dielectric) and imaginary (approximately absorption) spectra from the KKT of ZIF-8 showing the evolution of a new absorption feature at ~385 cm^{-1} upon a pelletisation pressure 0.300 GPa. An artefact is introduced at ~450 cm^{-1} due to the KKT being performed over a selected spectral range instead of zero to infinity. This is eliminated by extrapolation and shows any artificial negative values disappear.

A7.4 Roughness Measurements

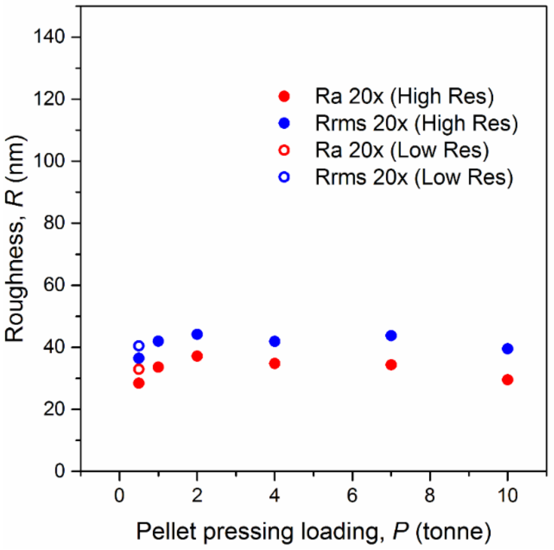

Figure A7.8. Plot of the surface roughness against pelletisation pressure for the ZIF-8 pellets.

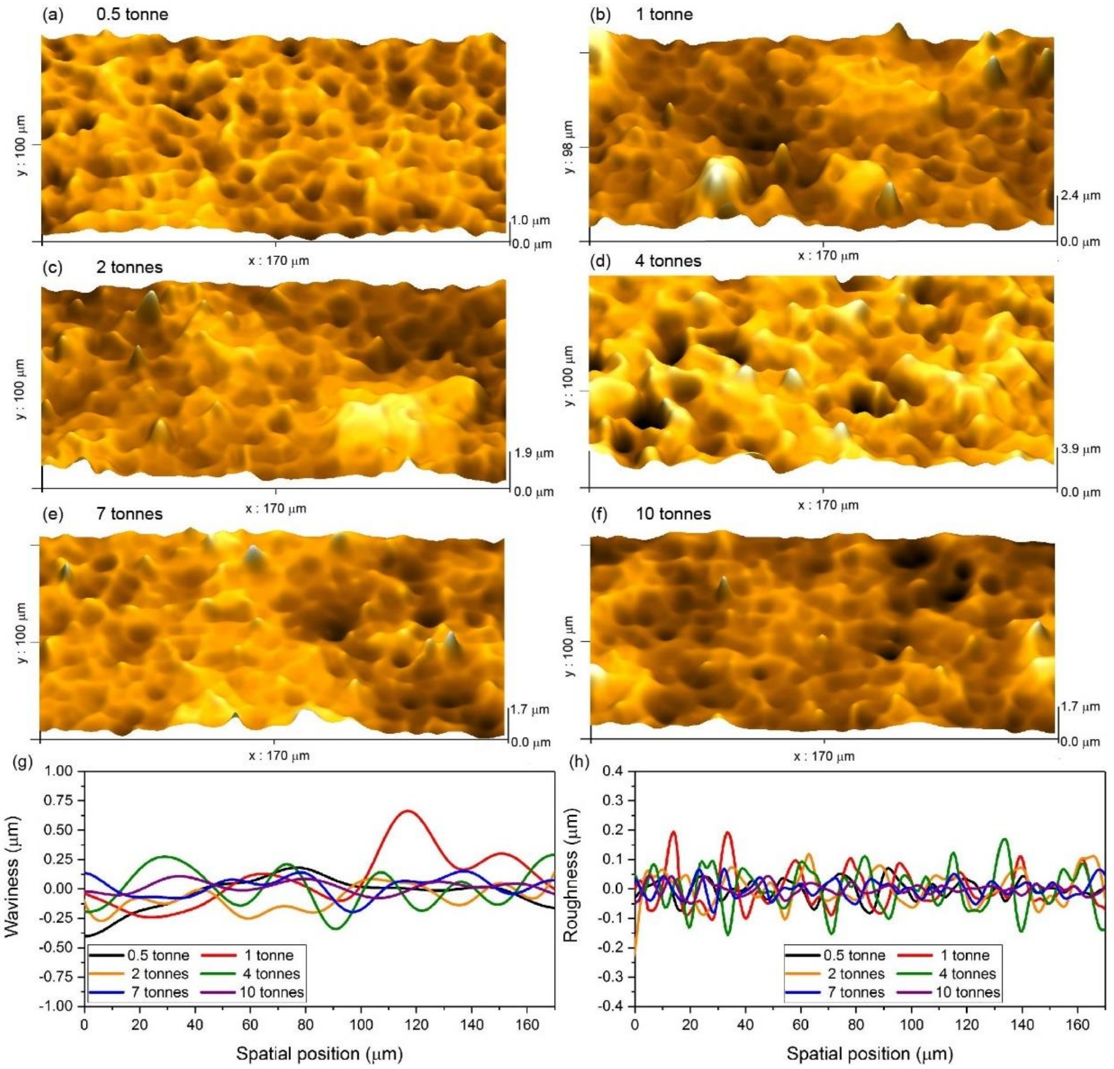

Figure A7.9. Morphology of pellets pressed by different loads to evaluate surface roughness. Reconstructed 3D surface profiles (using Alicona InfiniteFocus, 50x objective magnification equipped with 20 nm vertical resolution) of pellets pressed under loads (a) 0.5 tonne, (b) 1 tonne, (c) 2 tonnes, (d) 4 tonnes, (e) 7 tonnes, (f) 10 tonnes; (g) Linear waviness and (h) roughness profile (the width of profile line is 80 µm) of pellets under various loads.

Note: Figure A7.9 was produced by a collaborator.

References

1. A. K. Cheetham, C. N. Rao and R. K. Feller, *Chem. Commun.*, 2006, 4780-4795.
2. M. R. Ryder and J. C. Tan, *Mater. Sci. Technol.*, 2014, **30**, 1598-1612.
3. H. Furukawa, K. E. Cordova, M. O'Keeffe and O. M. Yaghi, *Science*, 2013, **341**, 1230444.
4. D. J. Tranchemontagne, J. L. Mendoza-Cortes, M. O'Keeffe and O. M. Yaghi, *Chem. Soc. Rev.*, 2009, **38**, 1257-1283.
5. M. O'Keeffe and O. M. Yaghi, *Chem. Rev.*, 2012, **112**, 675-702.
6. K. Sumida, D. L. Rogow, J. A. Mason, T. M. McDonald, E. D. Bloch, Z. R. Herm, T. H. Bae and J. R. Long, *Chem. Rev.*, 2012, **112**, 724-781.
7. M. P. Suh, H. J. Park, T. K. Prasad and D. W. Lim, *Chem. Rev.*, 2012, **112**, 782-835.
8. J. R. Li, J. Sculley and H. C. Zhou, *Chem. Rev.*, 2012, **112**, 869-932.
9. Y. Cui, Y. Yue, G. Qian and B. Chen, *Chem. Rev.*, 2012, **112**, 1126-1162.
10. L. E. Kreno, K. Leong, O. K. Farha, M. Allendorf, R. P. Van Duyne and J. T. Hupp, *Chem. Rev.*, 2012, **112**, 1105-1125.
11. J. C. Tan and A. K. Cheetham, *Chem. Soc. Rev.*, 2011, **40**, 1059-1080.
12. W. Zhang and R. G. Xiong, *Chem. Rev.*, 2012, **112**, 1163-1195.
13. M. Kurmoo, *Chem. Soc. Rev.*, 2009, **38**, 1353-1379.
14. J. Lee, O. K. Farha, J. Roberts, K. A. Scheidt, S. T. Nguyen and J. T. Hupp, *Chem. Soc. Rev.*, 2009, **38**, 1450-1459.
15. M. D. Allendorf and V. Stavila, *CrystEngComm*, 2015, **17**, 229-246.
16. H. C. Zhou, J. R. Long and O. M. Yaghi, *Chem. Rev.*, 2012, **112**, 673-674.
17. A. G. Slater and A. I. Cooper, *Science*, 2015, **348**, aaa8075.
18. P. Silva, S. M. Vilela, J. P. Tome and F. A. Almeida Paz, *Chem. Soc. Rev.*, 2015, **44**, 6774-6803.
19. W. Li, S. Henke and A. K. Cheetham, *APL Mater.*, 2014, **2**, 123902.
20. J. C. Tan, B. Civalleri, A. Erba and E. Albanese, *CrystEngComm*, 2015, **17**, 375-382.
21. I. Buchan, M. R. Ryder and J. C. Tan, *Cryst. Growth Des.*, 2015, **15**, 1991-1999.
22. B. Van de Voorde, R. Ameloot, I. Stassen, M. Everaert, D. De Vos and J.-C. Tan, *J. Mater. Chem. C*, 2013, **1**, 7716.
23. B. Van de Voorde, I. Stassen, B. Bueken, F. Vermoortele, D. De Vos, R. Ameloot, J.-C. Tan and T. D. Bennett, *J. Mater. Chem. A*, 2015, **3**, 1737-1742.
24. D. Bazer-Bachi, L. Assie, V. Lecocq, B. Harbuzaru and V. Falk, *Powder Technol.*, 2014, **255**, 52-59.
25. M. R. Ryder and J. C. Tan, *Dalton Trans.*, 2016, **45**, 4154-4161.
26. J. M. Ogborn, I. E. Collings, S. A. Moggach, A. L. Thompson and A. L. Goodwin, *Chem. Sci.*, 2012, **3**, 3011-3017.
27. S. C. McKellar and S. A. Moggach, *Acta Crystallogr B Struct Sci Cryst Eng Mater*, 2015, **71**, 587-607.
28. A. J. Graham, J. C. Tan, D. R. Allan and S. A. Moggach, *Chem. Commun.*, 2012, **48**, 1535-1537.
29. P. Zhao, T. D. Bennett, N. P. Casati, G. I. Lampronti, S. A. Moggach and S. A. Redfern, *Dalton Trans.*, 2015, **44**, 4498-4503.
30. P. Serra-Crespo, A. Dikhtiarenko, E. Stavitski, J. Juan-Alcaniz, F. Kapteijn, F. X. Coudert and J. Gascon, *CrystEngComm*, 2015, **17**, 276-280.

31. J. C. Tan, T. D. Bennett and A. K. Cheetham, *Proc. Natl. Acad. Sci. U. S. A.*, 2010, **107**, 9938-9943.
32. W. Li, A. Thirumurugan, P. T. Barton, Z. Lin, S. Henke, H. H. Yeung, M. T. Wharmby, E. G. Bithell, C. J. Howard and A. K. Cheetham, *J. Am. Chem. Soc.*, 2014, **136**, 7801-7804.
33. J. C. Tan, P. Jain and A. K. Cheetham, *Dalton Trans.*, 2012, **41**, 3949-3952.
34. S. Henke, W. Li and A. K. Cheetham, *Chem. Sci.*, 2014, **5**, 2392-2397.
35. R. J. Marshall, S. L. Griffin, C. Wilson and R. S. Forgan, *J. Am. Chem. Soc.*, 2015, **137**, 9527-9530.
36. G. Ferey and C. Serre, *Chem. Soc. Rev.*, 2009, **38**, 1380-1399.
37. J. N. Grima and R. Caruana-Gauci, *Nat. Mater.*, 2012, **11**, 565-566.
38. A. U. Ortiz, A. Boutin, A. H. Fuchs and F. X. Coudert, *Phys. Rev. Lett.*, 2012, **109**, 195502.
39. M. R. Ryder, B. Civalleri and J. C. Tan, *Phys. Chem. Chem. Phys.*, 2016, **18**, 9079-9087.
40. J. C. Tan, J. D. Furman and A. K. Cheetham, *J. Am. Chem. Soc.*, 2009, **131**, 14252-14254.
41. J. C. Tan, B. Civalleri, C. C. Lin, L. Valenzano, R. Galvelis, P. F. Chen, T. D. Bennett, C. Mellot-Draznieks, C. M. Zicovich-Wilson and A. K. Cheetham, *Phys. Rev. Lett.*, 2012, **108**, 095502.
42. T. D. Bennett, J. C. Tan, Y. Yue, E. Baxter, C. Ducati, N. J. Terrill, H. H. Yeung, Z. Zhou, W. Chen, S. Henke, A. K. Cheetham and G. N. Greaves, *Nat. Comm.*, 2015, **6**, 8079.
43. W. Zhou, H. Wu and T. Yildirim, *Chem. Phys. Lett.*, 2010, **499**, 103-107.
44. K. Banlusan, E. Antillon and A. Strachan, *J. Phys. Chem. C*, 2015, **119**, 25845-25852.
45. V. I. Hegde, J. C. Tan, U. V. Waghmare and A. K. Cheetham, *J. Phys. Chem. Lett.*, 2013, **4**, 3377-3381.
46. T. D. Bennett, P. J. Saines, D. A. Keen, J. C. Tan and A. K. Cheetham, *Chem. Eur. J.*, 2013, **19**, 7049-7055.
47. Z. A. D. Lethbridge, R. I. Walton, A. S. H. Marmier, C. W. Smith and K. E. Evans, *Acta Mater.*, 2010, **58**, 6444-6451.
48. G. N. Greaves, A. L. Greer, R. S. Lakes and T. Rouxel, *Nat. Mater.*, 2011, **10**, 823-837.
49. R. Gatt, L. Mizzi, J. I. Azzopardi, K. M. Azzopardi, D. Attard, A. Casha, J. Briffa and J. N. Grima, *Sci. Rep.*, 2015, **5**, 8395.
50. W. Li, M. R. Probert, M. Kosa, T. D. Bennett, A. Thirumurugan, R. P. Burwood, M. Parinello, J. A. Howard and A. K. Cheetham, *J. Am. Chem. Soc.*, 2012, **134**, 11940-11943.
51. W. Miller, K. E. Evans and A. Marmier, *Appl. Phys. Lett.*, 2015, **106**.
52. W. Cai and A. Katrusiak, *Nat. Comm.*, 2014, **5**, 4337.
53. A. B. Cairns, J. Catafesta, C. Levelut, J. Rouquette, A. van der Lee, L. Peters, A. L. Thompson, V. Dmitriev, J. Haines and A. L. Goodwin, *Nat. Mater.*, 2013, **12**, 212-216.
54. L. H. Rimmer, M. T. Dove, A. L. Goodwin and D. C. Palmer, *Phys. Chem. Chem. Phys.*, 2014, **16**, 21144-21152.
55. N. Lock, M. Christensen, Y. Wu, V. K. Peterson, M. K. Thomsen, R. O. Piltz, A. J. Ramirez-Cuesta, G. J. McIntyre, K. Noren, R. Kutteh, C. J. Kepert, G. J. Kearley and B. B. Iversen, *Dalton Trans.*, 2013, **42**, 1996-2007.

56. N. Lock, Y. Wu, M. Christensen, L. J. Cameron, V. K. Peterson, A. J. Bridgeman, C. J. Kepert and B. B. Iversen, *J. Phys. Chem. C*, 2010, **114**, 16181-16186.
57. V. K. Peterson, G. J. Kearley, Y. Wu, A. J. Ramirez-Cuesta, E. Kemner and C. J. Kepert, *Angew. Chem., Int. Ed.*, 2010, **49**, 585-588.
58. J. C. Tan, P. J. Saines, E. G. Bithell and A. K. Cheetham, *ACS Nano*, 2012, **6**, 615-621.
59. J. C. Tan, C. A. Merrill, J. B. Orton and A. K. Cheetham, *Acta Mater.*, 2009, **57**, 3481-3496.
60. T. D. Bennett, A. L. Goodwin, M. T. Dove, D. A. Keen, M. G. Tucker, E. R. Barney, A. K. Soper, E. G. Bithell, J. C. Tan and A. K. Cheetham, *Phys. Rev. Lett.*, 2010, **104**, 115503.
61. A. D. Katsenis, A. Puskaric, V. Strukil, C. Mottillo, P. A. Julien, K. Uzarevic, M. H. Pham, T. O. Do, S. A. Kimber, P. Lazic, O. Magdysyuk, R. E. Dinnebier, I. Halasz and T. Friscic, *Nat. Comm.*, 2015, **6**, 6662.
62. M. Fuentes-Cabrera, D. M. Nicholson, B. G. Sumpter and M. Widom, *J. Chem. Phys.*, 2005, **123**, 124713.
63. F. Birch, *J. Geophys. Res.*, 1952, **57**, 227-286.
64. W. Zhou and T. Yildirim, *Phys. Rev. B*, 2006, **74**, 180301(R).
65. D. F. Bahr, J. A. Reid, W. M. Mook, C. A. Bauer, R. Stumpf, A. J. Skulan, N. R. Moody, B. A. Simmons, M. M. Shindel and M. D. Allendorf, *Phys. Rev. B*, 2007, **76**, 184106.
66. A. Samanta, T. Furuta and J. Li, *J. Chem. Phys.*, 2006, **125**, 084714.
67. T. D. Bennett, S. Cao, J. C. Tan, D. A. Keen, E. G. Bithell, P. J. Beldon, T. Friscic and A. K. Cheetham, *J. Am. Chem. Soc.*, 2011, **133**, 14546-14549.
68. H. Wu, T. Yildirim and W. Zhou, *J. Phys. Chem. Lett.*, 2013, **4**, 925-930.
69. A. U. Ortiz, A. Boutin, A. H. Fuchs and F. X. Coudert, *J. Chem. Phys.*, 2013, **138**, 174703.
70. A. U. Ortiz, A. Boutin and F. X. Coudert, *Chem. Commun.*, 2014, **50**, 5867-5870.
71. M. Tafipolsky, S. Amirjalayer and R. Schmid, *J. Phys. Chem. C*, 2010, **114**, 14402-14409.
72. S. Bundschuh, O. Kraft, H. K. Arslan, H. Gliemann, P. G. Weidler and C. Woll, *Appl. Phys. Lett.*, 2012, **101**, 101910.
73. T. D. Bennett, J. Sotelo, J. C. Tan and S. A. Moggach, *CrystEngComm*, 2015, **17**, 286-289.
74. C. S. Coates, M. R. Ryder, J. A. Hill, J. C. Tan and A. L. Goodwin, *APL Mater.*, 2017, **5**, 066107.
75. I. Stassen, M. Styles, T. Van Assche, N. Campagnol, J. Fransaer, J. Denayer, J. C. Tan, P. Falcaro, D. De Vos and R. Ameloot, *Chem. Mater.*, 2015, **27**, 1801-1807.
76. T. L. Easun, F. Moreau, Y. Yan, S. Yang and M. Schroder, *Chem. Soc. Rev.*, 2017, **46**, 239-274.
77. B. Civalleri, F. Napoli, Y. Noel, C. Roetti and R. Dovesi, *CrystEngComm*, 2006, **8**, 364-371.
78. A. D. Becke, *J. Chem. Phys.*, 1993, **98**, 5648-5652.
79. P. J. Stephens, F. J. Devlin, C. F. Chabalowski and M. J. Frisch, *J. Phys. Chem.*, 1994, **98**, 11623-11627.
80. C. T. Lee, W. T. Yang and R. G. Parr, *Phys. Rev. B*, 1988, **37**, 785-789.
81. W. Zhou, H. Wu, T. J. Udovic, J. J. Rush and T. Yildirim, *J. Phys. Chem. A*, 2008, **112**, 12602-12606.

82. Y. Hu, H. Kazemian, S. Rohani, Y. Huang and Y. Song, *Chem. Commun.*, 2011, **47**, 12694-12696.
83. D. Fairen-Jimenez, S. A. Moggach, M. T. Wharmby, P. A. Wright, S. Parsons and T. Duren, *J. Am. Chem. Soc.*, 2011, **133**, 8900-8902.
84. Y. Hu, Z. Liu, J. Xu, Y. Huang and Y. Song, *J. Am. Chem. Soc.*, 2013, **135**, 9287-9290.
85. G. Kumari, K. Jayaramulu, T. K. Maji and C. Narayana, *J. Phys. Chem. A*, 2013, **117**, 11006-11012.
86. S. Aguado, G. Bergeret, M. P. Titus, V. Moizan, C. Nieto-Draghi, N. Bats and D. Farrusseng, *New J. Chem.*, 2011, **35**, 546-550.
87. H. Noei, O. Kozachuk, S. Amirjalayer, S. Bureekaew, M. Kauer, R. Schmid, B. Marler, M. Muhler, R. A. Fischer and Y. M. Wang, *J. Phys. Chem. C*, 2013, **117**, 5658-5666.
88. C. M. Brown, A. J. Ramirez-Cuesta, J. H. Her, P. S. Wheatley and R. E. Morris, *Chem. Phys.*, 2013, **427**, 3-8.
89. S. K. Callear, A. J. Ramirez-Cuesta, W. I. F. David, F. Millange and R. I. Walton, *Chem. Phys.*, 2013, **427**, 9-17.
90. G. N. Greaves, F. Meneau, O. Majerus, D. G. Jones and J. Taylor, *Science*, 2005, **308**, 1299-1302.
91. M. Shruti, L. Cheng-Hua, U. Muhammad and L. Kuang-Lieh, *Sci. Technol. Adv. Mater.*, 2015, **16**, 054204.
92. M. Usman, S. Mendiratta and K. L. Lu, *ChemElectroChem*, 2015, **2**, 786-788.
93. B. D. Hatton, K. Landskron, W. J. Hunks, M. R. Bennett, D. Shukaris, D. D. Perovic and G. A. Ozin, *Mater. Today*, 2006, **9**, 22-31.
94. B. Hoefflinger, *ITRS: The International Technology Roadmap for Semiconductors*, Springer, Berlin, Heidelberg, 2011.
95. *International Roadmap for Devices and Systems - More Moore White Paper*, 2016.
96. W. J. Li, J. Liu, Z. H. Sun, T. F. Liu, J. Lu, S. Y. Gao, C. He, R. Cao and J. H. Luo, *Nat. Comm.*, 2016, **7**, 11830.
97. K. Zagorodniy, G. Seifert and H. Hermann, *Appl. Phys. Lett.*, 2010, **97**, 251905.
98. R. Warmbier, A. Quandt and G. Seifert, *J. Phys. Chem. C*, 2014, **118**, 11799-11805.
99. L. M. Yang, P. Ravindran, P. Vajeeston and M. Tilset, *Phys. Chem. Chem. Phys.*, 2012, **14**, 4713-4723.
100. E. Redel, Z. B. Wang, S. Walheim, J. X. Liu, H. Gliemann and C. Woll, *Appl. Phys. Lett.*, 2013, **103**, 091903.
101. Z. G. Gu, S. C. Chen, W. Q. Fu, Q. Zheng and J. Zhang, *ACS Appl. Mater. Interfaces*, 2017, **9**, 7259-7264.
102. S. Van Cleuvenbergen, I. Stassen, E. Gobechiya, Y. Zhang, K. Markey, D. E. De Vos, C. Kirschhock, B. Champagne, T. Verbiest and M. A. van der Veen, *Chem. Mater.*, 2016, **28**, 3203-3209.
103. S. Eslava, L. P. Zhang, S. Esconjauregui, J. W. Yang, K. Vanstreels, M. R. Baklanov and E. Saiz, *Chem. Mater.*, 2013, **25**, 27-33.
104. S. S. Yu, G. J. Yuan and H. B. Duan, *RSC Adv.*, 2015, **5**, 45213-45216.
105. S. Mendiratta, M. Usman, C. C. Chang, Y. C. Lee, J. W. Chen, M. K. Wu, Y. C. Lin, C. P. Hsu and K. L. Lu, *J. Mater. Chem. C*, 2017, **5**, 1508-1513.
106. S. Mendiratta, M. Usman, T. T. Luo, S. F. Lee, Y. C. Lin and K. L. Lu, *CrystEngComm*, 2014, **16**, 6309-6315.

107. M. Sanchez-Andujar, S. Yanez-Vilar, B. Pato-Doldan, C. Gomez-Aguirre, S. Castro-Garcia and M. A. Senaris-Rodriguez, *J. Phys. Chem. C*, 2012, **116**, 13026-13032.
108. V. Stavila, A. A. Talin and M. D. Allendorf, *Chem. Soc. Rev.*, 2014, **43**, 5994-6010.
109. R. Dovesi, R. Orlando, A. Erba, C. M. Zicovich-Wilson, B. Civalleri, S. Casassa, L. Maschio, M. Ferrabone, M. De La Pierre, P. D'Arco, Y. Noel, M. Causa, M. Rerat and B. Kirtman, *Int. J. Quantum Chem.*, 2014, **114**, 1287-1317.
110. A. Mahmoud, A. Erba, K. E. El-Kelany, M. Rerat and R. Orlando, *Phys. Rev. B*, 2014, **89**, 045103.
111. P. Hohenberg and W. Kohn, *Phys. Rev.*, 1964, **136**, 864-871.
112. W. Kohn and L. J. Sham, *Phys. Rev.*, 1965, **140**, 1133-1138.
113. J. P. Perdew, K. Burke and M. Ernzerhof, *Phys. Rev. Lett.*, 1996, **77**, 3865-3868.
114. S. Grimme, J. Antony, S. Ehrlich and H. Krieg, *J. Chem. Phys.*, 2010, **132**, 154104.
115. B. Civalleri, C. M. Zicovich-Wilson, L. Valenzano and P. Ugliengo, *CrystEngComm*, 2008, **10**, 405-410.
116. J. M. Crowley, J. Tahir-Kheli and W. A. Goddard, 3rd, *J. Phys. Chem. Lett.*, 2016, **7**, 1198-1203.
117. P. Pernot, B. Civalleri, D. Presti and A. Savin, *J. Phys. Chem. A*, 2015, **119**, 5288-5304.
118. M. Ferrero, M. Rerat, R. Orlando and R. Dovesi, *J. Comput. Chem.*, 2008, **29**, 1450-1459.
119. M. Rerat, L. Maschio, B. Kirtman, B. Civalleri and R. Dovesi, *J. Chem. Theory Comput.*, 2016, **12**, 107-113.
120. M. Ferrero, B. Civalleri, M. Rerat, R. Orlando and R. Dovesi, *J. Chem. Phys.*, 2009, **131**, 214704.
121. C. H. Hendon, D. Tiana, M. Fontecave, C. Sanchez, L. D'Arras, C. Sassoye, L. Rozes, C. Mellot-Draznieks and A. Walsh, *J. Am. Chem. Soc.*, 2013, **135**, 10942-10945.
122. C. G. Broyden, *J. Inst. Maths Applics*, 1970, **6**, 76-90.
123. C. G. Broyden, *J. Inst. Maths Applics*, 1970, **6**, 222-231.
124. R. Fletcher, *Comput. J.*, 1970, **13**, 317-322.
125. D. Goldfarb, *Math. Comput.*, 1970, **24**, 23-26.
126. D. F. Shanno, *Math. Comput.*, 1970, **24**, 647-656.
127. J. F. Nye, *Physical Properties of Crystals*, Clarendon Press, Oxford, 1985.
128. W. F. Perger, J. Criswell, B. Civalleri and R. Dovesi, *Comput. Phys. Commun.*, 2009, **180**, 1753-1759.
129. *Mathematica, Version 10.1*, Wolfram Research Inc., 2015.
130. A. Marmier, Z. A. D. Lethbridge, R. I. Walton, C. W. Smith, S. C. Parker and K. E. Evans, *Comput. Phys. Commun.*, 2010, **181**, 2102-2115.
131. Y. Noel, C. M. Zicovich-Wilson, B. Civalleri, P. D’Arco and R. Dovesi, *Phys. Rev. B*, 2001, **65**.
132. L. Maschio, B. Kirtman, M. Rerat, R. Orlando and R. Dovesi, *J. Chem. Phys.*, 2013, **139**, 164101.
133. L. Maschio, B. Kirtman, M. Rerat, R. Orlando and R. Dovesi, *J. Chem. Phys.*, 2013, **139**, 164102.
134. A. J. Ramirez-Cuesta, *Comput. Phys. Commun.*, 2004, **157**, 226-238.
135. D. Tiana, C. H. Hendon and A. Walsh, *Chem. Commun.*, 2014, **50**, 13990-13993.

136. F. Fernandez-Alonso and D. L. Price, *Neutron Scattering*, Academic Press, New York, 2013.
137. P. Debye, *Ann. Phys.*, 1913, **348**, 49-92.
138. I. Waller, *Z. Phys.*, 1923, **17**, 398-408.
139. O. Arnold, J. C. Bilheux, J. M. Borreguero, A. Buts, S. I. Campbell, L. Chapon, M. Doucet, N. Draper, R. F. Leal, M. A. Gigg, V. E. Lynch, A. Markvardsen, D. J. Mikkelson, R. L. Mikkelson, R. Miller, K. Palmen, P. Parker, G. Passos, T. G. Perring, P. F. Peterson, S. Ren, M. A. Reuter, A. T. Savici, J. W. Taylor, R. J. Taylor, R. Tolchenoy, W. Zhou and J. Zikoysky, *Nucl. Instrum. Meth. A*, 2014, **764**, 156-166.
140. G. Cinque, M. D. Frogley, K. Wehbe, J. Filik and J. Pikjanka, *Synchrotron Radiat. News*, 2011, **24**, 24-33.
141. A. Greenaway, B. Gonzalez-Santiago, P. M. Donaldson, M. D. Frogley, G. Cinque, J. Sotelo, S. Moggach, E. Shiko, S. Brandani, R. F. Howe and P. A. Wright, *Angew. Chem., Int. Ed.*, 2014, **53**, 13483-13487.
142. S. S. Chui, S. M. Lo, J. P. Charmant, A. G. Orpen and I. D. Williams, *Science*, 1999, **283**, 1148-1150.
143. O. M. Yaghi and Q. Li, *MRS Bull.*, 2011, **34**, 682-690.
144. M. T. Wharmby, J. P. Mowat, S. P. Thompson and P. A. Wright, *J. Am. Chem. Soc.*, 2011, **133**, 1266-1269.
145. R. L. Martin, L. C. Lin, K. Jariwala, B. Smit and M. Haranczyk, *J. Phys. Chem. C*, 2013, **117**, 12159-12167.
146. J. Gascon, M. D. Hernandez-Alonso, A. R. Almeida, G. P. van Klink, F. Kapteijn and G. Mul, *ChemSusChem*, 2008, **1**, 981-983.
147. V. Guillerm, F. Ragon, M. Dan-Hardi, T. Devic, M. Vishnuvarthan, B. Campo, A. Vimont, G. Clet, Q. Yang, G. Maurin, G. Ferey, A. Vittadini, S. Gross and C. Serre, *Angew. Chem., Int. Ed.*, 2012, **51**, 9267-9271.
148. W. Liang, R. Babarao, T. L. Church and D. M. D'Alessandro, *Chem. Commun.*, 2015, **51**, 11286-11289.
149. B. Van de Voorde, D. Damasceno Borges, F. Vermoortele, R. Wouters, B. Bozbiyik, J. Denayer, F. Taulelle, C. Martineau, C. Serre, G. Maurin and D. De Vos, *ChemSusChem*, 2015, **8**, 3159-3166.
150. A. Buonaugurio, J. Graham, A. Buytendyk, K. H. Bowen, M. R. Ryder, Z. G. Keolopile, M. Haranczyk and M. Gutowski, *J. Chem. Phys.*, 2014, **140**, 221103.
151. Z. G. Keolopile, M. R. Ryder and M. Gutowski, *J. Phys. Chem. A*, 2014, **118**, 7385-7391.
152. Z. G. Keolopile, M. R. Ryder, B. Calzada, M. Gutowski, A. M. Buytendyk, J. D. Graham and K. H. Bowen, *Phys. Chem. Chem. Phys.*, 2017, **19**, 29760-29766.
153. A. Phan, C. J. Doonan, F. J. Uribe-Romo, C. B. Knobler, M. O'Keeffe and O. M. Yaghi, *Acc. Chem. Res.*, 2010, **43**, 58-67.
154. A. L. Spek, *J. Appl. Crystallogr.*, 2003, **36**, 7-13.
155. T. Beyer, G. M. Day and S. L. Price, *J. Am. Chem. Soc.*, 2001, **123**, 5086-5094.
156. M. R. Ryder, B. Civalleri, T. D. Bennett, S. Henke, S. Rudic, G. Cinque, F. Fernandez-Alonso and J. C. Tan, *Phys. Rev. Lett.*, 2014, **113**, 215502.
157. J. H. Cavka, S. Jakobsen, U. Olsbye, N. Guillou, C. Lamberti, S. Bordiga and K. P. Lillerud, *J. Am. Chem. Soc.*, 2008, **130**, 13850-13851.
158. S. B. Kalidindi, S. Nayak, M. E. Briggs, S. Jansat, A. P. Katsoulidis, G. J. Miller, J. E. Warren, D. Antypov, F. Cora, B. Slater, M. R. Prestly, C. Marti-Gastaldo and M. J. Rosseinsky, *Angew. Chem., Int. Ed.*, 2015, **54**, 221-226.

159. J. E. Mondloch, M. J. Katz, W. C. Isley, 3rd, P. Ghosh, P. Liao, W. Bury, G. W. Wagner, M. G. Hall, J. B. DeCoste, G. W. Peterson, R. Q. Snurr, C. J. Cramer, J. T. Hupp and O. K. Farha, *Nat. Mater.*, 2015, **14**, 512-516.
160. P. Deria, D. A. Gomez-Gualdron, W. Bury, H. T. Schaef, T. C. Wang, P. K. Thallapally, A. A. Sarjeant, R. Q. Snurr, J. T. Hupp and O. K. Farha, *J. Am. Chem. Soc.*, 2015, **137**, 13183-13190.
161. Q. Zhang, J. Su, D. Feng, Z. Wei, X. Zou and H. C. Zhou, *J. Am. Chem. Soc.*, 2015, **137**, 10064-10067.
162. X. Liu, N. K. Demir, Z. Wu and K. Li, *J. Am. Chem. Soc.*, 2015, **137**, 6999-7002.
163. H. Ledbetter and A. Migliori, *J. Appl. Phys.*, 2006, **100**, 063516.
164. A. L. Goodwin, D. A. Keen and M. G. Tucker, *Proc. Natl. Acad. Sci. U. S. A.*, 2008, **105**, 18708-18713.
165. G. W. Peterson, J. B. DeCoste, T. G. Glover, Y. Huang, H. Jasuja and K. S. Walton, *Micropor. Mesopor. Mat.*, 2013, **179**, 48-53.
166. O. Shekhah, J. Liu, R. A. Fischer and C. Woll, *Chem. Soc. Rev.*, 2011, **40**, 1081-1106.
167. Y. S. Li, F. Y. Liang, H. Bux, A. Feldhoff, W. S. Yang and J. Caro, *Angew. Chem., Int. Ed.*, 2010, **49**, 548-551.
168. N. Rangnekar, N. Mittal, B. Elyassi, J. Caro and M. Tsapatsis, *Chem. Soc. Rev.*, 2015, **44**, 7128-7154.
169. A. Betard and R. A. Fischer, *Chem. Rev.*, 2012, **112**, 1055-1083.
170. K. W. Chapman, G. J. Halder and P. J. Chupas, *J. Am. Chem. Soc.*, 2008, **130**, 10524-10526.
171. M. Maczka, W. Zierkiewicz, D. Michalska and J. Hanuza, *Spectrochim. Acta, Part A*, 2014, **128**, 674-680.
172. S. Yang, J. Sun, A. J. Ramirez-Cuesta, S. K. Callear, W. I. David, D. P. Anderson, R. Newby, A. J. Blake, J. E. Parker, C. C. Tang and M. Schroder, *Nat. Chem.*, 2012, **4**, 887-894.
173. P. A. Fleury, *Annu. Rev. Mater. Sci.*, 1976, **6**, 157-180.
174. P. Zhao, G. I. Lampronti, G. O. Lloyd, M. T. Wharmby, S. Facq, A. K. Cheetham and S. A. Redfern, *Chem. Mater.*, 2014, **26**, 1767-1769.
175. S. A. Moggach, T. D. Bennett and A. K. Cheetham, *Angew. Chem., Int. Ed.*, 2009, **48**, 7087-7089.
176. T. D. Bennett and A. K. Cheetham, *Acc. Chem. Res.*, 2014, **47**, 1555-1562.
177. A. Comotti, S. Bracco, T. Ben, S. Qiu and P. Sozzani, *Angew. Chem., Int. Ed.*, 2014, **53**, 1043-1047.
178. Y. Wu, A. Kobayashi, G. J. Halder, V. K. Peterson, K. W. Chapman, N. Lock, P. D. Southon and C. J. Kepert, *Angew. Chem., Int. Ed.*, 2008, **47**, 8929-8932.
179. M. Peplow, *Nature*, 2015, **525**, 18-21.
180. V. N. Vukotic, C. A. O'Keefe, K. Zhu, K. J. Harris, C. To, R. W. Schurko and S. J. Loeb, *J. Am. Chem. Soc.*, 2015, **137**, 9643-9651.
181. A. Comotti, S. Bracco, P. Valsesia, M. Beretta and P. Sozzani, *Angew. Chem., Int. Ed.*, 2010, **49**, 1760-1764.
182. M. Inukai, T. Fukushima, Y. Hijikata, N. Ogiwara, S. Horike and S. Kitagawa, *J. Am. Chem. Soc.*, 2015, **137**, 12183-12186.
183. A. J. Howarth, Y. Y. Liu, P. Li, Z. Y. Li, T. C. Wang, J. Hupp and O. K. Farha, *Nat. Rev. Mater.*, 2016, **1**, 15018.
184. D. A. Keen and M. T. Dove, *J. Phys.: Condens. Mat.*, 1999, **11**, 9263-9273.

185. D. W. Lewis, A. R. Ruiz-Salvador, A. Gomez, L. M. Rodriguez-Albelo, F. X. Coudert, B. Slater, A. K. Cheetham and C. Mellot-Draznieks, *CrystEngComm*, 2009, **11**, 2272-2276.

186. E. O. Beake, M. T. Dove, A. E. Phillips, D. A. Keen, M. G. Tucker, A. L. Goodwin, T. D. Bennett and A. K. Cheetham, *J. Phys.: Condens. Matter*, 2013, **25**, 395403.

187. M. T. Wharmby, S. Henke, T. D. Bennett, S. R. Bajpe, I. Schwedler, S. P. Thompson, F. Gozzo, P. Simoncic, C. Mellot-Draznieks, H. Tao, Y. Yue and A. K. Cheetham, *Angew. Chem., Int. Ed.*, 2015, **54**, 6447-6451.

188. T. D. Bennett, P. Simoncic, S. A. Moggach, F. Gozzo, P. Macchi, D. A. Keen, J. C. Tan and A. K. Cheetham, *Chem. Commun.*, 2011, **47**, 7983-7985.

189. A. U. Ortiz, A. Boutin, A. H. Fuchs and F. X. Coudert, *J. Phys. Chem. Lett.*, 2013, **4**, 1861-1865.

190. L. Vina, S. Logothetidis and M. Cardona, *Phys. Rev. B*, 1984, **30**, 1979-1991.

191. Y. C. Shen, P. C. Upadhya, E. H. Linfield and A. G. Davies, *Appl. Phys. Lett.*, 2003, **82**, 2350-2352.

192. M. R. Ryder, B. Van de Voorde, B. Civalleri, T. D. Bennett, S. Mukhopadhyay, G. Cinque, F. Fernandez-Alonso, D. De Vos, S. Rudic and J. C. Tan, *Phys. Rev. Lett.*, 2017, **118**, 255502.

193. M. R. Ryder, Z. Zeng, Y. Sun, T. D. Bennett, I. Flyagina, K. Titov, E. M. Mahdi, B. Civalleri, C. S. Kelley, M. D. Frogley, G. Cinque and J. C. Tan, *arXiv:1802.06702 [cond-mat.mtrl-sci]*.

194. W. Volksen, R. D. Miller and G. Dubois, *Chem. Rev.*, 2010, **110**, 56-110.

195. M. R. Ryder, B. Civalleri, G. Cinque and J. C. Tan, *CrystEngComm*, 2016, **18**, 4303-4312.

196. M. R. Ryder, T. D. Bennett, C. S. Kelley, M. D. Frogley, G. Cinque and J. C. Tan, *Chem. Commun.*, 2017, **53**, 7041-7044.

197. K. W. Chapman, G. J. Halder and P. J. Chupas, *J. Am. Chem. Soc.*, 2009, **131**, 17546-17547.

198. C. E. Wilmer, M. Leaf, C. Y. Lee, O. K. Farha, B. G. Hauser, J. T. Hupp and R. Q. Snurr, *Nat. Chem.*, 2012, **4**, 83-89.

199. P. Li, N. A. Vermeulen, C. D. Malliakas, D. A. Gomez-Gualdron, A. J. Howarth, B. L. Mehdi, A. Dohnalkova, N. D. Browning, M. O'Keeffe and O. K. Farha, *Science*, 2017, **356**, 624-627.

200. F. X. Coudert, *Chem. Mater.*, 2015, **27**, 1905-1916.

201. T. Helgaker, J. Olsen and P. Jorgensen, *Molecular Electronic Structure Theory*, Wiley-Blackwell, 2013.

202. A. Szabo and O. N. S., *Modern Quantum Chemistry: Introduction to Advanced Electronic Structure Theory*, Dover Publications Inc., 1996.

203. J. Simons, *An Introduction to Theoretical Chemistry*, Cambridge University Press, 2003.

204. J. C. Slater, *Phys. Rev.*, 1929, **34**, 1293-1322.

205. C. Møller and M. S. Plesset, *Phys. Rev.*, 1934, **46**, 618-622.

206. K. S. Park, Z. Ni, A. P. Cote, J. Y. Choi, R. Huang, F. J. Uribe-Romo, H. K. Chae, M. O'Keeffe and O. M. Yaghi, *Proc. Natl. Acad. Sci. U. S. A.*, 2006, **103**, 10186-10191.

207. M. J. Frisch, G. W. Trucks, H. B. Schlegel, G. E. Scuseria, M. A. Robb, J. R. Cheeseman, G. Scalmani, V. Barone, B. Mennucci, G. A. Petersson, H. Nakatsuji, M. Caricato, X. Li, H. P. Hratchian, A. F. Izmaylov, J. Bloino, G. Zheng, J. L. Sonnenberg, M. Hada, M. Ehara, K. Toyota, R. Fukuda, J. Hasegawa, M. Ishida,

T. Nakajima, Y. Honda, O. Kitao, H. Nakai, T. Vreven, J. A. Montgomery Jr., J. E. Peralta, F. Ogliaro, M. J. Bearpark, J. Heyd, E. N. Brothers, K. N. Kudin, V. N. Staroverov, R. Kobayashi, J. Normand, K. Raghavachari, A. P. Rendell, J. C. Burant, S. S. Iyengar, J. Tomasi, M. Cossi, N. Rega, N. J. Millam, M. Klene, J. E. Knox, J. B. Cross, V. Bakken, C. Adamo, J. Jaramillo, R. Gomperts, R. E. Stratmann, O. Yazyev, A. J. Austin, R. Cammi, C. Pomelli, J. W. Ochterski, R. L. Martin, K. Morokuma, V. G. Zakrzewski, G. A. Voth, P. Salvador, J. J. Dannenberg, S. Dapprich, A. D. Daniels, Ö. Farkas, J. B. Foresman, J. V. Ortiz, J. Cioslowski and D. J. Fox, *Gaussian 09, Revision B.01*, Gaussian, Inc., Wallingford, CT, USA, 2009.

208. R. A. Kendall, T. H. Dunning and R. J. Harrison, *J. Chem. Phys.*, 1992, **96**, 6796-6806.
209. J. Sadlej, A. Jaworski and K. Miaskiewicz, *J. Mol. Struct.*, 1992, **274**, 247-257.
210. N. Sundaraganesan, S. Ilakiamani, P. Subramani and B. D. Joshua, *Spectrochim. Acta, Part A*, 2007, **67**, 628-635.
211. D. A. Carter and J. E. Pemberton, *J. Raman Spectrosc.*, 1997, **28**, 939-946.